

Geotechnical Investigation of
Sediment Remobilization Processes
using Dynamic Penetrometers

Doctoral Thesis

*Submitted for the doctoral degree in natural sciences
at the Faculty of Geosciences of Bremen University*

*Zur Erlangung des Doktorgrades der Naturwissenschaften
im Fachbereich Geowissenschaften der Universität Bremen*

*by
vorgelegt von*

Nina Stark

Bremen, September 2010

Abstract

The understanding of naturally and anthropogenically induced subaqueous sediment remobilization processes is of high importance for the increasing industrial and touristy usage of coastal zones, estuaries, rivers and lakes. Geotechnical properties such as sediment strength play an important role in sediment dynamical processes, however, they are poorly represented in theoretical approaches and field studies, because geotechnical *in-situ* measurements are highly complicated in such challenging areas (e.g., strong hydrodynamics, close to offshore constructions). From previous studies it can be assumed that dynamic penetrometers might be capable of such measurements. The aim of this thesis was to find out (i) whether dynamic penetrometers are suitable for measurements in areas of sediment remobilization, and (ii) if so, what kind of complementary data can be delivered for the research of sediment remobilization.

Different types of dynamic penetrometers were introduced: lance-like or projectile-like shapes, expendable and recoverable probes with different set ups of sensors and data acquisition systems. However, none of the existing penetrometers matched all of the requirements assumed for the detection of sediment remobilization. Following that, a new device was designed: the *Nimrod*, truly free falling with a projectile-like shape and equipped with accelerometers (measuring deceleration and inclination), pore pressure and temperature sensor. A choice of three different tip geometries (flat circular tip, hemisphere, cone) provides a high sensitivity over a wide range of sediment types (very soft mud to hard sand). The *Nimrod* was tested in streams, rivers and ports before being successfully deployed in the North Sea and the Baltic Sea. In the North Sea the device demonstrated an outstanding suitability for sandy seafloors due to its robustness, the decoupling from the boat during deployment and the high data recording frequency (1 kHz). Following that and the fact that a lot of sediment remobilization features can be found in sandy areas, the investigation of different sandy sediments was intensified by adding measurements on carbonate sands in Hawaii. Different penetration signatures could be found for quartz sand compared to carbonate sand. Furthermore, an approach was presented to estimate quasi-static bearing capacity from the dynamic

Abstract

deceleration – depth profiles of the penetrometer to consider the change of penetration velocity and penetration surface area.

In data sets from the Jade tidal inlet channel (North Sea) and shore breaks in Hawaii hints of sediment remobilization were detected in the penetrometer signatures. More detailed surveys in areas of sediment remobilization followed: (i) subaqueous dunes in the Danish Wadden Sea, (ii) sorted bedforms close to Tairua, NZ, (iii) a shifting sandbar at Raglan's harbor mouth, NZ, (iv) scouring at offshore wind energy converter foundations (North Sea), (v) mud accumulation and mud layers in different ports, (vi) disposal sites and (vii) geothermal lakes in New Zealand.

First, the results confirmed that layers of mixed up sediment or fresh sediment redeposition are reflected in the sediment strength – depth profiles derived from the dynamic penetrometer and that a quantification of these layers is possible with an accuracy of ~ 1 cm. In doing so, e.g., variations of sediment remobilization over a tidal cycle were observed. Additionally, changes of sediment strength patterns over time were monitored: over a tidal cycle along subaqueous dunes, and especially, at offshore wind energy converters (WEC) over a few months after WEC erection.

Furthermore, areas of sediment erosion and sediment accumulation were localized and quantified providing a suitable base for the development of a conceptual model of the formation and/or maintenance of the respective sediment dynamic feature. This succeeded for sandy areas (e.g., sorted bedforms, shifting sandbar) as well as for muddy areas (e.g., ports, lakes). In the latter the results may also play an important role for decisions about the further industrial use of areas or further interventions such as dredging.

In summary, the new penetrometer *Nimrod* proved its suitability for the investigation of sediment remobilization processes and delivered complementing data about ongoing sediment remobilization with time (e.g., tides, timeline after WEC erection) and space (indication of areas of sediment erosion or accumulation). During the different surveys the dynamic penetrometer results were supported by acoustic methods, sediment sampling and/or numerical modelling of hydrodynamics. A stronger geotechnical perspective was introduced into the investigation of the sediment remobilization processes.

However, some questions could not be answered by the field experiments due to a lack of continuity of boundary conditions

such as currents, stability of the vessel or sediment homogeneity. Examples are the detailed investigation of penetration rate effects, or the finding of a correlation between *in-situ* density and measured sediment strength. To address such issues, in this thesis also first attempts of physical modelling in a wave channel and of numerical modelling using the geotechnical code FLAC3D are presented and discussed as an outlook to future works.

Zusammenfassung

Das Verständnis von natürlich wie auch anthropogen induzierten marinen Sedimentremobilisationsprozessen ist entscheidend für die steigende industrielle und touristische Nutzung von Küstenzonen, Ästuaren, Flüssen und Seen. Geotechnische Eigenschaften wie die Sedimentfestigkeit spielen eine wichtige Rolle in sedimentdynamischen Prozessen, sind jedoch wenig repräsentiert in den entsprechenden theoretischen Ansätzen und Feldexperimenten. Aus vorausgehenden Studien kann angenommen werden, dass prinzipiell dynamische Penetrometer für solche Messungen geeignet sein könnten. Das Ziel dieser Arbeit war es herauszufinden, ob eine solche Eignung bestätigt werden kann, und falls ja, welche Art von neuen Informationen zur Erforschung von Sedimentremobilisationsprozessen dadurch ermittelt werden können.

Verschiedene Typen von dynamischen Penetrometern sind bekannt. Jedoch erfüllte keines der bekannten Geräte alle Anforderungen, die für die Messung von Sedimentremobilisationsprozessen angenommen werden. Demzufolge wurde ein neues Gerät entwickelt: *Nimrod*, frei fallend, mit einer projektilähnlichen Form und ausgestattet mit Sensoren zur Messung von Abbremsung, Neigung, Temperatur und Porendruck. Nach der Konstruktion wurde *Nimrod* in diversen Bächen, Flüssen und Häfen sowie in der Nord- und Ostsee getestet, wobei die erfolgreiche Konzeption des Geräts belegt werden konnte. Bei Einsätzen in der Nordsee fiel die Eignung für Messungen auf sandigen Böden auf. Vor allem wegen der geringen Eindringtiefe gelten dynamische Penetrometer allgemein als wenig geeignet für Messungen in sandigen Gebieten. *Nimrods* Robustheit, die absolute Entkopplung von jeglichen Schiffsbewegungen und die hohe Datenaufnahmefrequenz (1 kHz) führen jedoch zu einer hohen Datenpräzision bei der Messung auch von sandigen Oberflächensedimenten. Demzufolge wurden Messungen in sandigen Gebieten ausgeweitet mittels Messkampagnen auf Karbonatsand in Hawaii. Dabei konnten die Penetrationssignaturen von Quarzsand und Karbonatsand deutlich voneinander unterschieden werden. Außerdem wurde in diesem Rahmen ein Ansatz eingeführt, um quasi-statische Tragfähigkeit aus dynamischen Abbremsung – Tiefe Profilen des Penetrometers abzuschätzen.

In Daten aus dem Tidekanal des Jadebusens (Nordsee) und aus Brandungen in Hawaii zeigten sich erste Hinweise auf Sedimentremobilisation in den Penetrationssignaturen. Weitere detaillierte Erkundungen in Gebieten charakterisiert durch Sedimentremobilisation folgten: (i) subaquatische Dünen im Dänischen Wattenmeer, (ii) morphologische Strukturen mit Körngrößensortierung nahe Tairua, NZ, (iii) eine sich verlagernde Sandbank bei Raglan, NZ, (iv) Kolk an Offshore-Windenergieanlagen (Nordsee), (v) Schlickablagerung und Schlicklagen in verschiedenen Häfen, (vi) in Gebieten ausgewählt für die Verklappung von gebaggertem Hafensediment und (vii) in geothermalen Seen, NZ.

Die Ergebnisse bestätigten, dass Lagen von aufgemischtem oder frisch abgelagertem Sediment in Sedimentfestigkeit – Tiefen Profilen von dynamischen Penetrometern mit einer Genauigkeit von ~ 1 cm detektiert und quantifiziert werden können. Auf diese Weise wurden zum Beispiel Variationen von Sedimentremobilisation entlang subaquatischer Dünen über einen Tidenzyklus beobachtet.

Außerdem wurden Änderungen der Sedimentfestigkeit über die Zeit festgestellt, einerseits über einen Tidenzyklus auf subaquatischen Dünen, und andererseits über einige Monate nach der Installation von Offshore-Windenergieanlagen in der Nordsee.

Desweiteren konnten Erosionszonen bzw. Akkumulationszonen lokalisiert und quantifiziert werden. Diese Ergebnisse bilden eine Basis zur Entwicklung eines konzeptionellen Modells für die Formation und Entwicklung von morphologischen Strukturen. Dies wurde anhand von Ergebnissen von z.B. morphologische Strukturen mit Körngrößensortierung nahe Tairua, NZ, belegt. Auch in schlickigen Gebieten konnten dafür Beispiele (z.B. Schlickablagerungen in Häfen in Neuseeland) gefunden werden. Gerade in industriell genutzten Gebieten mag dies die Entscheidungsfindung betreffend weiterer ingenieurstechnischer Eingriffe wie Baggern unterstützen.

Es kann zusammengefasst werden, dass *Nimrod* seine Eignung für die Untersuchung von Sedimentremobilisationsprozessen beweisen und zusätzliche Daten über aktuelle Sedimentremobilisationsprozesse abhängig von Zeit (z.B. innerhalb eines Tidenzyklus) und Raum (z.B. Lokalisierung von Erosionszonen) liefern konnte. In den verschiedenen Kampagnen wurden die geotechnischen Messungen von akustischen Methoden, Sedimentprobennahme und/oder numerischer Modellierung der

Zusammenfassung

Hydrodynamik unterstützt.

Allerdings konnten einige Zusammenhänge im Feld nicht vollständig geklärt werden, da die Kontrolle über Randbedingungen wie Strömungen, Schiffsbewegung oder die Homogenität des Sediments nicht ausreichte, um zum Beispiel die genutzten Ansätze zur Berücksichtigung der sich ändernden Penetrationsgeschwindigkeit im Detail und unter kontrollierten Bedingungen zu überprüfen, oder als weiteres Beispiel, eine Korrelation zwischen *in-situ* Dichte und gemessener Sedimentfestigkeit zu finden. Für solche Fragestellungen wurde begonnen einen numerischen Ansatz zur Simulation von Penetrometermessungen auf sandigen Böden zu entwickeln und ein Ausblick auf weitere numerische und physikalische Modellierung gegeben.

Contents

1	Introduction	13
1.1	Motivation	13
1.2	Description of the PhD project	17
2	State-of-the-art	19
2.1	Dynamic penetrometers	19
2.1.1	The benefit of penetrometers in marine sciences and in marine geotechnical exploration	19
2.1.2	Penetrometers in marine sciences: Quasi-static vs. dynamic instruments	20
2.1.3	Performance and theory of dynamic penetrometers	21
2.1.4	First experiments on penetration rate effects	23
2.1.5	Comparison of different marine dynamic penetrometers and their performance offshore	25
2.1.6	Requirements in areas of sediment remobilization	29
2.2	Sediment dynamics	29
2.2.1	Theoretical introduction	29
2.2.2	Techniques used for the investigation of sediment dy- namics <i>in-situ</i>	39
3	<i>Nimrod</i>	45
3.1	Design	45
3.1.1	Shape	46
3.1.2	Material	50
3.1.3	Sensors	55
3.1.4	Data acquisition and power supply	56
3.1.5	Realization	56
3.2	Preliminary testing	61
3.2.1	Pressure resistance and sealing	61

3.2.2	Estimate of force needed for the recovery of the instrument	61
3.2.3	Test of sensors and assembled device	62
3.3	Proof of concept	63
3.3.1	Measurements on various sediments	63
3.3.2	Measurements on sand	70
4	Geological applications	95
4.1	Quartz vs. carbonate sand	95
4.1.1	Geological manuscript I	96
4.2	Subaqueous dunes	121
4.2.1	Geological manuscript II	121
4.3	Sorted bedforms	143
4.3.1	Geological manuscript III	143
5	Ongoing projects	169
5.1	Cohesionless sediments	169
5.1.1	Scouring at WEC tripod foundations (RAVE)	169
5.1.2	Wave flume	187
5.1.3	Shifting sandbar	192
5.2	Cohesive sediments	206
5.2.1	Fluid mud and mud accumulation in ports	206
5.2.2	Harbor mud disposal sites	211
5.2.3	The diversion wall in Lake Rotoiti as a sediment trap for fine sediment transported from Lake Rotorua via the Ohau Channel to Lake Rotoiti and the Kaituna River, New Zealand	216
5.3	Attempt of a numerical simulation	224
5.3.1	Numerical modeling of dynamic penetrometer – sediment – interaction (a state-of-the-art)	226
5.3.2	Choice of commercial code	231
5.3.3	Set up	232
5.3.4	Exemplary test run	238
6	Conclusions	243
7	Outlook	247
8	Acknowledgements	251
9	References	257

A Abstracts	269
B List of field work	277
C More data	281
C.1 Emden harbor, GER	281
C.2 Kiel harbor, GER: <i>Tirpitzhafen</i>	283
C.3 Kaneohe Bay, HI	285
C.4 Lake Tarawera, NZ	286
C.5 Port of Taranaki, New Plymouth, NZ	288
C.6 Port of Tauranga, NZ, 2010	290
C.7 Lake Rotoiti, NZ: crater and geothermal area	291
C.8 Lake Rotorua, NZ: pockmarks and geothermal area	293
D Penetrometer raw data	297
E FLAC3D input code example	299
F Erklärung	309

Chapter 1

Introduction

1.1 Motivation

Remobilization processes of seafloor sediments spark an increasing interest in coastal conservation as well as coastal and marine engineering. Naturally evolved sediment remobilization features, such as sandbars, bedforms and fluid mud, influence the coastline (e.g., Mimura and Nunn, 1998) and have an impact on the industrial or touristy utilization of those areas (e.g., port development, beach erosion) (e.g., Phillips and Jones, 2006). Vice versa, marine engineering induces and modifies hydrodynamics as well as sediment dynamics with a potential back-coupling impacting on the stability of the construction or the surrounding environment (e.g., Whitehouse, 1998). Following that, the understanding of subaqueous sediment dynamics is a key parameter for the conservation of coastlines as well as for the utilization of coastal zones.

Sediment dynamics are investigated using (i) physical models, (ii) numerical models, and (iii) *in-situ* experiments. These three approaches can be understood as the three main pillars for the investigation of sediment dynamics (Fig. 1.1).

For the prediction of sediment remobilization, numerical models play an important role. They aim for the determination of mud discharge (e.g., Waelles et al., 2007) in areas of potential port expansion or the prediction of scour depressions at structures of marine engineering (e.g., Li and Cheng, 1999), for example. However, the quality of the numerical models highly depends on the understanding of the process and the input of parameters (e.g., Copeland, 1987). This knowledge can be gathered by field studies and physical models. The latter are carried out in flumes or tanks, and offer the opportunity to study sediment remobilization processes in a well controlled

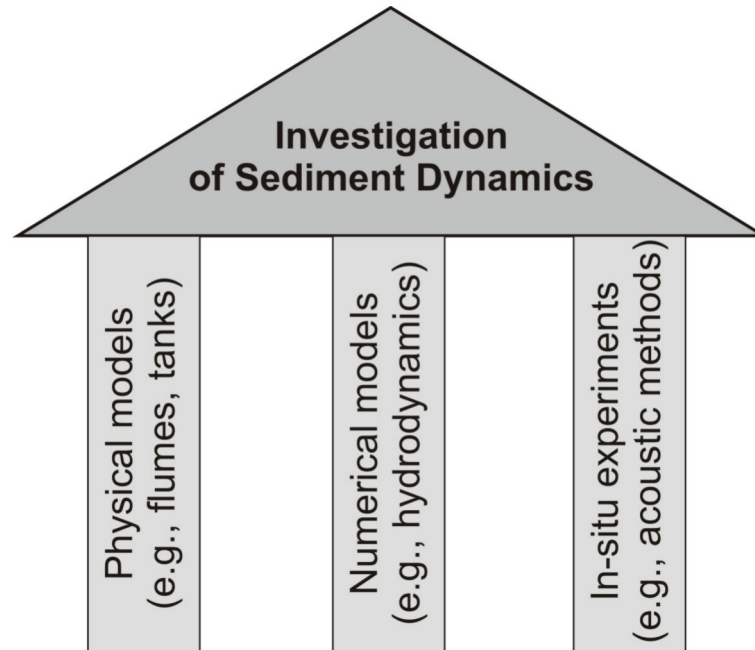


Figure 1.1: The three pillars of the investigation of sediment dynamics.

environment (e.g., Blom et al., 2003), e.g., waves and/or currents can be set up in a chosen configuration. In doing so, the influence of wave height on scour development can be determined, for example. Nevertheless, also physical model results follow their set up configuration. In consequence, influencing factors occurring in the field might be neglected or even be missed (e.g., Weill et al., 2008). Furthermore, flume and tank experiments are highly affected by boundary effects (e.g., Hughes, 1993). Even the biggest flumes and tanks are still very small-scale models compared to open waters.

Thus, field studies as the third pillar of investigations for the understanding of sediment remobilization processes are required. Such field studies focus on (i) hydrodynamics, (ii) morphodynamics and (iii) sediment dynamics. Under the term hydrodynamics primarily currents, tides and waves are united. They are addressed, e.g., with acoustic methods such as acoustic Doppler current profilers (e.g., Muste et al., 2004), pressure gauges (e.g., Trupin and Wahr, 2007), buoys such as the waverider (e.g., O'Reilly et al., 1996), and underwater as well as water surface gliders (e.g., Rudnick et al., 2004). The understanding of hydrodynamics is in a fast developing progress. However, especially, the complexity of turbulences and the interaction on different scales is one example of ongoing research (e.g., Lorke and Wuest, 2005). Here, also interactions with the bathymetry have to be mentioned (e.g.,

Soulsby et al., 1993). The morphodynamics in areas of sediment remobilization are mainly investigated using imaging techniques such as single beam echosounder systems, multi beam echosounder systems and side scan sonars. They show small- and large-scale variations of the bathymetry depending on the hydrodynamics and the sediment (e.g., Ernstsens et al., 2006).

The sediment dynamics cover different processes, such as bedload transport or sediment suspension (Swamee and Ojha, 1991). Focussing on the sediment, the question is which sediment is mobilized when and in which form (e.g., bedload or suspended load). Blinding out hydrodynamics and morphodynamics, physical and geotechnical properties come to the fore. The grain size distribution is addressed most (e.g., Soulsby, 1997) following the fact that sorting can be found (i) along features of sediment remobilization (e.g., Goff et al, 2005), and (ii) and in the different forms of sediment transport (Swamee and Ojha, 1991). However, also, e.g., density, friction angle and cohesion influence the threshold shear stress, and in doing so, the mobility of sediments (Das, 1990; Soulsby, 1997).

These properties are mirrored in sediment strength measurements using cone penetrometers (Lunne et al., 1997). Following onshore standards, such instruments measure tip resistance, sleeve friction, pore pressure, inclination and sometimes temperature (Lunne et al., 1997). Sediment density, friction angle, cohesion and pore pressure influence the shearing behavior of the sediment (Terzaghi, 1943; Das, 1990) reflected in the sediment resistance opposed to a penetrometer (Lunne et al., 1997). This is measured using the tip resistance sensor. The magnitude of side friction and side adhesion can be monitored using the sleeve friction sensor. Pore pressure can be determined separately using the respective sensor and should be considered during the calculation of sediment resistance from the measured tip resistance. In consequence, key parameters concerning the mobility of sediments (e.g., density, friction angle, cohesion) are expressed in sediment strength profiles of cone penetrometers.

In the process, penetrometers can be deployed in a dynamic and a quasi-static manner (e.g., Dayal, 1980; Stoll et al., 2007). In case of the latter, the penetrometer is pushed by an engine into the sediment keeping a constant penetration velocity. However, these devices require a big frame to support the engine and keep the penetrometer stable during the penetration process. This appears as a disadvantage in the research of sediment remobilization processes, because the frame would disturb, on the one hand, the uppermost layers of the seafloor, and on the other hand, the bottom currents. Dynamic penetrometers penetrate the seafloor by their own weight and momentum, and in doing so, do not require a frame. Furthermore, the deployments are technically simpler so that dynamic penetrometers can be

used in more challenging areas. Due to the change of momentum during penetration, deceleration sensors have to be added to the devices. These can be also used to estimate sediment strength (e.g., Eastgaard et al., 1997; Stoll et al., 2007), different grain size groups (e.g., Stoll and Akal, 1999; Stark and Wever, 2008) and variations in density (e.g., Boguslavskii et al., 1996). This would make even simple dynamic penetrometers an attractive tool to complement field studies in areas of sediment dynamics, especially, if the dynamic penetrometer fulfils the following criteria:

1. The deployment technique should be quick and simple. Even a deployment by hand should be possible. This would offer the possibility for surveys from small vessels which are capable of navigating in challenging areas such as areas with breaking waves or close to offshore structures (e.g., wind energy converters).
2. The design of the device should provide a fast and stable vertical fall through the water column to minimize disturbances by hydrodynamics and increase the accuracy in positioning.
3. The data acquisition system should work on a high frequency (~ 1 kHz) leading to a high resolution after data processing. A vertical resolution of about 1 cm is required to detect very small-scale changes of remobilized sediment layers.
4. A big range in sensitivity for sediment resistance must be targeted to cover sediment remobilization processes on all types of sediments (mud, sand, etc.).

In the literature a variety of dynamic penetrometers can be found fulfilling one or the other of the above mentioned requirements, but none of the devices seems to match perfectly (e.g., Dayal, 1980; Ingram, 1982; Beard, 1985; Stoll and Akal, 1999; Stegmann et al., 2006a; Stoll et al., 2007).

Consequently, the aim of this dissertation is (i) the development of a dynamic penetrometer suitable for the investigation of a variety of sediment remobilization processes *in-situ*, (ii) to test the hypothesis that sediment strength - penetration depth profiles derived by dynamic penetrometers can be correlated to sediment mobility, and (iii) to implement the new results to the ongoing research about sediment dynamics in coastal zones and the shallow marine realm.

1.2 Description of the PhD project

The dissertation time started October 2007. The first six months were used for the general study of dynamic penetrometers (chapter 2.1) including gathering experiences and ideas using the already existing shallow-water free-fall cone penetration test lance (FF-CPTU) (e.g., Stegmann, 2006a), and for the design and construction of the new dynamic penetrometer called *Nimrod* (chapter 3). In April 2008, *Nimrod's* construction phase was finalized and the device was ready for testing.

In the following six months, *Nimrod* was tested first in the Kuhgraben, a small local river close to the University of Bremen (chapter 3.2). Then first deployments in sandy areas were carried out in the framework of a cruise in the Jade tidal inlet channel, North Sea, with R/V Senckenberg, and during the first cruise to the wind energy test field *Alpha Ventus*, German Bight, North Sea, with R/V Wega. In summer 2008, the device was deployed on mud during a cruise in the Eckernförder Bight, Baltic Sea, with R/V Schwedeneck. The results of these tests proved the suitability of the device in areas containing different sediments, and were successfully processed and interpreted leading to a publication in *Sea Technology* (chapter 3.3.1). Furthermore, they gave first hints that sediment remobilization and grain size distributions might be monitored using *Nimrod* (subaqueous dunes in the Jade tidal inlet channel). Consequently, the next step was to intensify the deployment in areas of sediment remobilization as well as the deployment strategies in sandy areas.

In November 2008, a cruise with R/V Senckenberg to an area characterized by subaqueous dunes in the Knudedyb tidal inlet channel (Danish Wadden Sea) offered the possibility to measure variations of sediment remobilization with time within a whole tidal cycle supported by imaging acoustic methods (multi beam echosounder), acoustic Doppler current profiling (ADCP) and estimation of suspension material using backscatter signals from up-looking ADCP resulting in a manuscript submitted to *Geo-Marine Letters* (chapter 4.2).

In December 2008 and January 2009, a research stay at the University of Hawaii made it possible to deploy the instrument on carbonate sand to prove the suitability for sand differentiation resulting in a nomination and publication in the framework of the student poster award at the OCEANS 09 conference in Biloxi, US, (chapter 3.3.2). Another manuscript submitted to *Geotechnical and Geological Engineering* about the comparison of the geotechnical behavior of carbonate sands to quartz sands (chapter 4.1) followed after having tested the Hawaiian carbonate sands and the North Sea quartz sands in the geotechnical laboratory in 2009.

In April 2009, the second cruise to the windfarm test field *Alpha Ventus* with R/V *Wega* completed the *in-situ* measurements in this area prior to wind energy converter erection and formed a baseline of geotechnical values characterizing the area in its undisturbed state. In November 2009 and April 2010, two cruises after wind energy converter erection followed, delivering unique measurements close to the foundations using *Nimrod* as well as acoustic methods (multi beam echosounder, side scan sonar) and standard FF-CPTU measurements (the latter in a distance of ~ 50 m from the wind energy converters). The results were presented at the European Geological Union General Assembly in a session about “Sciences in support of renewable energies offshore”, were accepted for presentation at the OCEANS 2010 in Sydney, and another manuscript is in preparation (chapter 5.1.1).

In summer 2009 and spring 2010, two research stays at the University of Waikato, New Zealand, offered additional work in areas of different sediment remobilization features including slowly evolving sorted bedforms (chapter 4.3), a shifting sandbar in the harbor mouth of Raglan (chapter 5.1.3), fluid mud measurements in the Port of Tauranga and Lyttelton Port of Christchurch (chapter 5.2.1), a harbor mud disposal site at the continental shelf edge (chapter 5.2.2) and fine sediment remobilization in geothermal lakes (chapter 5.2.3). These surveys are presented in a manuscript submitted to the Journal of Sedimentary Research, two abstracts were accepted for the COASTAL SEDIMENTS 2011 conference, and two manuscripts are currently in preparation.

During the approximately 20 surveys the device proved to deliver reliable information about sediment strength which can be used for the interpretation of sediment remobilization processes. However, concerning absolute strength values, smallest changes in physical properties of the sediment (e.g., grain size, grain shape) can lead to significant variations in strength. This is especially poorly investigated for deployments of dynamic penetrometers on sandy sediments. Following that, the idea came up to set up a numerical model simulating a dynamic penetration of *Nimrod* into sandy seafloors to specify the effects of small changes in physical properties of sand on the penetration signals. Since beginning 2010 such a model is in development using FLAC3D. The idea and a start-up are presented in chapter 5.3.

In summary, the PhD project included (i) the development, testing and start-up of a new dynamic penetrometer suitable for the investigation of sediment remobilization processes, (ii) geotechnical and geophysical measurements and interpretations in the framework of geological and geo-engineering projects focussing on sediment remobilization, and (iii) a preliminary attempt of numerical modeling of the sediment - penetrometer interaction.

Chapter 2

State-of-the-art

2.1 Dynamic penetrometers

2.1.1 The benefit of penetrometers in marine sciences and in marine geotechnical exploration

For various fields of marine sciences (e.g., slope stability research), naval applications (e.g., mine burial) and in the framework of marine geotechnical exploration (e.g., offshore wind energy) the sediment strength in terms of shear strength, cohesion or bearing capacity of marine sediments is required. Laboratory methods are one way to derive this information. Generally, they offer a wide range of possibilities to test different geotechnical properties of the sediment, and follow international standards. To mention just a few examples, the vane shear apparatus or the falling cone are standard methods to estimate shear strength, and the friction angle can be determined by uniaxial, triaxial or rotary shear tests (e.g., Das, 1990).

However, a possible issue regarding the laboratory methods might be the sampling method. Usually, material is taken as grab samples or sediment cores. Even though the sampling and coring devices are well developed, it can be assumed that the texture of the sediment may be disturbed by sampling, transport and storage until the sample is investigated in the laboratory (Blomqvist, 1991). Furthermore, it might come to a drainage of the sample, and for sure, the sample is exposed to significant changes in environmental conditions (e.g., pressure, temperature, etc.). Following that, a deviation between *in-situ* strength and the results from the laboratory must be considered (e.g., Johnson et al., 1988). This makes *in-situ* sediment strength measurements an important complement to laboratory methods.

Traditionally, simple methods such as the “diver’s-fist-blow” (A diver tries

to penetrate the seafloor with his fist and measures how deep he gets into the seafloor.) were used to get an idea of the sediment strength (soft/hard). Similarly, the number of slaves required to push a cone into soil served as a measure for strength. Of course, these methods do not satisfy the requirements of scientific accuracy. Additionally, a lot of offshore conditions prohibit diver operations, and in general, diver operations can be elaborate and expensive. This also hampers the use of vane shears applied by divers, or from moored platforms.

A type of instrument is required that can be operated from a vessel at the water surface. Penetrometers were used onshore since the 1940s (Lunne et al., 1997) and were first utilized for offshore deployments in the 1970s (Dayal et al., 1973).

2.1.2 Penetrometers in marine sciences: Quasi-static vs. dynamic instruments

Conform to the development onshore, so-called quasi-static penetrometers (e.g., Ruiter and Fox, 1975) as well as dynamic penetrometers (e.g., Dayal et al., 1973) were introduced to the marine realm.

Quasi-static penetrometers penetrate the seafloor with a constant velocity (standard: 0.02 m/s after Lunne et al., 1997) and are driven by an engine, whereas dynamic penetrometers hit the seafloor with a certain impact velocity (e.g., achieved during free fall) and decelerate with loss of momentum until the device stops. Both systems have advantages and disadvantages. Quasi-static penetrometers (e.g., STATPEN, Fig. 2.1, Stoll, 2006) are designed after onshore standards (e.g., ASTM D2441). Hence, data processing techniques from onshore methods can be adopted. The results are reliable and can often correlate well with standard methods (Stoll, 2006). Regarding data quality and reliability, quasi-static *in-situ* penetrometers are the method of choice. However, the deployment of such devices requires (i) time, (ii) a vessel (including winch) big enough to handle the device (a few hundred kilograms and a frame in the range of meters), and (iii) good weather conditions, ergo, it is time- and cost-consuming and highly weather-dependent.

These limitations do not necessarily apply to dynamic penetrometers. The dimensions of dynamic penetrometers vary from decimeters length and a few kilograms (e.g., XBP, Stoll and Akal, 1999) to a few meters and hundreds of kilograms (e.g., deep-water FFCPTU, Kopf et al., 2007) (Fig. 2.2). Considering all variations, they cover a wide range of water and weather conditions. Following that, they can be a very cost- and time-effective device



Figure 2.1: The marine static penetrometer STATPEN (Stoll, 2006).

and make a high deployment frequency possible (Stegmann et al., 2006a). The disadvantages are a (i) complicated non-linear backcoupling between the measured sediment resistance and the decrease in penetration velocity with depth (Dayal et al., 1973), (ii) a lack of control during deployment due to the free-fall technique, and (iii) a small penetration depth depending on the sediment strength (range of decimeters to meters). In the following section, the deployment performance and its consequences will be explained in detail.

2.1.3 Performance and theory of dynamic penetrometers

Dayal et al. (1973) defined a marine impact cone penetrometer as a “cone-tipped right circular cylinder which after impacting penetrates the target (a soil medium) under its own momentum gained during free or forced drop”, and concluded that “in addition to obtaining the strength profile, the soil types, location, and depth of different layers can also be estimated”. Matching this first definition, marine dynamic penetrometers fall freely or are lowered by a winch, are driven by their own weight and impact the seafloor with a certain velocity. Even in case of free fall, the impact velocity will not

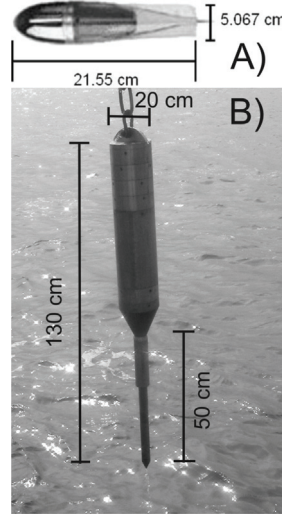


Figure 2.2: Two marine dynamic penetrometers: A) the eXpendable Bottom Penetrometer (XBP) as an example for an projectile-like design, and B) the shallow water cone penetration test lance (FFCPTU) developed at MARUM, University of Bremen. The configuration of the FFCPTU can be changed by, e.g., adding rods.

exceed a so-called terminal velocity following the equation of motion including inertial force, driving force (here weight) and opposite-directed resistive force. Resistive forces are, e.g., drag, drag of the tether, buoyancy. Dayal et al. (1973) formulated this the following way excluding the drag of the tether:

$$m_p \frac{d^2 x}{dt^2} + W_B - \frac{1}{2} C_D \rho_W A \left(\frac{dx}{dt} \right)^2 = 0, \quad (2.1)$$

with m_p being the mass of the penetrometer, x the distance in time t , W_B the buoyant weight of the penetrometer, C_D the drag coefficient, ρ_W mass density of water and A the frontal area of the penetrometer.

During impact and penetration process the sediment opposes a resistance against the probe. This resistance contains (i) a base resistance acting on the surface of the penetrometer tip, (ii) a skin or local side friction at the shaft, and (iii) the additional mass of the displaced sediment. After Dayal et al. (1973) the latter leads to change of momentum at a rate with respect to time defined by:

$$A\nu^2 + \frac{1}{2}(m + Az) \frac{d(\nu^2)}{dz}, \quad (2.2)$$

where ν stands for the velocity, m for the mass of the penetrometer and the displaced sediment and z for the vertical penetration. The rate of change

of momentum depends on penetration depth, and influencing the resistive force, expresses the non-linear backcoupling between penetration rate and measured sediment resistance. Disturbing the measured value of sediment resistance, it is one the main issues of dynamic penetrometers.

The skin friction depends on penetration depth z , cohesion c and friction angle of the soil ϕ . After Dayal et al. (1973) the total skin friction can be defined as:

$$2\pi cz + \pi K_0 \rho g r z^2 \tan \phi, \quad (2.3)$$

introducing r as the radius of the penetrometer, K_0 as the earth pressure coefficient (0.5 for sand and 1.0 for clay), ρ as the density and g as gravitational acceleration.

The base resistance at the penetrometer tip is the expression of sediment strength which is aimed for. It was introduced by Terzaghi (1943) as the maximum load a soil can bear before failure, or the maximum resistance a sediment can bring up before failure, and can be defined as bearing capacity q_u . It can be expressed in terms of cohesion c , surcharge q and soil weight γ :

$$q_u = q_c + q_q + q_\gamma = cN_c + qN_q + \frac{1}{2}\gamma BN_\gamma, \quad (2.4)$$

with q_c being the contribution of cohesion, q_q the contribution of surcharge, q_γ the contribution of soil weight, N the bearing capacity factors depending on the soil friction angle and B being the width of penetrating object (Das, 1990). Terzaghi's bearing capacity equation has been refined by several investigators (e.g., Meyerhof, 1953; Lundgren and Mortensen, 1953; DeBeer and Vesic, 1958; Balla, 1962; DeBeer, 1970; Hansen, 1970; Vesic, 1973) concerning dependence of bearing capacity factors on friction angle, shape factors, depth factors and inclination factors.

The approach is based on a concept of shear failure (Fig. 2.3) developed by Terzaghi (1943) and modified by Meyerhof (1953).

2.1.4 First experiments on penetration rate effects

Before using the proposed penetrometer offshore, Dayal and Allen (1975) addressed the problem of penetration rate effects using laboratory experiments. Therefore, the dynamic cone penetrometer was pushed with varying controlled velocities (static or dynamic, max. 0.81 m/s) into pottery clay and into sand, respectively. For cohesive soils the authors proposed the following empirical relationship:

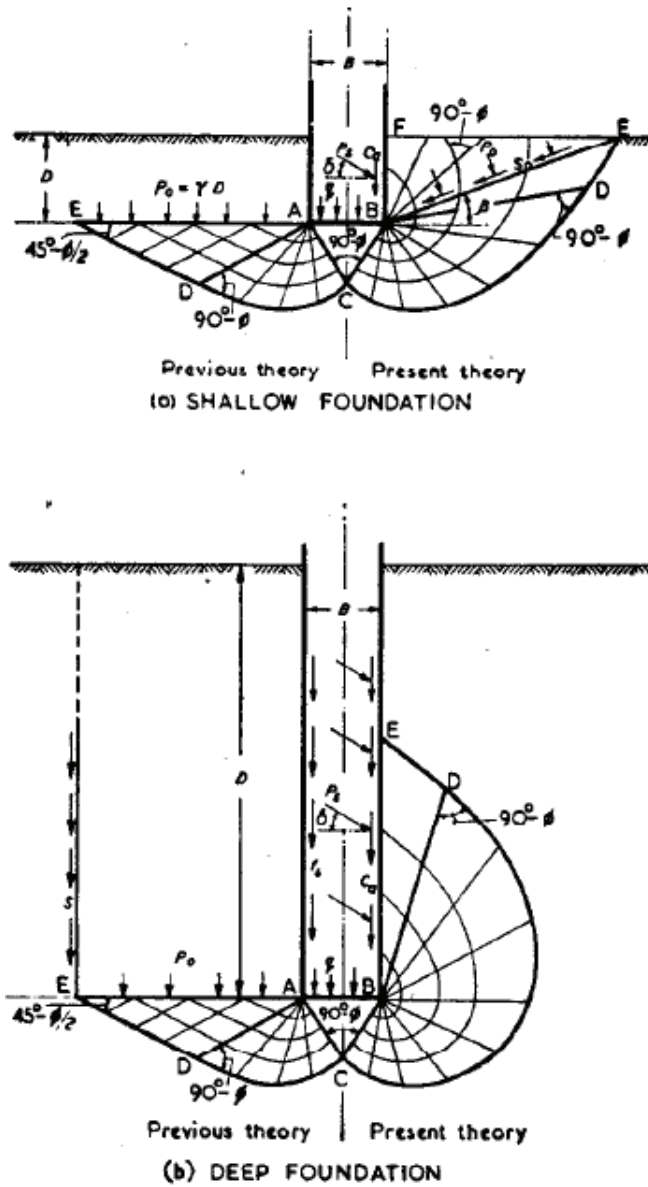


Figure 2.3: For illustration: the bearing capacity theory after Terzaghi (here on the left, presented as previous theory) and after Meyerhof (here on the right, presented as present theory) for deep and shallow foundations (Meyerhof, 1953) indicating the shear failure and deformation zones. Details will not discussed here. The findings let to the bearing capacity approach and its modifications.

$$c = c_s + K_L c_s \log_{10} \left(\frac{\nu}{\nu_s} \right), \quad (2.5)$$

with c being the apparent cohesion for the dynamic yielding case, c_s the cohesion for the static yielding case, K_L being the soil viscosity coefficient, ν the penetration velocity and ν_s the static penetration velocity the results are related to. Dayal and Allen (1975) did not observe significant differences of cone resistance or friction sleeve resistance in case of sand.

More investigations about penetration rate effects or strain rate effects were addressed using later developed dynamic penetrometers. Their results mainly follow the above mentioned approach by Dayal and Allen (1975) and will be introduced in the next section as an outcome of *in-situ* measurements.

2.1.5 Comparison of different marine dynamic penetrometers and their performance offshore

The different marine dynamic penetrometers can mainly be separated into two basic designs (Fig. 2.2): (i) a lance-like system and (ii) a projectile-like shape. Other concepts can be found, too, (e.g., Burying Mock Mine Body in Poeckert et al., 1996), but they often have a very specific purpose (e.g., simulation of mine burial) and will be neglected here. Furthermore, the systems can be distinguished into recovered devices and expendable instruments.

Lance-like dynamic penetrometers are widely used (e.g., Richardson et al., 2001; Osler et al., 2006; Stegmann et al., 2006a/b; Kopf et al., 2007). Conceptually, they consist of a rod of varying length (mostly range of meters) with a tip of varying geometry (mostly cone, but also a disc, T-bar or a ball are possible) and a main body containing electronics, weights, etc. The device penetrates the seafloor with the lance and the main body remains outside of the sediment. The lance-like systems are often characterized by a high number of sensors measuring deceleration, tilt, tip resistance, sleeve friction and pore pressure.

With a conical tip this system is probably the dynamic offshore penetrometer most similar to *in-situ* sediment strength tests onshore. Here, only some examples will be presented to provide an idea about the concept. One of the first results using a marine dynamic cone penetrometer was published by Dayal (1980). He showed that the free fall device was useful for obtaining the *in-situ* strength profiles and location of different layers. A penetration depth of about 4 m was reached and Dayal (1980) assumed that a penetration depth up to 15 m would be possible. However, he confirmed the influence of

penetration rate effects and indicated the importance of correlation of static and dynamic methods.

Osler et al. (2006) used a free fall cone penetrometer (FFCPT) in combination with a moving vessel profiler for deployments underway. In this case, a hydrostatic pressure sensor and an optical backscatter sensor were added for supporting the detection of the water-sediment interface. He concluded that the FFCPT can accurately characterize a diverse range of marine sediments, but he did not show absolute sediment strength results, and in doing so, did not address rate effects. Furthermore, he documented a significant decrease of penetration depth from soft, muddy sediments to sandy sediments.

Stegmann et al. (2006a) presented another FFCPT system including a pore pressure sensor (FFCPTU) designed at the working group for marine geotechnics at MARUM, University of Bremen. The device has been used for soil classification and soil characterization (Fig. 2.4) in marine and lacustrine environments and is in general agreement with standard industry CPT probes (e.g., cone surface area 15cm^2). Furthermore, it was proven that the device is deployable from small platforms and boats, and long-term deployments were suggested. At MARUM the FFCPTU was above all applied addressing scientific questions in projects concerning slope stability (e.g., Kopf et al., 2007; Stegmann et al., 2007; Strasser et al., 2007), gassy sediments (Kopf et al., 2009; Seifert et al., 2008) and fluid mud (Seifert et al., *subm.*). Most of the deployments focus on soft sediments (Stegmann et al., 2006b; Seifert et al., 2008) due to the decrease in penetration depth in case of sandy sediments (Stegmann et al., 2006a), corresponding well to the results by Osler et al. (2006). Concerning sediment strength values, Stegmann et al. (2006b) admitted that the results are affected by penetration rate effects.

In summary, the FFCPT/FFCPTU concept has been proven to deliver reliable information about the sediment type as well as specific geotechnical properties such as sediment strength or dynamic pore pressure (Fig. 2.4). However, for the determination of specific strength values penetration rate effects have to be considered. Furthermore, the penetration depth decreases significantly when deploying the device on sand. Also, having the center of gravity near the top of the instrument this leads to a risk of falling or kinking in case of sandy areas.

Besides FFCPT/FFCPTU systems, only a second lance-like penetrometer will be briefly introduced in this thesis as an example of the variety of penetrometers. The Canadian Seabed Terminal Impact Naval Gauge (STING) was described the first time by Poeckert et al. (1996) and is based on experiences gained with the Electronic Sediment Profiler (ESP) (more information about this system can be found in Poeckert et al., 1996). Main difference to FFCPT/FFCPTU systems is the disc-shaped tip geometry with diame-

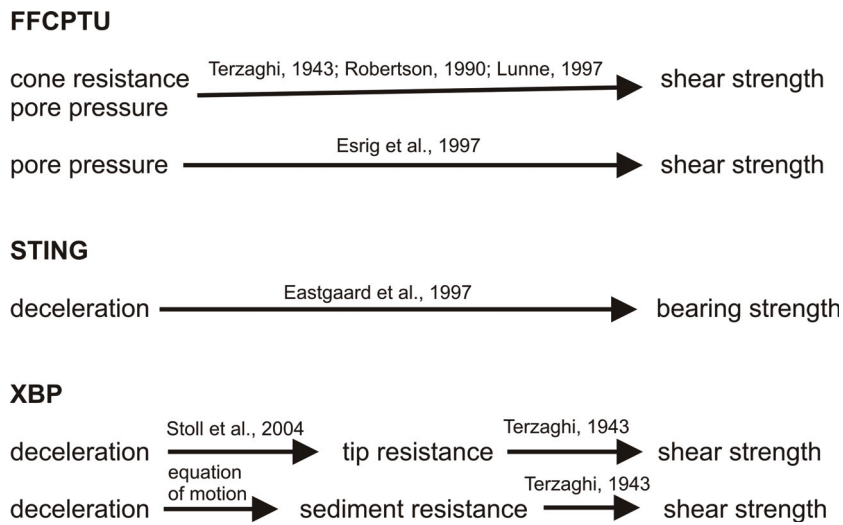


Figure 2.4: Overview of the different data processing methods to estimate sediment strength for the respective device. On the left the ingoing and measured properties are represented, on the right the output. Along the arrows, the references for the respective approach are noted.

ters ranging from 3-7 cm. The influence of tip geometry on measured sediment strength is well-known (e.g., Cassidy and Houlsby, 2002; Mulhearn, 2003). Following the approach to determine sediment strength (Eq. 2.4), an increase in width of the penetrating object will increase the measured sediment strength, and in doing so, will enhance the sensitivity of the device. Another difference to the FFCPT/FFCPTU systems is that the STING only contains deceleration sensors. The sediment strength is calculated using the deceleration data and the equation of motion considering weight, buoyancy, drag and penetrometer surface area (Fig. 2.4). This analysis makes various assumptions about the forces (Poeckert et al., 1996) and applies a simplified approach to considerate penetration rate effects (Hurst and Murdoch, 1991). Nevertheless, the device was successfully used in the framework of naval applications such as mine burial experiments (Richardson et al., 2001) as well as in the framework of environmental and geological projects such as mapping of contaminated sediments (e.g., Zeman and Patterson, 2003), mud deposition or fluid mud (e.g., Reed et al., 2009). The derived strength could be correlated to acoustic classes of sediments (Preston et al., 1999) and matches numerical model results in clay (Abelev et al., 2009 a,b). However, the STING is less suitable in sandy areas due to the same reasons found for the FFCPT/FFCPTU.

The concept of a more projectile-like dynamic penetrometer was first intro-

duced by Ingram (1982). The expendable system would be a most convenient and rapid method to classify seafloor strength. This method was realized as eXpendable Bottom Penetrometers by Stoll and Akal (1999). The probe measures deceleration only (similar to the STING). The influence of skin friction of the shaft can be neglected, because the probe diameter decreases in the tail-fin area (Stoll and Akal, 1999). A rapid classification into the sediment strength classes hard, middle, soft was achieved. Stoll (2006) compared dynamic penetrometer results (XBP and PROBOS – a STING modification) with the results derived by the quasi-static penetrometer STATPEN. They found empirically an allometric dependence between peak deceleration of the XBP and peak tip resistance of the STATPEN (Fig. 2.4). Also, they used different approaches to consider penetration rate effects. As another outcome they presented that the XBP is capable of resolving layers of different sand density in a laboratory experiment (Stoll, 2006). In a follow-up publication (Stoll et al., 2007) the authors suggested that the approach by Dayal and Allen (1975) is the most suitable for the estimation of penetration rate effects. This study also agrees with the approach by Aubeny and Shi (2006) used to consider penetration rate effects for XBP deployments. However, they used the equation of motion to derive sediment resistance from deceleration and considered a simplified approach of Terzaghi's bearing capacity approach to deliver cohesion (study is on cohesive sediments only) (Fig. 2.4). They compared the quasi-static strength results to miniature vane results carried out in the laboratory and found similar trends between the two methods. However, the miniature vane shear did not deliver peak or layering information seen in the penetrometer results. Stark and Wever (2008) focussed on the fine-scaled changes in deceleration - depth profiles and concluded that the XBP resolves even changes from mud to silt or inhomogeneities such as plant fibres and shells.

Regarding small and projectile-like dynamic penetrometers, it can be concluded that they offer a strength classification of the seafloor with a high time-efficiency. Furthermore, it is possible to calculate values of sediment strength from the deceleration, too. An empirical approach (Stoll, 2006) as well as an approach following the equation of motion (Aubeny and Shi, 2006) were combined with a simplified Terzaghi's bearing capacity equation successfully. In both cases, the need for consideration of penetration rate effects is highlighted. In doing so, the approach by Dayal and Allen (1975) seems to be the most appropriate. A limitation of such probes is the low penetration depth. In soft sediments they can reach a penetration depth of about 3 m. In case of sand, the penetration depth exceeds rarely 0.2 m. Consequently, these instruments are only suitable for the investigation of the uppermost sediment layers. Also, being an expendable system can lead to high costs in

case of a high number of deployments.

2.1.6 Requirements in areas of sediment remobilization

A dynamic penetrometer suitable for the investigation of sediment remobilization should be capable of displaying layers of different sediment density. Stoll (2006) proved this in case of sand using the XBP, and, e.g., Reed et al. (2009) confirmed this for mud using the STING. However, the suitability of the respective device for the respective sediment type can be associated with the different tip geometries. Also, the study by Seifert et al. (subm.) suggests that a flexible tip geometry is the key to a high resolution for a wide range of sediment types. The STING seems to realize this idea with a range of tip diameters. However, the disc-shaped tip limits the penetration into sandy seafloors significantly leading to a focus on muddy sediments.

After examination of different dynamic penetrometers (chapter 2.1.5), the XBP seems to be the most promising device for the investigation of sediment remobilization processes. However, the suitability for fluid mud has not been tested, yet. Furthermore, using the XBP can become quite expensive in case of spatially high resolution surveys. Following that, a device similar to the XBP, but reusable and with different tip geometry options seems to be matching most the requirements of dynamic penetrometer investigations of sediment remobilization.

2.2 Sediment dynamics

Hydrodynamics, morphodynamics and sediment dynamics influence each other and form a complex system, which might reach an equilibrium, might be under steady evolution or might be stable unless extreme events (e.g., storms) hit the system. In the following section, a brief overview will be given about the theoretical background and about currently used measurement techniques.

2.2.1 Theoretical introduction

The following introduction into seabed mechanics and their dependence on hydrodynamics and morphodynamics is based on the publication by Sleath (1984), Soulsby (1997), Balson and Collins (2007) and Hearn (2008). More

details can be found there.

Basics in hydrodynamics

Waves and currents affect the seafloor and the coast in different ways. However, already waves, currents and the combination of both can vary significantly in their appearance as well as in their interpretation.

Regarding waves, they can be theoretically described as irrotational or rotational flows having different relations between wave height, wave length and water depth. Furthermore, there are more specific wave types such as edge waves along slopes or breaking waves at the shore.

Changing the focus to currents, laminar flows and turbulences can be distinguished. The transition when disturbances of the laminar flow are amplified or turbulences are damped out are quantified by the Reynolds number. Steady currents in the marine environment are, e.g., tides and tidal currents or large-scale ocean currents.

Mostly, it has to be dealt with a combination of waves and currents. There are theories to predict the change in wave characteristics produced by a known steady current (e.g., Brevik, 1980) or to predict a current profile if the waves are known (e.g., Lundgren, 1972).

The described hydrodynamics, and above all their fluid velocities and pressure near the seafloor, are affected by the morphology and the sediment (Fig. 2.5). Seafloor roughness (e.g., mud or sand and gravel) (e.g., Brebner et al., 1966), the bedform (e.g., flat, rippled, sloped) (e.g. Raudkivi, 1963) and the permeability of the seafloor (e.g., Liu, 1973) affect the velocity and the direction of flow as well as the transition between laminar flow and turbulence.

Basics in bedforms

Vice versa, the morphology of the seafloor is formed by the interaction of flow in the water column and sediment at their interface. Fig. 2.6 and Fig. 2.7 present examples of bedforms resulting from wave action or currents, respectively.

Nevertheless, the formation of bedforms is still not entirely understood and is studied in numerous theoretical attempts (e.g., Exner, 1925; Raudkivi, 1963; Richards, 1980). The number of formation theories expresses the high complexity, and the combination of waves and currents complicates matters. Also, there have been several approaches to categorize different bed regimes

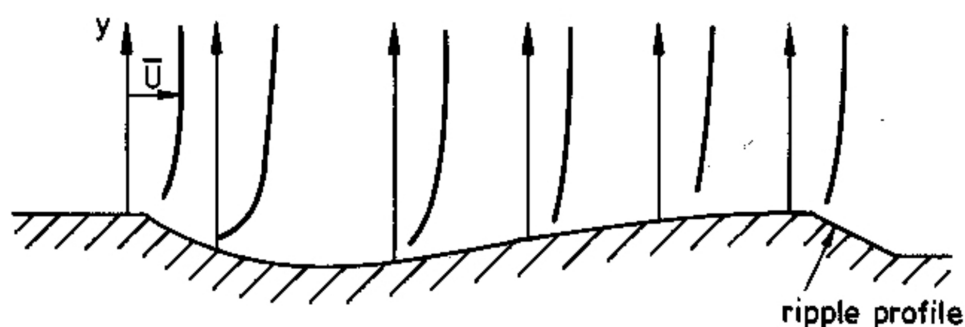


Figure 2.5: Influence of a rippled bed on a current velocity profile (modified after Sleath, 1984).

and classify bedforms (e.g., Shields, 1936; Reynolds, 1965; Holtorff, 1982; Ashley, 1990). In the framework of this thesis the approach by Ashley (1990) is used for dunes (Fig. 2.8): Ripples as well as dunes are characterized by a relatively gentle upstream slope (stoss) and a more steep lee slope.

Basics in sediment dynamics

Sediment can be transported as bedload or can get into suspension. Bedload remains more or less continuously in rolling or sliding contact with the bed. A special type of bedload is saltation, in which particles of sediment are carried in successive leaps along the bed. To get into suspension, sediment has to be entrained from the bed and is carried away with the flow. When or if the sediment starts moving and in which way depends on the hydrodynamics, the morphology and the sediment.

Only a few sediment properties can be mainly found in sediment dynamic theories. The grain size distribution is one of them and can be determined by, e.g., sieving, the pipette method, using a hydrometer or a laser diffraction spectrophotometer. A sieve defines a particle diameter as the length of the side of a square hole through which the particle can just pass (e.g., Konert and Vandenberghe, 1997). Commonly, the sieves are shaken during the analysis and standard sieves are used (e.g., ASTM D422). In case of cohesive soils, it may be difficult to break lumps into individual particles. Then the soil should be mixed with water and be washed through the sieves (e.g., Das, 1990). The pipette method as well as the hydrometer analysis is based on the principle of sedimentation of soil particles in water following Stokes' law (e.g., Das, 1990). The particle is defined as an equivalent of a sphere set-

Bed form	Plan view	Cross section AA	Typical height-to-length ratios
Rolling-grain ripples			< 0.1
Vortex ripples (other names: 2-D vortex ripples; vortex ripples of 1st type; dunes)			0.1 - 0.25
Vortex ripples (other names: 3-D vortex ripples; vortex ripples of 2nd type; dunes)			0.1 - 0.2
Brick pattern ripples (other names: vortex ripples)			0.1 - 0.25
Offshore bars			

Figure 2.6: Examples of bedforms shaped by oscillatory flow (after Sleath, 1984).

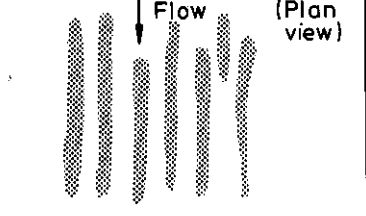
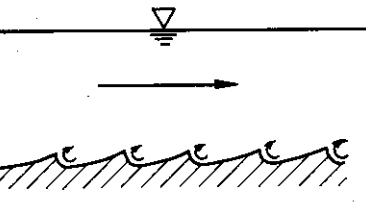
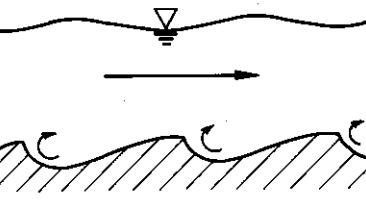
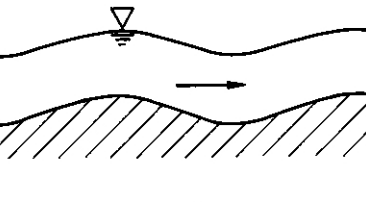
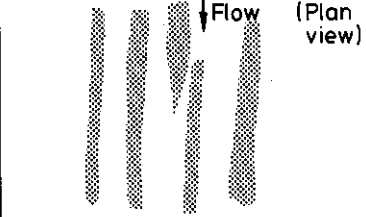
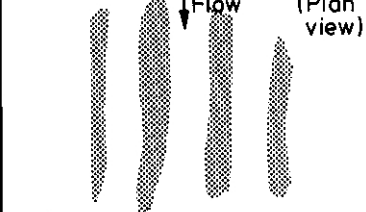
Bed form	General outline	Typical height
Parting lineation (other names: primary current lineation; streaming lineation)		1-5D
Ripples (other names: small-scale ripples)		10-100 D
Dunes (other names: large-scale ripples; sand waves; megaripples)		100-10000 D
Antidunes		
Sand ribbons		50-500 D
Tidal current ridges		7-30 m

Figure 2.7: Examples of bedforms shaped by steady flow (after Sleath, 1984). D expresses the median grain size.

Ashley (1990) Dune Classification				
First Order Descriptors				
Size:	Small	Medium	Large	Very Large
Spacing	0.6-5 m	5-10 m	10-100 m	>100 m
Height	0.075-0.4 m	0.4-0.75 m	0.75-5 m	>5 m
Shape:	2-Dimensional			
	3-Dimensional			
Second Order Descriptors (important)				
<ul style="list-style-type: none"> • Superposition: simple or compound. • Sediment Characteristics (size, sorting). 				
Third Order Descriptors (useful)				
<ul style="list-style-type: none"> • Bed form profile (stoss and lee slope lengths and angles). • Fullbeddedness (fraction of bed covered by bed forms). • Flow structure (time-velocity characteristics). • Relative strengths of opposing flows. 				
Dune behavior-migration history (vertical and horizontal).				

Figure 2.8: Ashley (1990) dune classification (after Whitmeyer and Fitzgerald, 2006).

ting with the same speed as the unknown sized particle (Stokes-diameter) (e.g., Konert and Vandenberghe, 1997). A laser diffraction spectrophotometer sees a particle as a two dimensional object und determines its grain size as a function of the cross-sectional area of that particle (e.g., Konert and Vandenberghe, 1997). For a single measurement only 0.05–2 g of the sample is needed and a range of 0.4–900 μm can be reached (Loizeau et al., 1994). However, Loizeau et al. (1994) showed that clay particles may be underestimated, and Konert and Vandenberghe (1997) observed a coarsening of clay fractions caused by the non-sphericity of the particles.

Another important physical property is the grain shape which can be observed using, e.g., binocular microscopes or scanning electron microscopes. The angularity as well as the surface roughness influences the sediment strength (e. g., Norris, 1977; Cho et al., 2006). More angular grains show higher friction angles (e.g., Das, 1990) leading to a higher sediment strength, and Kock and Huhn (2007) presented that the spatial and temporal shear zone development depends on the surface roughness of particles.

Grain size and grain shape also have an influence on the packing of particles, and in doing so, on the density ρ or specific weight γ :

$$\gamma = \rho g \quad (2.6)$$

with g being the gravitational acceleration.

Furthermore, geotechnical properties such as the angle of friction ϕ and the

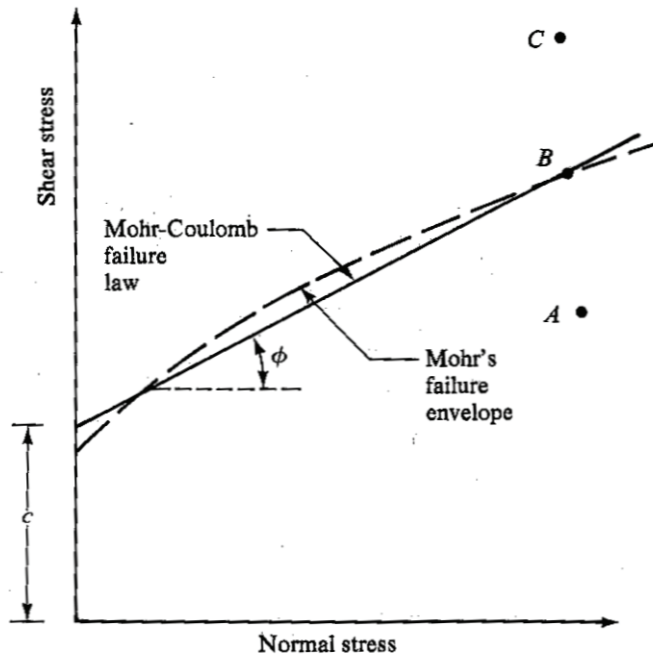


Figure 2.9: The Mohr failure envelope following equation 2.7 and the Mohr-Coulomb failure law following equation 2.8 (modified after Das, 1990). If the normal stress and shear stress on a plane in a soil mass follow the failure envelope (e.g., point B) failure will occur along this plane. A state of stress below the failure envelope (e.g., hitting point A) will not provoke failure, and a state above the failure envelope (e.g., hitting point C) cannot exist.

porosity are of importance. The angle of friction is introduced in the framework of the Mohr-Coulomb failure criterion. Mohr (1900) presented a theory showing that a material fails through a critical combination of normal stress σ and shear stress τ :

$$\tau_f = f(\sigma). \quad (2.7)$$

Combined with results by Coulomb (1776), this led to the approximation of shear stress on a failure plane as linear function of normal stress:

$$\tau_f = c + \sigma \tan \phi, \quad (2.8)$$

adding the cohesion c (Fig. 2.9). The angle of friction can be determined using, e.g., an uniaxial shear box.

The porosity of a sediment n is the ratio of the volume of voids V_v to the total volume V :

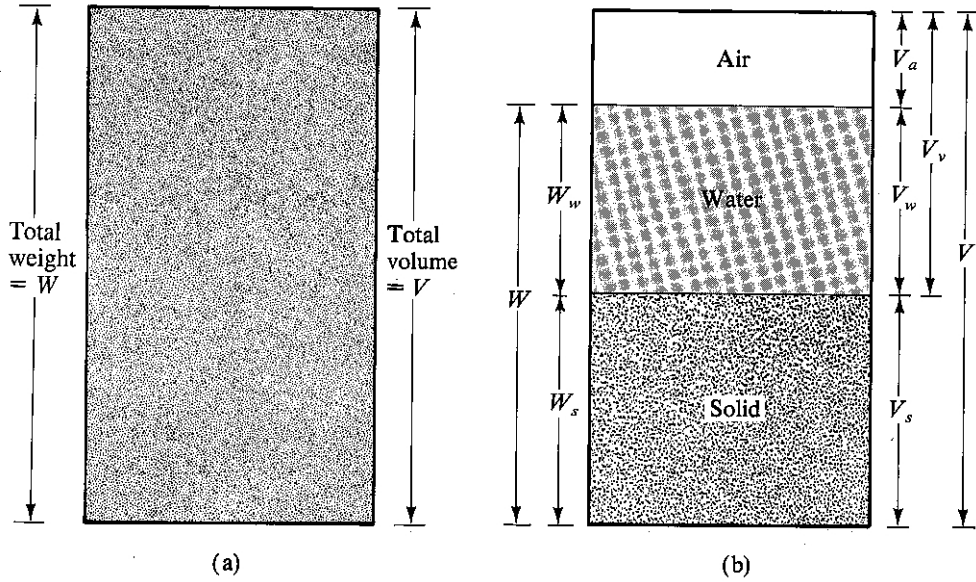


Figure 2.10: For illustration of the volume relationships: the soil element in natural state (a) and depicted in the three phases (b) (after Das, 1990).

$$n = \frac{V_v}{V}. \quad (2.9)$$

Another geotechnical volume relationship is the void ratio e defined as the ratio of the volume of voids to the volume solids V_s (Das, 1990) (Fig. 2.10):

$$e = \frac{V_v}{V_s} \quad (2.10)$$

The bed permeability might effect the mobilization of sediment in two ways: (i) the seepage will modify the flow in the boundary layer above the bed, which will change the shear stress exerted by the flow on the bed, and (ii) a vertical force will be applied by the seepage on the grains of the sediment. However, e.g., Martin (1970) as well as Watters and Rao (1971) concluded that there is no significant effect by seepage on initial motion conditions. Regarding the morphology, bedforms which induce turbulence such as ripples facilitate entrainment of sediment from the bed into the flow.

Concerning the hydrodynamics, the question is at which flow velocity the force on the sediment particles (Fig. 2.11) is strong enough to overcome the threshold bed shear stress, and in doing so, induce initial motion. Thereby, different approaches have to be applied for steady flows and waves, especially in case of cohesionless sediments. For example, in steady flows the threshold

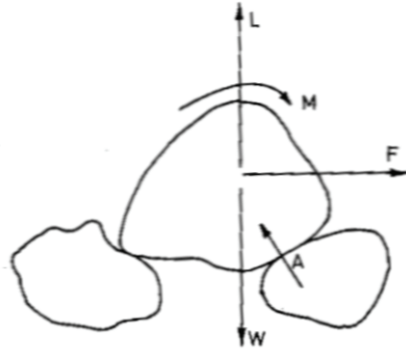


Figure 2.11: Forces on a particle of sediment at the surface of the bed regarding initiation of motion (after Sleath, 1984): The necessary magnitude of the force F depends on shear stress and grain size. The lift L depends on shear stress, grain size, shear velocity and kinematic viscosity. The immersed weight W depends on the relationship of density of sediment and fluid and the grain size. In case of initiation of motion the particle will gain a momentum M and start with a rotational motion around point A .

bed shear stress for initial motion in non-cohesive sediments can be expressed by the Shields parameter (Soulsby, 1997):

$$\Theta_{cr} = \frac{\tau_{cr}}{g(\rho_s - \rho)d}, \quad (2.11)$$

with τ_{cr} being the threshold bed shear stress, ρ_s the grain density, ρ the water density and d the grain diameter. Soulsby and Whitehouse (1997) introduced an equation depending only on the dimensionless grain size D^* :

$$\Theta_{cr} = \frac{0.30}{1 + 1.2D^*} + 0.055 [1 - \exp(-0.020D^*)], \quad (2.12)$$

with

$$D^* = \left[\frac{g \left(\frac{\rho_s}{\rho} - 1 \right)}{\nu^2} \right]^{\frac{1}{3}}. \quad (2.13)$$

Here ν is the kinematic viscosity of water.

After Soulsby (1997), the corresponding threshold depth-averaged speed on a flat bed is:

$$\overline{U}_{cr} = 7 \left(\frac{h}{d_{50}} \right)^{\frac{1}{7}} \left[g \left(\frac{\rho_s}{\rho} - 1 \right) d_{50} f(D^*) \right]^{\frac{1}{2}}, \quad (2.14)$$

with h being the water depth.

Soulsby (1997) also found that for current speeds significantly above the threshold of motion, sand is entrained off the bed and brought into suspension, where it is carried at the same speed as the current. The proportion of sediment carried in suspension is generally much larger than that being carried simultaneously as bedload. To remain in suspension, the settling velocity of the grains must be smaller than the upward turbulent component of velocity.

In case of waves and cohesionless sediments, there are plenty of theoretical as well as empirical approaches to define the initial motion (e.g., Bagnold, 1946; Larras, 1956; Sato et al., 1962; Lenhoff, 1982). Mainly, they consider the amplitude of horizontal component of velocity outside of the oscillatory boundary layer at the bed U_∞ , fluid density ρ and density of the sediment ρ_s , median grain size D , period of oscillation T and gravitational acceleration g . In some approaches also the friction angle ϕ is considered as in the approach by Kurihara et al. (1956):

$$\frac{U_\infty}{\left(\frac{\rho_s - \rho}{\rho} g D \tan \phi\right)^{\frac{1}{2}}} = 1.95. \quad (2.15)$$

For cohesive sediments, there is no formula which is generally accepted formula for the initial motion (Sleath, 1984). An example was presented by Migniot (1977) whose experimental results link the critical shear stress to the yield strength τ_y :

$$\tau_{cr} = \begin{cases} 0.256(\tau_y)^{0.46} & \text{for } \tau_y < 1 \frac{N}{m^2} \\ 0.256\tau_y & \text{for } \tau_y > 1 \frac{N}{m^2} \end{cases} \quad (2.16)$$

Another important aspect in cohesive sediment remobilization and deposition is flocculation, what is a collection of particles in suspension (e.g., Mehta, 1993). In marine and estuarine muds aggregation is mainly a consequence of particle collision provoked by Brownian motions of the particles (random particly movements in fluids), differential settling of particles when a particle with large settling velocity overtakes a particle with low settling velocity or turbulent motions caused by eddies (e.g., Winterwerp, 2002).

In conjunction with aggregation, a highly investigated feature of cohesive sediment remobilization in steady flows is fluid mud. It plays an important role in the formation of turbidity maxima, shoaling of navigation channels, pollutant transport, etc. (Kusuda et al., 1993). Such a layer is characterized by two significant concentration gradients at the top and bottom boundary, respectively (Kusuda et al., 1993). The boundary between water and fluid

mud layer is called lutocline (Parker and Kirby, 1982). Furthermore, the fluid mud layer itself can be divided into two parts: mobile fluid mud layer and stationary “fluid” mud layer (also called bed mud layer) (Ross and Mehta, 1989).

Despite extensive examination (e.g., Smith and Kirby, 1989), the precise mechanisms of formation, growth and dissipation processes are not entirely understood. These processes are under influence of settling of suspended solids, consolidation of bed mud, erosion (fluidization) of the cohesive bed, entrainment of mobile fluid mud into overlying water as well as applied shear stress (Kusuda et al., 1993). Furthermore, the above mentioned flocculation plays an important role in the formation and growth of fluid mud (e.g., Nichols, 1984). When aggregates settle on the bed, they may form a space-filling network, called a gel, and a measurable strength builds up (Winterwerp, 2002). The concentration of the gel depends on the aggregate size, the diameter of the primary mud particles and the density of the primary particles (Winterwerp, 2002). Another aspect might be the salinity. Kineke et al. (1996) presented correlations of salinity stratifications and fluid mud development. In general, fluid mud can be associated to different environmental conditions such as organic matter in the sediment (e.g., Mehta, 1991) or nitrogen dynamics (e.g., Abril et al., 2000), too.

2.2.2 Techniques used for the investigation of sediment dynamics *in-situ*

Following the theory, several approaches to address sediment dynamics can be used. Some studies focus, e.g., on morphological changes (e.g., Ernstsens et al., 2006; Coco and Murray, 2007), others concentrate on the role of sediment properties, e.g., grain size (e.g., Flemming, 2000; Svenson et al., 2009). In the following sections, an overview of different *in-situ* techniques will be given. Laboratory methods to determine sediment properties, such as grain size analysis, were described in chapter 2.2.1. Neither, numerical models of sediment remobilization processes will be introduced here, although, they play a central role in the investigation of sediment remobilization processes (e.g., Murray and Thielert, 2004; Gutierrez et al., 2005; Winter et al., 2006; Coco et al., 2007a/b).

Acoustic methods

Acoustic methods are an important tool to display changes in morphology. For example, multi-beam echosounder (MBES) (or even single beam

echosounder) results visualize the formation and development of bedforms leading to an estimation of the amount of remobilized sediment (e.g., Bartholomä et al., 2004; Wienberg and Hebbeln, 2004; Ferrini and Flood, 2005; Diesing et al., 2006; Ernstsens et al., 2006; Phillips et al., 2007). Changes in geometry in the range of a few centimeters can be detected and illustrated. Recently, long-term observations (spanning years in case of slowly evolving bedforms, and only hours in case of, e.g., bedforms influenced by tides) spark an increasing interest.

To depict and map mainly the horizontal geometry of bedforms, towed side scan sonar (SSS) (Fig. 2.12) is a commonly used tool (e.g., Anthony and Leth, 2002; Goff et al., 2005; Spiers and Healy, 2007). Even for long-term observations of sediment dynamics side scan sonar is suitable. Wever et al. (2008) presented the concept of a stationary, circumferential-looking side scan sonar system mounted to a moored tower (Fig. 2.13) remaining at the seafloor for hours, days or even months.

A tool specialized to detect layering and stratigraphy below the seafloor via acoustic sub-bottom profiling is chirp sonar (Fig. 2.14). Mainly, it is applied for the investigation of long-term sediment dynamics (Zeiler et al., 2000; Goff et al., 2005).

Furthermore, the wide-ranged application of acoustic Doppler current profilers (ADCP) has to be mentioned. They can be deployed from the vessel as well as with a mooring system. Depending on their position in the water column, they can look down/up through the water column or can monitor the uppermost layer of the sediment. The current and possible turbulences can be measured (e.g., Chereskin, 1995; Lu and Lueck, 1999; Lorke et al., 2004) as well as bed load motion (e.g., Rennie and Villard, 2003; Gaeuman and Jacobson, 2006). The amount of suspended sediment can be estimated from the backscatter signal (e.g., Holdaway et al., 1999; Vincent, 2007).

In summary, acoustic methods are capable of estimation of the amount of sediment that is remobilized, and of determination where the sediment goes to. However, important geotechnical and physical information are lacking (e.g., density, strength, etc.), and the resolution is limited to the range of centimeters.

Sediment sampling

Sediment can be sampled by grab samplers or sediment corers. Grab samples (Fig. 2.15) deliver sediment from the uppermost surface in moderately to highly disturbed condition, and consequently, are not suitable for an ex-



Figure 2.12: Example of a towed side scan sonar system. Here, the Edgetech 4700 system suitable for high speed and a long range used during the *Research at Alpha Ventus* (RAVE) surveys.



Figure 2.13: Stationary, circumferential sonar tower of the working group for marine geotechnics at MARUM, University of Bremen, deployed during the *Research at Alpha Ventus* (RAVE) surveys.



Figure 2.14: Example of a chirp sonar sub-bottom profiler. Here, the Edgetech 3100 X-Star portable system used during the *Research at Alpha Ventus* (RAVE) surveys.

act analysis of the sediment texture. Nevertheless, the samples can be used for detailed analysis of the physical properties of the particles such as grain size distribution, grain shape, water content, wet and dry density, and tests regarding the geotechnical behavior under different conditions (e.g., loads) (e.g., Ziervogel and Bohling, 2003). Examples for an application in sediment dynamic investigations are studies on grain size variations along and across dunes (e.g., Ernstsén et al., 2005; Svenson et al., 2009) as well as studies on sorted bedforms (e.g., Diesing et al., 2006).

With sediment coring it is attempted to preserve the sediment texture and to recover an undisturbed sediment stratigraphy (e.g., Murray and Thielér, 2004). All in all, these goals are met, although, it may still come to changes in, e.g., density, due to the recovering process, transport or storage (Blomqvist, 1991). This affects especially (i) non-cohesive sediments with a loose binding between the particles (e.g., sands), or (ii) cohesive sediments with a low viscosity (e.g., fluid mud, mobile layers), two important types of sediment in the framework of sediment dynamics, and also for this thesis.

For suspended sediment and bedload, sediment traps became an important tool. Different concepts of sediment traps for sand (e.g., Emerson, 1991; Wilcock and McArdeU, 1993; Green et al., 2004) as well as for fluid mud/mobilized mud (Chou et al., 1993; Disperens et al., 1993; Cooper and Pilkey, 2007) were presented in the past. However, these systems are often diffi-



Figure 2.15: Example of a grab sampler. Here, the ShipekTM system deployed in the framework of dune investigations.

cult or impossible to install in areas highly affected by hydrodynamics (e.g., Emerson, 1991).

Other methods

Other methods include particle tracking or sediment tracing. In that case, labelled particle tracers are added to the system and observed. The tracer should mimic the hydraulic properties of the sediment of interest, so that the tracer is transported in the same fashion as the native sediment (Black et al., 2007), but otherwise should not change its properties with time and should not influence the transporting system in any way. Examples for tracers used to track sediments are natural fluorescent mineral fluorite (Waters, 1986), labelling of grains with rare earth elements (Zhang et al., 2001) and use of fluorescent glass beads (Ventura et al., 2001). Limitations of the particle tracking methods are, e.g., excessive dilution in case of suspended sediment (e.g., Ingle, 1966), and burial in case of bedload (e.g., Knoth and Nummeda, 1977).

Another method for high-resolution observation of small-scale variability in a bedform field are Burial Recording Mines (BRM) introduced by Wever et al. (2004) in the framework of mine burial experiments. These devices monitor the sand height around them using 24 light barriers. Long-term observations

(in the range of weeks) are possible (Wever et al., 2004). Problems of the system might be the stability in case of sloped beds as well as under strong currents or waves.

A third method recently becoming more popular is *lidar*. This system is deployed submerged (e.g., Hansdorf et al., 1999) as well as airborne (e.g., Tulldahl, 2007) for seafloor classification. The CHARTS bathymetric *lidar* used by the U.S. Army Corps of Engineers, for example, is a diode pumped, pulsed, Nd:YAG laser. The laser transmits 3000 pulses per second and each pulse is composed of light at two wavelengths: 1064 nm (infrared) and 532 nm (green). The receivers detect the return of both wavelengths, however, the infrared light reflects the water surface while the green light propagates through the water column to reflect from the seafloor (Macon et al., 2008). A resolution of up to 0.5 m is documented (e.g., Macon et al., 2008) indicating *lidar* as a tool for quick bathymetrical surveys, especially for big areas and shallow to shore areas.

Geotechnical methods in sediment dynamic research

Following the theory (chapter 2.2.1), geotechnical and physical properties such as shear stress and density play an important role in the process of sediment remobilization. Regarding the applied *in-situ* methods (chapter 2.2.2), these properties are poorly investigated. Sediment cores try to preserve the *in-situ* texture, but especially changes of density with sediment remobilization are often not represented in sediment cores. Bathymetrical surveys show the morphological changes as a consequence of sediment remobilization and estimate the amount of sediment remobilized, but are not capable of highlighting different phases of the remobilization process itself (e.g., when and where does the sediment loosen up). In consequence, *in-situ* geotechnical methods delivering highly resolved strength differences at the uppermost seafloor surface and depicting the formation of softer and potentially mobile layers would be a great complement in the investigation of sediment dynamics. Dynamic penetrometers seem to be a suitable tool for this task.

Chapter 3

Nimrod

3.1 Design

The aim was to develop a new truly free-falling penetrometer whose performance is in some ways comparable to an eXpendable Bottom Penetrometer (stable free-fall, high data sampling frequency, high sensitivity, water depths up to 200 m, etc.). However, three differences must be highlighted: (i) it should be possible to recover the system by hand, (ii) a pressure sensor will be added following the efficient outcome of pore pressure measurements using FFCPTU systems, and (iii) the device should include a choice of different tip geometries. Furthermore, the system should offer the possibility for upgrades by adding new sensors (e.g., temperature).

In consequence, some key aspects had to be considered:

- Fluid mechanics (shape, weight)
- Material (low skin friction, high stability against impact and hydrostatic pressure, weight)
- Recovery system (low influence on free fall behavior)
- Sensors (coverage of a high range of decelerations, pressure range up to ~ 2500 kPa)
- Data acquisition system (providing ~ 1 kHz for ~ 16 channels).

Additionally, during design it had to be considered that the system should be cost-efficient and easy in handling during preparation of surveys, repair/replacement of parts, and on board.

3.1.1 Shape

Shape, surface roughness, weight and weight distribution have a significant impact on the performance of the proposed device. The underlying theory will be briefly introduced in this chapter.

Principles of buoyancy

To initiate the fall through the water column of an object, the weight W has to overcome the buoyancy B :

$$W = mg, \quad (3.1)$$

$$B = \rho gV = \gamma V, \quad (3.2)$$

where m is the mass of the penetrometer, g the gravitational acceleration, ρ the density of the fluid, γ the specific weight of the fluid and V the volume of the displaced fluid (if the device is completely submerged, this equals the volume of the device) (e.g., Crowe et al., 2005).

Looking ahead to additional drag and tether drag of the device, the weight should overcome the buoyancy significantly. Hence, the relation between the volume and the mass of the instrument has to be suitable to provide the free fall principle. The stability of an immersed body depends on the location of center of gravity and center of volume related to each other. The body is stable if the center of volume is above the center of gravity (Crowe et al., 2005). That means the mass of the penetrometer has to focus on the tip.

Introduction into flow separation, drag and streamlining

Installing an object in a laminar flow (as a model of an object moving through a fluid) influences the flow. The Reynolds number (already briefly mentioned in the chapter 2.2.1) is an important parameter to predict the change of the flow. For the problem addressed here it can be defined as:

$$Re = \frac{\rho u_0 d}{\mu}, \quad (3.3)$$

where d is the diameter of the object (here a cylinder), ρ is the density of the fluid, μ is the viscosity of the fluid and u_0 being the free stream velocity. Figure 3.1 illustrates the changes of flow with changing Reynolds number. In case of $Re \ll 1$, the flow pattern upstream and downstream of the object are the mirror image of each other, even though the flow pattern above and below

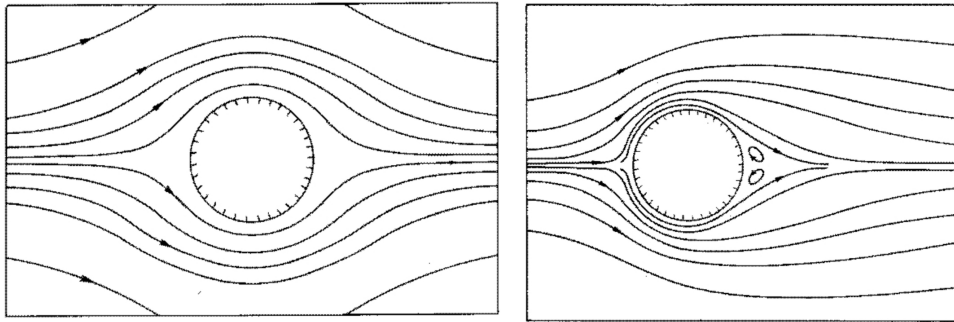


Figure 3.1: Flow pattern around a circular cylinder at low Reynolds numbers (left) and at $Re = 10$ (right) (modified after Tritton, 1988).

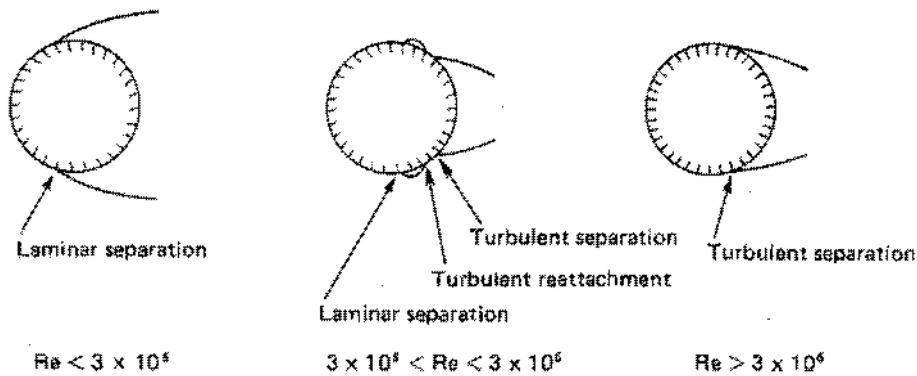


Figure 3.2: Change of separation point depending on the Reynolds number (after Tritton, 1988).

the object is changed appreciably (up to many diameters from the object). Increasing Re leads to a disappearance of the upstream-downstream symmetry, and flow separation occurs (Tritton, 1988). Now, the flow pattern has to be divided into three sections: (i) in front of the cylinder, (ii) the midsection with the separation point, and (iii) the wake behind the cylinder. Furthermore, a boundary next to the cylinder front down to the separation point occurs. In the boundary layer the velocity of the real (viscous) fluid changes from 0 at the cylinder surface to free-stream velocity (Crowe et al., 2005). Examples for different separation points are given in figure 3.2. Besides Re , the point of separation also depends on roughness of cylinder surface (Crowe et al., 2005).

In the previous section it was already mentioned that it is not only the buoyancy that is working against the free fall of the object. Generally, one

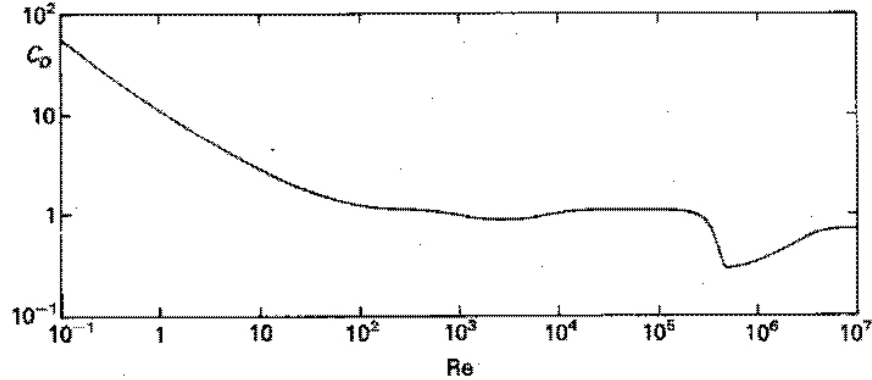


Figure 3.3: Empirical variation of drag coefficient with Reynolds number for a circular cylinder (after Tritton, 1988).

also has to apply a force in order to move an object through a stationary fluid (or in the more complex case: through a fluid flowing in a different pattern than the object moves) (Tritton, 1988). Vice versa, the force in the flow direction exerted by the fluid on an obstacle is known as drag F_d and is conventionally presented using the drag coefficient C_d (e.g., Tritton, 1988):

$$C_D = \frac{F_D}{A_p \rho \frac{u_0^2}{2}} \quad (3.4)$$

using A_p as the projected area of the object. The drag coefficient depends on Re (Fig. 3.3), shape of object (Fig. 3.4) and surface roughness of the object. A rougher surface will force the boundary layer to become more turbulent at a lower Re . Following that, the drag coefficient for an object with smooth surface will be smaller than the drag coefficient of an object with a rougher surface. Furthermore, the drag as well as the drag coefficient can be distinguished into form drag and skin-friction drag (Crowe et al., 2005). If separation can be eliminated, the drag will be reduced. That is the idea of streamlining. It reduces the extreme curvature on the downstream side of the body, ergo, reduces or even eliminates separation. Streamlining is applied on an object by elongating it (Crowe et al., 2005). Then the form drag is reduced, but the skin-friction is increased due to the increase of surface area. The optimum is reached if the sum of skin-friction drag and form drag is at its minimum.

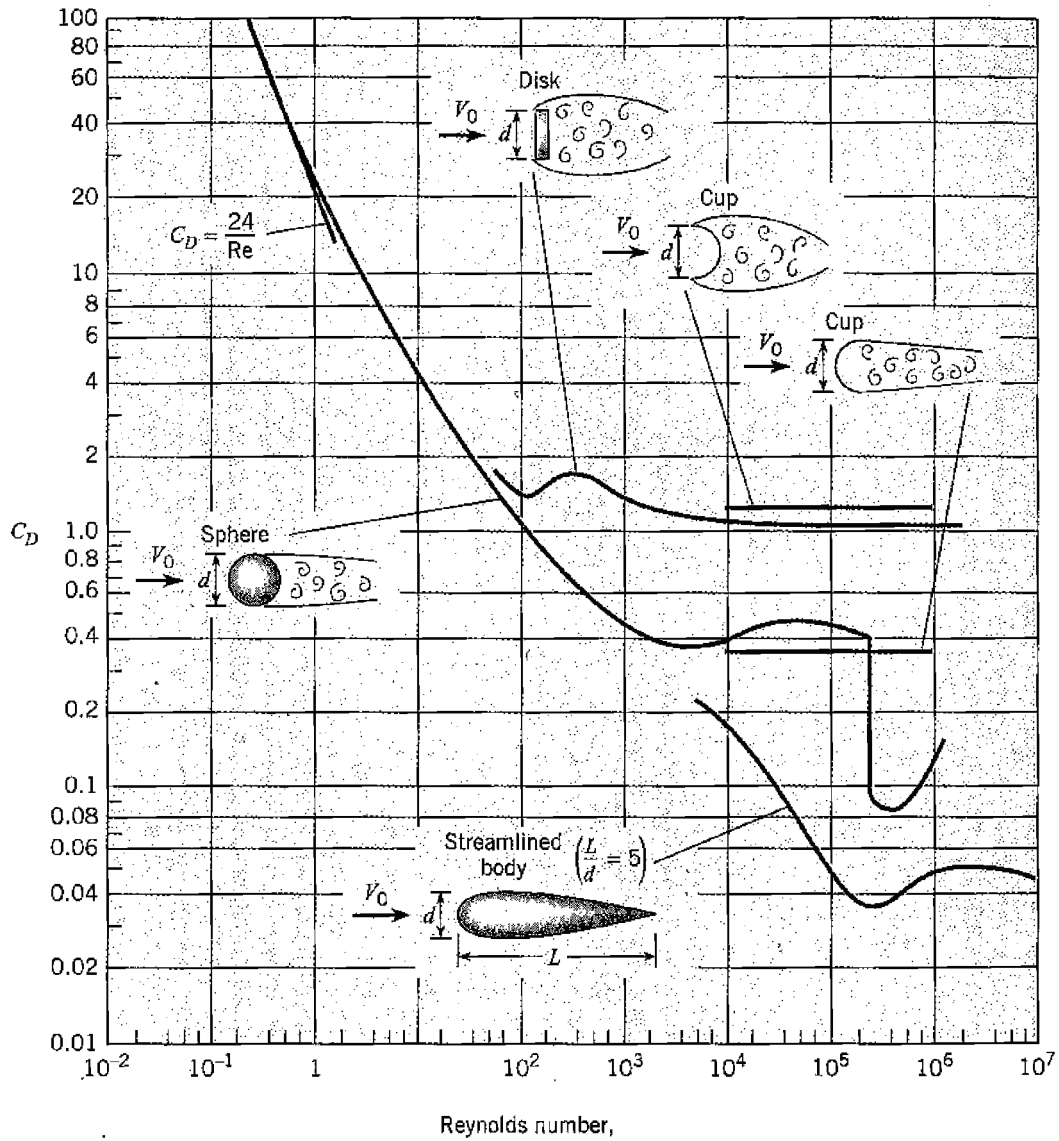


Figure 3.4: Change of drag coefficient with Reynolds number in case of different object geometries (modified after Crowe et al., 2005).

Drag of a realistic penetrometer shape

Unfortunately, the penetrometer cannot be designed only after fluid dynamical aspects. The shape has to be suitable to carry the sensors and data acquisition system, too. Looking for shapes applied for most energy-efficient underwater transportation leads to submarines and torpedos, in which the torpedo comes the principle of a penetrometer closer. In the literature estimates for torpedo drag and corresponding suggestions for torpedo shapes can be found. This section as well as the design of the penetrometer *Nimrod* follow mainly the estimations by Brooks and Lang (1967).

A projectile-/torpedo-shaped object can be distinguished into three sections: nose/tip, main body/middle section and conical tail. Fins will be added to the tail. For the determination of the drag due to the shape of the object (form drag), the length of the respective section will be considered in relation to the diameter. This is the so-called fineness ratio. It is one of the main parameters influencing the form drag. For example, figure 3.5 presents the influence of the fineness ratio regarding the whole torpedo length on form drag, whereas figure 3.6 shows the influence of the fineness ratio regarding tail and main body length, respectively. Concerning the nose, Brooks and Lang (1967) concluded that the nose length compared to the tail length has a significant influence. However, the nose geometry is negligible regarding the difference between approximately cylindrical tip and ellipsoid. Tip geometries without a smooth transition from tip to main body, like a cone or cylinder are not considered here (Fig. 3.7).

Adding fins supports the stability of the object. Crucial is the number of the fins, four cruciformed fins is most common, and the width (b in Fig. 3.8). The wider the fins the more stability they provide. However, Brooks and Lang (1987) suggest that the drag of fins is affected mostly by the length (c in Fig. 3.8). The maximum length, equal to the tail length, leads to the minimum drag assuming the maximum width equals the width of the widest part of the conical tail.

3.1.2 Material

In accordance to section 3.1.1, the mass of the penetrometer should focus on the tip. Furthermore, the whole system has to be robust enough to withstand hard impacts (especially the tip) without breaking or deforming and should be well protected against corrosion. Considering costs, an examination of materials led to the following choice:

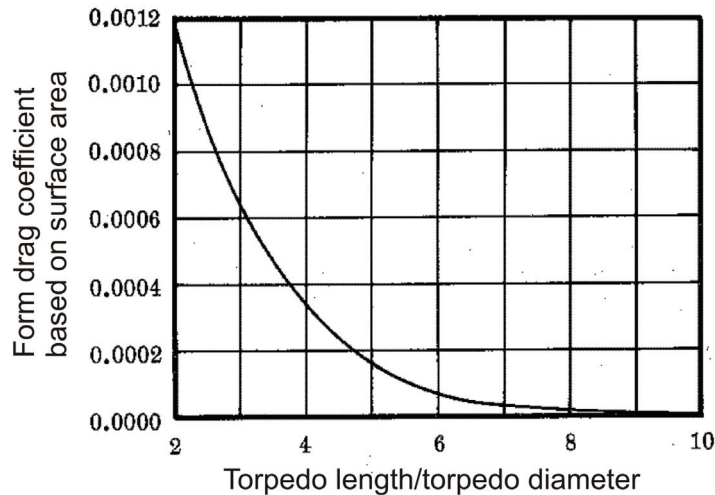


Figure 3.5: Form drag coefficient for streamlined bodies vs. fineness ratio (modified after Brooks and Lang, 1967).

- Tip: massive steel
- Main body: aluminium tube
- Tail:
 - version 1) polyvinylchloride (PVC) cone and fins
 - version 2) polyvinylchloride (PVC) cone and aluminium fins
 - version 3) aluminium cone and fins

Steel provides the desired weight and robustness, but using steel for other parts than the tip would lead to an unfitting relationship of center of gravity to center of volume. Aluminium as a tube of about 1 cm wall thickness offers the necessary resistance towards water pressure and unforeseen side impacts. PVC in this thickness would be insufficient in robustness and would risk the destruction of the device. For the tail section and the fins a massive PVC seemed to be suitable, but in case of failure, PVC could be replaced by aluminium.

All of the materials can be finished to match the required smoothness of the surface and to achieve the necessary protection against corrosion.

However, the contact of steel and aluminium as well as aluminium and aluminium in a sensible area, such as threads, under high loads and salt water conditions might lead to problems with the threads. Following that, fine threads should be avoided.

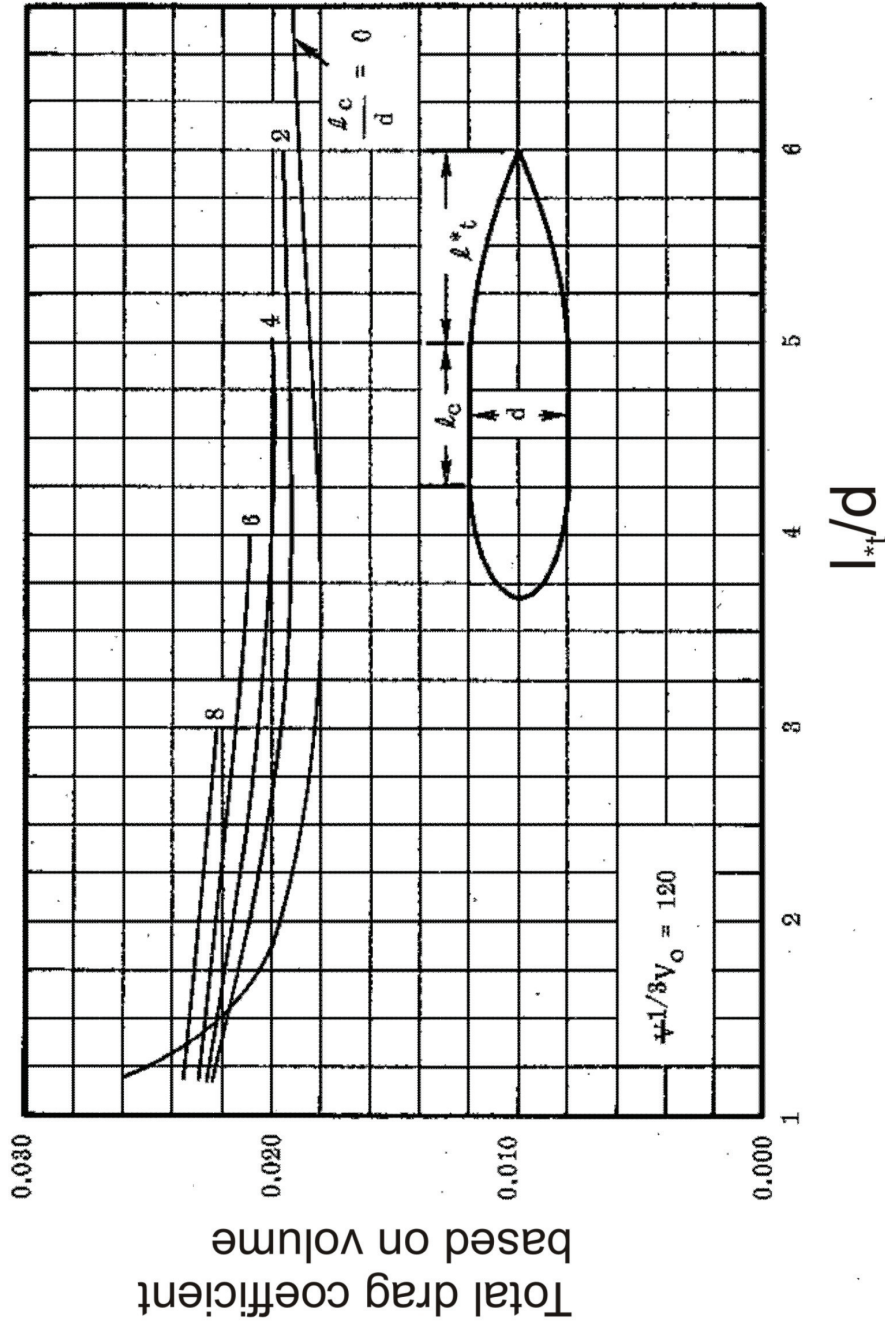


Figure 3.6: Influence of middle section fineness ratio on drag coefficient depending on tail cone fineness ratio for a body without fins. As long as the tail is longer than the object in diameter, the smaller the middle section the smaller the drag coefficient. This changes adding fins. V_0 expresses the free stream velocity, and M the object body volume (modified after Brooks and Lang, 1967).

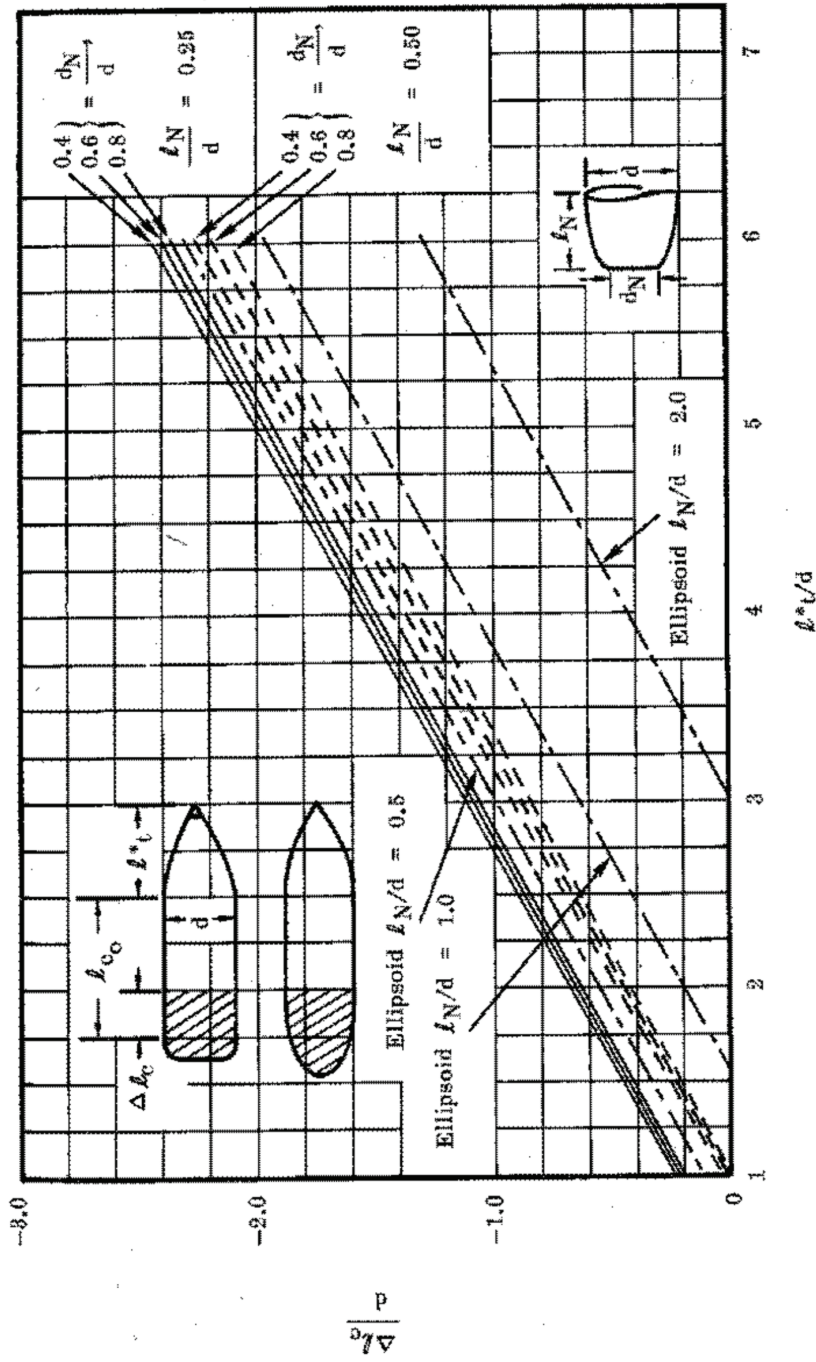


Figure 3.7: Nose shape correction factor $\Delta l_c/d$ versus tail-cone fineness ratio l^*/d (after Brooks and Lang, 1967). The shorter the nose and the more rounded the smaller (see negative values of the nose correction factor) the nose correction and the smaller the drag coefficient.

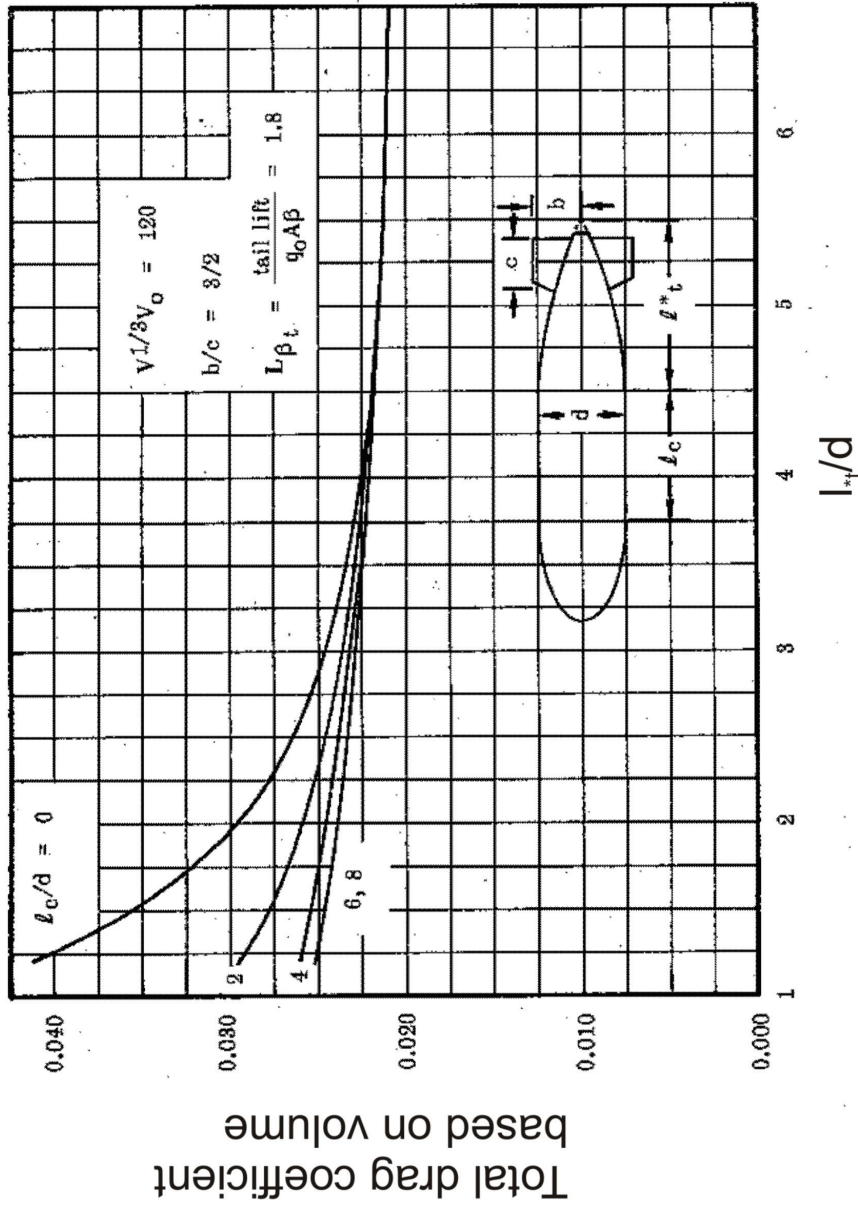


Figure 3.8: Drag coefficient based on volume for torpedos with stabilizing fins versus tail-cone fineness ratio. The bigger the tail-cone fineness ratio, that means the longer the tail with respect to the diameter the probe, the smaller the drag coefficient. This applies especially on objects with a short middle section l_c/d . The longer the middle section the smaller the effect of tail length. V expresses the local velocity, V_0 the free stream velocity, A the cross-sectional area of the object, β the inclination of the object and q_0 the free stream dynamic pressure (modified after Brooks and Lang, 1967).

3.1.3 Sensors

In the first version of *Nimrod*, only deceleration sensors and pressure sensors were targeted.

Deceleration sensors

The deceleration sensors should cover a range from 0.1 g to 200 g with a resolution of 0.1 g in case of a small deceleration. In case of harder impacts, a lower accuracy (~ 5 g in case of 200 g) can be accepted. The accuracy of the deceleration plays an important role, because penetration depth as well as sediment strength will be calculated from the measured deceleration.

Commonly used accelerometers matching the above mentioned requirements are micro-electric-mechanical systems (MEMS), piezoelectric accelerometers and piezoresistive accelerometers.

The principle of MEMS is a micro-scaled spring-mass-spring construction mostly made of silica. The displacement caused by de-/acceleration leads to a change of capacitance that can be measured. The system is widely-used and cheap. To cover a wide range of decelerations with high accuracy, a few of the sensors in different ranges are required.

In case of piezoelectric or piezoresistive sensors only one sensor can satisfy a wide range with high accuracy. For example, the piezoelectric accelerometer principle includes a piezoceramic or quartz crystal whose deformation leads to a small electric signal. However, such sensors are much more expensive than MEMS.

Independently from the type of sensor, the accelerometers can be located in the main body of the device, close to the energy supply, because a homogenous deceleration of the whole device is assumed during impact and penetration. The materials were especially chosen to make deformation negligible even in case of hard impacts.

Pressure sensor

The pressure transducer should deliver information about hydrostatic pressure and pore pressure. Water depths up to 200 m are aspired. Following that, the sensor should cover a range of ~ 2500 kPa with an accuracy of at least 5 kPa to detect even small changes in pressure.

There are different principles to measure pressure: e. g., piezoelectric, piezoresistive, etc. The piezoelectric pressure sensor is based on the same principle as

the piezoelectric accelerometers (see previous section). In case of the piezoresistive effect, the electric resistance of a material (mostly silica) is changed by pressure. This influences the electric signal, and hence, can be detected. In standard cone penetration testing two positions for the pressure sensor inlets are commonly used: in the conical tip or directly behind it (e.g., Lunne et al., 1997). Small channels shielded by a filter direct the water to the pressure sensor. The filter prevents clogging of the channels or the sensor. The proposed device needs a very robust tip. Pressure channel borings in the tip might decrease the robustness. Thus, the pressure channel inlets are planned behind the tip. Furthermore, a single part working as a cover and pressure sensor carrier would add the possibility of an easy access to the pressure transducer.

3.1.4 Data acquisition and power supply

As above mentioned a data logger logging 16 channels at a frequency of 1 kHz was required to ensure a sufficient vertical resolution during fast penetration of the sediment column. This can be found easily, however, the problems are weight, geometry and resilience. The data logger will be installed in the main body. Hence, the maximum width is about 6 cm, the length should not exceed about 10 cm and the height should be smaller than 4 cm. Additionally, it should weigh less than 1 kg. Otherwise, it would shift the center of gravity to the direction of the tail leading to a pejection of free fall performance. Third, the data logger has to bear the same deceleration as the whole device (up to 200 g are expected from XBP measurements).

Concerning data storage, a simple technique such as a common Secure Digital Memory card (SD card) was chosen after positive experiences from FFCPTU systems.

The power supply has to deliver reliable power for all sensors and the data logger for several hours. Expeditions with FFCPTU systems show that at least 8 hours non-stop data logging should be possible.

3.1.5 Realization

Considering shape, material, sensors and electronics, a hull consisting of 3 main parts (Fig. 3.9) and two sealing units was designed. The tip is a massive and very robust single part without any sensors and electronics. Made of steel it delivers the required weight and robustness. Three exchangeable tips of different geometry were designed (Fig. 3.10). The hemispherical tip

is in accordance with the above described form drag calculations. It matches the best fluid dynamical shape, and hence, provides the most stable free fall and penetration performance. The conical tip relates to the idea of standard cone penetration tests and will make a comparison to such standard methods more easy. Furthermore, the sharpened tip will increase the penetration depth into harder sediments, ergo, will be more suitable for deployments on sand. Vice versa, the cylindrical tip increases the penetration resistance and makes the device more sensitive towards very soft sediments such as fluid mud.

Behind the tip, an adapter housing the pressure sensor and its tubing connects the tip with the main body (Fig. 3.11). Thus, the access to the pressure sensor is convenient, and the electronics can be accessed from the front, too. The adapter is made of aluminium. Regarding the relation between center of volume and center of gravity, it would be possible to use steel, however, the fine-mechanical manufacture of aluminium concerning the small pressure channel borings is more easy.

The aluminium hull is thick enough to tolerate pressures equivalent to 250 m water depth, and matches exactly the length required for the electronics. A shorter version would improve the fluid dynamical shape, but would not leave enough space for the electronics including accumulators, A/D converters, sensors and data logger (Fig. 3.12). Concerning the location, the more heavy accumulator packs are located closer to the tip to support the center of gravity and center of volume relationship. The electronics are mounted on a polyoxymethylene (POM) carrier which is clamped between the front adapter and a back adapter. Both adapters seal the main body housing with o-rings. The back adapter is made of aluminium, too.

The tail has a conical shape and four cruciformed fins. In the first version of the instrument fins and tail were made of PVC. After breakage of the fins after approximately 50 deployments, they were backed up by aluminium sheets. Finally, tail and fins were exchanged by aluminium parts.

Concerning, the lengths and the diameter (Fig. 3.11): About 9 cm seems to be a sufficient inner diameter to fit the electronics into the main body. Brooks and Lang (1967) showed that a short hemispherical nose decreases the drag (Fig. 3.6). In case of the conical tip, a 60° apex angle was targeted. Following that, the tips have a length of 10–11 cm. Concerning, the main body Brooks and Lang (1967) presented that a middle section fineness ratio > 6.5 would minimize the effect on the drag coefficient (Fig. 3.7). However, a middle section fineness ratio > 4 comes close to the optimum. On the other hand, the longer the middle section the bigger the skin-friction drag. Including the measure of the electronics we have chosen a length of 46 cm for the main body leading to a middle section fineness ratio of 4.2. This seems

to be a sufficient compromise. Figure 3.7 also suggests a tail fineness ratio > 3.9 . On the other hand, we have to consider, that the tail should not become too heavy. Following that, we have chosen a length of 25 cm leading to a tail fineness ratio of 2.3.

The deceleration sensors used are MEMS sensors. These proved to deliver reliable results during FFCPTU campaigns (Stegmann et al., 2006a). To cover a wide range of deceleration with high accuracy, sensors in the range of ± 1.7 g, ± 18 g, ± 35 g, ± 70 g and ± 250 g were installed.

The pressure sensor is a piezoresistive system already equipped with a thread around the sealed sensor, which was easy to include into the front-adapter concept. The sensor has a range from 0 - 5000 kPa.

In case of the data logger, no suitable system was found in the catalogues. A special-tailored system had to be developed. AVISARO (Hannover) designed successfully such a data logger fulfilling the above mentioned requirements. At the end of March 2008, six months after start of the development, the new device *Nimrod* was ready for testing.

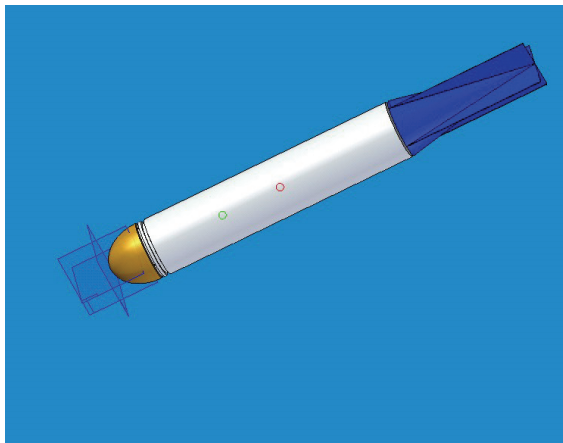


Figure 3.9: First sketch of the new device with hemispherical tip (drawn using *SolidEdgeTM*). The tip is illustrated in orange, the main body in white and the tail including fins in blue. The ring-shaped cut-out between tip and main body is part of the adapter and leaves space for the filter shielding the pressure sensor borings. The green ring indicates the center of gravity and the red ring the center of volume considering the hull. Including the sensors (especially the pressure transducer) and electronics (especially the accumulators) leads to a shift of center of gravity towards tip.

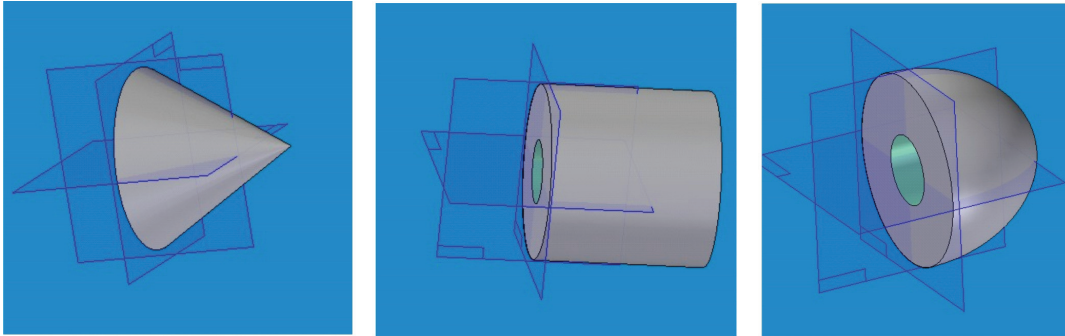


Figure 3.10: Sketches of the tip geometries: cone (left), cylinder (middle) and hemisphere (right).

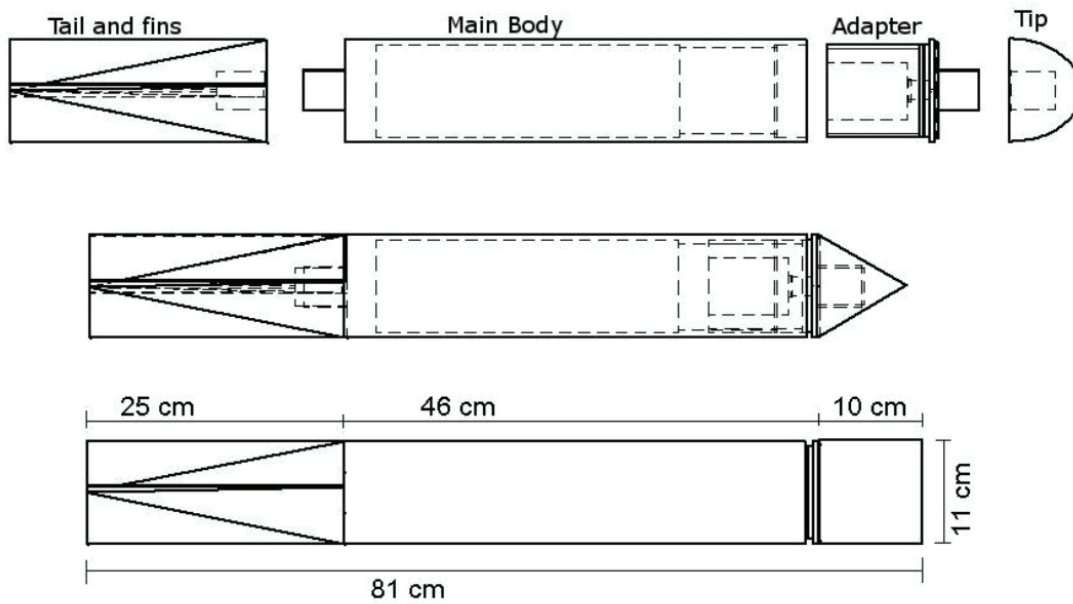


Figure 3.11: Final *Nimrod* hull concept.

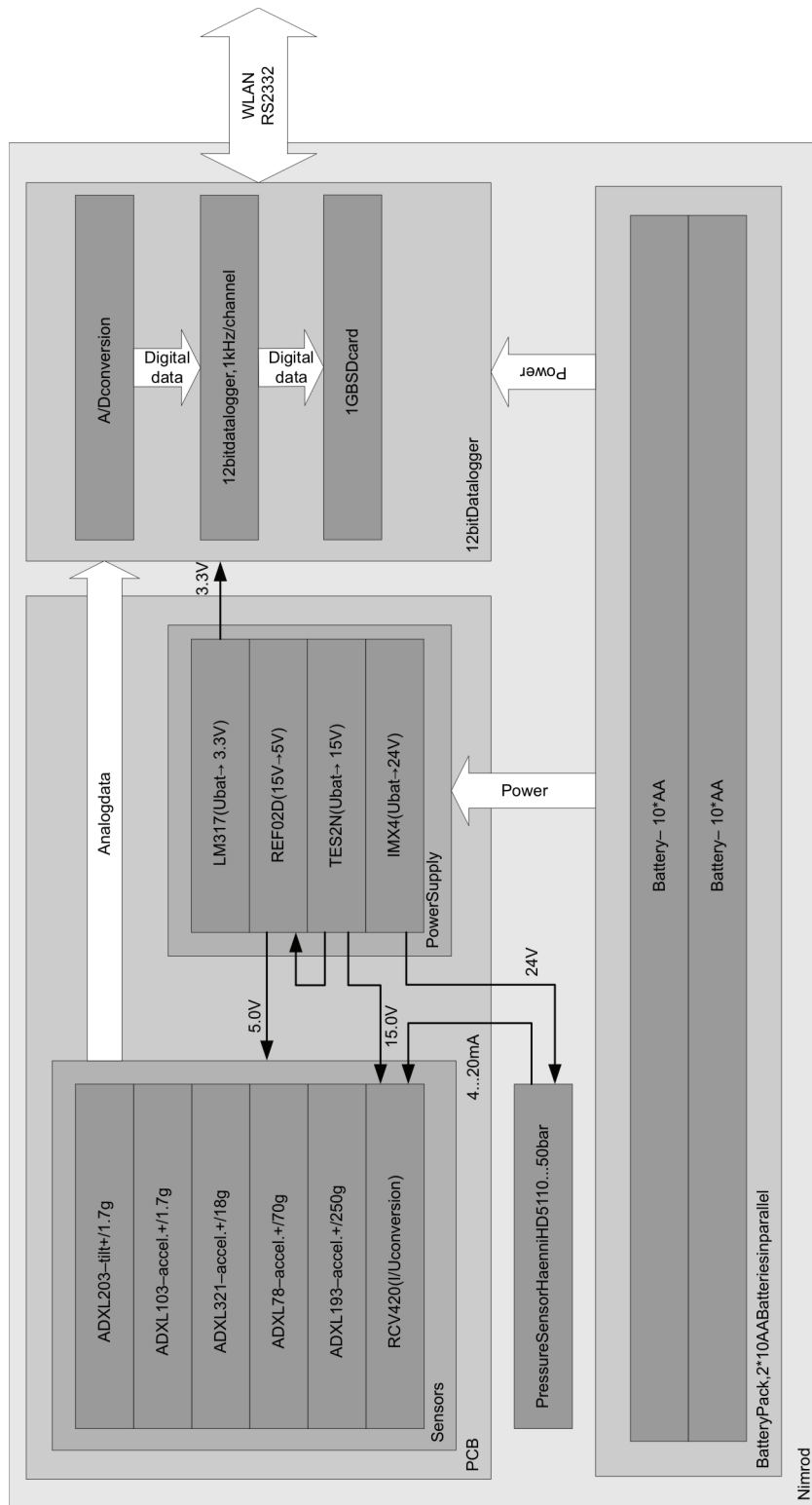


Figure 3.12: Sketch of the data acquisition system. The power from the batteries or accumulators goes to the power supply unit and the data logger. The power supply unit amplifies or damps the power to the requirements of the sensors. This goes to the sensors which send their data to the data logger. There the data is digitalized and saved on a SD memory card or can be downloaded via WLAN.

3.2 Preliminary testing

First tests are an important step in the development of a new instrument. In this section an overview of the tests from finishing of construction to first deployment on a ship is given.

3.2.1 Pressure resistance and sealing

The new device should be applicable for water depths ranging up to 200 m. Before the instrument was exposed to any impacts and water pressures, the new hull was assembled and tested in the pressure tank at MARUM. Pressures up to 2500 kPa were applied on the hull of *Nimrod* without failure of sealing or deformation.

3.2.2 Estimate of force needed for the recovery of the instrument

Tether drag is well known for disturbing the acceleration during free fall of dynamic penetrometers (e.g., Preston et al., 1999). In consequence, for a truly free falling device, a tether with a small potential to increase drag has to be chosen, meaning a small diameter and smooth surface. On the other hand, the tether has to be strong enough to withstand the pull during recovery of the device. To estimate that, the device was embedded into sand. After that, the sand was saturated with water. To consolidate the sand, the container was exposed to vibrations and load was put on the top of the sand. Then the instrument was pulled out vertically using an electronic winch and force gauge between winch and device (Fig. 3.13). Due to the conical tail and the thin fins, the maximum force needed during 5 tests was about 1 kN. Following that, the tether for recovering *Nimrod* should have a small diameter, but should still bear at least 1.5 kN. This would leave the knot connecting the tether to the *Nimrod* and the threads as the weak points during recovery. However, the knot can be supported by tie wraps and tape, whereas the thread between tail and main body can be secured using a second line connecting the main body with the tether. The threads are designed long to minimize the risk of turning loose, but a regular control in between the deployments is recommended.



Figure 3.13: Left: Force gauge between winch-hook and tether. Right: *Nimrod* being pulled out after embedment in the water-saturated sand.

3.2.3 Test of sensors and assembled device

Various dry and wet tests were done. Table 3.1 gives an overview how the instrument, and especially, the sensors were tested before the instrument was deployed the first time from a boat.

To calibrate the pressure sensor, three of the channels going to the pressure sensor were closed and the fourth was connected to an air pressure pump delivering a well-defined pressure.

The small ranged accelerometers could be tested by elevator rides. The high range accelerometers were finally addressed during first deployments in the Kuhgraben, a small stream close to MARUM, and in the port of Bremen (Tab. 3.1). A calibration was carried out by the manufacturer of the accelerometers.

After these preliminary tests (about 30 deployments), we concluded that the *Nimrod* was ready for tests in the framework of scientific cruises.

Location	Technique	Pressure Sensor	Accelerometer (small range)	Accelerometer (big range)
Laboratory	Air pump	x		
Elevator	Elevator rides		x	
Kuhgraben	Fall from a bridge	x	x	x
Port Bremen	Fall from a pier	x	x	x

Table 3.1: Overview of preliminary tests. The crosses indicate which sensor was addressed within the respective test.

3.3 Proof of concept

The next step was to deploy *Nimrod* in a geological context and to test its suitability for geological attempts.

3.3.1 Measurements on various sediments

In spring and summer of 2008, three research cruises offered this possibility: i) with R/V Senckenberg to the Jade tidal inlet channel, North Sea, (ii) with R/V Wega to the proposed wind energy test field *Alpha Ventus*, North Sea, and (iii) with R/V Breitgrund in the Eckernförde Bay, Baltic Sea. The two former research areas are characterized by sandy sediments, the latter by muddy sediments. In total, 260 *Nimrod* deployments were carried out at 140 positions. The results and *Nimrod*'s approval for geological surveys were presented within a publication in *Sea Technology*:

Stark, N., Hanff, H., Kopf, A., (2009).

***Nimrod*: A tool for rapid geotechnical characterization
of surface sediments.**

Sea Technology 50(4), pp. 10-14.

Equipped with a pressure sensor and accelerometers, a time and cost-effective probe to measure the impact signature of the sea floor

Soil mechanical properties of shallow sub-seafloor sediment such as strength, bearing capacity or excess pore pressure, are of emerging significance. They

are important parameters in offshore engineering (e.g., offshore rigs, wind energy plants), research on slope stability or sediment (re-)mobilization, and in several navy applications (e.g., mine burial).

Measurements that deliver such physical properties may be performed in the laboratory or *in-situ* on the seafloor, however, the first is usually lacking in quality by a number of factors. Sampling may affect the *in-situ* texture, specimens may be altered between sampling and laboratory experiment or laboratory conditions cannot completely simulate the natural stress state, to name just a few. As a consequence, there is need for *in-situ* instruments capable of measuring key parameters at a high frequency during penetration. The majority of the currently used techniques rely on pushed penetrometers and, less often, various types of free-falling penetrometers. Resistance (i.e. bearing capacity, or first-order undrained shear strength), deceleration, (pore) pressure, tilt, and friction (as a measure of sediment viscosity) are among the parameters recorded.

Pushed penetrometers have the advantage of a controlled, quasi-static deployment at constant rate (usually 2 centimeters per second). Their disadvantage lies with the heavy frame that has to be lowered to the seafloor to allow the build up of the force required for penetration. Hence, they are dependent on large vessels and powerful cranes and winches.

Similarly, some free-falling penetrometers profile the sea floor by their own momentum as a function of weight and velocity.

Often they depend on ship equipment like winches, too, which may result in significant disturbance of the measurement because of the coupling between the probe and ship movement (owing to heave).

In contrast, small penetrometers are truly free-falling and independent from a winch. They therefore measure the deceleration of the probe and allow the user to derive strength, but lack information about the influence of pore pressure (and hence do not record effective strength). Thus, University of Bremen researchers identified the need for a system that is independent from ship equipment, deployable in more difficult environments (e.g., huge waves, strong currents, adjacent to constructions), and capable of monitoring all parameters required to estimate *in-situ* strength and pore pressure at very high frequency.

Such a probe is further desired to be user-friendly as well as time and cost-effective so that it may be deployed by ship personnel without excessive training. Taking all those pre-requisites into account, this article presents a lightweight tool for seafloor geotechnical characterization whose data can easily be downloaded using a wireless link. Deployment and recovery is possible by just one person without any further ship equipment and takes about three minutes depending on the water depth.

Basic design

The new probe, *Nimrod* (Fig. 3.14), is a shallow water (max. 200 meters depth) free-falling penetrometer deployable on a tether (4 millimeters across) that does not interfere with the probe's performance.

Its weight, which varies from 13 to 15 kilograms depending on the tip geometry, is sufficient to induce a fall with a constant terminal velocity of up to eight meters per second through the water column, but low enough that it can easily be handled by an individual. The terminal velocity is reached after roughly five meters in the water column and the relationship between center of gravity and center of volume stabilizes the orientation during the fall. Fins support this stabilization without disturbing the process of penetration.

Nimrod's modular hull design consists of the tail, main body, an adapter and the exchangeable tip. Its tail is made of light polyvinyl chloride and has a conical shape with four crosswise strengthened fins, which run parallel to the main body.

The fins can be fortified with thin aluminium sheets.

The dimension of the hull and the fins were taken from fluid-dynamical designs. The design supports a stable fall as well as an easy recovery out of the sediment.

Two center-lined borings allow to connect the main tether to the biggest portion of the tail or to the back of the main body to ensure a safe connection; an additional boring offers connection of a safety tether.

The main body is an aluminium cylinder that hosts the electronics, four accelerometers that can measure acceleration and deceleration from ± 1.7 multiples of gravitational acceleration for very soft sediments up to ± 250 multiples of gravitational acceleration for hard sediments and two tilt sensors (± 20 degree from vertical position). *Nimrod's* key component is a tiny lightweight data logger, which transforms and records the analogous output of each transducer digitally at very the high sampling rate of 1 kilohertz and a resolution of 12 binary digits on a standard Secure-Digital-memory-card (SD-card). The recorded data may be transferred either by Wireless Local Area Network (WLAN) or manually by SD-card exchange.

While designing *Nimrod's* electronic package, special attention had to be paid to the energy efficiency because of the limited space for power supply. Three switched-mode power supply units (SMPS) were implemented to optimize voltage conversions. Custom-made battery packs provide an operating time of ≥ 20 hours with a single charge.

The adapter in front of the main body is aluminium and houses the pressure

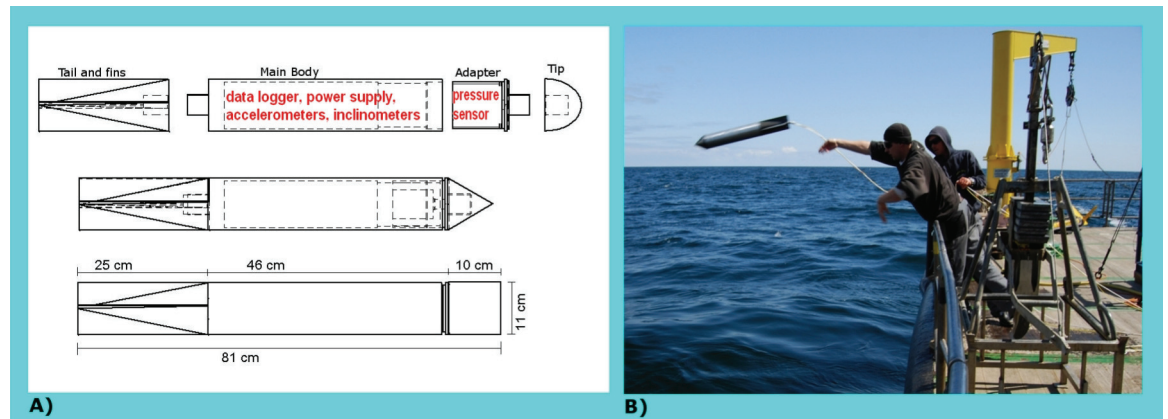


Figure 3.14: A) *Nimrod*'s modular design consists of tip (three geometries), adapter, main body and tail. B) *Nimrod* can be easily handled by a single person.

sensor (range 0 to 5 megapascal). Four crosswise borings allow hydraulic communication with the transducer. A filter of porous plastic shields the hydraulic borings from clogging. Along with the pressure unit, the adapter is the sealing of the main body and enables connection to the exchangeable tips.

Since both the total penetration depth and the sensitivity of the measurement depend on the tip geometry, *Nimrod* currently offers a choice of three tip geometries depending on the anticipated sediment. The conical tip enables good penetration into stiff sand. The cylindrical tip offers the possibility to detect very soft layers as fluid mud, because the flat tip provides maximum resistance upon impact. The hemispherical tip is the choice for all sediments in between (e.g. silt, mud and indurated clay).

All tips are made of steel and thus provide both the main mass of the whole instrument and the required distance between center of gravity and center of volume. Their rigidity and sturdiness make the tips shockproof making *Nimrod* very robust.

Experimental results

After an extensive testing phase in large tubs at the Center for Marine Environmental Sciences (MARUM) at the University of Bremen and in small streams near Bremen, the team evaluated *Nimrod*'s capability on first deployments during three cruises.

The first cruise took place in the dune-dominated Jade estuary in the North Sea with R/V Senckenberg. Sediment samples showed a stiff, medium to

coarse sand with occasional shells and shell fragments. Acoustic methods provided evidence of a very thin mobile layer overlying the dunes depending on time in the tidal cycle. Given that the resolution of many acoustic methods is limited to layers ≥ 5 centimeters, *Nimrod* was used to potentially characterize these uppermost sediments.

The device was deployed at about 30 different positions along the dune using the conical tip. Despite the fact that the penetration depth was rather small (up to 20 centimeters) in the stiff sediment, *Nimrod* clearly displayed in the deceleration - depth profile a thin, poorly consolidated layer of 4-10 centimeters overlying the stiffer material forming the main body of the dune. The high logging frequency not only allowed identification of the mobile layer, but resolved internal changes within these uppermost sediments. For both layers a typical range of maximum deceleration has been monitored: the mobile layer shows 6 ± 2 multiples of gravitational acceleration while the stable underground ranges from 12 to 37 multiples of gravitational acceleration (depending on the position along the dune)(Fig. 3.15). This range of maximum deceleration in the underlying dune sand is due to seafloor inclination of the dune ridges. The steeper the ridge, the smaller is the maximum deceleration. The soft mobile layer is less influenced by the inclination because the probe interpenetrates this layer regardless what the slope angle may be.

The second cruise occurred with WVFS Wega some 50 kilometers north of the barrier island of Borkum in the North Sea, where the first German offshore wind farm is currently installed. Acoustic sub-bottom profiling monitored very homogenous sediment, which was later confirmed by sampling fine sand with small amounts of shell fragments. *Nimrod* was deployed thrice at approximately 40 different positions in the area. The data present homogenous deceleration profiles without evidence of layering and maximum decelerations of about 40 ± 5 multiples of gravitational acceleration when using the conical tip. As a mean value the maximum deceleration is about 25 percent higher than in the Jade due to the finer, consolidated, well sorted sand. When comparing three deployments at the same position, data show only small variations (≤ 5 percent). During the deployment with the hemispherical or the cylindrical tip, the maximum deceleration increases to about 120 percent and 150 percent of the maximum deceleration using the conical tip, respectively.

A cruise with WFS Breitgrund in Eckernförde Bay in Germany offered the chance to use *Nimrod* in an area of soft to very soft sediment, as evidenced by clay-rich oozes recovered in gravity cores. *Nimrod* was deployed three times at each of the 20 positions inside and outside a gassy pockmark. In the soft sediment *Nimrod* reached penetration depths of 2 meters and a maximum deceleration of only 4 ± 2 multiples of gravitational acceleration depending

on the position when using the hemispherical tip (Fig. 3.15).

Pore pressure was monitored successfully as a steadily increasing parameter when falling through the water column (i.e., hydrostatic pressure) and an increasing signal upon impact and penetration (partly artificial and partly excess pore pressure) (Fig. 3.16). Again, the results of the different deployments at one position showed a very low variability and provided significant confidence in reproducibility of the data.

During the wealth of initial tests, it could be shown that all sensors delivered clear information about the different steps of deployment. Immediately before launching, the inclinometers usually show an unstable and subvertical starting position while the person deploying the system holds it and the pressure sensor records ambient air pressure. Upon hitting the water surface the probe veers off the course due to a very turbulent surface. However, in the water column it stabilizes very quickly to a range of ± 5 degree from vertical. Because of currents, *Nimrod* sometimes keeps a decreasing oscillation. The pressure sensor records a linear pressure increase with increasing water depth. The deceleration sensors monitor terminal velocity (5-8 meters per second dependingly mainly on tip geometry) after a few meters until impact and penetration into the seafloor.

Depending on sediment strength and tip geometry a deceleration from 1 to 200 multiples of gravitational acceleration and a penetration depth from 0.01 to 2 meters were reached in the different areas of testing. The pressure sensor displayed both increase and decrease in pressure during penetration depending on penetration depth and type of sediment. Using the inclinometers, it is possible to check if the probe remained in its vertical position during impact and penetration, and this was achieved in more than 95 percent of the deployments.

To summarize, about 200 *Nimrod* deployments confirmed the quick and comfortable handling, a good fluid dynamic performance, stable electronics, and reliable and reproducible high-resolution results. The different tip geometries were successfully applied to varied penetration depths and resolutions, and those tips took the geological scenario encountered in the various study areas. Furthermore, the results are found comparable to other methods such as expendable Bottom Penetrometer (XBP) and Cone Penetration Tests (CPT).

Acknowledgments

This development was funded by MARUM DFG-Centre of Excellence, Univ. Bremen, Germany. We further acknowledge the outstanding help of Matthias Colsmann (AVISARO, Hannover), Matthias Lange and Sergey Dzuhinov

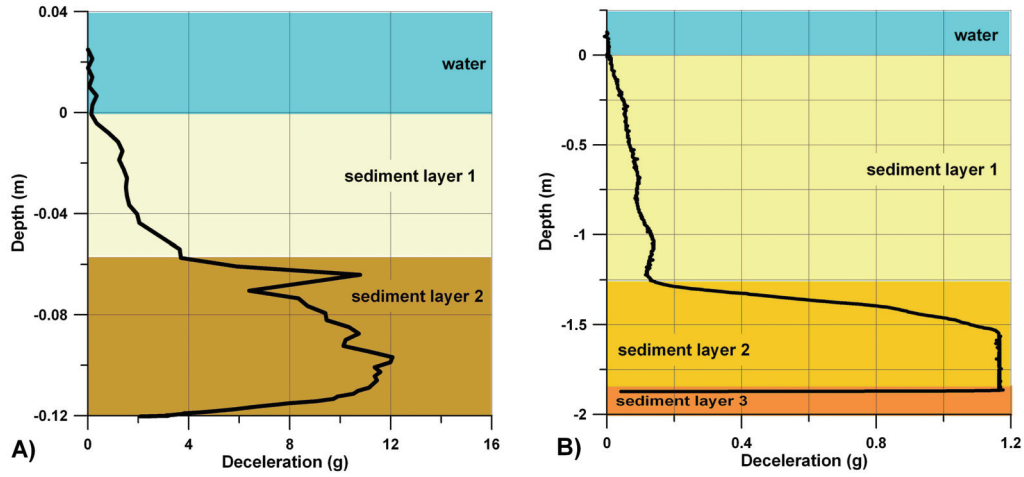


Figure 3.15: Deceleration versus depth profile (A) with the conical tip in Jade Bay in the North Sea and (B) with the hemispherical tip in Eckernförde Bay.

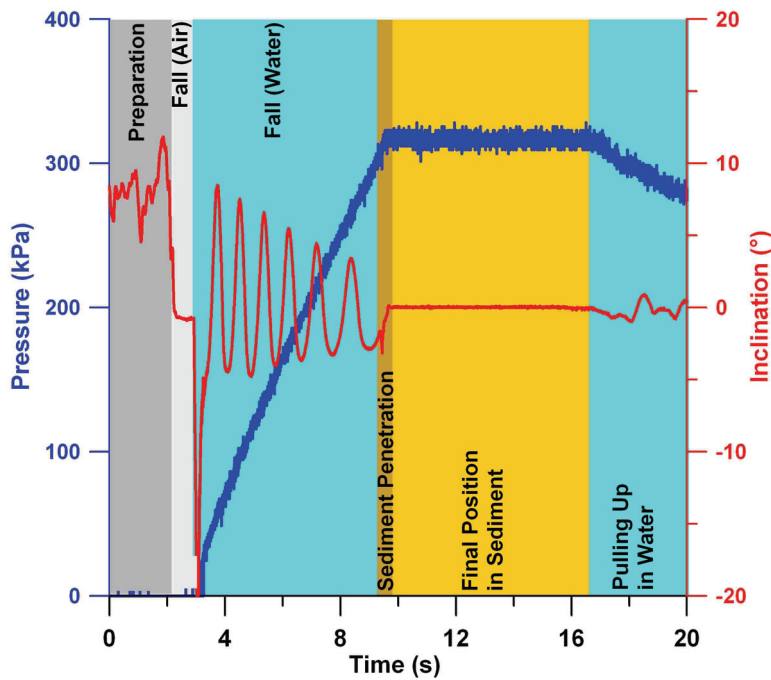


Figure 3.16: Time versus pressure/inclination profile of a *Nimrod* deployment in Eckernförde Bay. The figure displays all steps of deployment (holding to recovery).

(MARUM, Bremen), Roy Wilkens (SOEST, Honolulu), and Thomas Wever and Ralf Lühder (FWG, Kiel). The authors thank Verner Ernstsen (MARUM, Bremen) and the crew of R/V Senckenberg, Maria Lambers-Huesmann (BSH, Hamburg) and the crew of WVFS Wega, and Hannelore Fiedler (FWG, Kiel) and the crew of WFS Breitgrund for the possibility to use NIMROD during their expeditions.

3.3.2 Measurements on sand

The use of dynamic penetrometers on sandy sediments is problematic. The impacts are hard, the penetration depth is small, and lance-like systems are at risk of breaking or kinking. However, the *Nimrod* delivered reliable results for the uppermost sediment surface from the Jade tidal inlet channel (medium to coarse sand) and the proposed wind energy test field *Alpha Ventus* (fine sand).

Following that, more measurements were carried out on sandy seafloors: at Halekulani Sand Channel, Waikiki, Kailua Bay and Waimanalo Bay, all close to the Island of O’ahu, Hawaii. The results were compared to the results from the North Sea to study the differences of quartz and carbonate sand as well as the effects of grain size, grain shape and density on the dynamic penetrometer profiles. *Nimrod’s* performance on different types of sand was compared and published at the MTS/IEEE OCEANS Conference at Biloxi, MS, USA, including hints of sediment remobilization in the penetrometer signatures. Furthermore, the attempt to derive an equivalent of quasi-static bearing capacity from the deceleration profiles is presented here:

**Stark, N., Hanff, H., Stegmann, S.,
Wilkens, R., Kopf, A., (2009).
Geotechnical investigations of sandy seafloors
using dynamic penetrometers.
MTS/IEEE OCEANS 2009, Biloxi, USA.
ISBN 978-0-933957-38-1.**

Abstract

Geotechnical *in-situ* characterization of the strength of the shallowest sub-seafloor sediment is an important factor in offshore engineering (e.g., scouring at wind energy plants), coastal engineering (e.g., sediment erosion close to the shores and beaches), navy applications (e.g., mine burial) and research (e.g., dunes in tide-affected areas). Dynamic penetrometers are well known as time- and cost-saving means to derive sediment physical properties *in-situ* and to detect layering or changes of strength of the shallow marine deposits. However, until now such instruments were rarely used on hard sandy seafloor because of their small penetration depth. The aim of this study is to unravel how applicable dynamic penetrometers are on sand and what kind of information they can deliver. Deceleration – depth signatures of the devices are used to compute quasi-static bearing capacity and related to governing parameters such as mineralogical composition, grain size distribution and sedimentary layering.

We present the results of measurements on sand with two different types of dynamic penetrometers (FFCPTU and *Nimrod*) developed at MARUM (University of Bremen, Germany). The devices were operated with different penetration velocity, with different deploying technique and in variable sedimentary conditions. The parameters monitored during penetration are deceleration and tip resistance. Data analysis follows two approaches. First, we directly compared deceleration - depth profiles from both instruments to extract typical profiles for the different materials and to quantify areas of sediment remobilization. Second, dynamic bearing capacity is derived from the deceleration (*Nimrod*) and from the tip resistance (FFCPTU) respectively. Following an empirical approach (Dayal and Allen, 1975; *Can. Geotech. J.*) dynamic bearing capacity can be converted into quasi-static bearing capacity for a chosen threshold penetration velocity to consider the varying impact force and penetration rates of the devices. This allows a better comparison of different dynamic penetrometers to each other and to standard CPT records.

A comprehensive data set was acquired in four research areas, which differ in type of sand, grain size and appearance of processes of sediment remobilization. The first research area stretches along a dune in a tidal inlet channel in the Jade estuary, North Sea. The sediment consists of medium to coarse quartz sand (after

Udden-Wentworth scale). Acoustic sub-bottom profiling indicates sediment movement induced by the tides. The second area is in the North Sea, 50 km north of the island of Borkum (Germany) in the planned wind energy farm *Alpha Ventus*. Sediment sampling yielded fine-grained sand and acoustic sub-bottom profiling showed very homogeneous sediment with no hints for significant sediment mobilization. The third (Kailua Bay) and fourth (Waimanalo Bay) regions are located at the windward side of O’ahu, Hawaii, USA. Sediment in both areas is carbonate sand, with the Kailua material generally being finer-grained. In Waimanalo Bay, deployments focussed on the zone of the shorebreak to shed light on sediment mobilization.

In our study, we observed short penetration times of 0.1–0.25 s and small penetration depths (< 0.5 m) with the consequences of a high risk of tilting and disturbances by ship movement in case of winch-lowered deployments. In contrast, true free-fall, fluid-dynamical shape, tip-oriented center of mass and high sampling rate were identified as advantages during the deployments. However, we found typical impact signatures for the different research areas with either penetrometer and could further show that owing to the high sampling rate, layering can be detected at a cm-scale. Mineralogical composition has a significant effect on the penetrometer’s response. The carbonate sand (Waimanalo Bay, Kailua Bay) caused a significantly higher maximum deceleration (*Nimrod*: carbonate sand: 120–210 g, quartz sand: 25–85 g) and corresponding quasi-static bearing capacity (*Nimrod*: carbonate sand: 80–200 kPa, quartz sand: 17–69 kPa). Beside that, we observed an increase in maximum deceleration and quasi-static bearing capacity in carbonate sand as well as in quartz sand when grain size decreased. Using *Nimrod* on carbonate sand we found maximum decelerations of up to 210 g in areas of a dominant grain size of 0.063–0.3 mm (Kailua Bay) and up to 155 g in areas of a dominant grain size of 0.3–0.63 mm (Waimanalo Bay).

One of the foremost goals of this study was to test whether the dynamic penetrometers can resolve thin layers of mobilized sediment in areas as affected by tides, waves, etc. Therefore, we compared the impact signatures in an area, where no significant sediment mobilization is expected (area *Alpha Ventus*) with one which is well-known for tide-affected sediment movement along a dune (Jade estuary), and two areas with a shorebreak contributing to beach erosion (Waimanalo Bay and Kailua Bay). In summary,

we found (i) no layering in the area *Alpha Ventus*, (ii) a looser layer (quasi-static bearing capacity 3 – 10 kPa) of 0.02 – 0.06 m thickness depending on position along the dune and tide in the Jade estuary and (iii) a looser layer (quasi-static bearing capacity 5 – 25 kPa) of 0.03 – 0.1 m thickness in the areas of the shorebreaks (Waimanalo and Kailua Bay).

Introduction

Geotechnical properties of the upper layers of the seafloor spark an increasing interest in different disciplines. In offshore engineering the strength of the seafloor is important for all kinds of installations as much as for cable tracks and pipelines. The Navy uses such information for burial prediction in mine hunting. In research, strength and pore pressure are important parameters for slope stability and sediment remobilization at ocean margins.

Generally, the soil mechanical behavior of seafloor sediments can be investigated using quasi-static or dynamic methods in the laboratory (e.g., vane shear (quasi-static), falling cone test (dynamic)) or *in-situ* (e.g., pushed cone penetrometers (quasi-static), dynamic penetrometers) (Johnson et al., 1988; Wong et al., 1993; Stoll et al., 2004; Stoll et al., 2007). These methods deliver properties such as sediment strength, shear strength, bearing capacity or pore pressure and information about inhomogeneities such as layering (e.g., Das, 1990). *In-situ* methods complement the well-established laboratory methods, which can be hampered by the often highly disturbed nature of the sediment owing to coring or sampling, transport and storage. In case of quasi-static *in-situ* measurements, (e.g., STATPEN, Stoll et al., 2004) a continuous profile of several meters of the sub-seafloor sedimentary succession can be derived, but these methods are very time- and cost-consuming. Also, they are very sensitive to weather or currents, because heavy equipment has to be lowered to the seafloor.

In contrast, dynamic methods are very time- (and hence cost-) efficient (Stoll and Akal, 1999; Stegmann et al., 2006a; Stark et al., 2009). A seagoing device is deployed within short periods of time, collects data (depending on the respective device, e. g., deceleration, pressure, tip resistance, sleeve friction) whilst profiling the water column and seafloor, and can quickly be recovered for data download or may even deliver the results in real-time using telemetric means (Stoll and Akal, 1999; Stegmann et al., 2006a; Stark et al., 2009). Furthermore, they can be deployed in more challenging areas and conditions. Depending on the respective probe they can go winch-lowered or free-falling and deliver sediment strength, shear strength and excess pore pressure

(Lunne et al., 1997; Stoll et al., 2004; Aubeny and Shi, 2006; Stegmann et al., 2006b) as well as information about layering and sediment inhomogeneities (e.g., stones, plant fibres) of the uppermost meters of the seafloor (Stoll and Akal, 1999; Stark and Wever, 2008). Dynamic penetrometers are especially suitable for investigations of processes at the seafloor surface such as sediment remobilization due to tides, currents and waves, scouring at installations or burial of mines, cables or pipelines. So far, dynamic penetrometers were used largely on soft sediments (Johnson et al., 1988; Aubeny and Shi, 2006; Stegmann et al., 2006b; Kopf et al., 2007; Seifert et al., 2008; Stark and Wever, 2008; Kopf et al., 2009) because of the low penetration depth on sandy seafloors.

This study is a comprehensive approach (i) to introduce and compare two dynamic penetrometer systems developed at MARUM, Bremen, (ii) to deploy them in areas of different hydrologic regime and sediment composition, (iii) to measure strength and derive bearing capacity as crucial parameters from sediment remobilization and redeposition, and (iv) to identify mobile layers (and sedimentary layering as a whole). Therefore, we investigated impact signatures in terms of deceleration – depth profiles and the corresponding quasi-static bearing capacity of two instruments (FFCPTU and *Nimrod*) in four research areas, which differ in (a) mineralogical composition (quartz sand in the Jade estuary and area *Alpha Ventus*, both North Sea; carbonate sand in Waimanalo Bay and Kailua Bay, both Hawaii, USA), (b) grain size and (c) hydrodynamic conditions (tides, Jade estuary; shorebreak, Waimanalo and Kailua Bay).

Methods and regional geology

***In-situ* instruments used** Two different modular dynamic penetrometers were recently developed at MARUM Research Centre, Bremen, Germany (Fig. 3.17). Besides a number of minor differences as well as similarities in geometry and specifications (for details, see Tab. 3.2) the main conceptual difference is the penetration performance. *Nimrod* is approximately fluid-dynamically shaped, possesses fins and a fall stabilizing relationship between center of mass and center of volume owing to its very robust conical steel tip (60° opening angle). Thus, *Nimrod* finds its right falling and penetration orientation even in case of waves, stronger currents or shallow water depths (Stark et al., 2009). The design is largely along the lines of eXpendable Bottom Penetrometers (Stoll and Akal, 1999; Aubeny and Shi, 2006), which are used for sediment classification by considering the deceleration of the probe (Stoll and Akal, 1999; Stoll et al., 2004), whereby *Nimrod* offers different tip

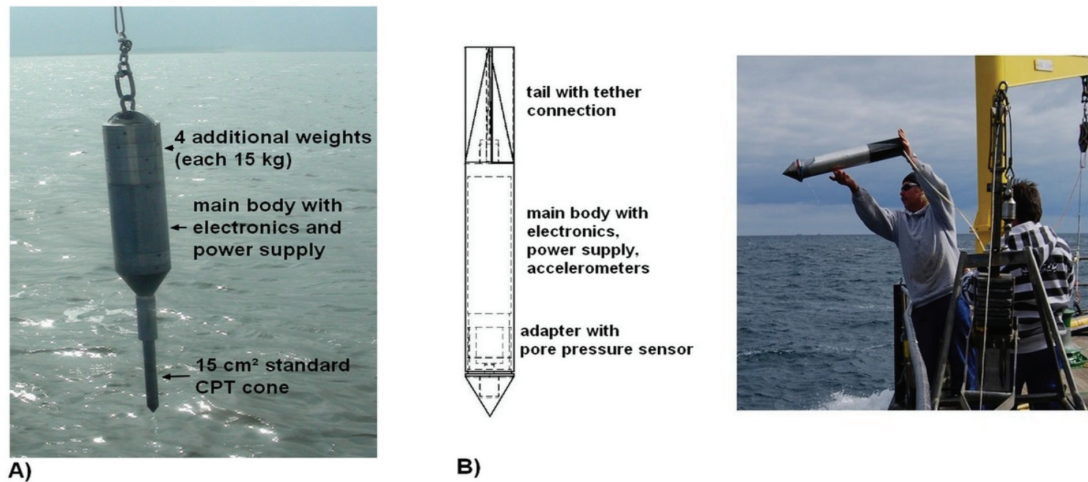


Figure 3.17: The two shallow-water dynamic penetrometers developed at the MARUM, University of Bremen: the free-fall CPT lance (A) and *Nimrod* (B).

geometries and measures the pressure additionally to the deceleration (Stark et al., 2009).

The CPT lance (Lunne et al., 1997; Stegmann et al., 2006a; Stegmann et al., 2006b; Kopf et al., 2007; Seifert et al., 2008; Kopf et al., 2009) has a smaller and more delicate conical tip (60°) which hosts some of the transducers, e.g., strain gauges, pore pressure, temperature in a 15 cm^2 cone. Here, just the CPT probe and the overlying rods but not the wider pressure housing penetrate the sea floor. The center of mass lies in the upper main body, so that in case of free-falling performance and strong currents there is the risk of turning during the fall or kinking during impact. Thus, a short rod (Fig. 3.17) and winch-lowered deployments were preferred for measurements on sand. Additionally to deceleration and pressure, the CPT lance measures tip resistance, sleeve friction and temperature.

Both instruments are self-contained and the data acquisition is similar. Accumulator packs provide the necessary power, and switched mode power supply units (SMPS) together with linear regulators convert voltages for each sensor efficiently (Stegmann et al., 2006; Stark et al., 2009). The analog raw data are converted by an A/D converter, logged and saved on a memory card. For detailed information about the configuration and differences of the two devices see Tab. 3.2.

	CPT lance	<i>Nimrod</i>
Tip geometry	Cone	Cone
Cone angle	60°	60°
Diameter	4 cm	11 cm
Length	1.2 m	0.81 m
Mass	100 kg	13 kg
Pore water inlet	behind cone	behind cone
Center of mass	Cover, Main body	Tip
Deployment	Winch lowered	Free falling
Tether diameter	20 mm	4 mm
Mean impact velocity	0.5 m/s	6 m/s
Pressure sensor	absolute, 2 MPa	absolute, 5 MPa
Accelerometers	MEMS, 1.7 g, 5 g, 18 g, 100 g	MEMS, 1.7 g, 18 g, 70 g, 250 g
Inclinometer	20°	20°
Tip resistance sensor	100 MPa	no
Sleeve friction	100 MPa	no
Data logging	40 Hz	1000 Hz

Table 3.2: Technical details and used configurations of the penetrometers.

Data processing Direct interpretation of dynamic penetrometers (Stoll and Akal, 1999; Stoll et al., 2004; Stark and Wever, 2008; Stark et al., 2009) is crucial for the detection and quantification of layering, but to predict how much load the seafloor could bear in concrete values as sediment strength, bearing capacity or shear strength are demanded. The following section will describe the method we used to derive sediment resistance and bearing capacity, as exemplified for *Nimrod*.

Nimrod impacts with the terminal velocity it reached during the fall through the water column and is then decelerated depending on sediment properties, properties of the probe itself and free-fall behavior. The terminal velocity results from properties of the seawater (e.g., currents, density, Meschede, 2001), of the device (e.g., geometry, Mott, 2005; surface roughness, Meschede, 2001) and the used tether (e.g., length, Mott, 2005; surface roughness, Meschede, 2001). Regarding the probe as a single particle in equilibrium (after reaching the terminal velocity in the water column), the sediment exerts a sediment resistance force F_{sr} against the probe and decelerates it (Aubeny and Shi, 2006):

$$m_{Nim}dec = F_{sr}, \quad (3.5)$$

where dec stands for measured deceleration and m_{Nim} for the mass of *Nimrod* in water (with conical tip 8 kg).

After Aubeny and Shi (2006) this sediment resistance force includes a sediment shearing resistance force F_s and buoyancy of the probe in soil F_b :

$$F_{sr} = F_b + F_s. \quad (3.6)$$

Inertial forces are negligible here (Aubeny and Shi, 2006). The buoyancy of the probe in soil is neglected here because of small penetration depths of a few centimeters.

Dynamic penetrometers have different penetration rates, which decrease during the penetration process, whereas quasi-static methods keep a constant penetration rate. This leads to a variable strain dependency of the sediment strength reflecting properties such as deceleration, tip resistance or sleeve friction. Stoll et al. (2004), Aubeny and Shi (2006) as well as Stoll et al. (2007) used strain rate factors to convert quasi-static sediment resistance to higher, dynamic penetration rates and vice versa. Stoll et al. (2007) illustrated that a difference in penetration velocity of about 3 m/s can lead to six times higher sediment resistance results in case of a medium compacted sand. To allow a direct comparison of different dynamic penetrometers and to standard methods, the empirical approach by Dayal and Allen (1975) uses the strain rate factor f_{ac} , which depends on the actual penetration velocity v and a reference velocity v_0 (see eq. 3.7). When inserted in eq. 3.8, it serves to convert the rate-dependent sediment resistance force to a value corresponding to a quasi-static penetration at the constant reference velocity. We have chosen $v_0 = 0.02 \text{ m/s}$ for the calculations presented in this paper, because this rate reflects the standard quasi-static CPT routine (Lunne et al., 1997; Cai et al., 2009). It follows that:

$$f_{ac} = 1 + K \log \left(\frac{v}{v_0} \right), \quad (3.7)$$

with K being a dimensionless factor ranging from 1.0 to 1.5 (Stoll et al., 2007).

To convert the sediment resistance force from high-speed dynamic deployments to quasi-static (= constant rate) values, the dynamic sediment resistance force F_{sr} has to be divided by the strain-rate factor f_{ac} :

$$F_{qsr} = \frac{F_{sr}}{f_{ac}}, \quad (3.8)$$

where F_{qsr} is the sediment resistance force for a quasi-static penetration with constant penetration rate v_0 .

The bearing capacity q_u is the maximum load per unit area that a soil can bear prior to failure (e.g., Terzaghi, 1943; Das, 1990). Regarding the soil as a grid of several, very thin layers of particles the penetration can be viewed as a sequence: The probe hits the upper layer. The load per unit area or pressure on the soil exceeds the bearing capacity. The upper layer fails and the probe hits the next layer, and so on. Thereby, the deceleration as a function of soil resistance force for each layer is the maximum resistance force the sediment withstands until it fails and the probe keeps penetrating (Aubeny and Shi, 2006). That means the sediment resistance force can be used to calculate the bearing capacity by:

$$q_{u(q)} = \frac{F_{(q)sr}}{A}, \quad (3.9)$$

where A is the area of the plain subjected to load. It has to be taken into account that as long as the penetration depth is smaller than the tip height (*Nimrod*: 11 cm, CPT lance 4 cm) the loaded surface varies with penetration depth.

To describe the contributing mechanisms, the bearing capacity can be expressed as an effect of cohesion, q_c , effect of surcharge, q_q , and of the unit weight of the soil, q_γ , by, e.g., Terzaghi (1943), Das (1990):

$$q_u = q_c + q_q + q_\gamma = cN_c + qN_q + \frac{1}{2}\gamma BN_\gamma. \quad (3.10)$$

They are defined by the cohesion c , the load on the surrounding sediment surface q , the unit weight γ , the width of the penetrating object B and the so called bearing capacity factors N , which depend on the friction angle (Das, 1990). In this study we only investigated cohesionless sands so that in contrast to the presented calculations of cohesive soils (Stoll et al., 2004; Aubeny and Shi, 2006; Stoll et al., 2007) q_c can be neglected. q_q is a function of the load on the surrounding sediment, which equals the hydrostatic pressure in surface sediments, so that q_q is zero at the sea floor and increases with depth. q_γ also expresses the influences of the unit weight of the material, which has to be moved. Furthermore, after the modified general ultimate bearing capacity equation all summands should be multiplied by a factor of depth, a factor of shape and a factor of inclination (Das, 1990). In case of the factor of depth the relationship between width of the penetrating object and penetration depth is important (Meyerhof, 1953). Concerning the shape, after Cassidy and Houlsby (2002) the conical apex angle and the surface roughness of the cone has to be regarded. An inclined penetrating probe or an inclined seafloor goes into the factor of inclination (Das, 1990).

From the above, a quasi-static bearing capacity - depth profile results, which

defines the maximum load the sediment can bear at any given depth using a defined penetration object and assuming a constant penetration rate. In case of *Nimrod*, deceleration went into the calculations, whereas in case of the FFCPTU the analysis was done based on deceleration and for comparison based on tip resistance. Therefore, we assumed that measured tip resistance force equals the dynamic sediment resistance force (see eq. 3.9 above).

Because of the small instrument penetration (mostly < 0.2 m), changes of hydrostatic pressure are negligible. Also, excess pore pressure is neglected here, because the penetration depth was too small to achieve reliable results of excess pore pressure (pressure sensor located behind the conical tip in u2 position) with either instrument.

Regional geological context and deployment strategies The measurements for this study were carried out in two areas of quartz sand in the North Sea and two areas of carbonate sand in the Pacific. The first area is located in the Jade estuary (western German Bight, North Sea) and stretches out along a dune strongly influenced by tides. Here, we expected a mobilized loose layer on a harder underground after acoustic sub-bottom profiling (Svenson et al., 2009). The thickness of this layer depends on tidal phase as well as on location on the dune relative to the direction of the current (Bartolomä et al., 2004). Grab samples recovered medium to coarse and very coarse sand (after Udden-Wentworth scale) with some gravel and often a layer of shells and shell fragments at the top (Tab. 3.3). The second area is the area of the *Alpha Ventus* wind energy test field ~ 50 km north of the island of Borkum, North Sea. The measurements presented here took place before installations were started. Based on acoustic sub-bottom profiling and grab samples sediments can be described as homogenous very fine to medium sand (after Udden-Wentworth scale) without layering at the positions of penetrometer deployments (Tab. 3.3). Third, we went to the windward side of the island of O’ahu, Hawaii, in the Northern Pacific and measured in Kailua Bay and Waimanalo Bay 10 to 100 meters from the shore. Sediment samples in Waimanalo dominantly comprise calcareous medium-grained sand with minor fine or coarse sand fractions (Udden-Wentworth scale). In Kailua, silty sand with about 70 % fine to coarse sand and about 30 % coarse silt (Tab. 3.3) is found. Both locations are characterized by visually very light-colored material abraded from an adjacent coral reef.

Waimanalo Bay as well as Kailua Bay are well-known for a smooth shore-break with a mean wave height < 0.5 m, which is the dominant reason for beach erosion in these areas (Fletcher et al., 1997). During the survey period

the shorebreak was noticeably higher in Waimanalo Bay than in Kailua Bay. In general, we prefer to make 2 - 5 measurements with each instrument at each position to identify and quantify variations more easily, and to assess repeatability and potential error. Unfortunately, this is only possible if the environment offers keeping the exact geographic position of the vessel for durations of a minimum of 5 minutes.

In the tidal inlet channel in the Jade area, currents were too strong to reliably keep the position for significant periods of time. As a consequence, we carried out the *Nimrod* and CPT measurements almost continuously while drifting driven by the current across the dunes. This resulted in a series of 5 - 8 deployments for each instrument over a 600 m-long transect across the dune (Tab. 3.3).

In the area *Alpha Ventus*, it was achieved to keep the position owing to relatively calm seas during an expedition in May 2008. Here, we deployed both the CPT lance and *Nimrod* thrice at each position (Tab. 3.3); in addition, we took a grab sample at every third position. The entire area is covered with side-scan and acoustic sub-bottom profiling measurements.

In both North Sea areas the CPT lance was lowered by winch (Tab. 3.3) and *Nimrod* was manually deployed truly free falling (Fig. 3.17).

In Hawaii we only used *Nimrod* truly free falling by hand from a one-seat kayak, launched twice at each position. Meanwhile the kayak drifted (ca. 1 - 10 m) depending on the currents and duration of deployment (about one minute depending on the water depth).

Results

Observations of deployments Deploying dynamic penetrometers on sand reveals several difficulties. Most of them are related to the small penetration depth. With both instruments we could not reach a penetration depth > 0.5 m. In 90 % of the deployments the devices achieved a penetration depth of < 0.2 m (Tab. 3.3). For comparison, in case of soft, muddy sea floors *Nimrod* penetrates more than 2 m into the sediment (Stark et al., 2009) and the CPT lance has already shown penetration depths of up to 10 m with extension of the rods (Stegmann et al., 2006).

Consequences of the small penetration depth are (i) a higher risk of tilting and falling to the side and (ii) strong disturbances by ship movement (Fig. 3.18) in case of winch-lowered devices. Concerning a penetration time of 0.1 - 0.25 s, a high sampling rate is important to derive reliable penetration profiles. The above mentioned problems are the main reasons, why some of the deployments were not interpretable (Tab. 3.3).

Another issue of deploying dynamic penetrometers on sand is the risk of damage of the instrument. In Kailua Bay we measured decelerations of *Nimrod* with up to 210 g.

Deceleration - depth profiles In the Jade estuary, North Sea, *Nimrod* deployments resulted in two different types of profiles (Fig. 3.19), both of which show a 0.02–0.06 m thin layer of looser sediment (about $2\text{ g} \pm 1\text{ g}$) above a harder underground. The strength of the underground varies in the two types of profiles, as is expressed in a deceleration of $10\text{ g} \pm 2\text{ g}$ in some deployments, but 25–40 g in others. However, even the maximum values appear to be low for sandy seafloor when compared to the results of other areas of quartz sand (Tab. 3.4) and other free-falling penetrometers (Stoll and Akal, 1999; Stoll et al., 2004; Stoll et al., 2007). With the CPT probe, maximum deceleration of $0.3\text{--}0.6 \pm 0.1\text{ g}$ and a maximum tip resistance of 130–700 kPa were reached (impact velocity 0.4–0.6 m/s). However, the total number of interpretable deceleration – depth profiles of the CPT lance was too low (Tab. 3.3) to identify a typical signature in this research area. In the area *Alpha Ventus* we derived a typical profile with either penetrometer (Fig. 3.20). *Nimrod* displays decelerations ranging up to 55–85 g and a penetration depth ranging from 0.09–0.11 m with penetration velocities ranging from 7–10 m/s. The CPT lance monitors maximum decelerations mostly from 15–28 g and a tip resistance ranging from 1000–1700 kPa with a comparable penetration depth of 0.06–0.11 m (Fig. 3.20) and with penetration velocities ranging from 1.0–1.5 m/s. A penetration depth comparable to that of *Nimrod* is reached due to a higher weight and smaller surface area of the probe (Tab. 3.2).

In Kailua Bay and Waimanalo Bay we only deployed *Nimrod*. In Waimanalo Bay (Fig. 3.21, left) we found a typical deceleration - depth profile for the harder underlying sediment with a maximum deceleration of 120–155 g (penetration velocity 9–11 m/s) under a looser layer of varying thickness of 0.03–0.10 m and a deceleration of up to 20 g. Due to the changing thickness of the overlying layer the penetration depth ranges from 0.12–0.24 m. In Kailua Bay a comparable profile was monitored at some positions (Fig. 3.21, right, dashed lines). But, at most of the spots a much steeper gradient can be observed with maximum decelerations ranging from 120–210 g and a penetration depth of 0.07–0.11 m.

Research area	Sand type	Dominant grain size (mm)	Sediment influencing hydrodynamics	Device	No. of deployments	Interpretable deployments	Impact velocity (m/s)	Mean penetration depth (m)
Jade	quartz	0.4 - 0.7	tides (0.7 - 1.3 m/s)	Nimrod	26	88 %	4 - 5	0.14
Jade	quartz	0.4 - 0.7	tides (0.7 - 1.3 m/s)	CPT	32	10 %	0.4 - 0.6	0.12
<i>Alpha Ventus</i>	quartz	0.063 - 0.3		Nimrod	129 (3/position)	92 %	7 - 10	0.08
<i>Alpha Ventus</i>	quartz	0.063 - 0.3		CPT	129 (3/position)	89 %	0.9 - 1.4	0.08
Waimanalo Bay	carbonate	0.3 - 0.63	shore break	Nimrod	26 (2/position)	62 %	9 - 12	0.13
Kailua Bay	carbonate	0.063 - 0.3	shore break	Nimrod	34 (2/position)	85 %	10 - 13	0.1

Table 3.3: Geological context and deployment differences in the research areas.

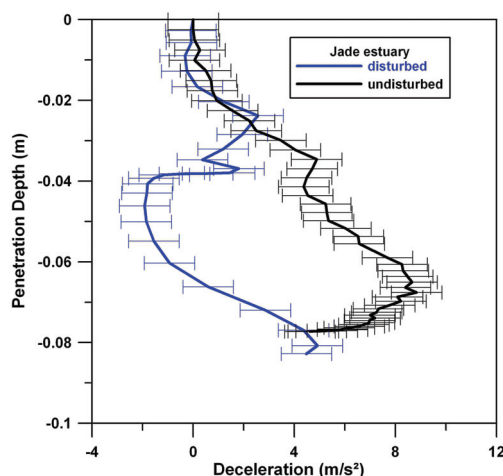


Figure 3.18: In the Jade estuary in the North Sea we deployed the CPT lance winch-lowered. Sometimes it was strongly influenced by ship movement (blue line), especially in case of slow winch velocities (here: about 0.4 m/s). The probe impacts and penetrates the seafloor until it is pulled up and pushes down again. For comparison, the black line shows an undisturbed deployment at a comparable position and with the same winch.

In general, it can be shown that the monitored deceleration on the carbonate sand (Waimanalo Bay, Kailua Bay) is significantly higher than of the quartz sand (Jade estuary, area *Alpha Ventus*), whereby the penetration depth was not decreased. Furthermore, the deceleration increases the finer the sediment is (Tab. 3.4).

Quasi-static bearing capacity The deceleration of a dynamic penetrometer is strongly influenced by its penetration surface, geometry and penetration velocity. Both instruments have a conical tip, but the surface area and the penetration velocity differs a lot (Tab. 3.2). The impact velocity and the penetration velocity vary between the different research areas (Tab. 3.3). Making them comparable we used the approach described above to calculate the quasi-static bearing capacity. An uncertainty occurs due to the factor $K = 1 - 1.5$. It leads to deviations of about 15%. During the analysis we calculated the quasi-static bearing capacity with $K = 1.25$ and considered the 15% deviation in the resulting ranges and errors (Fig. 3.22).

In the Jade estuary *Nimrod* measured quasi-static bearing capacities ($v_0 = 0.02$ cm/s) ranging from 3–10 kPa in the upper sediment layer (Fig. 3.20, grey shaded area) and 17–41 kPa in the deeper one. The CPT lance delivers

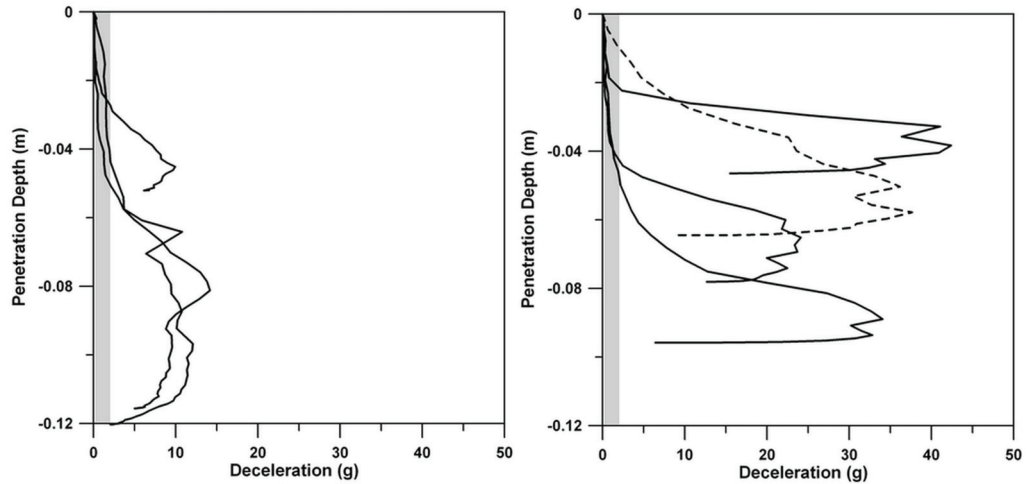


Figure 3.19: Deceleration - depth profiles measured with *Nimrod* in the Jade estuary (random extract). Two types of profiles can be distinguished: One with a maximum deceleration about 10 g (left) and one with max. deceleration ranging from 25–40 g (right). Both show in most of the cases a looser layer (grey shade) above the stiffer underground. Just in one case this layer cannot be observed (dashed line).

Research area	Sand type	Dominant grain size (mm)	Maximum deceleration (g)
Jade	quartz	0.4 - 0.7	25 - 40
<i>Alpha Ventus</i>	quartz	0.063 - 0.3	55 - 85
Waimanalo Bay	carbonate	0.3 - 0.63	120 - 155
Kailua Bay	carbonate	0.063 - 0.3	120 - 210

Table 3.4: Type of sand, dominant grain size and maximum deceleration of *Nimrod* in the four research areas.

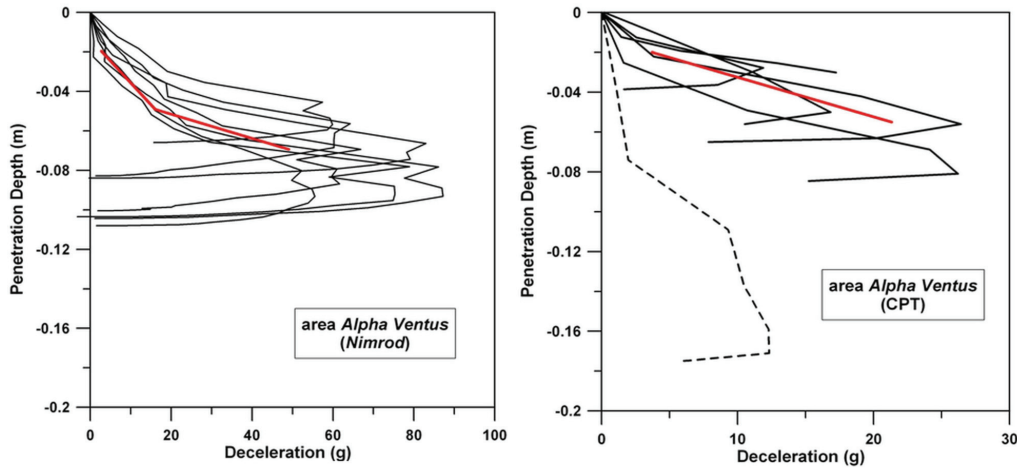


Figure 3.20: *Nimrod* (left) and CPT lance (right) measurements (random extract) from the area *Alpha Ventus*. With both instruments a typical profile with comparable gradient (red line) can be displayed. The dashed profile shows an example of the few ($< 5\%$) measurements, which does not match the general profile shape.

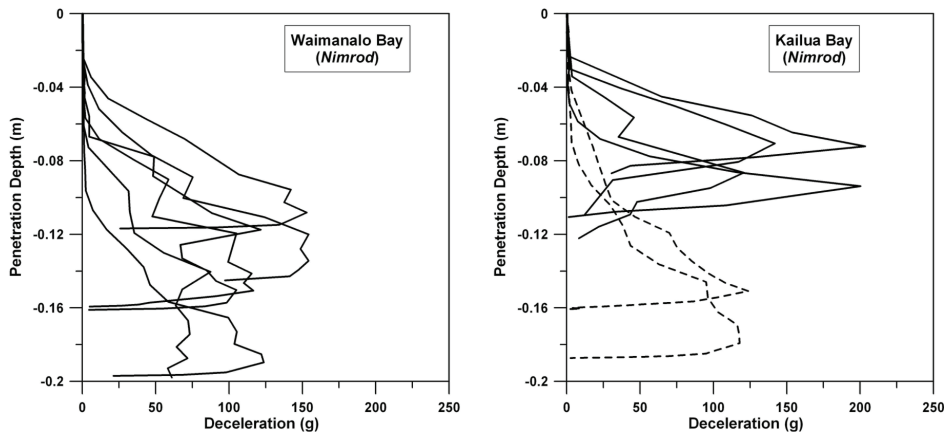


Figure 3.21: Random extract of *Nimrod* deployments in Waimanalo Bay (left) and Kailua Bay (right). In Waimanalo the profiles show a very comparable shape, but shifted depending on the thickness of a looser overlying layer. In Kailua Bay this profile can be found (dashed lines), too, but mostly the results show a another profile of higher gradient and higher maximum deceleration values.

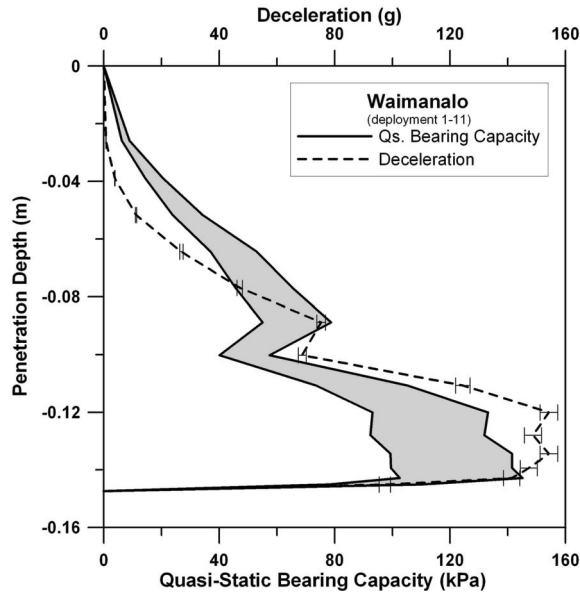


Figure 3.22: Example (Waimanalo Bay, deployment 1-11) for the calculation from deceleration (dashed line) to quasi-static bearing capacity using $K = 1 - 1.5$ (grey shade). The upper black line shows the results for $K = 1$ and the lower for $K = 1.5$.

5-25 kPa in the upper layer and 30-115 kPa in the underground (Tab. 3.5).

In the area *Alpha Ventus* we reached quasi-static bearing capacities ranging from 39–69 kPa with *Nimrod* and 184–260 kPa with the CPT lance (Tab. 3.5). Thus, the CPT lance presents 3 - 4 times higher quasi-static bearing capacities than *Nimrod* in this research area.

In Waimanalo Bay and Kailua Bay we sometimes found an overlying loose sediment layer of a quasi-static bearing capacity of 5–25 kPa above a harder underground of 80–120 kPa (Tab. 3.5). In Kailua Bay a maximum of 210 kPa was reached at 5 positions.

In summary, after consideration of penetration velocity and penetration surface the carbonate sand (Waimanalo Bay, Kailua Bay) shows a significantly higher bearing capacity than the quartz sand (Jade estuary, area *Alpha Ventus*) (Fig. 3.23, Tab. 3.5). Furthermore, in the quartz sand as well as in the carbonate sand we found a higher maximum bearing capacity in areas of smaller grain size (area *Alpha Ventus*, Kailua Bay) (Tab. 3.5, Fig. 3.23). Likewise, layering is represented in the quasi-static bearing capacity profiles (Tab. 3.5, Fig. 3.23) as well as in the deceleration profile. This confirms that the observed layering in the deceleration - depth profiles is not just an artifact of changes in penetration velocity.

Research area	Device	Quasi-static bearing capacity (kPa)	
		<i>Layer1</i>	<i>Layer2</i>
Jade	<i>Nimrod</i>	3 - 10	17 - 41
Jade	CPT	5 - 25	30 - 115
<i>Alpha Ventus</i>	<i>Nimrod</i>		39 - 69
<i>Alpha ventus</i>	CPT		184 - 260
Waimanalo	<i>Nimrod</i>	5 - 25	85 - 120
Kailua	<i>Nimrod</i>	5 - 25	80 - 200

Table 3.5: Ranges maximum bearing capacity.

Discussion

With this article we want to show that dynamic penetrometers deliver useful and detailed information about geotechnical properties in the uppermost layers of sandy seafloors. We compared two different types of dynamic penetrometers (Fig. 3.17, Tab. 3.2) and applied an approach of direct interpretation of deceleration - depth profiles and an approach to deliver quasi-static bearing capacity. Furthermore, we were interested in the effects of differences in type of sand, grain size and hydrodynamic features (here by means of tides and shorebreaks) on the penetration signature.

Observations during deployments and first sight of data elucidated that dynamic penetrometers satisfy a number of prerequisites for the successful use on sand. To avoid falling to the side or kinking the center of gravity should be concentrated on the tip. Furthermore, the device should be decoupled from the ship (free-fall or rapid winch speeds) to minimize artifacts from heave. Finally, a high sampling rate (e.g., 1 kHz) is required to obtain a satisfying number of data points per penetration depth interval. Nevertheless, we observed typical impact signatures for the different research areas with either penetrometer (Fig. 3.19 - 3.21, 3.23).

Regarding the differences in the quasi-static bearing capacity values between the two instruments (Tab. 3.5), it does not seem sufficient to only consider the different penetration rates and surface areas to make two different types of dynamic penetrometers comparable to each other. Another influencing factor could be the relationship between penetration depth and width of the penetrating object, which goes into the so-called depth factor (Meyerhof, 1953; Das, 1990). This relationship differs for the CPT lance and *Nimrod* significantly due to the larger surface area of the latter (Tab. 3.2) while both

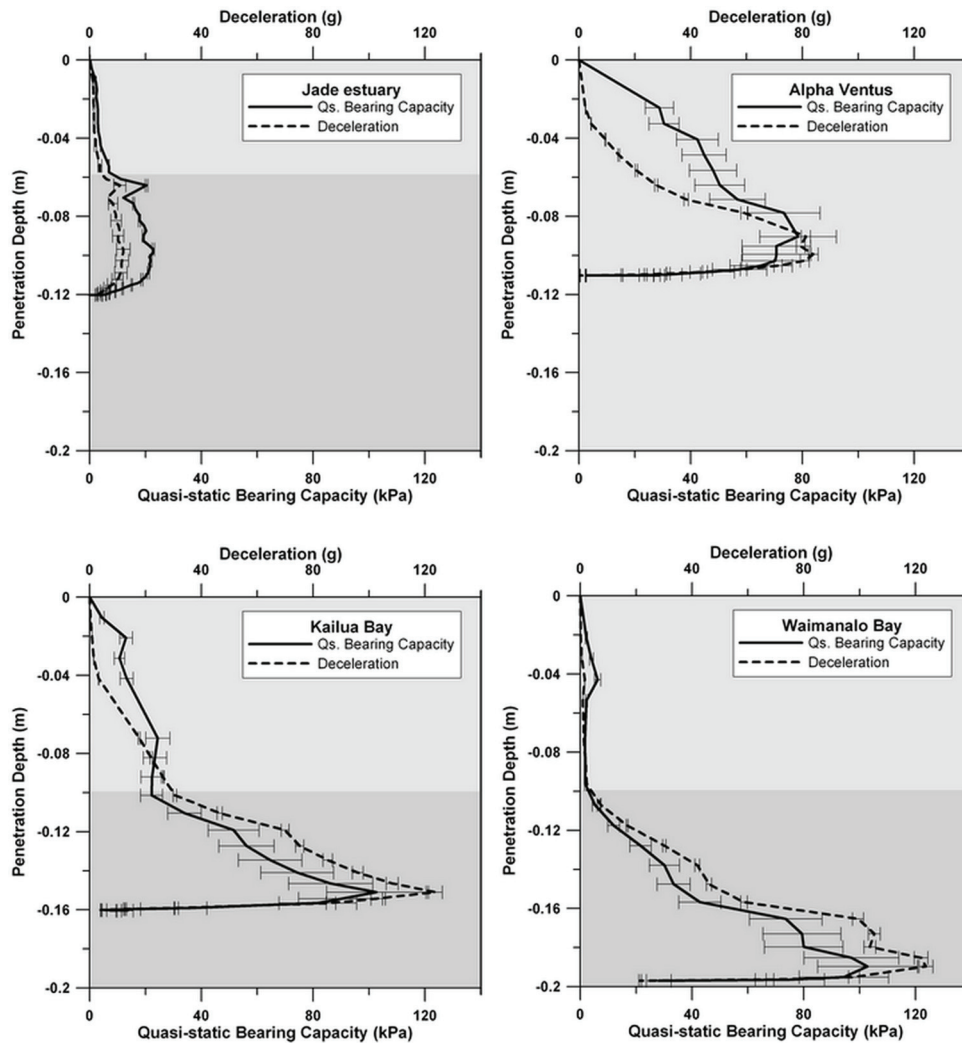


Figure 3.23: Comparing the quasi-static (constant penetration rate 2 cm/s) bearing capacity - depth (solid lines) and deceleration - depth profiles (dashed lines) of the four research areas to each other display significant differences. The maximum strength of the carbonate sand (Waimanalo and Kailua Bay, lower plots) exceeds the maximum strength of the quartz sand (Jade estuary and area *Alpha ventus*, upper plots) at least about 25 %. In Kailua Bay as well as in Waimanalo Bay the deployments were made close to the shore, where surface layers are affected by the shorebreak. This leads to a two-layer system in the strength - penetration depth profiles. In Kailua Bay the shorebreak was not very pronounced, as is expressed by a higher sediment strength of the mixed up layer in comparison to Waimanalo Bay. The area *Alpha Ventus* shows no sediment remobilization or layering based on the strength - penetration depth profiles. The research environment in the Jade estuary varies from the other areas. Given that measurements took place along a large subaquatic dune, the inclination of the impact spots causes reduced sediment strength readings. This effect is accentuated by the possible displacement of coarse and well-rounded particles during impact.

have similar penetration depths (Tab. 3.3). The effect is even stronger in the area *Alpha Ventus* because of the small penetration depth in the indurated sands encountered here (Tab. 3.3). This idea is supported by other studies, which came to the conclusion that shape, depth and inclination factors are mostly required for the use of the bearing capacity theory in cone penetration testing (Meyerhof, 1953; Yu and Mitchell, 1998). However, the bearing capacity theory represents an approximation, although it is widely accepted by many engineers (e.g., Yu and Mitchell, 1998), and other studies (e.g., Mulhearn, 2003; Stoll et al., 2007) corroborate how complex the comparison of different types of dynamic penetrometers is.

Despite this difficulty, differences in the mineralogical composition are mirrored in the results (Tab. 3.4, Fig. 3.23). In contrast to quartz sand, most of the carbonate sand grains are angular and have rather irregular interlocking shapes (most likely relict from their skeletal origins) and the shape of the particles relates directly to physical characteristics of the sand (Nutt and Houlby, 1991; Halley, 2000), as we find (i) a higher deceleration (Tab. 3.4), (ii) higher quasi-static bearing capacity values (Tab. 3.5) and (iii) a higher gradient in the penetration profiles (Fig. 3.23) of carbonate sand (Waimanalo Bay, Kailua Bay) than of quartz sand (Jade estuary, area *Alpha Ventus*). Based on this determination, the behavior of quartz sand and carbonate sand during deployment of dynamic penetrometers will be further investigated and supplemented by laboratory studies and numerical modelling.

Furthermore, it is known that grain size and water content influence the compaction of sediments (Das, 1990). Because all surveys were done under water saturated conditions, the grain size should have a recognizable influence on the sediment strength. Finer sands should lead to a higher sediment strength than coarse sands, because they can be compacted more easily (Das, 1990) and have a larger effective surface area. Moreover, if the coarse particles are well-rounded they can be pushed or rolled aside more easily. This could be one reason for the comparatively small strength in Jade area. The inclined seafloor surface on the dune increases this effect additionally beside the fact that an inclined sea floor decreases the bearing capacity anyway (Terzaghi, 1943; Meyerhof, 1953; Das, 1990).

When regarding sediment affecting hydrodynamics, the four research areas have different characteristics (Tab. 3.3). In the area *Alpha Ventus* acoustic sub-bottom profiling and sediment samples did not indicate a sediment mobilization, which is supported by homogenous one-layer profiles in our data (Fig. 3.23). In the Jade estuary we know that the sediment along the dune is temporarily mobilized by strong tides (Svenson et al., 2009). The penetrometer profiles depict a two layer system with an unconsolidated upper layer of 0.02–0.06 m thickness (Fig. 3.23). This finding corresponds to earlier

work where Wever et al. (2008) attested considerable mobilization and re-deposition by sand height changes of 0.4 m per hour in the Jade estuary and Bartolomä et al. (2004) differences in height of 0.05 – 0.08 m in dune troughs and 0.15–0.8 m on dune crests over one tidal period in a comparable tidal inlet channel. In Kailua Bay and Waimanalo Bay the smooth shorebreak (mean wave height < 0.5 m) is one of the main factors contributing to the longshore sand transport, which led to a beach degradation of 16.3 % in about 50 years (Fletcher et al., 1997). Visual observation showed a higher shorebreak in Waimanalo Bay than in Kailua Bay at the days of measurements. At the positions correlating to the areas of the shorebreak we found an upper layer of looser sediment with varying thickness of 0.03–0.1 m, whereby this layer is more developed in Waimanalo Bay, what corresponds to the bigger shorebreak (Fig. 3.23).

In summary, it is possible to resolve sedimentological and physical properties in vertical profiles at a cm-scale. Our study shows that dynamic penetrometers, when operating at high sampling rates and penetrating unaffected by the platform they are deployed from, deliver information about sediment strength, bearing capacity and layering even in the uppermost surface layers of hard sandy seafloors. With additional ground-truthing, such data can further be used for interpretations concerning sediment type, grain size distribution and compaction state.

Acknowledgements

We acknowledge the German Research Association (via MARUM, Center of Excellence at the University of Bremen, and GLOMAR, Bremen International Graduate School for Marine Sciences) and Bundesministerium für Umwelt (via the RAVE project) for funding this study. We thank the crews of R/V Senckenberg and R/V Wega and the chief scientists Verner Ernstsen (MARUM) and Maria Lambers-Huesmann (BSH, Hamburg) for support. Furthermore, we thank Christian Svenson, Nils Hoever and Sergey Dzhuninov for their help during the measurements. We are particularly indebted to Matthias Lange (MARUM) and Matthias Colsmann (AVISARO, Hannover) for technical support.

References

Johnson, G.W., Hamilton, T.K., Ebelhar, R.J., Mueller, J.L., Pelletier, J.H., (1988). Comparison of in-situ vane, cone penetrometer, and laboratory test re-

sults for Gulf of Mexico deepwater clays. Vane shear strength testing in soils: field and laboratory studies, ASTM International.

Stoll, R.D., Sun, Y.F., Bitte, I., (2004). Measuring sea bed properties using static and dynamic penetrometers. Lamont-Doherty Earth Observatory of Columbia University, N.Y.

Stoll, R.D., Sun, Y.F., Bitte, I., (2007). Seafloor properties from penetrometer tests. IEEE Journal of Oceanic Engineering, Vol. 32(1).

Wong, J.F.F., Wong, M.F., Kassim, K., (1993). Comparison between dilatometer and other in-situ and laboratory tests in Malaysian alluvial clay. 11th Southeast Asian Geotechnical Conference, Singapore, pp. 275-279.

Aubeny, C.P., Shi, H., (2006). Interpretation of impact penetrometer measurements in soft clay. J. Geotech. Geoenviron. Eng., Vol. 132(6), pp. 770-777.

Kopf, A., Stegmann, S., Krastel, S., Foerster, A., Strasser, M., Irving, M., (2007). Marine deep-water free-fall CPT measurements for landslide characterisation off Crete, Greece (Eastern Mediterranean Sea), Part 2: Initial data from the western Cretan Sea. Submarine Mass Movements and their consequences, Springer, Netherlands, pp.199-208.

Kopf, A., Stegmann, S., Delisle, G., Panahi, B., Aliyev, C.S., Guliyev, I., (2009). In situ cone penetration tests at the active Dashgil mud volcano, Azerbaijan: Evidence for excess fluid pressure, updoming, and possible future violent eruption. Marine and Petroleum Geology, doi: 10.1016/j.marpetgeo.2008.11.005.

Lunne, T., Robertson, P.K., Powell, J.J.M., (1997). Cone Penetrating Testing in Geotechnical Practice, Spon Press, London.

Mulhearn, P.J., (2003). Influences of Penetrometer Tip Geometry on Bearing Strength estimates. International Journal of Offshore and Polar Engineering, Vol. 13, No. 1.

Robertson, P.K., Campanella, R.G., (1983). Interpretation of cone penetration tests. Can. Geotech. J., Vol. 20(4).

Seifert, A., Stegmann, S., Moerz, T., Lange, M., Wever, T., Kopf, A., (2008). In situ pore-pressure measurements in soft sediments of the western Baltic Sea. Geo-Mar Lett, doi 10.1007/s00367-008-0102-x.

Stark, N., Wever, T.F., (2008). Unraveling subtle details of expendable bottom penetrometer (XBP) deceleration profiles. *Geo-Mar Lett*, doi 10.1007/s00367-008-0119-1.

Stark, N., Hanff, H., Kopf, A., (2009). Nimrod: a tool for rapid geotechnical characterization of surface sediments. *Sea Technology*, April 2009, pp. 10-14.

Stegmann, S., Villinger, H., Kopf, A., (2006). Design of a modular, marine free-fall cone penetrometer. *Sea Technology*, 47(2), pp.27-33.

Stegmann, S., Moerz, T., Kopf, A., (2006). Initial results of a new free fall-cone penetrometer (FF-CPT) for geotechnical in situ characterisation of soft marine sediments. *Norwegian Journal of Geology*, Vol. 86, pp. 199-208.

Stegmann, S., Kopf, A., (2007). Marine deep-water free-fall CPT measurements for landslide characterisation off Crete, Greece (eastern Mediterranean Sea)-part I: a new 4000m cone penetrometer. *Submarine Mass movements and their consequences*, 3rd international symposium, Netherlands, pp. 171-177.

Stoll, R.D., Akal, T., (1999). XBP-tool for rapid assessment of seabed sediment properties. *Sea Technology*, 40(2), pp.47-51.

Meschede, D., (2001). *Gerthsen Physik*. 21st ed., Springer, Berlin.

Mott, R.L., (2005). *Applied Fluid Mechanics*. 4th ed., Macmillan Publishing Company, New York.

Dayal, U., Allen, J.H., (1975). The effect of penetration rate on the strength of remolded clay and sand samples. *Can. Geotech. J.*, 12, 336.

Cai, G., Liu, S., Tong, L., Du, G., (2009). Assessment of direct CPT and CPTU methods for predicting the ultimate bearing capacity of single piles. *Engineering Geology*, 104, pp. 211-222.

Das, B.M., (1990). *Principles of Geotechnical Engineering*. 2nd ed., PWS-Kent Publishing Company, Boston, Massachusetts.

Terzaghi, K., (1943). *Theoretical soil mechanics*. John Wiley and Sons, New York.

Meyerhof, G.G., (1953). The bearing capacity of foundations under eccentric and inclined loads. Proceedings, 3rd International Conference on Soil Mechanics and Foundation Engineering, Vol. 1, pp. 16-26.

Cassidy, M., Houlsby, G.T., (2002). Vertical bearing capacity factors for conical footings on sand. *Géotechnique*, Vol. 52(9), pp. 687-692.

Svenson, C., Ernstsen, V.B., Winter, C., (2009). Cruise Jade, Germany, 14.-18.4.2008 and 28.-30.4.2008, FK Senckenberg, Draft Report.

Bartolomä, A., Ernstsen, V.B., Flemming, B.W., Bartholdy, J., (2004). Bedform dynamics and net sediment transport paths over a flood-ebb tidal cycle in the Grabdyb channel (Denmark), determined by high-resolution multi-beam echosounding. *Geografisk Tidsskrift, Danish Journal of Geography*, Vol 104,(1), pp. 45-55.

Fletcher, C.H., Mullane, R.A., Richmond, B.M., (1997). Beach loss along armored shorelines on Oahu, Hawaiian islands. *Journal of Coastal Research*, Vol. 13(1), pp. 209-215.

Yu, H.S., Mitchell, J.K., (1998). Analysis of cone resistance: review of methods. *Journal of Geotechnical and Geoenvironmental Engineering*, Vol. 124, No. 2.

Halley, R.B., (2000). 11 things a geologist thinks an engineer should know about carbonate beaches. Conference Proceedings Carbonate Beaches 2000, Key Largo, pp. 1-14.

Nutt, N.R.F., Houlsby, G.T., (1991). Calibration tests on the cone pressuremeter in carbonate sand. Report No. OUEL 1887/91, Soil Mechanics Report No. 120/91, Oxford University, UK.

Wever, T.F., Voss, H., Luehder, R., (2008). High-resolution observation of small-scale variability in a bedform field. *Marine and River Dynamics*, Leeds, UK.

Chapter 4

Geological applications

After finalizing the testing phase, *Nimrod* was applied within several geological projects. Most of them addressed features of sediment remobilization. The main scientific questions are: (i) Is the dynamic penetrometer *Nimrod* suitable to complement sediment remobilization investigations with new or supporting information? (ii) Is a quantification of remobilized material possible (via layering in sediment strength signatures)? (iii) Do *in-situ* sediment strength patterns deliver new information supporting the understanding of sediment remobilization processes?

In this chapter only the projects are introduced which led to a submitted manuscript within the PhD-time. Further projects having the potential to be published will be presented in chapter 5.

4.1 Quartz vs. carbonate sand

Many sediment remobilization features can be found in sandy areas including bars, dunes, sorted bedforms, scouring. To make a reliable interpretation of dynamic penetrometer results measured on sandy seafloors possible, it is important to understand the impact signatures on sand. The publication presented in chapter 3.3.2 revealed that dynamic penetrometers (in that case *Nimrod*) are capable of delivering more detailed information about the sand, however, the use of dynamic penetrometers in sandy areas is still limited and the signatures are incompletely understood.

Comparing the dynamic penetrometer signatures measured on quartz sand to those measured on carbonate sand showed significant differences in the profiles (chapter 3.3.2). In the following manuscript laboratory measurements were used to explain the different signatures derived using *Nimrod*.

4.1.1 Geological manuscript I

Stark, N., Wilkens, R., Ernstsens, V.B.,
Lambers-Huesmann, M., Stegmann, S., Kopf, A.,
Geotechnical properties of sandy seafloors and the
consequences for dynamic penetrometer interpretations:
quartz sand vs. carbonate sand.
Submitted to Geotechnical and Geological Engineering.

Abstract

The industrial and recreational usage of coastal zones (including offshore wind energy plants, waterway deepening, beach conservation and restoration) is of emerging importance. Sediment dynamics in these areas result in sandy deposits because of strong currents, tidal processes and wave action, the latter of which are difficult to simulate in laboratory geotechnical tests. Here, we present data from *in-situ* penetrometer tests using the lightweight, free-fall penetrometer *Nimrod* and complementary laboratory experiments to characterize the key physical properties of sandy seafloors in areas dominated by quartzose (North Sea, Germany) and calcareous (Hawaii, USA) mineralogy.

The carbonate sands have higher friction angles (carbonate: 31–37°; quartz: 31–32°; diatomite: 27°) and higher void ratios (carbonate: 1.10–1.40; quartz: 0.81–0.93; diatomite: 8.2–9.4) than their siliceous counterparts, which have partly been attributed to the higher angularity of the coral-derived particles. During the *in-situ* tests, we consistently found higher sediment strength (expressed in deceleration as well as in quasi-static bearing capacity) in the carbonate sand (carbonate: 68–210 g; quartz: 25–85 g), which also showed a greater compressibility. Values were additionally affected by seafloor inclination (e.g., along a sub-aqueous dune or a sand channel), or layering in areas of sediment mobilization (by tides, shorebreak or currents). The study shows that the differences in *in-situ* measured penetration

profiles between carbonate sands and quartz sands are supported by the laboratory results and provide crucial information about mobile layers overlying sands of various physical properties.

Introduction

In the context of the increasing industrial usage of coastal zones and processes of coastal conservation and restoration, geotechnical investigations of coastal sediments gain in importance. Thereby, *in-situ* methods represent an important complement to laboratory methods. They can call attention to the factors influencing soil mechanics, which are special for the respective area (e.g., sediment mobilization by hydrodynamic features, seafloor inclination).

Instruments frequently used for geotechnical *in-situ* tests are dynamic penetrometers (consider the use of, e.g., Stoll and Akal, 1999; Stoll et al., 2004; Aubeny and Shi, 2006; Stegmann et al., 2006a,b; Kopf et al., 2007; Stegmann and Kopf, 2007; Stark and Wever, 2008; Stark et al., 2009a). Many of the coastal areas investigated in this study consist mainly of sand. This often makes the deployment of *in-situ* tools difficult, because they depend on penetration into the sediment and stiff sand is hard to penetrate.

In the case of dynamic penetrometers a decrease in penetration depth with an increase of sediment strength is usually expected (e.g., Stoll and Akal, 1999; Stark and Wever, 2008). However, in a study on the usability of dynamic penetrometers on sand, Stark et al. (2009b) observed a significant difference of the penetration profiles as well as of maximum deceleration and derived quasi-static bearing capacity values between quartz sand and carbonate sand. In particular, the carbonate sand reached significantly higher decelerations as well as quasi-static bearing capacities ($> 25\%$), whereas the penetration depth did not decrease.

It is well-known that the soil mechanical behavior of quartz sands differs from that of carbonate sands (e.g., Kwag et al., 1999). Carbonate sand often has a higher friction angle than quartz sand (Terzaghi, 1943; Pizzimenti and Silva, 1997; Salehzadeh et al., 2008). Das (1990) showed that sand consisting of angular grains generally has a higher friction angle compared to sand consisting of rounded particles. Besides the friction angle, carbonate sands are well-known for a higher void ratio (e.g., Kwag et al., 1999) and a higher probability of particle asperity crushing (Chuhan et al., 2003), which results in a greater compressibility. As the penetration process of the dynamic penetrometers is a combination of compression and shearing, we assume that the different behavior in compression and shearing of the two different sands

leads to differences in *in-situ* penetration profiles. A higher compressibility makes a deeper penetration possible and the high friction angle causes a higher shear strength. The purpose of this study is (i) to compare the geotechnical behavior of marine quartz sands (German Bight, North Sea: Innenjade tidal channel and an area connected to the offshore windfarm *Alpha Ventus*, ~ 50 km north of the island of Borkum) to marine carbonate sands (North Pacific at the windward side (east) and the south shore of the island O'ahu, Hawaii, USA) in laboratory and *in-situ* using the dynamic penetrometer *Nimrod* (Stark et al., 2009a), (ii) to understand *in-situ* measurements using laboratory results and (iii) to test the above mentioned theory explaining the different penetration profiles of the two types of sand with a different relation of compression and shearing. Besides the mineralogy, the research areas also differ in grain size (from fine sand to coarse sand), particle shape and appearance of sediment mobilizing hydrodynamics such as tides, currents and shorebreaks. To test whether mineralogy or physical character (grain size, particle shape, etc.) are responsible for the different behavior, the laboratory tests were additionally applied on diatomite, whose mineralogy is comparable to quartz, but whose physical characteristics are different.

Methods

We compare primarily *in-situ* dynamic penetrometer data for marine sands. In order to improve our understanding of the relationship between shearing and compression during the penetration process, the following sedimentological and geotechnical laboratory methods were used: grain size analysis, grain shape, deformation under load (oedometer), void ratio, friction angle, and dry unit weight. Additionally, the laboratory tests were carried out on diatomite samples from Morocco.

Dynamic penetrometers *Nimrod*, a shallow-water free-falling penetrometer, was recently developed at MARUM, University of Bremen (Fig. 4.1, Tab. 4.1). It is approximately fluid-dynamically shaped, possesses fins and a fall stabilizing relationship between center of gravity and center of volume owing to its massive steel tip (Stark et al., 2009a/b). During impact and penetration into the sediment it measures deceleration and pressure (Tab. 4.1) and can deliver information concerning the sediment strength, layering and inhomogeneities such as plant fibres or stones (Stark et al., 2009a).

From the deceleration *dec* profile with depth, the stiffness of the sand (i. e., bearing capacity q_u) can be calculated. Generally, the bearing capacity can

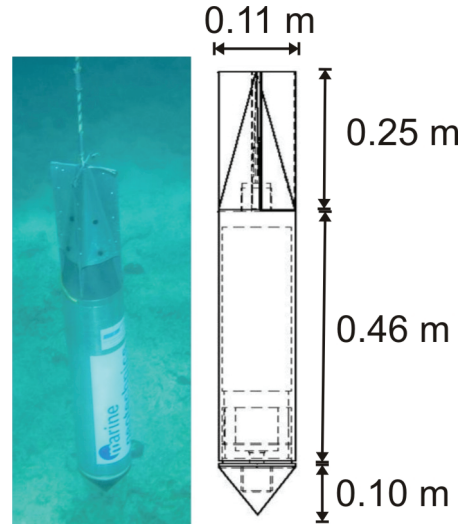


Figure 4.1: The truly free-falling dynamic penetrometer *Nimrod* recently developed at MARUM, University of Bremen, during deployment at Halekulani Sand Channel, O’ahu, Hawaii, USA (left), and a schematic diagram (right).

<i>Nimrod</i>	
Tip geometry	Cone
Cone Angle	60°
Diameter	11 cm
Length	81 cm
Mass	13 kg
Pore water inlet	behind cone
Center of mass	tip
Deployment	free falling
Tether diameter	ca. 4 mm
Mean impact velocity	6 m/s
Pressure sensor	absolute 5MPa
Accelerometers	MEMS, 1.7 g, 18 g, 70 g, 250g
Inclinometer	20°
Data logging	100 Hz

Table 4.1: Technical details of the dynamic penetrometer *Nimrod*.

be expressed in terms of effects of cohesion q_c , effects of surcharge q_q , and effects of unit weight of the soil q_γ , by (Terzaghi, 1943; Das, 1990):

$$q_u = q_c + q_q + q_\gamma = cN_c + qN_q + \frac{1}{2}\gamma BN_\gamma. \quad (4.1)$$

considering the cohesion c , the load on the surrounding sediment surface q , the unit weight γ , the width of the penetrating object B , and the so-called bearing capacity factors N , which depend primarily on the friction angle (Das, 1990). In this study we investigated cohesionless sediments, so q_c can be neglected. q_q is a function of the load on the surrounding sediment, which equals the hydrostatic pressure in the case of surface sediments. Following that, q_q is zero at the sea floor and increases with depth. q_γ expresses the influences of the unit weight of the material, which has to be moved. Furthermore, after the modified general ultimate bearing capacity equation all summands should be multiplied by a factor of depth, a factor of shape and a factor of inclination (Das, 1990). In the case of the depth factor the relationship between width of the penetrating object and penetration depth is important (Meyerhof, 1953). Concerning the shape, after Cassidy and Houlsby (2002) the conical apex angle and the surface roughness of the cone have to be included. An inclined penetrating probe or an inclined seafloor goes into the factor of inclination (Das, 1990).

The bearing capacity can also be expressed as the maximum load per unit area that a soil can bear prior to failure (Terzaghi, 1943; Das, 1990). Regarding the soil as a grid of several, very thin layers of particles the penetration can be viewed as a sequence: 1) The probe hits the upper layer, 2) the load per unit area or pressure on the soil exceeds the bearing capacity, 3) the upper layer fails and the probe hits the next layer, and so on. Thereby, the derived sediment resistance force for each layer is the maximum resistance force the sediment can exhibit until it fails and the probe continues penetrating (Aubeny and Shi, 2006). This means that the bearing capacity can be expressed by the sediment resistance force:

$$q_u = \frac{F_{sr}}{A}, \quad (4.2)$$

where A is the area of the plain subjected to load and F_{sr} the sediment resistance force. Regarding the probe as a single particle in equilibrium (after reaching the terminal velocity in the water column), the sediment exerts the sediment resistance force F_{sr} against the probe and decelerates it (Aubeny and Shi, 2006):

$$m_{Nimdec} = F_{sr}, \quad (4.3)$$

with m_{Nim} being the weight of *Nimrod* in water (with conical tip 8 kg). After Aubeny and Shi (2006) the sediment resistance force includes a sediment shearing resistance force F_s and buoyancy of the probe in soil F_b :

$$F_{sr} = F_b + F_s. \quad (4.4)$$

Inertial forces are negligible here (Aubeny and Shi, 2006). The buoyancy of the probe in soil is neglected here because of the small penetration depths of a few centimeters.

The next step is to consider the nonlinear backcoupling between measured deceleration and penetration rate. Dynamic penetrometers slow down during penetration, whereas quasi-static methods keep a constant penetration rate. The former leads to a strain dependency of the sediment strength reflecting properties such as deceleration. Stoll et al. (2004, 2007) as well as Aubeny and Shi (2006) used strain rate factors to convert quasi-static sediment resistance to higher, dynamic penetration rates and vice versa. Stoll et al. (2007) illustrated that a difference in penetration velocity of about 3 m/s can lead to six times higher sediment resistance results in the case of a compacted medium sand. To allow a direct comparison of different dynamic penetrometers and to standardized methods, the empirical approach by Dayal and Allen (1975) uses the strain rate factor f_{ac} , which depends on the actual penetration velocity v and a reference velocity v_0 :

$$f_{ac} = 1 + K \log \left(\frac{v}{v_0} \right), \quad (4.5)$$

with K being a dimensionless factor ranging from 1.0 to 1.5 (Stoll et al., 2007).

To convert the sediment resistance force from high-speed dynamic deployments to quasi-static (= constant rate) values, the dynamic sediment resistance force F_{sr} and accordingly the dynamic bearing capacity q_{udyn} has to be divided by the strain-rate factor f_{ac} :

$$q_{uqs} = \frac{q_{udyn}}{f_{ac}}. \quad (4.6)$$

The reference velocity v_0 used here equals 0.02 m/s as a standard for quasi-static penetration tests (Cai et al., 2009).

Grain size analysis and grain shape The grain size distribution was determined by sieving and classified using the Udden-Wentworth scale (see,

e.g., Nichols, 1999). The particle angularities were examined using a binocular microscope and described after ASTM (1994).

Oedometer experiments The compression behavior and the void ratio of the sand were investigated by uniaxial consolidation testing in an Oedometer (Das, 1990). Loading steps ranged from 35 to 3100 kPa. After obtaining the time-deformation plots for various loading increments the void ratio was calculated as a function of normal load (Das, 1990):

$$e_i = e_{i-1} \left(\frac{\Delta H_i}{H_i} \right), \quad (4.7)$$

being the void ratio regarding the stress p in loading step i , ΔH_i being the deformation due to the stress p and H_i being the height of solids in the soil sample.

Friction angle Direct shear tests were carried out to derive the shear strength and the friction angle of the specimens (Das, 1990):

$$\tau = \sigma \tan \phi, \quad (4.8)$$

where τ is the shear stress, σ is the normal stress and ϕ the friction angle for cohesionless sediment.

Dry unit weight The dry unit weight (also known as grain density) was measured via a common scale after drying samples of defined volume in an oven.

Regional geological context

The *in-situ* measurements and sampling were carried out in two areas of quartz sand in the North Sea and three areas of carbonate sand in the Pacific. Besides the sediment composition, the research areas differ in hydrodynamics and processes of sediment mobilization in the uppermost layers of the seafloor.

The area of the *Alpha Ventus* wind energy test field ~ 50 km north of the island of Borkum, North Sea, is well investigated in the framework of soil investigations for wind turbine installations and the research program RAVE

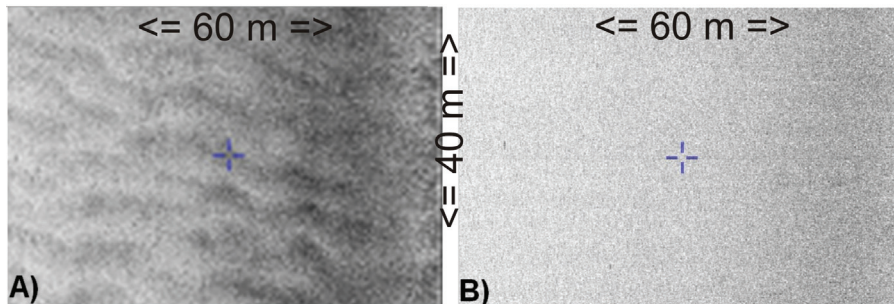


Figure 4.2: Two examples of sidescan sonar pictures from the area *Alpha Ventus*, North Sea. A) shows slight ripple structures (blue cross at $54^{\circ} 0.089'N$ $6^{\circ} 35.404'E$). B) presents the prevailing plain seafloor (blue cross at $54^{\circ} 0.8296'N$ $6^{\circ} 36.8631'E$).

(Research at *Alpha Ventus*). Sidescan sonar pictures (Fig. 4.2) as well as acoustic sub-bottom profiling show an approximately plain and homogenous seafloor surface in a water depth ranging from 27 m to 30 m. Small ripple fields can be detected in only a few spots. Following that, it can be assumed that sediment remobilization is insignificant here (Fig. 4.2).

In the Innenjade tidal channel, the influence of the tides (0.7–1.3 m/s) is mirrored in the development and movements of subaqueous dunes (Fig. 4.3) (Svenson et al., 2009). Considering the initial acoustic monitoring (Svenson et al., 2009), effects of sediment mobilization might show up in the penetrometer profiles, for example, in terms of layering due to density changes at the uppermost surface. The magnitude of these effects should depend on the tidal phase as well as on the location along the dune relative to the direction of the current (Bartholomä et al., 2004). Additionally, the inclination of the seafloor affects the monitored sediment strength (Meyerhof, 1953). Due to the dune shape (Fig. 4.3) it can be assumed that the dynamic penetrometer results may be significantly influenced by the seafloor inclination depending on the respective position along the dune.

Kailua Bay is well-known for a smooth shorebreak with a mean wave height < 0.5 m, which is the dominant reason for beach erosion in these areas (Fletcher et al., 1998). Following that, we expected effects of sediment mobilization in the dynamic penetrometer profiles. Again, these effects might be seen in layering expressing density changes at the uppermost sediment surface. In Waimanalo Bay the significant wave height ranges from 0.3 up to 4 m (Sutherland and Lee, 1994). During the survey period the shorebreak was noticeably higher in Waimanalo Bay than in Kailua Bay. Sediments of the bay and coastal plain of Kailua are $> 90\%$ biogenic carbonate and result from destruction of primary reef framework (coral and encrusting coralline algae)

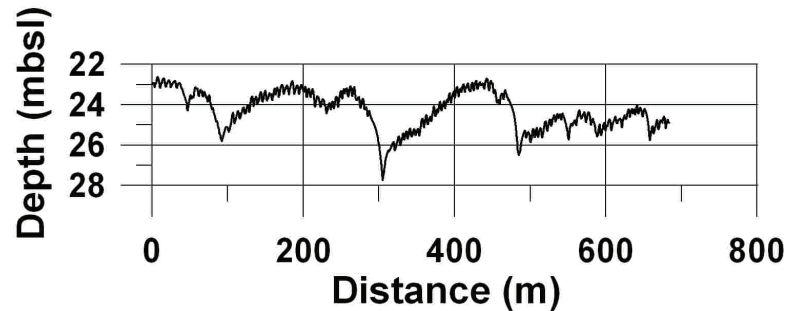


Figure 4.3: The dune stretching along the investigated site in the Innenjade tidal channel, North Sea, monitored using a Sediment Echo Sounder (SES-2000) by Innomar shows the different inclination of the seafloor in this area (one of measurement positions: $53^{\circ} 39' 8.3''\text{N}$, $8^{\circ} 7' 27.7''$; length of transects ca. 300 m).

and by direct sedimentation through the biological activity of calcifying organisms (Harney and Fletcher, 2003). In Waimanalo Bay the sedimentology is assumed to be similar in composition as a broad reef platform with sand deposits in depressions and paleochannels also exists there (Romine et al., 2009).

The third area of carbonate sand is Halekulani Sand Channel (Fig. 4.4) located off the southern shore of the Hawaiian Island of O'ahu. It extends from the shoreline to water depths up to almost 60 m. Fu et al. (2004) assumed that the channel was part of an ancient stream drainage that was cut during a glacial low sea level stand. It is affected by wave climate in the summer months down to water depths of 100 m resulting in loose, poorly consolidated sediment in the upper 10's of meters of the sand deposits (Fu et al., 2004).

Results

Grain size and grain shape For each research area the grain sizes of more than 90% of the samples correspond to sand (Tab. 4.2), whereas the diatomite is silt-size and smaller (< 0.063 mm). We did not do a more exact grain size analysis of the diatomite, because our focus is on sands and for comparison to the sands a more exact size analysis was not necessary. The sand samples can be separated into two groups of dominant grain size. The first represents medium to coarse sands (Innenjade tidal channel and Waimanalo Bay) and the second very fine to medium sands (area *Alpha Ventus*, Kailua Bay and Halekulani Sand Channel) (Tab. 4.2).

In the case of quartz sand the particles in both areas are rounded to well rounded (after Pettijohn et al., 1987), whereas the particles in the carbonate

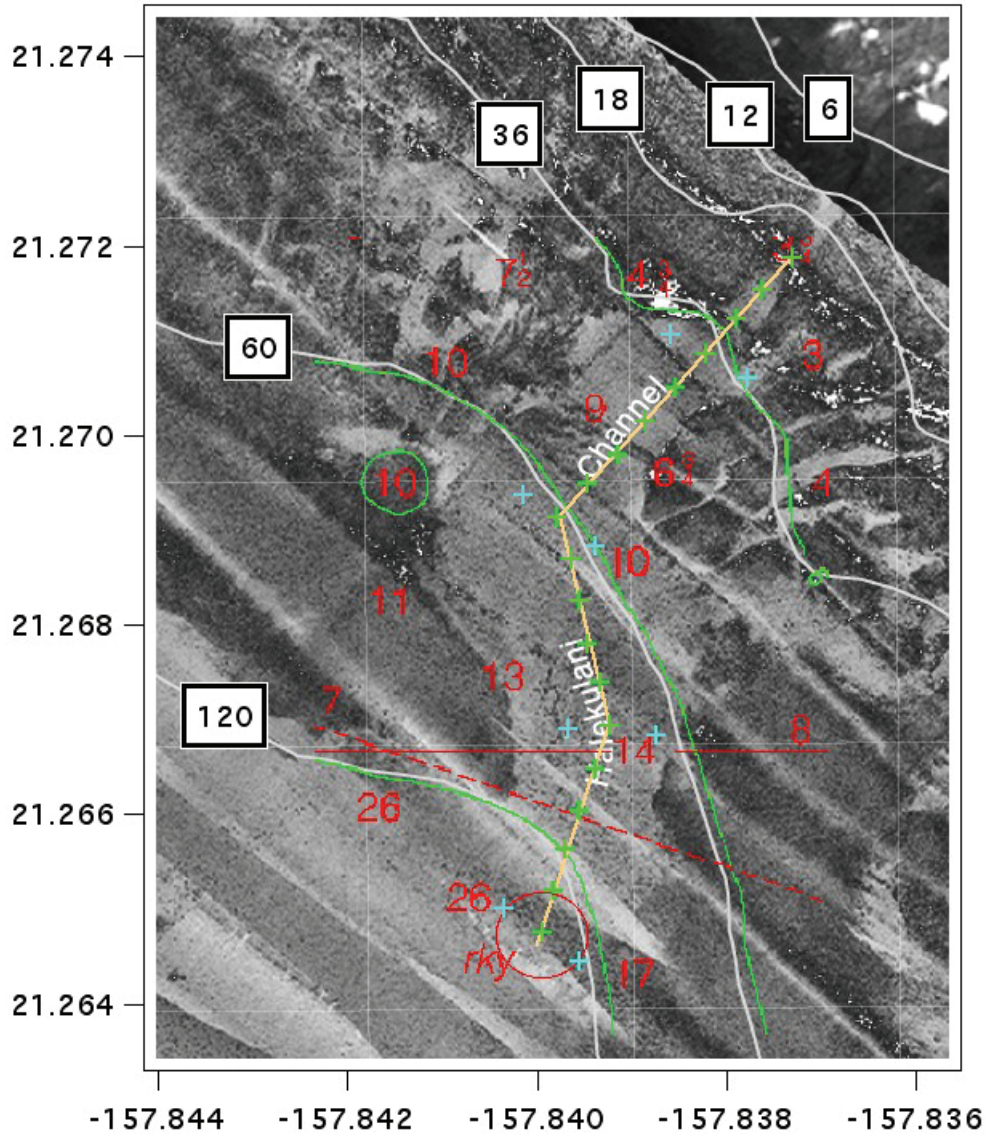


Figure 4.4: Sidescan sonar picture from Halekulani Sand Channel (HSC), O'ahu, Hawaii. The HSC goes from the shoreline south through reef structures. The green lines show the bathymetry contours and the respective values (white boxes) are the water depths in feet. The yellow line with the green crosses represent the track and position of *Nimrod* measurements. The red lines and number are not of relevance for this study.

Research area	Sand type	Grain size (mm)	Grain shape	Color
Jade	Quartz	0.4 - 0.7	rounded	pale brown (10YR 6/3)
<i>Alpha Ventus</i>	Quartz	0.063 - 0.3	rounded	very pale brown (10YR 7/3)
Diatomite	Diatomite	< 0.063	rounded	pinkish white (10R 8/2)
Waimanalo	Carbonate	0.3 - 0.63	sub-/angular	pale yellow (2.5Y 8/3)
Kailua	Carbonate	0.063 - 0.3	sub-/angular	pale yellow (2.5Y 8/3)
Halekulani	Carbonate	0.063 - 0.3	sub-/angular	light gray (2.5Y 7/2)

Table 4.2: Classification of the investigated sands including grain size, grain shape and color.

sand areas can be described as subangular to very angular (Tab. 4.2). The diatomite is well rounded.

Geotechnical laboratory measurements The quartz samples from the Innenjade tidal channel and the test field *Alpha Ventus* show similar results. The unit weight is 19.6 and 19.9 kN/m^3 , respectively, and the dry unit weight of the samples from the Innenjade tidal channel (13.0 kN/m^3) is slightly lower than the dry unit weight of the samples of the test field *Alpha Ventus* (15.4 kN/m^3) (Tab. 4.3). The water content is about 25 % in the samples of both areas of quartz sand (Tab. 4.3). The carbonate samples differ significantly from each other and show unit weights ranging from 16.3 to 22.2 kN/m^3 , and compared to the quartz sand, generally smaller dry unit weights from 9.4 to 12 kN/m^3 and higher water contents from 29 to 33 % (Tab. 4.3). The samples from Kailua Bay and Waimanalo Bay (both windward side of O’ahu) are similar, whereas the samples from the Halekulani Sand Channel (south shore of O’ahu) are less dense and have a higher water content. Diatomite has a very low dry unit weight of about 2.2 kN/m^3 and a very high water content in a saturated state of 327 % (Tab. 4.3).

The coefficient of friction μ of the quartz samples (Innenjade: $\mu = 0.61$, test field *Alpha Ventus*: $\mu = 0.64$; Tab. 4.3) as well as the friction angle ϕ (Innenjade: $\phi = 31^\circ$, test field *Alpha Ventus*: $\phi = 32^\circ$; Tab. 4.3) are similar and show a comparable response to shear. The coefficient of friction and the friction angle of the samples from Kailua Bay match these ranges, too, with $\mu = 0.59$ and $\phi = 31^\circ$, whereas the other two areas of carbonate sand present

higher coefficients of friction and friction angles (Waimanalo Bay: $\mu = 0.69$, $\phi = 34^\circ$; Halekulani Sand Channel: $\mu = 0.76$, $\phi = 37^\circ$; Tab. 4.3). The diatomite shows a low coefficient of friction of $\mu = 0.52$ and a low friction angle of $\phi = 27^\circ$ (Tab. 4.3), which is closer to the results of the quartz sand samples.

Using tables after Vesic (1973) the bearing capacity factor due to surcharge N_q and the bearing capacity factor due to unit weight N_γ can be estimated from the friction angle (Tab. 4.3). Cassidy and Houlsby (2002) presented a specification of bearing capacity factors due to unit weight N_γ for conical penetration objects depending on friction angle, conical apex angle and surface roughness (Tab. 4.3). Having the friction angle ϕ , the bearing capacity factors N_q and N_γ and the unit weight γ offers the possibility of calculating the bearing capacity of the respective sediments depending on these geotechnical parameters determined by laboratory experiments, penetration depth, inclination, and shape of the penetrating object (Eq. 4.1). Assuming that *Nimrod* penetrates vertically and that there is no inclination of the seafloor, the highest bearing capacity is calculated for the Halekulani Sand Channel (about 250 kPa at a penetration depth of 0.2 m) followed by Waimanalo Bay (~ 190 kPa), the test field *Alpha Ventus* (~ 155 kPa), Kailua Bay and the Innenjade tidal channel (both ~ 130 kPa) and the diatomite (~ 45 kPa) (Fig. 4.5).

Experiments on compressibility and void ratio (Eq. 4.7) attest that the samples from the test field *Alpha Ventus* (quartz sand) have the lowest void ratios of the measured samples ranging from 0.81–0.83 for loads ≤ 3100 kPa. The coarser quartz sand from the Innenjade tidal channel shows slightly higher void ratios ranging from 0.90–0.93. The carbonate samples have higher void ratios of 1.10–1.15 in Kailua Bay, 1.19–1.27 in Waimanalo Bay and 1.35–1.40 in the Halekulani Sand Channel (Tab. 4.3, Fig. 4.6). The diatomite exceeds all these values with void ratios of 8.20–9.40 (Tab. 4.3, Fig. 4.6). A trend of increasing void ratio (Tab. 4.3) with increasing grain size (Tab. 4.2) can only be seen for the quartz sands (Innenjade and test field *Alpha Ventus*) and the carbonate sands from the windward side of O’ahu (Kailua Bay and Waimanalo Bay). The diatomite, as well as the samples from the Halekulani Sand Channel, do not follow this trend.

Observing settlements and deformation of the samples under low loads of 150 kPa (Fig. 4.7), the maximum compression occurred in case of quartz sand from the test field *Alpha Ventus* ($\sim 10\%$ settlement versus the initial height), followed by the coarser quartz sand from the Innenjade tidal channel ($\sim 9\%$), fine carbonate sand from the Halekulani Sand Channel ($\sim 7\%$), the Diatomite ($\sim 5\%$), Kailua Bay ($\sim 4\%$) and Waimanalo Bay ($\sim 3.5\%$).

Research area	μ	ϕ	N_q^*	N_γ^*	N_γ^{**}	γ (kN/m^3)	γ_a (kN/m^3)	w (%)	e^{***}
<i>Alpha Ventus</i>	0.64	32	23.18	30.22	10	19.9	15.4	25	0.81
Jade	0.61	31	20.63	25.99	9	19.6	13.05	25	0.9
Diatomite	0.52	27	13.2	14.47	5	10.6	2.23	327	8.17
HSC	0.76	37	42.92	66.19	17	16.3	9.42	33	1.35
Kailua	0.59	30	18.4	22.4	7.95	22.2	12.07	29	1.4
Waimanalo	0.69	34	29.44	41.06	12	18.7	11.77	29	1.19

Table 4.3: Geotechnical results from the laboratory expressed by: coefficient of friction μ , friction angle ϕ , bearing capacity factors N , unit weight γ , dry unit weight γ_a , water content w and the void ratio e for a loading step from 3.139 kN to 6.278 kN (***)). The bearing capacity factors are taken from the estimations by Vesic (1973) (*) and Cassidy and Housby (2002) (**) respectively regarding the friction angle.

Research area	Penetration depth (m)	Impact velocity (m/s)	Maximum deceleration (g)	Qs. bearing capacity (kPa)
<i>Alpha Ventus</i>	0.05 - 0.24	6 - 12	55 - 85	39 - 69
Jade	0.05 - 0.18	4 - 8	25 - 40	17 - 41
HSC	0.09 - 0.14	6 - 10	68 - 126	40 - 95
Kailua	0.07 - 0.34	10 - 13	120 - 210	80 - 200
Waimanalo	0.04 - 0.14	9 - 13	120 - 155	85 - 120

Table 4.4: *In-situ* results from the *Nimrod* presented via penetration depth, impact velocity, maximum deceleration and range of quasi-static bearing capacity for a assumed constant penetration velocity of 0.02 m/s.

In-situ* measurements: *Nimrod In the different study areas and for the different deployments the impact velocity of the free-falling penetrometer *Nimrod* varied from 4 to 13 m/s and depended on both the water depth and the tether used (Tab. 4.4). The mean impact velocity in the Innenjade tidal channel was $4 \text{ m/s} \pm 1 \text{ m/s}$. In the test field *Alpha Ventus*, *Nimrod* mostly impacted with $7 \text{ m/s} \pm 1 \text{ m/s}$ and in the Hawaiian areas with $10 \text{ m/s} \pm 1 \text{ m/s}$.

This led to maximum deceleration values ranging from 25–40 g in the Innenjade tidal channel, from 55–85 g in the test field *Alpha Ventus*, from 68–126 g in the Halekulani Sand Channel, from 120–155 g in Waimanalo Bay and from 120–210 g in Kailua Bay (Tab. 4.4), and to mean penetration depths of about 0.08–0.18 m with penetration depths of up to 0.34 m in a single case (Tab. 4.4). It was possible to derive a characteristic deceleration - depth profile for the different study areas (e.g., Fig. 4.8). In most of the deployments in the Innenjade tidal channel, Kailua Bay and Waimanalo Bay a two layer system with varying thickness of the upper layer can be observed (e.g., Fig. 4.9), whereas there is no layering in the profiles from the *Alpha Ventus* area and in approximately a third of the Halekulani Sand Channel (e.g., Fig. 4.10).

Generally, the maximum decelerations reached in the areas of carbonate sand (Halekulani Sand Channel, Kailua Bay and Waimanalo Bay) are significantly higher than the maximum deceleration reached in the areas of quartz sand (Innenjade, test field *Alpha Ventus*) (Tab. 4.4), while the penetration depth is similar or increased. Furthermore, areas with an inclined seafloor (Innenjade, Halekulani Sand Channel) show lower maximum values compared to their flat counterparts (test field *Alpha Ventus*, Waimanalo Bay, Kailua Bay). It has to be considered also that the sediment along the slopes exposed to flow may be different compared to flat areas.

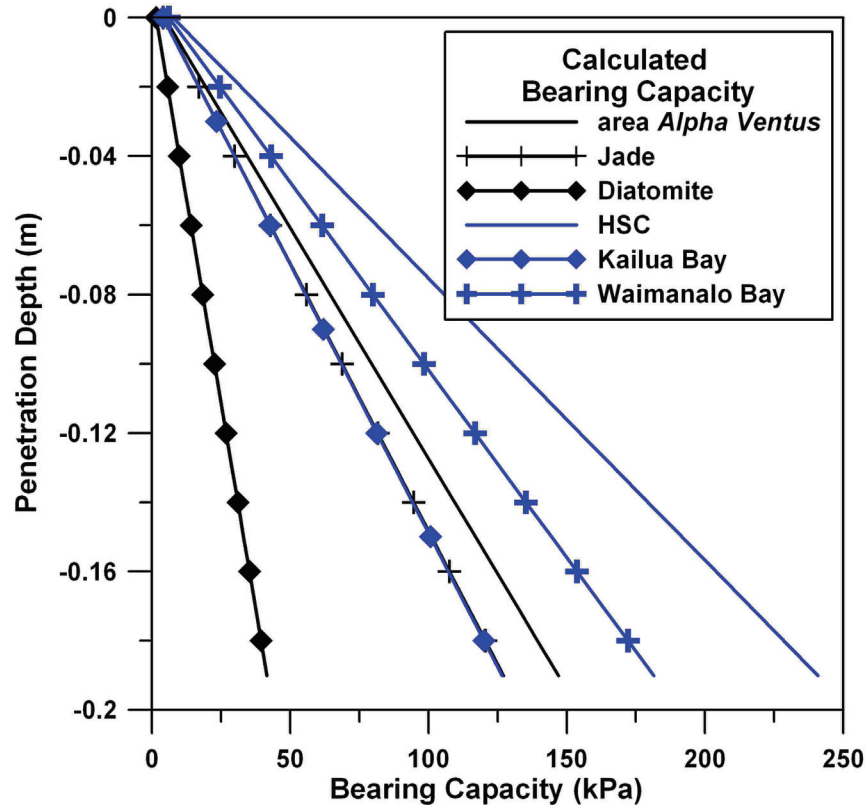


Figure 4.5: The calculated bearing capacity applying the friction angle (determined using an uniaxial shear box) to the ultimate bearing capacity equation (Eq. 4.1; Das, 1990). The carbonate sands (blue) tend to higher bearing capacities and show a greater increase in bearing capacity with depth than the quartz sands (black). Only the carbonate sand from Kailua Bay (blue with rhombs) does not follow this tendency. This goes along with the comparatively low friction angle derived for the sand from Kailua Bay and seems to be an artifact of disturbances in the sample or during the measurements. The diatomite presents a very low bearing capacity (black with rhombs).

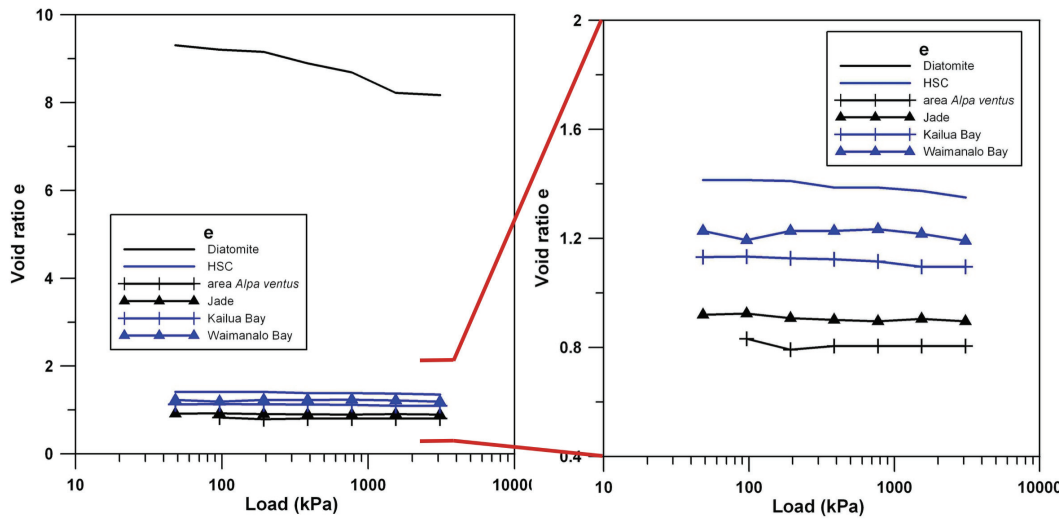


Figure 4.6: Void ratios of all sediments (left) and an expanded view without showing the results of the diatomite (right). The diatomite stands out, whereas the sands range from about 0.7 to 1.5 with carbonate sands (blue) showing higher void ratios.

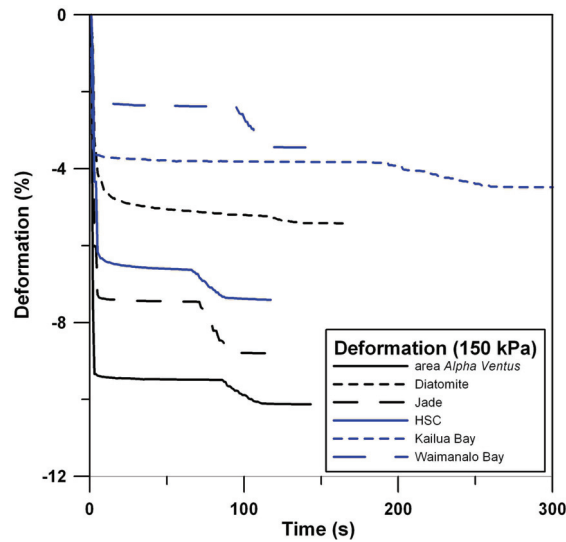


Figure 4.7: Deformation or rather settlement of the sediment sample under minor load shows that the carbonate sand (blue) and the diatomite (black dashed) which have higher void ratios and a greater settlement under increased loads tend to a lower settlement under minor loads. That hints at less repositioning of the particles, which is the first step during initial loading.

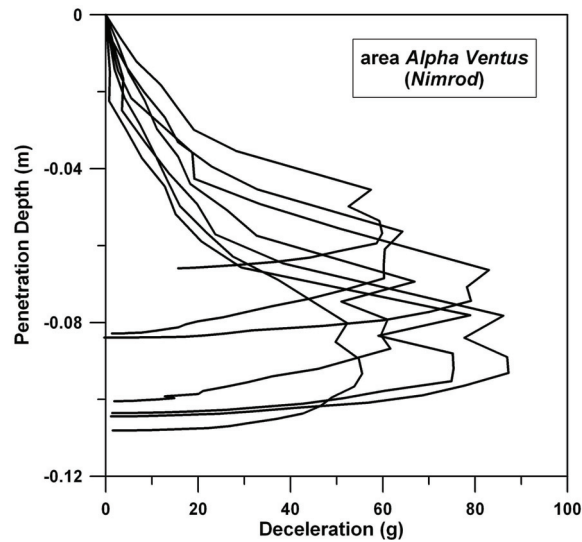


Figure 4.8: Example for the reproducibility of a typical impact signature for a homogenous research area (here area *Alpha Ventus*).

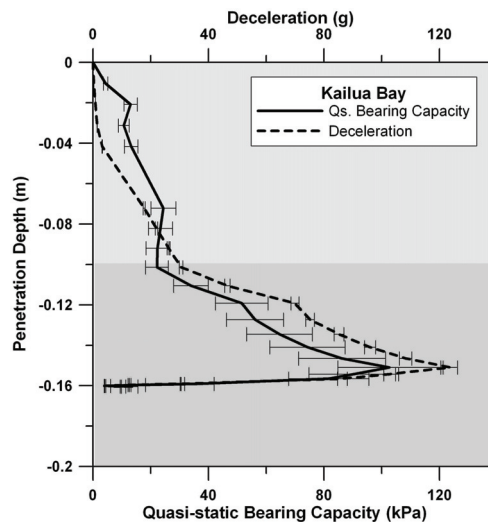


Figure 4.9: Layering determined from *in-situ* measurements using *Nimrod* expressed in deceleration (black dashed line) as well as quasi-static bearing capacity (black line) with the help of an example from Kailua Bay. Both profiles illustrate a different gradient from the surface to a penetration depth of about 0.1 m (light grey shaded area) and below that (dark grey shaded area).

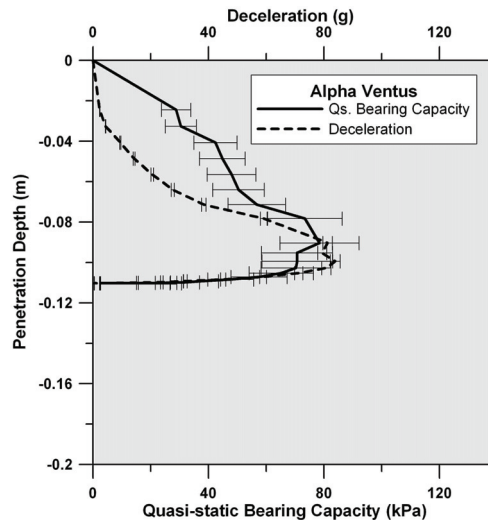


Figure 4.10: *Nimrod* deployment from the test field *Alpha Ventus* showing deceleration (black dashed line) and quasi-static bearing capacity (black line). No layering can be detected.

These trends as well as the layering still show good agreement, considering varying impact velocity and penetration depth, when calculating the quasi-static bearing capacity (Eq. 3.6 - 3.10) (Tab. 4.4, Fig. 4.9 - 4.10).

Discussion

Sediment strength – penetration depth: carbonate sand vs. quartz sand The *in-situ* dynamic penetrometer results present a higher sediment strength of carbonate sand compared to the quartz sand. This agrees with the laboratory tests, which measured a higher coefficient of friction as well as a higher friction angle for the carbonate sands (corresponds with, e.g., Kwag et al., 1999), but not with the penetration depth. In the case of a higher friction angle, which leads to a higher shear strength (Terzaghi, 1943), we expect a lower penetration depth. But for the carbonate sands, we find a slightly longer and deeper penetration processes. Our hypothesis is that the carbonate sands might be more compressible and that the additional depth is reached by a strong compression, which is limited in the case of the quartz sands. This effect might increase in areas of sediment remobilization, where the particle packing is still relatively fresh and not well settled.

A higher compressibility can be a consequence of a lower density, which can be caused by less settled sediment (e.g., recently mixed by hydrodynamic or

anthropogenic influences) or a particle shape disallowing a dense packing of particles. The former applies certainly for the carbonate sand sites. Shorebreaks and beach erosion are well known in Kailua Bay and Waimanalo Bay (e.g., Sutherland and Lee, 1994; Fletcher et al., 1998), and at the Halekulani Sand Channel the influence of the wave climate on the upper seafloor surface was already mentioned by Fu et al. (2004). Furthermore, often our quasi-static bearing capacity – depth profiles depict a very loose, mixed up sediment layer in these areas. However, this is also the case in the Innenjade tidal channel, where we find neither uncommonly high deceleration values nor an increased penetration depth.

Hence, we focused on the influence of particle shape on density and compression in the laboratory. The results show lower dry unit weights, higher void ratios and higher water contents for the carbonate sands than for the quartz sands. The values match well results presented by, e.g., Das (1990), Pizzimenti and Silva (1997), Kwag et al. (1999) and Byrne and Houlsby (2001). Diatomite followed the trend of the carbonate sands, but with much more extreme values (Tab. 4.3). This points out, that these geotechnical properties are, above all, a consequence of the physical appearance of the particles. The biogenic shapes of the carbonate sands lead to a less dense packing of particles than the quartz sand. Moreover, the network of carbonate particles is also weaker. Kwag et al. (1999) as well as Chuhan et al. (2003) showed that particle asperity crushing occurs quickly in carbonate sands. After crushing, the remaining particles are smaller and allow a denser packing. This biogenic characteristic makes the carbonate sand much more compressible with a large loss of volume. Following that, the laboratory tests support our explanation for the differences in the *in-situ* penetration profiles: If *Nimrod* impacts on carbonate sand, it creates a stronger compression of the sediment than in case of quartz sand, which leads to a greater penetration depth. As the shear strength of carbonate sand is higher, the sediment around the penetration probe provides more resistance against pushing sediment to the side, what leads to higher values of quasi-static bearing capacity and deceleration after the phase of compression.

Varying impact velocity The deployment of dynamic penetrometers is characterized by a decrease of penetration velocity during the penetration process, and also by different impact velocities depending on the respective device and deployment technique. Stoll and Akal (1999) found that the expendable Bottom Penetrometer reaches in general a similar terminal velocity of about 7 m/s after a few meters of fall through the water column. For

Nimrod, we did not observe such a similarity in impact velocity. One difference is the use of different tethers. Differences in tether material change the buoyancy of the tether and influenced the friction along the tether. Especially in deeper water, this may have a strong influence. During deployments of eXpendable Bottom Penetrometers a very thin filament, which breaks upon finishing the measurements, is used as a connection between the device and data recorder. *Nimrod* requires a tether with maximum thickness of 6 mm, and still there may be differences in material and structure. Thus, a consideration of impact velocity during the interpretation might seem to be necessary even if there is no change of device, when the tether and/or water depth changes. However, comparing the resulting deceleration values to the quasi-static bearing capacity values (Tab. 4.4) it is noticeable that the trends and relations in maximum values are similar and well characterized by the deceleration values.

Quasi-static bearing capacity: laboratory vs. *in-situ* Further calculations relating deceleration to quasi-static bearing capacity (or other geotechnical properties) are important to apply the results in a general geotechnical context. To revise our calculation method and the results, we compared the resultant quasi-static bearing capacity values (Tab. 4.4) to the bearing capacity derived from the friction angle determined by the uniaxial shear box in the laboratory (Fig. 4.5). Despite some issues which hamper this comparison (e.g., the samples were highly disturbed, the approach used [Terzaghi, 1943; Das, 1990] does not mention the penetration velocity, inclination of the seafloor is not considered, the penetration shape is approximated for N_q as circular because no values for a conical shape are known to the authors) the bearing capacities derived from the friction angle in the laboratory and the ones delivered *in-situ* by *Nimrod* match well in the test field *Alpha Ventus* which is the most plain and homogenous of the research areas (penetration depth 0.08 m: calculation: ~ 70 kPa; *in-situ*: ~ 60 kPa). The results from Waimanalo Bay also match (penetration depth 0.10 m: calculation: ~ 100 kPa; *in-situ*: ~ 100 kPa). The appearance of layering, however, makes an allocation of comparable penetration depth more difficult. The *in-situ* results in the Innenjade tidal channel (penetration depth 0.10 m: calculation: ~ 60 kPa; *in-situ*: ~ 35 kPa) and the Halekulani Sand Channel (penetration depth 0.10 m: calculation: ~ 130 kPa; *in-situ*: ~ 80 kPa) are significantly smaller compared to the calculated bearing capacities.

This may be explained by the missing consideration of seafloor inclination. Meyerhof (1953) showed that the influence of inclination can decrease the

bearing capacities significantly. Our results support this and show that the inclined seafloor bears less load compared to a plain seafloor consisting of the same sediments. The samples do not mirror this effect, which may lead to the deviations seen in the results. However, the results presented here are not sufficient to prove this hypothesis. The number of deployments are not sufficient to show, e.g., differences of the results on the stoss and the leeward slope of a dune, which differ significantly in inclination. Additionally, it may be that an increased exposure to flow might hamper settlement on the inclined seafloor surface compared to flat areas. Further *in-situ* studies as well as numerical modelling would provide more information about the influence of seafloor inclination on dynamic penetrometer results.

The results from Kailua Bay (penetration depth 0.10 m: calculation: ~ 60 kPa; *in-situ*: ~ 120 kPa) are also a mismatch. As already mentioned above, the friction angles determined seem to be too small. This leads to calculated bearing capacities which are obviously smaller than the *in-situ* monitored values. We assume that disturbance of the samples or an error during the laboratory measurements is the reason for an unreliable friction angle, and that the *in-situ* results are correct after comparing them to the other laboratory and *in-situ* measurements, especially from Waimanalo Bay.

Conclusions

Concerning the *in-situ* measurements we can conclude:

1. Dynamic penetrometer strength – depth profiles of carbonate sands can be distinguished from strength – depth profiles of quartz sands. Due to their different physical sediment properties (e.g., void ratio, friction angle, particle shape, grain size etc.) they show a different relation between compression and shearing during penetration of an object, which is mirrored in the profiles.
2. Our data suggest that in uncomplicated areas it may be possible to calculate a quasi-static bearing capacity from *in-situ* dynamic measurements. For more complicated areas the influence of, e.g., seafloor inclination, on the quasi-static bearing capacities must be considered. This requires more investigations using field studies and numerical models.
3. A consideration of impact velocity seems important. The approach presented here by Dayal and Allen (1975) delivers reasonable results, but more investigations (*in-situ*, physical and numerical models) have to be done to improve the calculations.

Generally, the *in-situ* strength testing of a sandy seafloor using dynamic penetrometers is an expedient complement to laboratory investigations. Sands with different geotechnical properties can be distinguished from each other and the results give a hint of tendencies toward shearing and compression. The influence of inclination and sediment remobilization on the monitored sediment strength should be investigated in more detailed studies to fix the dependence of the recorded strength to seafloor inclination and find out if a quantification of sediment mobilization is possible with dynamic penetrometers.

Acknowledgements

We acknowledge the German Research association (via MARUM, Center of Excellence at the University of Bremen, and GLOMAR, Bremen International Graduate School for Marine Sciences) and the *Bundesministerium für Umwelt, Naturschutz und Reaktorsicherheit* (via *Bundesamt für Schifffahrt und Hydrographie* and the RAVE project) for funding this study. We thank the crews of R/V Senckenberg and R/V Wega for support. Furthermore, we thank Christian Svenson, Nils Hoeber, Jennifer Dussault and Sergio Jaramillo for their help during in-situ measurements and Sergey Dzhuninov, Annika Förster, Daniel Otto, Katharina Behrens, Stephan Kreiter and Tobias Mörz for their help during laboratory measurements. We are particularly indebted to Hendrik Hanff, Matthias Lange (MARUM) and Matthias Colsmann (AVISARO, Hannover) for technical support, and to Thies Granit GmbH for providing diatomite.

References

- Aubeny, C.P., Shi, H., (2006). Interpretation of impact penetrometer measurements in soft clay. *J. Geotech. Geoenviron. Eng.* 132(6), pp. 770 - 777.
- Bartolomä, A., Ernstsens, V.B., Flemming, B.W., Bartholdy, J., (2004). Bedform dynamics and net sediment transport paths over a flood-ebb tidal cycle in the Grabdyb channel (Denmark), determined by high-resolution multi-beam echosounding. *Geografisk Tidsskrift, Danish Journal of Geography* 104(1), pp. 45 - 55.
- Cai, G., Liu, S., Tong, L., Du, G., (2009). Assessment of direct CPT and CPTU methods for predicting the ultimate bearing capacity of single piles. *Engineering Geology* 104, pp. 211 - 222.

Cassidy, M., Houlsby, G.T., (2002). Vertical bearing capacity factors for conical footings on sand. *Géotechnique* 52(9), pp. 687 - 692.

Chuhan, F.A., Kjeldstad, A., Bjorlykke, K., Hoeg, K., (2003). Experimental compression of loose sands: relevance to porosity reduction during burial in sedimentary basins. *Can. Geotech. J.* 40, pp. 995 - 1011.

Das, B.M., (1990). *Principles of Geotechnical Engineering*. 2nd ed., PWS-Kent Publishing Company, Boston, Massachusetts.

Dayal, U., Allen, J.H., (1975). The effect of penetration rate on the strength of remolded clay and sand samples. *Can. Geotech. J.* 12, pp. 336.

Fletcher, C.H., Mullane, R.A., Richmond, B.M., (1997). Beach loss along armored shorelines on Oahu, Hawaiian islands. *Journal of Coastal Research* 13(1), pp. 209 - 215.

Fu, S.S., Tao, C., Prasad, M., Wilkens, R.H., Frazer, L.N., (2004). Acoustic properties of coral sands, Waikiki, Hawaii. *J. Acoust. Soc. Am.* 115(5), pp. 2013 - 2020.

Harney, J.N., Fletcher, C.H., (2003). A budget of carbonate framework and sediment production, Kailua Bay, Oahu, Hawaii. *Journal of Sedimentary Research* 73(6), pp. 856 - 868.

Kopf, A., Stegmann, S., Krastel, S., Foerster, A., Strasser, M., Irving, M., (2007). Marine deep-water free-fall CPT measurements for landslide characterisation off Crete, Greece (Eastern Mediterranean Sea), Part 2: Initial data from the western Cretan Sea. *Submarine Mass Movements and their consequences*, Springer, Netherlands, pp. 199 - 208.

Kwag, J.M., Ochiai, H., Yasufuku, N., (1999). Yielding stress characteristics of carbonate sand in relation to individual particle fragmentation strength. *Engineering for Calcareous Sediments*, Balkema, Rotterdam, ISBN 30 5809 037X, pp. 79 - 86.

Meyerhof, G.G., (1953). The bearing capacity of foundations under eccentric and inclined loads. *Proceedings, 3rd International Conference on Soil Mechanics and Foundation Engineering* 1, pp. 16-26.

Nichols, G., (1999). *Sedimentology and Stratigraphy*, Balckwell Science Ltd, Ox-

ford, ISBN 0- 632-03578-1.

Okrusch, M., Matthes, S., (2005). Mineralogie, Springer, Berlin.

Pettijohn, F.J., Potter, P.E., Siever, R., (1987). Sand and Sandstone, Springer, NY.

Pizzimenti, P.B., Silva, A.J., (1997). Stress-strain behavior of surficial carbonate sediments from Key West, Florida, USA. *Marine Georesources and Geotechnology* 15, pp. 335 - 362.

Romine, B.M., Fletcher, C.H., Frazer, L.N., Genz, A.S., Barbee, M.M., Lim, S., (2008). Historical shoreline change, southeast Oahu, Hawaii; Applying polynomial models to calculate shoreline change rates. *Journal of Coastal Research* DOI: 10.2112/08-1070.1.

Salehzadeh, H., Hassanlourad, M., Procter, D.C., Merrifield, C.M., (2008). Compression and extension monotonic loading of a carbonate sand. *International Journal of Civil Engineering* 6, pp. 266 - 274.

Stark, N., Wever, T.F.. (2008). Unraveling subtle details of expendable bottom penetrometer (XBP) deceleration profiles. *Geo-Mar Lett* DOI: 10.1007/s00367-008-0119-1.

Stark, N., Hanff, H., Kopf, A., (2009). Nimrod: a tool for rapid geotechnical characterization of surface sediments. *Sea Technology* 50(4), pp. 10 - 14.

Stark, N., Hanff, H., Stegmann, S., Wilkens, R., Kopf, A., (2009). Geotechnical investigations of sandy seafloors using dynamic penetrometers. *OCEANS 2009, MTS/ IEEE Biloxi*.

Stegmann, S., Villinger, H., Kopf, A., (2006). Design of a modular, marine free-fall cone penetrometer. *Sea Technology* 47(2), pp. 27 - 33.

Stegmann, S., Moerz, T., Kopf, A., (2006). Initial results of a new free fall-cone penetrometer (FF-CPT) for geotechnical in-situ characterisation of soft marine sediments. *Norwegian Journal of Geology* 86, pp. 199 - 208.

Stegmann, S., Kopf, A., (2007). Marine deep-water free-fall CPT measurements for landslide characterisation off Crete, Greece (eastern Mediterranean Sea)-part I: a new 4000m cone penetrometer. *Submarine Mass movements and their conse-*

quences, 3rd international symposium, Netherlands, pp. 171 - 177.

Stoll, R.D., Akal, T., (1999). XBP-tool for rapid assessment of seabed sediment properties. *Sea Technology* 40(2), pp. 47 - 51.

Stoll, R.D., Sun, Y.F., Bitte, I., (2004). Measuring sea bed properties using static and dynamic penetrometers. Lamont-Doherty Earth Observatory of Columbia University, N.Y.

Stoll, R.D., Sun, Y.F., Bitte, I., (2007). Seafloor properties from penetrometer tests. *IEEE Journal of Oceanic Engineering* 32(1).

Sutherland, R.A., Lee, C., (1994). Discrimination between coastal subenvironments using textural characteristics. *Sedimentology* 41, pp. 1133 - 1145.

Svenson, C., Ernstsen, V.B., Winter, C., (2009). Cruise Jade, Germany, 14.-18.4.2008 and 28.-30.4.2008, FK Senckenberg, Draft Report.

Terzaghi, K., (1943). *Theoretical soil mechanics*. John Wiley and Sons, New York.

Vesic, A., (1973). Analysis of ultimate loads of shallow foundations. *J. Soil Mech. Fdns Div Am. Soc. Civ. Engrs* 99(1), pp. 45 - 74.

4.2 Subaqueous dunes

During the survey in the Jade tidal inlet channel we had already detected hints for sediment remobilization in the sediment strength profiles. However, this data set was not sufficient to make detailed conclusions. In the following manuscript data from a survey along subaqueous dunes in the Danish Wadden Sea are presented. The data set made it possible to depict the sediment remobilization during a tidal cycle and to compare the results with acoustic methods (MBES, ADCP).

4.2.1 Geological manuscript II

Stark, N., Hanff, H., Svenson, C., Graff, A., Ernstsen,
V.B., Lefebvre, A., Winter, C., Kopf, A.

Temporal variations of the surface sediment layer along
active subaqueous dunes.

Submitted to Geo-Marine Letters.

Abstract

In-situ geotechnical measurements of surface sediments were carried out along large subaqueous dunes in the tidal inlet channel Knudedyb in the Danish Wadden Sea using a small free-falling penetrometer. Vertical profiles showed typical stratification patterns of a thin surface layer of low sediment strength and a stiffer substratum below. Variations in the thickness of the surface layer during the tidal cycle were observed and related to mean current velocities, high-resolution bathymetry and qualitative distributions of suspended sediment in the water column. The results presented (i) an ebb dominance in sediment remobilization, and (ii) a general accretion of the bed towards low water. Furthermore, we found approximately continuously a loose top layer likely influenced by bedload transport and small events of suspended sediment resettlement (thickness: $0.06 \text{ m} \pm 0.01 \text{ m}$), and a significant increase of thickness (e.g., from 0.08 m to 0.16 m) related to periods of overall

deposition.

Introduction

Processes of seabed sediment remobilization such as the formation and development of bedforms or scouring are of interest in scientific research as well as in coastal engineering. They are investigated in field studies, physical models (e.g., Rubin and McCulloch 1980) and numerical models (e.g., Siegle et al., 2004; Winter et al., 2006; Coco et al., 2007a/b). In the field, sediment sampling (e.g., Zeiler et al., 2000; Svenson et al., 2009), acoustic visualization methods such as Multibeam Echo Sounder or Side Scan Sonar (e.g., Anthony and Leth, 2002; Ernstsen et al., 2006b; Wever et al., 2008), and acoustic Doppler current profilers (e.g., Bartholomä et al., 2004; Kostaschuk and Best, 2005; Gaeuman and Jacobson, 2006) are widely used to enhance the understanding of sediment remobilization processes.

For an in-depth understanding of small scale processes at the bed, information of *in-situ* state variables is crucial, as undisturbed sampling is difficult for parameters like density and sediment strength of looser layers at the uppermost sediment surface (Blomqvist, 1991). This study aims towards a determination of *in-situ* soil properties of the upper bed and their variability throughout tidal cycles.

To determine the density of sediment transported as bedload, bedload samplers can be used (e.g., Emerson, 1991), however, they can be difficult to install, and might miss parts of the bedload layer in the vertical direction (Emerson, 1991). A method to derive sediment strength and estimate sediment strength *in-situ* is a diver-held vane shear apparatus (Dill and Moore, 1965), but divers cannot stabilize sufficiently to correctly deploy the instrument in areas of stronger tides. Alternatively, penetrometers can be used as they deliver a vertical distribution of seafloor sediment strength (e.g., Stoll et al., 2004; Aubeny and Shi, 2006; Stegmann et al., 2006b; Stark and Wever, 2008; Stark et al., 2009b). They are either pushed by an engine into the sediment with a constant velocity (static penetrometer) or penetrate the seafloor by their own weight and momentum (dynamic penetrometer) with a decreasing velocity depending on the sediment strength. During the penetration they measure sediment resistance, sleeve friction, pore pressure and/or temperature depending on the respective device. Especially, dynamic penetrometers are easy to deploy even in challenging areas and conditions, e.g., with strong currents (e.g., Stoll and Akal, 1999; Stegmann et al., 2006a; Stark et al., 2009a).

First preliminary tests using the small dynamic penetrometer, *Nimrod*, devel-

oped by the working group for Marine Geotechnics at MARUM, University of Bremen, on subaqueous sand dunes in the Jade estuary in April 2008 have shown that the instrument is suitable for (i) measurements in areas of strong currents, and (ii) indication of sediment remobilization processes (Stark et al., 2009a/b). Consequently, in a following research cruise to the Knudedyb tidal inlet channel in the Danish Wadden Sea, a more detailed study was carried out in November 2008. The aims were (i) to test if dynamic penetrometers can provide complementary information about the ongoing sediment remobilization as a snapshot in space and time, and (ii) to study *in-situ* the geotechnical behavior of a sandy seafloor mobilized in the framework of subaqueous dunes depending on tidal phases.

Regional context

The Knudedyb tidal inlet is located in the Danish Wadden Sea close to the city of Esbjerg (Fig. 4.11). The tidal inlet is ebb-dominated and the tides are semi-diurnal with a mean tidal range of 1.5 m and a tidal prism of 175 million m^3 (Lundbak, 1947). The bed of the channel is composed of sandy material and is typically covered with large compound bedforms. According to Ashley (1990), they can be classified as very large dunes and superimposed, medium-sized simple dunes. The mean grain size averaged along the survey area is 0.46 mm (medium sand; according to Udden-Wentworth scale). The sediment is well sorted and contains a negligible amount of fine material such as mud or clay, but contains shell fragments.

An about 500 m-long transect covering three primary bedforms with numerous superimposed dunes (Fig. 4.12) was surveyed using the *Nimrod*, a multi-beam echosounder and an acoustic Doppler current profiler. The largest primary dune along the transect (No. 3 in Fig. 4.12) reached a height of ~ 8 m and had a length of ~ 290 m (Fig. 4.12). The superimposed secondary dunes had an average wavelength of 3.5 m and height of 0.16 m.

Methods

Dynamic penetrometer The dynamic penetrometer used for this study is the shallow-water free-falling penetrometer, *Nimrod* (Fig. 4.13), especially suitable for deployments in challenging areas (Stark et al., 2009a/b). Its shape is based on fluid-dynamical designs and includes fins and a fall stabilizing relationship of center of gravity and center of volume. Thus, it falls vertically ($\pm 5^\circ$) through the water column even in case of stronger currents.

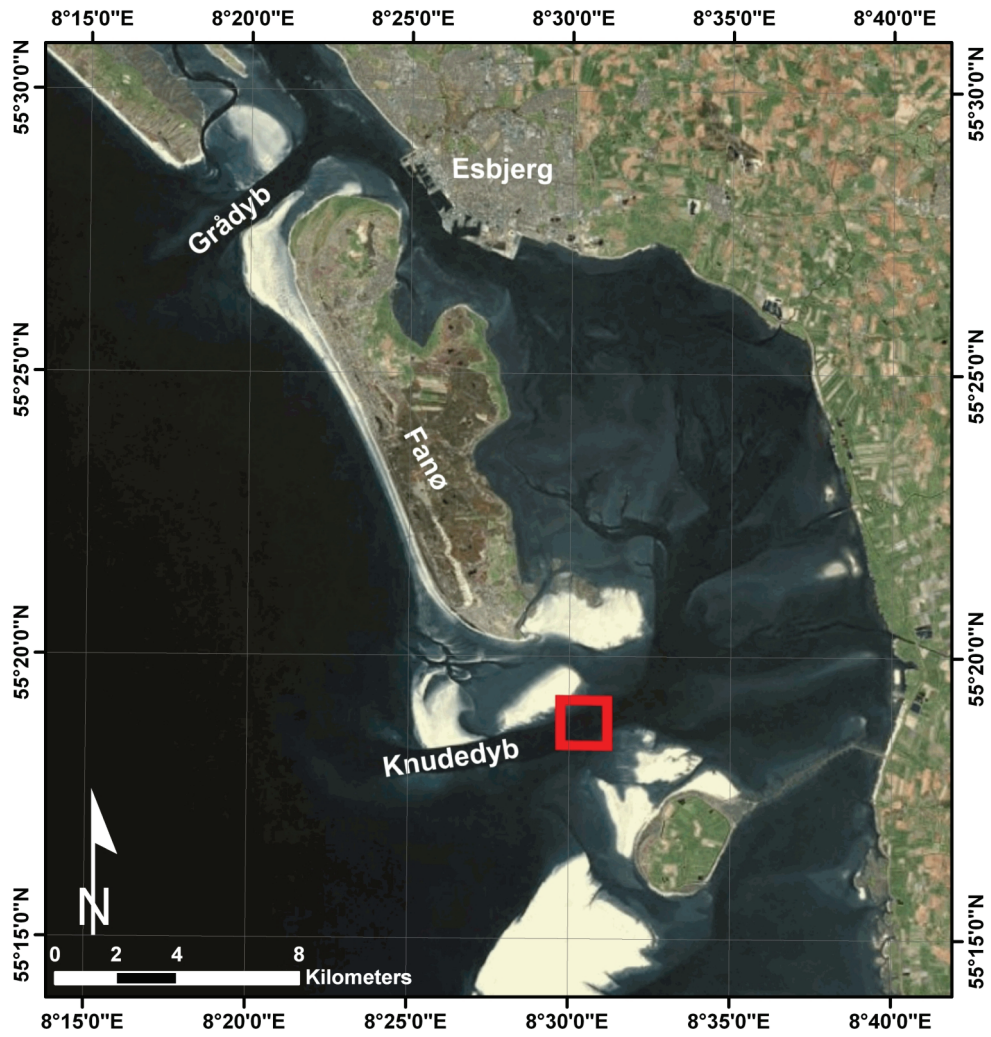


Figure 4.11: Satellite picture of the region close to Esbjerg. The red square represents the survey area.

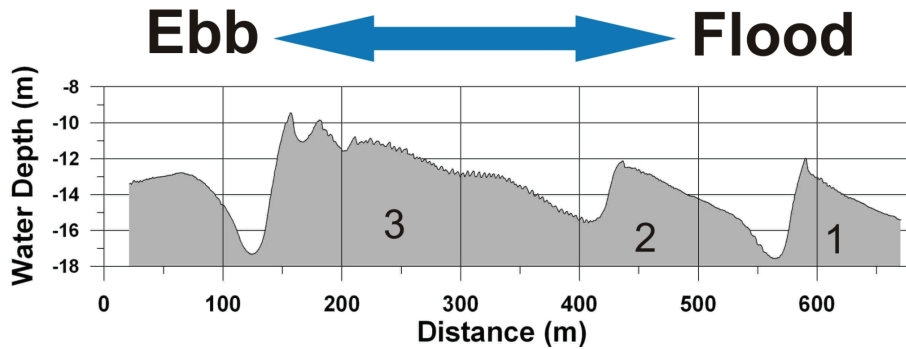


Figure 4.12: Bathymetry of the investigated bedforms with indication of ebb and flood direction. The transect covered three primary bedforms (1-3).

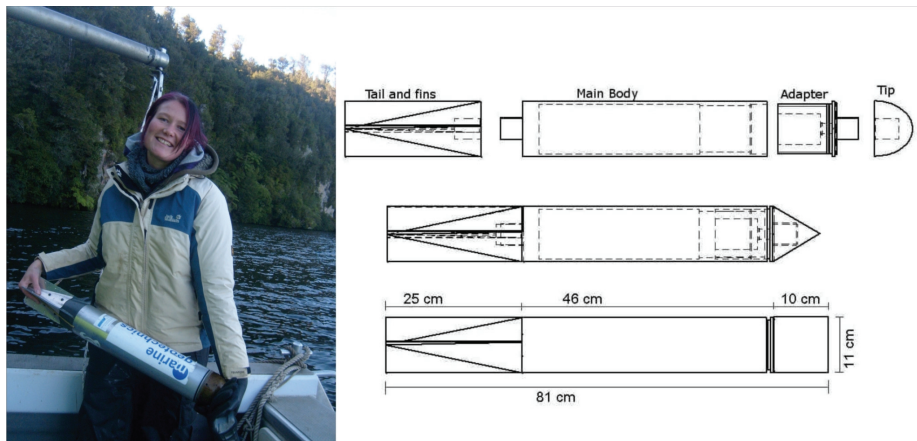


Figure 4.13: The dynamic penetrometer *Nimrod* with the author during a survey in New Zealand (left). A detailed sketch of the instrument with the three available tip geometries (right). In this study the hemispherical tip was used.

Deceleration of the probe and pressure are continuously recorded at high sampling rates, and in doing so, deliver information on soil properties during impact and penetration into the bed sediments. These can be related to sediment strength, layering and inhomogeneities such as plant fibres or stones (Stark et al., 2009a). Layering and abrupt changes in sediment strength due to changes of physical properties of the particles or density are displayed in the vertical deceleration - depth profiles. With a data logging frequency of 1 kHz and an impact velocity of ~ 8 m/s, the resulting vertical resolution is less than 1 cm. The impact velocity and penetration depth are derived by single and double integration of the deceleration over time, respectively.

To increase the sensitivity regarding the sediment strength, a hemispheric

tip geometry (Fig. 4.13) was chosen, which opposes a higher resistance against the sediment, instead of the conical tip usually used on sandy seafloors (Stark et al., 2009b).

Deceleration - depth profiles are influenced by the size and the geometry of the penetrating object (Terzaghi, 1943; Meyerhof, 1953; Das, 1990), and in case of dynamic penetrometers also by the decrease of penetration velocity during penetration (Stoll et al., 2004; Aubeny and Shi, 2005; Stoll et al., 2007). A calculation of bearing capacity offers the possibility to consider the size and geometry of the device (Terzaghi, 1943; Meyerhof, 1953; Das, 1990; Cassidy and Houlsby, 2002). For the *Nimrod*, the device's geometry remains the same, but the size of the penetration surface increases with the first ten centimeters (hemispheric tip length).

The bearing capacity can be expressed as the maximum load per unit area that a soil can bear prior to failure (Terzaghi, 1943; Das, 1990). Regarding the soil as a grid of several, very thin layers of particles, the penetration can be schematized as a sequence: i) the probe hits the upper layer, (ii) the load per unit area or pressure on the soil exceeds the bearing capacity, (iii) the upper layer fails and the probe hits the next layer, and so on. Thereby, the derived sediment resistance force for each layer is the maximum resistance force that the sediment can oppose until it fails and the probe keeps penetrating (Aubeny and Shi, 2006). Consequently, the sediment resistance force can be used to calculate a bearing capacity equivalent using:

$$q_u = \frac{F_{sr}}{A}, \quad (4.9)$$

where A is the area of the plain subjected to load and F_{sr} the sediment resistance force. Regarding the probe as a single particle in equilibrium (after reaching the terminal velocity in the water column), the sediment exerts the sediment resistance force F_{sr} against the probe and decelerates it as follow (Aubeny and Shi, 2006):

$$m_{Nim}dec = F_{sr}, \quad (4.10)$$

with m_{Nim} being the weight of *Nimrod* in water (with hemispherical tip 9 kg) and dec being the measured deceleration. After Aubeny and Shi (2006), the sediment resistance force includes a sediment shearing resistance force F_s and buoyancy of the probe in soil F_b :

$$F_{sr} = F_b + F_s. \quad (4.11)$$

Inertial forces are negligible here (Aubeny and Shi, 2006). The buoyancy of the probe in soil is neglected here because of the small penetration depths of

a few centimeters.

The next step is to consider the nonlinear back-coupling between measured deceleration and penetration rate. Dynamic penetrometers slow down during penetration, whereas quasi-static methods keep a constant penetration rate. The former leads to a strain rate dependency of the sediment strength reflecting properties such as deceleration. Stoll et al. (2004, 2007) as well as Aubeny and Shi (2006) used strain rate factors to convert quasi-static sediment resistance to higher, dynamic penetration rates and vice versa. Stoll et al. (2007) illustrated that a difference in penetration velocity of about 3 m/s can lead to sixfold increase in sediment resistance in case of medium compacted sand. To allow a direct comparison of different dynamic penetrometers and to standardized methods, the empirical approach by Dayal and Allen (1975) suggests that the strain rate factor f_{ac} , depends on the actual penetration velocity v and a reference velocity v_0 :

$$f_{ac} = 1 + K \log \left(\frac{v}{v_0} \right), \quad (4.12)$$

with K being a dimensionless factor ranging from 1.0 to 1.5.

To convert the sediment resistance force from high-speed dynamic deployments to quasi-static (= constant rate) values, the dynamic sediment resistance force F_{sr} and accordingly the dynamic bearing capacity q_{udyn} has to be divided by f_{ac} :

$$q_{uqs} = \frac{q_{udyn}}{f_{ac}}. \quad (4.13)$$

The used reference velocity v_0 equals 0.02 m/s, which is the standard for quasi-static penetration tests (Lunne et al., 1997; Cai et al., 2009). In consequence, the layering shown in the quasi-static bearing capacity - depth profiles can be assumed as being approximately free of artifacts of penetration rate or changes in penetration surface area (Stark et al., 2009b) and expresses a bearing capacity equivalent to the results of quasi-static standard methods under similar conditions (e.g., velocity, penetration angle, etc.).

During the survey carried out in Knudedyb in November 2008 and presented herein, 97 *Nimrod* deployments were achieved along the transect presented on figure 4.12. The device was deployed from the ship and quickly fell (3 s) through the water column (ca. 15 m depth) and the vessel was left to slowly drift with the current so that it mirrored the slight horizontal shift of the device as it fell through the water column. The position was recorded in the moment of impact into the sediment. This method yielded an accuracy of the positioning of ± 3 m after observation of tether angles, tether length and

accuracy of the ship positioning system (differential GPS).

Multibeam echo sounder (MBES) Bathymetry was recorded by means of a ship mounted *SeaBat*TM 8125 (Reson) multibeam echo sounder (MBES) system operating at 455 kHz, and the *QINSy*TM version 7.50 (QPS) data collecting and processing software package. The vertical resolution of the MBES system is at a sub-centimeter scale (www.reson.com), while the lateral resolution is a function of water depth and vessel speed. For instance, a water depth of 15 m results in an across-track resolution of 0.13-0.51 m, due to beam spreading at an angle of 0.5°. Assuming a sound velocity of 1500 m/s, the actual ping rate at a water depth of 15 m equals 25 Hz. At a vessel speed of 1 m/s, this results in an along-track resolution of 0.04 m. As the outermost beams were not used in the present analysis, a cell size of 0.2 × 0.2 m was chosen for the gridding of the bathymetric data. The MBES system was coupled with an *Aquarius*TM 5002 MK/SK (Magellan) dual-frequency (L1/L2) long-range kinematic (LRKTM) global positioning system (GPS). Positions and altitudes were output in World Geodetic System 1984 (WGS84) coordinates and displayed in relation to the Universal Transverse Mercator 32 (UTM32) map projection. Corrections for ship movements were applied using an *Octans Surface*TM (Ixsea Oceano) gyrocompass and motion sensor. The horizontal and vertical precision of the integrated MBES system during single surveys, conducted at vessel speeds more than twice of that chosen in this study (cf. above), is ± 20 cm and ± 2 cm, respectively, at a 95 % confidence level (Ernstsen et al., 2006a).

Transects were surveyed every 45 min on average over a complete tidal cycle. To derive the mean bed elevation, the change of bathymetry was determined and averaged over the transect.

Acoustic doppler current profiler (ADCP) Flow velocities were measured along the transect in 2008 and 2009 using a ship mounted *Workhorse Rio Grande*TM (Teledyne RD Instruments) acoustic Doppler current profiler (ADCP) operating at 1200 kHz, and the *WinRiver*TM (Teledyne RD Instruments) software package for acquisition. The vertical resolution of the ADCP was set to 0.20 m. The lateral resolution of the recordings was ~ 2 m at a ping rate of 0.5 Hz and a vessel speed of around 1 m/s. With a transect length of 600 m this results in about 300 pings (or ensembles) recorded along the transect per run.

The raw ADCP data were processed using m-adcp, a *MATLAB*TM (The

MathWorks) toolbox developed to process ADCP data at MARUM – Center for Marine Environmental Sciences, University of Bremen, Germany. For each run, the depth-averaged mean flow velocity along the transect was calculated by depth-averaging the mean flow velocities for each ensemble along the transect and then averaging the velocities along the transect.

During a previous field campaign in the same survey area (April 2008), an up-looking ADCP operating at 600 kHz was deployed over a time period of two days. The derived echo intensities (corrected for beam spreading and water adsorption, but uncalibrated) were used for a qualitative estimation of suspended sediment concentration in the water column with respect to the different tidal phases. A quantification of suspended sediment will not be presented in this article. The vertical resolution in the water column was 0.25 m, and the results were averaged over a time period of 60 s.

Results

Sediment strength The recorded readings of 97 deployments carried out with the *Nimrod* were analyzed for vertical deceleration and quasi-static bearing capacity profiles (e.g., Fig. 4.14). The penetration depth ranged from 0.07 to 0.64 m \pm 0.01 m and was on average 0.18 m. The mean impact velocity was 8 m/s \pm 3 m/s. In the deceleration – depth profiles as well as in the quasi-static bearing capacity profiles, two layers could be distinguished by the gradient (Fig. 4.14). The overlying layer (in the following called layer 1) represented predominantly decelerations of 0.2–4 g \pm 0.1 g and quasi-static bearing capacities of 0.1–2 kPa \pm 0.1 kPa (Tab. 4.5). An underlying substratum (in the following called layer 2) showed decelerations ranging from 8–88 g \pm 2 g with an average of 51 g \pm 2 g and quasi-static bearing capacities of 9–52 kPa \pm 5 kPa and an average of 30 kPa \pm 5 kPa (Tab. 4.5).

In layer 1, a change of sediment strength depending on the tidal phase was noticed (Fig. 4.15). During the ebb tide and towards low water, the range of sediment strength narrowed down to a deceleration of 1–2 g and a quasi-static bearing capacity of 0.5–1 kPa. During the flood and towards high water, the strength of layer 1 tended to increase to a deceleration of up to 7 g \pm 1 g and bearing capacity of up to 4 kPa \pm 0.5 kPa (Fig. 4.15).

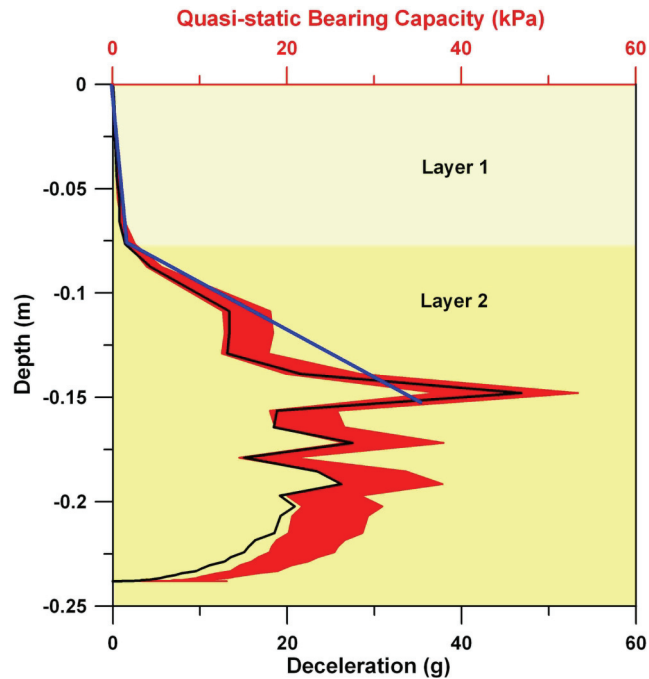


Figure 4.14: Example of a *Nimrod* deceleration-depth (black line) and quasi-static bearing capacity - depth (red area) profile. The presented quasi-static bearing capacity expresses a range of bearing capacity equivalent for a constant penetration velocity of 0.02 m/s. The different layers can be identified by a significant change in gradient of the quasi-static bearing capacity as well as the deceleration with depth (blue line).

Tidal phase	Deceleration (g) [layer1]	Qs. BC (kPa) [layer1]	Qs. BC (kPa) [layer2]
acc. ebb	0.2 - 2	0.3 - 1.4	< 50
max. ebb	1 - 2	0.4 - 0.8	< 50
dec. ebb	0.6 - 2	0.4 - 1.3	< 50
low water	0.6 - 1.6	0.4 - 1.2	< 50
acc. flood	1 - 4	0.1 - 1.6	< 60
max. flood	1 - 4	0.1 - 1.0	< 50
dec. flood	0.8 - 4	0.1 - 1.0	< 50
high water	1 - 4	0.1 - 2	< 50

Table 4.5: Measured mean maximum deceleration of layer 1 and derived quasi-static bearing capacity of layer 1 and 2 during the respective tidal phases.

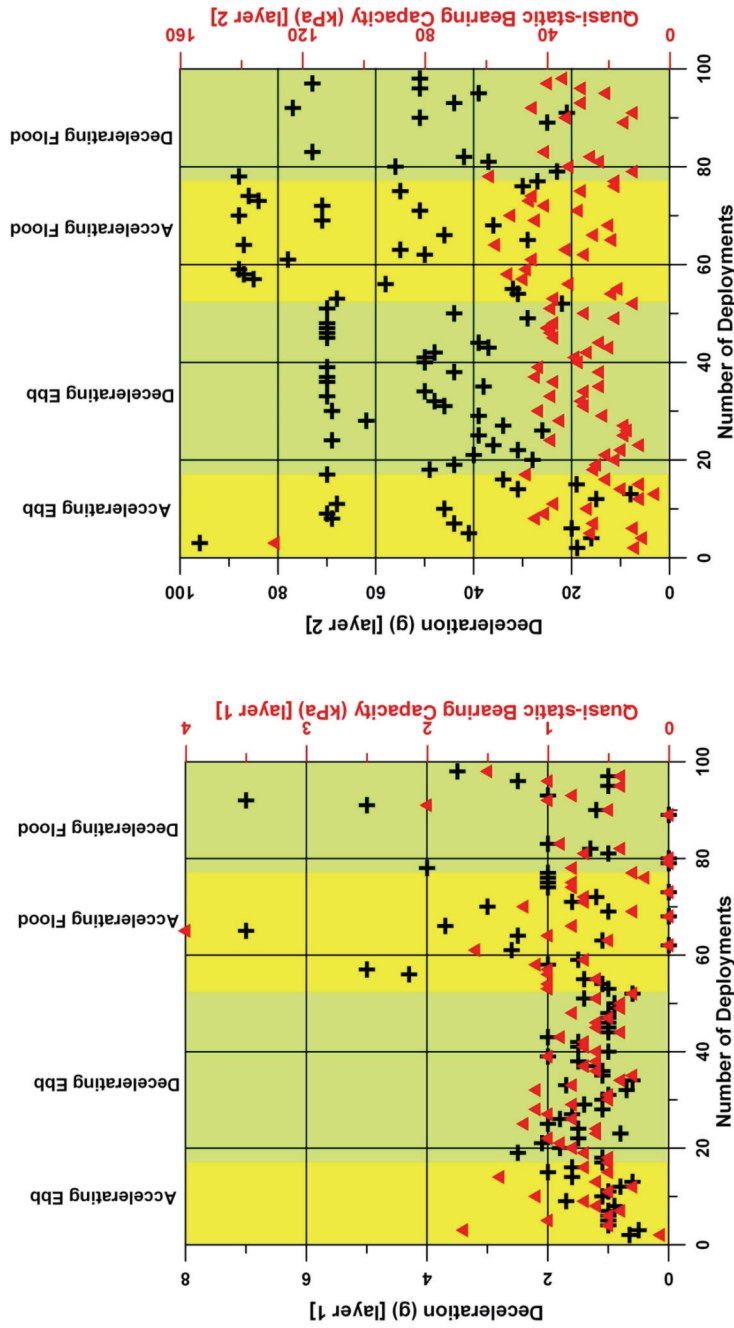


Figure 4.15: Deceleration (black crosses) and quasi-static bearing capacity (red triangles) of the overlying layer 1 (left) and the underlying layer 2 (right) of all deployments during the different tidal phases (green and yellow shades for decelerating and accelerating tides respectively). An increase in strength of layer 1 can be seen during the flood. The strength in layer 1 during ebb and during all tidal phases in layer 2 remains approximately constant considering that the measurement took place at different positions along the dune.

Layer 1 thickness variation with time During accelerating ebb current to maximum ebb current, the thickness of layer 1 varied from 0.05 to 0.09 m \pm 0.02 m (Fig. 4.16). During decelerating ebb and until low water, the thickness of layer 1 increased on average by about 0.04 m (Fig. 4.16) and reached a total thickness ranging from 0.03 to 0.16 m (Fig. 4.16). With accelerating flood, the thickness of layer 1 decreased abruptly back to a range of 0–0.1 m. With decelerating flood, the thickness of layer 1 reached no more than 0.08 m. The thickness of layer 1 tended to increase towards slack water phases and to decrease towards maximum current speeds (Fig. 4.16). However, the trend was much more pronounced within ebb current and towards low slack water (Fig. 4.16).

Mean current velocity and bathymetry The ebb-dominance observed in the asymmetric bedforms (Fig. 4.12) was shown in the flow velocity readings, in which the depth-averaged current velocity was asymmetric with a longer ebb phase, a maximum ebb velocity of \sim 1.2 m/s and a maximum flood velocity of \sim 0.8 m/s (Fig. 4.16).

The bathymetric surveys revealed a mean bed elevation change in the range of centimeters within a tidal cycle (Fig. 4.17). Starting from low water and until maximum flood current, a layer of sediment about 3 cm-thick eroded. Towards high water, a layer on average 4 cm-thick was accumulated. During accelerating ebb and maximum ebb current, a layer of sediment about 6 cm-thick was carried away again, followed by an accumulation of sediment up to 5 cm-thick during deceleration ebb current and towards low water.

The bathymetry therefore confirmed the increased sediment erosion as well as accumulation during ebb currents.

Estimation of turbidity in the water column The uncalibrated up-looking ADCP backscatter measurements gave a qualitative estimate on turbidity including the amount of suspended sediment in the water column (Fig 4.18). In general, the highest backscatter intensities, and consequently, the highest concentrations of suspended matter were observed from maximum ebb towards low water. During low water the signal decreased. The lowest concentrations were observed during decelerating flood and around high water (Fig. 4.18).

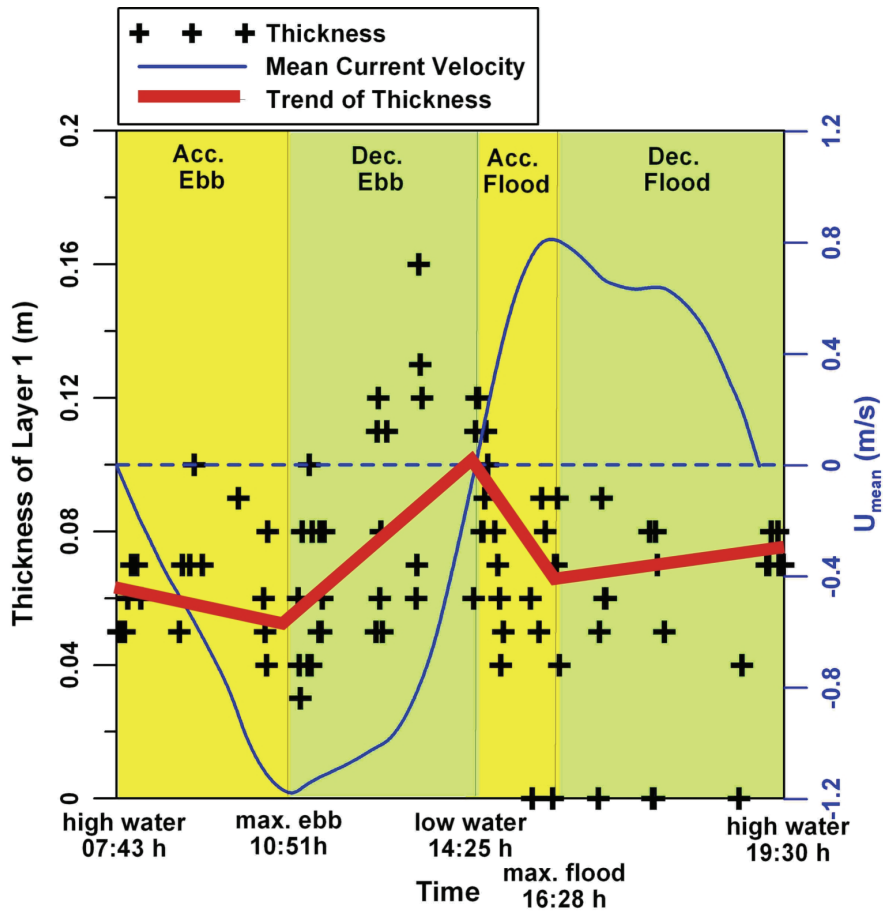


Figure 4.16: Development of the thickness of layer 1 with tidal phases (black crosses, red line). A thickening of the layer can be observed during decelerating ebb (dec. ebb) before an abrupt decrease after low water. This behavior can also be seen during flood and towards high water but with smaller amplitude. Mean current velocity (U_{mean} , blue solid line) was recorded using an ADCP. By convention, U_{mean} is positive during the flood and negative during the ebb.

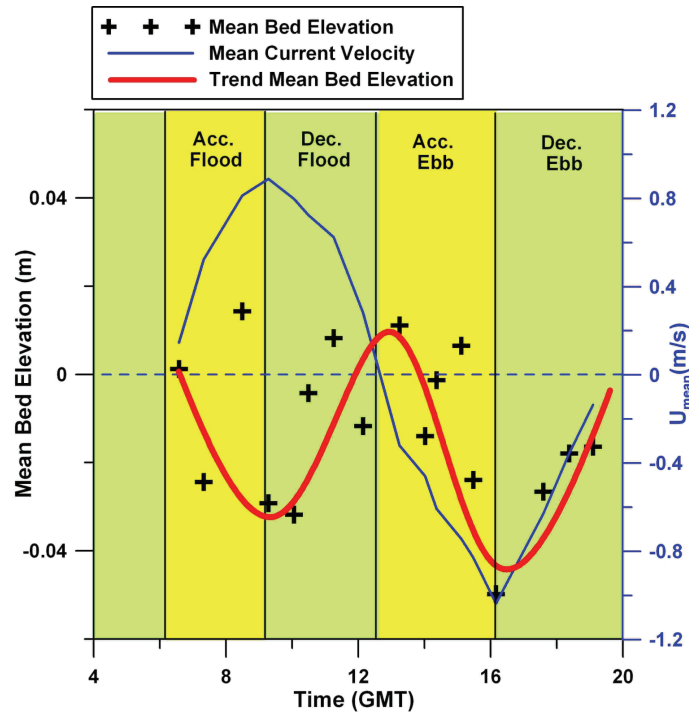


Figure 4.17: Mean bed elevation derived from MBES bathymetry and averaged over each transect, (black crosses and red trendline respectively) and mean current velocities recorded using an ADCP (blue line). Sediment erosion is strongest during maximum tides, however, it is more pronounced during maximum ebb.

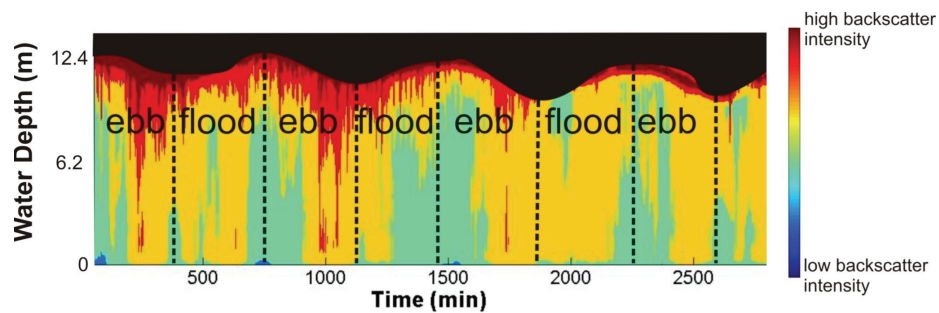


Figure 4.18: Time series of ADCP backscatterer intensity over the whole water column measured with an up-looking ADCP. The ebb and flood tides are separated by dashed lines. The highest backscatterer intensity can be monitored after maximum ebb current. The backscatterer intensity decreased at low water. During flood current sediment seemed to settle further, especially during decelerating flood. The lowest backscatterer intensities can be observed from decelerating flood, over water and until accelerating ebb.

Discussion

Differentiation of layers The observed layering in the soil strength profile (Fig. 4.14, Fig. 4.15, Tab. 4.5) may not be explained by changes in sediment type, as the bed material along the transect is mainly well sorted medium to coarse quartz sand. Following that, layering as a consequence of accumulation of fine material can be excluded. Also, shell fragments as a potential explanation for the observed layering can be eliminated. Stark and Wever (2008) showed that shell fragments lead to peak-like signatures in penetrometer results in case they are strong enough to influence the strength profiles. Instead, a change in sediment density or packing of particles is likely to be the cause of the variations in sediment strength recorded by *Nimrod*. In areas of sediment remobilization, the remobilized particles form looser structures or layers moving above a more consolidated substratum (Louge et al., 2010). Thus, layer 1 might be related to sediment in near-bed motion (bed-load) as well as sediment going into suspension or settling from suspension. Layer 2 matches such a substratum described by Louge et al. (2010) with an approximately constant signature during the whole tidal cycle. The derived quasi-static bearing capacities of the layer 2 are similar to results from, e.g., the Innenjade tidal channel (Stark et al., 2009b), where a survey with the same instrument was carried out. That area is also characterized by subaqueous dunes composed of bed material with similar grain size distributions. Results from other sandy areas (e.g., windfarm area *Alpha Ventus*, German Bight, North Sea; areas close to the shore around the island of O’ahu, Hawaii, USA) show a higher strength, but this can be explained by smaller average grain sizes, a relatively flat seabed and/or a different mineralogy (Stark et al., 2009b).

The increasing strength of layer 1 during flood and towards high water (Fig. 4.15) may be related to the ebb dominance in the area. The higher mean current velocities and the larger amount of bed material being remobilized during ebb tide lead to a loosening and mixing up of layer 1, and hence, a low sediment strength. In contrary, during the flood tide, more bed material remains settled and the consolidation of particles might increase the sediment strength during low water and flood. Additionally, such enhanced packing of the particles would hamper the sediment remobilization. This is a hypothesis following the geotechnical results from only one tidal cycle. More measurements, in the field as well as in flumes, and numerical modelling would be required to confirm it.

Quantification of surface sediment layer With current deceleration, suspended material settles from the water column, explaining the increasing thickness of layer 1. The abrupt decrease in thickness of layer 1 after low water could be a consequence of sediment settling during one-directional currents which might be more easily remobilized by the currents with a changed direction.

The MBES results confirm a stronger sediment remobilization during ebb current as observed with the *Nimrod* and the range of mean bed elevation corresponds to the range of layer 1. However, the bathymetry does not show such a significant difference of ongoing sediment remobilization between flood and ebb as the penetrometer does. Regarding the up-looking ADCP measurements, more bed material gets into suspension during maximum ebb current, a part of the sediment seems to settle close to low water and more settles with decelerating flood tide. Hence, the estimation of suspended matter in the water column over a tidal cycle supports an increase of sediment erosion during ebb tide and an increase of sediment settling from the water column towards low water.

Processes of sediment remobilization Geotechnical and acoustic methods agree on an ebb dominance of sediment remobilization in the study area. This supports the findings along another large compound dune in the Grådyb tidal inlet channel in the Danish Wadden Sea (Ernstsen et al., 2006b), which also revealed an increased lowering of the average bed elevation during the ebb tide compared to the flood tide. Layer 1 presumably comprises bed material instantly transported as bedload as well as bed material intermittently settled from suspension. Focussing on the estimates of suspended material in the water column, it can be observed that more sediment is suspended during maximum ebb currents and that a part of this suspended material is already resettled towards and during low water (Fig. 4.18). This suggests that the deposition of suspended bed material causes the increasing thickness of layer 1 towards low water (Fig. 4.16). Hence, the observations favour the hypothesis that mainly bedload and smaller events of suspended sediment deposition form a layer of remobilized sediment with a thickness of $\sim 0.06 \text{ m} \pm 0.02 \text{ m}$. A significant increase in thickness of layer 1 seems to be associated with events of higher suspended sediment deposition. This hypothesis could be tested with, e.g., a quantification of suspended sediment, as well as with physical and numerical modelling.

Impact on the research of sediment remobilization processes Concerning field studies, the dynamic penetrometer results provide a high vertical resolution, and in doing so, make the observation of thin layering in the range of a few centimeters possible. Following the above mentioned hypothesis, the results may support the indication and estimation of the sediment transported as bedload from the sediment transported as suspended load. Following the trend of sediment strength variation in layer 1, further investigations of *in-situ* sediment strength corresponding to ongoing sediment remobilization may improve the understanding of the relationship between sediment strength and sediment remobilization.

Conclusions

In this study it was tested if dynamic penetrometers can provide complementary information about ongoing sediment remobilization, especially, in terms of geotechnical properties such as sediment strength. Furthermore, the dynamic penetrometer results were compared to well established methods for the investigation of sediment remobilization such as Multibeam Echo Sounder and Acoustic Doppler Current Profiling.

The following conclusions can be made:

1. Two layers of different sediment strength are displayed in the *Nimrod* profiles. The upper layer 1 represents looser sediment influenced by sediment remobilization, and layer 2 characterizes a stiffer and more stable substratum.
2. The increase in thickness of layer 1 is coherent with the general accretion of the bed towards low water as seen in the MBES readings. We ascribe this to the settling of suspended bed material with decelerating flow.
3. Differences in sediment strength and thickness of layer 1 can be detected comparing flood and ebb. The asymmetry of the tide is also reflected in the mean current velocity, bathymetry and estimate of suspended material in the water column.
4. This study shows that dynamic penetrometers are suitable to deliver complementary information in terms of a quantification of the deposited sediment in snapshots in time and space with a high vertical resolution.

Nonetheless, further field measurements as well as complementary numerical and physical modelling are necessary to address remaining uncertainties

and questions. For example, repetition of the field study would allow one to test if the results represent a general behavior or are mainly influenced by other factors such as weather conditions. Such regular surveys are carried out using MBES and ADCP, but have not yet been done with the dynamic penetrometer. In addition, the relationship between sediment strength and ongoing sediment remobilization could be investigated in more detail in controlled flume experiments. Finally, the change of particle density and packing during erosion and accumulation and the correlation to the *in-situ* sediment strength could be analyzed using a numerical model based on geotechnical and sediment dynamical theories. In particular, although the latter is a highly complex project, it would greatly improve the geotechnical perspective on sediment remobilization processes, and the study presented herein would deliver a suitable base for such a numerical model.

Acknowledgements

We acknowledge the German Research Association (via MARUM, Center of Excellence at the University of Bremen, and GLOMAR, Bremen International Graduate School for Marine Sciences) for funding this study. We thank the crew of R/V Senckenberg for support. We are particularly indebted to Matthias Lange (MARUM) and Matthias Colsmann (AVISARO, Hannover).

References

- Anthony, D., Leth, J.O., (2002). Large-scale bedforms, sediment distribution and sand mobility in the eastern North Sea off the Danish west coast. *Marine Geology* 182, pp. 247 - 263.
- Ashley, G., (1990). Classification of large-scale subaqueous bedforms: a new look at an old problem. *Journal of Sedimentary Petrology* 60, pp. 160 - 172.
- Aubeny, C.P., Shi, H., (2006). Interpretation of impact penetrometer measurements in soft clay. *J Geotech Geoenviron Eng* 132(6), p. 770 - 777.
- Bartholdy, J., Pejrup, M., (1994). Holocene evolution of the Danish Wadden Sea. *Senckenbergiana Maritima* 24, pp. 187 - 209.
- Bartholdy, J., Flemming, B.W., Ernstsen, V.B., Winter, C., Bartolomä, A., (2010). Hydraulic roughness over simple subaqueous dunes. *Geo-Mar Let* 30(1), pp. 63 -

76.

Bartolomä, A., Ernstsens, V.B., Fleming, B.W., Bartholdy, J., (2004). Bedform dynamics and net sediment transport paths over a flood-ebb tidal cycle in the Gradyb channel (Denmark), determined by high-resolution multi-beam echosounding. *Geografisk Tidsskrift, Danish Journal of Geography* 104(1), pp. 45 - 55.

Blomqvist, S., (1991). Quantative sampling of soft-bottom sediments: problems and solutions. *Mar Ecol Prog Ser* 72, pp. 295-304.

Cai, G., Liu, S., Tong, L., Du, G., (2009). Assessment of direct CPT and CPTU methods for predicting the ultimate bearing capacity of single piles. *Engineering Geology* 104, pp. 211 - 222.

Cassidy, M., Houlsby, G.T., (2002). Vertical bearing capacity factors for conical footings on sand. *Géotechnique* 52(9), pp. 687 - 692.

Coco, G., Murray, A.B., Green, M.O., (2007). Sorted bed forms as self-organized patterns: 1. Model development. *J Geophys Res* 112 DOI:10.1029/2006JF000665.

Coco, G., Murray, A.B., Green, M.O., Thieler, E.R., Hume, T.M., (2007). Sorted bed forms as self- organized patterns: 2. Complex forcing scenarios. *J Geophys Res* 112 DOI: 10.1029/2006JF000666.

Das, B.M., (1990). *Principles of Geotechnical Engineering*. PWS-Kent Publishing Company, Boston.

Dayal, U., Allen, J.H., (1975). The effect of penetration rate on the strength of remolded clay and sand samples. *Can Geotech J* 12, pp. 336 - 348.

Dill, R.F., Moore, D.G., (1965). A diver-held vane-shear apparatus. *Marine Geology* 3, pp. 323 - 327.

Emerson, C.W. (1991). A method for the measurement of bedload sediment transport and passive faunal transport on intertidal sandflats. *Estuaries* 14(4), pp. 361 - 371.

Ernstsens, V.B., Noormets, R., Hebbeln, D., Bartholomä, A., Flemming, B.W., (2006). Precision of high-resolution multibeam echo sounding coupled with high-accuracy positioning in a shallow water coastal environment. *Geo-Mar Lett* 26, pp. 141 - 149.

Ernstsen, V.B., Noormets, R., Hebbeln, D., Winter, C., Bartholomä, A., Flemming, B.W., Bartholdy, J., (2006). Quantification of dune dynamics during a tidal cycle in an inlet channel of Danish Wadden Sea. *Geo-Mar Lett* 26(3), pp. 151 - 163.

Gaeuman, D., Jacobson, R.B., (2006). Acoustic bed velocity and bed load dynamics in a large sand bed river. *J Geophys Res* 111: DOI: 10.1029/2005JF000411.

Kostaschuk, R., Best, J., (2005). Response of sand dunes to variations in tidal flow: Fraser Estuary, Canada. *J Geophys Res* 110: DOI: 10.1029/2004JF000176.

Louge, M.Y., Valance, A., Ould el-Moctar, Dupont, P., (2010). Packing variations on a ripple of nearly monodisperse dry sand. *J Geophys Res* 115: DOI: 10.1029/2009JF001384.

Lundbak, A., (1947). *Det sydvestjyske vadehavs hydrografi*. Department of Geology, Aarhus.

Lunne, T., Powell, J.J.M., Robertson, P.K., (1997). *Cone Penetration Testing in Geotechnical Practice*. Spon Press, London, ISBN: 04192375X.

Meyerhof, G.G., (1953). The bearing capacity of foundations under eccentric and inclined loads. *Proc 3rd Int Conf on Soil Mechanics and Foundation Engineering* 1, pp. 16 - 26.

Rubin, D.M., McCulloch, D.S., (1980). Single and superimposed bedforms: a synthesis of San Francisco Bay and flume observations. *Sed Geol* 26, pp. 207 - 231.

Siegle, E., Huntley, D.A., Davidson, M.A., (2004). Physical controls on the dynamics of inlet sandbar systems. *Ocean Dynamics* 54, pp. 360 - 373.

Stark, N., Wever, T., (2008). Unraveling subtle details of expendable bottom penetrometer (XBP) deceleration profiles. *Geo-Mar Lett*, DOI: 10.1007/s00367-008-0119-1.

Stark, N., Hanff, H., Kopf, A., (2009). Nimrod: a tool for rapid geotechnical characterization of surface sediments. *Sea Technology*, April 2009, pp. 10 - 14.

Stark, N., Hanff, H., Stegmann, S., Wilkens, R., Kopf, A., (2009). Geotechnical investigations of sandy seafloors using dynamic penetrometers. *MTS/IEEE Oceans 2009*, Biloxi, USA.

Stegmann, S., Villinger, H., Kopf, A., (2006). Design of a modular, marine free-fall cone penetrometer. *Sea Technology* 47(2), pp. 27 - 33.

Stegmann, S., Moerz, T., Kopf, A., (2006). Initial results of a new free fall-cone penetrometer (FF-CPT) for geotechnical in-situ characterisation of soft marine sediments. *Norwegian J Geol* 86, pp. 199 - 208.

Stoll, R.D., Akal, T., (1999). XBP-tool for rapid assessment of seabed sediment properties. *Sea Technology* 40(2), pp. 47 - 51.

Stoll, R.D., Sun, Y.F., Bitte, I., (2004). Measuring sea bed properties using static and dynamic penetrometers, Lamont-Doherty Earth Observatory of Columbia University, NY, USA.

Stoll, R.D., Sun, Y.F., Bitte, I., (2007). Seafloor properties from penetrometer tests. *IEEE J Oceanic Eng* 32(1).

Svenson, C., Ernsten, V.B., Winter, C., Bartholomä, A., Hebbeln, D., (2009). Tide-driven sediment variations on a large compound dune in the Jade tidal inlet channel, Southeastern North Sea. *J of Coastal Res* 56, pp. 361 - 365.

Terzaghi, K., (1943). *Theoretical soil mechanics*. John Wiley and Sons, New York.

Venditti, J.G., Church, M., (2005). Morphodynamics of small-scale superimposed sand waves over migrating dune bed forms. *Water Resources Res* 41: DOI: 10.1029/2004WR003461.

Wever, T.F., Voss, H., Lühder, R., (2008). High-resolution observation of small-scale variability in a bedform field. *Marine and River Dune Dynamics* 1-3 April 2008, Leeds, UK.

Wienberg, C., Hebbeln, D., (2005). Impact of dumped sediments on subaqueous dunes, outer Weser Estuary, German Bight, southeastern North Sea. *Geo-Mar Lett* 25, pp. 45 - 53.

Winter, C., Chiou, M.D., Riethmüller, R., Ernsten, V.B., Hebbeln, D., Flemming, B.W., (2006). The concept of „representative tides“ in morphodynamic numerical modelling. *Geo-Mar Lett* 26, pp. 125 - 132.

Zeiler, M., Schulz-Ohlberg, J., Figge, K., (2000). Mobile sand deposits and shoreface sediment dynamics in the inner German Bight (North Sea). *Marine Geology* 170, pp. 363 - 380.

4.3 Sorted bedforms

In the above mentioned manuscript and survey an investigation of sediment remobilization with time was possible. Unfortunately, the spatial precision was insufficient for a detailed examination with space. However, such a study was possible in the framework of a survey with support by scuba divers on sorted bedforms close to Tairua Beach in the Coromandel area, NZ. The results are summarized in the following manuscript.

4.3.1 Geological manuscript III

Stark, N., Coco, G., Bryan, K., Kopf, A.
Geotechnical overview of slowly evolving sorted
bedforms in the inner shelf.
Submitted to Journal of Sedimentary Research.

Abstract

In this study we successfully tested a dynamic penetrometer using divers' support at chosen positions along a sorted bedform (~ 100 m wide) on the continental shelf off the Coromandel Peninsula close to Tairua, North Island of New Zealand. Sediment samples were taken by the divers at the exact position of penetrometer impact. This procedure was carried out along a 20 m-long transect crossing the northern and southern transition from fine to coarse sand zone, respectively, and along a 10 m-long transect in the middle of the coarse sand zone hitting alternately crest and troughs of the large wave-generated ripples within the sorted bedform. We found grain sizes > 0.25 mm in the fine sand domains and > 0.5 mm in the coarse sand domains. Towards the northern transition of the coarse grain domain, the dominant grain size was > 1 mm. This makes the grain size transition along the northern transition, which is in shallower water, sharper. These patterns corresponded well to the different patterns in sediment strength and layering measured by the dynamic penetrometer. The monitored sediment strength in the fine sand domain showed a deceleration of ~ 100 g and a quasi-static

bearing capacity equivalent to ~ 85 kPa, whereas in the coarse sand domains the dominant deceleration is ~ 60 g and the corresponding quasi-static bearing capacity ranges around ~ 40 kPa. A looser uppermost layer of lower bulk density was found at some positions and ranged in thickness from 2 – 6 cm. The results of sediment strength and layering suggest that the northern transition is an area dominated by sediment erosion, whereas sediment may be accumulated in the area of the southern transition. In general, no significant sediment remobilization occurred during the survey period (calm weather conditions). Overall, our data reveal a correlation between *in-situ* dynamic penetrometer sediment strength and grain size differences of the respective sands. Despite the large presence of shells in the coarse domains, our results indicate that the influence of shell hash on measured sediment strength is marginal.

Introduction

Studying sediment properties in the inner continental shelf has recently sparked an increasing interest because of their explicit effect on the long-term evolution of the coastal zone and the implication on the use (e.g. tourism, hazards) and conservation (e.g. sustainability) of the coastline. Understanding of the processes that shape the inner shelf requires knowledge of hydrodynamics as well as sediment dynamics (Soulsby, 1997) and how the feedback between these two processes is mediated by morphological evolution (Coco and Murray, 2007). In recent years a number of field studies have provided novel insights on the roles of sediment remobilization in the development of morphological patterns such as subaqueous dunes (e.g., Ernstsens, 2005; Winter et al., 2006; Svenson et al., 2009), small-scale features (e.g., Wever et al., 2008) or sorted bedforms/rippled scour depressions (e.g., Cacchione et al., 1984; Thieler et al., 2001; Hume et al., 2003; Green et al., 2004; Murray and Thieler, 2004; Trembanis et al., 2004; Ferrini and Flood, 2005; Goff et al., 2005; Phillips et al., 2007). These observational studies have paved the way for numerical modeling of some of these morphological features whose evolution has been shown to be critically governed by the presence of mixed grain sizes (e.g. Murray and Thieler, 2004; Coco et al., 2007 a and b). Field studies include grain size measurements (e.g., Svenson et al., 2009), acoustic methods such as side scan sonar (e.g., Hume et al., 2003; Wever et al., 2008) or multibeam echosounder (e.g., Ferrini and Flood, 2005; Ernstsens, 2005), and suspension measurements (e.g., Green et al., 2004). More recently, dynamic penetrometers have been applied in

areas of sandy sediment remobilization to derive geotechnical properties *in-situ* and detect layering in the vertical profile of the uppermost sediment surface (Stark and Wever, 2008; Stark et al., 2009b). For example, along a subaqueous dune close to the Danish coast the dynamic penetrometer succeeded in displaying the changes of a layer of looser and remobilized sand during a tidal cycle using the dynamic penetrometer *Nimrod* (Stark et al., unpubl. data). This offered a quantification of sediment remobilization with an outstandingly high resolution (~ 0.01 m) with time, and additionally, it revealed a new perspective on the area of sediment remobilization provided by the geotechnical properties such as sediment strength. The latter might improve the understanding of sediment remobilization processes.

However, dynamic penetrometers are mostly deployed from the sea surface providing a maximum spatial resolution of 3–5 m depending on, e.g., water depth, currents and stability of the vessel (Stark et al., 2009a/b). Investigations of small-scale features such as ripples or sharp transitions in grain size are hampered by the deploying technique. In this study we addressed this issue by using diver support. The divers deployed the dynamic penetrometer with a very a high precision of a few centimeters and took sediment samples at the impact positions. This study aimed (1) to test the performance of a dynamic penetrometer for the investigation of small-scale sediment remobilization features, and (2) to use the penetrometer results to understand the processes of remobilization around the transition and depression zones surrounding a sorted bedform. These observations and the corresponding sediment samples provide key measurements supporting the theory of “self-organization” to explain the formation, evolution and maintenance of these features (Murray and Thieler, 2004; Coco and Murray, 2007) by revealing areas of sediment erosion as well as areas of sediment accumulation considering coarse and fine sand, respectively.

Regional context

On the continental shelf off the Coromandel Peninsula close to Tairua beach, North Island of New Zealand, Hume et al. (2003) observed various features of sediment remobilization and among them, offshore shore-parallel sorted bedforms in water depths of ~ 20 m. Several mechanisms have attempted to address the formation of such features: rip currents during storms (Reimnitz, 1976), waves and currents in the vicinity of bathymetric irregularities (Cacchione et al., 1984), wave driven currents (Karl, 1980), or “self-organization” processes driven by feedbacks between seabed composition and hydrodynamics (Murray and Thieler, 2004; Coco et al., 2007a). The sorted bedforms

observed at Tairua were characterized by depression areas with a depth of 0.4–0.5 m compared to the surrounding areas, with the depressions containing coarse sand with a mean grain size ranging from 0.6–2 mm. The depression areas were also marked by the presence of large symmetrical wave orbital ripples. In contrast, the surrounding areas were covered by fine sands with a mean grain size of 0.07–0.12 mm and small symmetrical wave ripples. The large ripples inside the sorted bedforms were poorly sorted and had a height of 15–30 cm and a wave length of 70–100 cm. The transition locations were described as stable during the survey length (37 days) although this period included two storm events (Hume et al., 2003). Furthermore, the transitions between depressions and higher areas were described as sharp to diffuse. Green et al. (2004) investigated the amount of sediment which went into suspension over these features. They indicated that the sediment suspension changed through time with changes of waves, differences in substrate and depth, but that under moderate conditions no coarse sand was entrained into suspension. Moreover they demonstrated that suspended fine sand could settle down in the depressions, but tended to settle primarily on fine sand areas. Furthermore, there was no obvious interaction between fine and coarse sand suspension (Green et al., 2004). This is also supported by numerical modeling results by Murray and Thieler (2004).

Green et al. (2004) generally described the study area, as experiencing semidiurnal tides with a spring range of ~ 1.5 m and weak tidal currents (< 10 cm/s at 1 m above the seabed), and westerly to southwesterly winds (lee shore) (Green et al., 2004). The significant wave height is 0.9 m (Gorman et al., 2003), and the offshore profile at Tairua is convex between depths of 8 and 25 m (Green et al., 2004).

Methods

To achieve a high spatial resolution of the small-scale features and sorted bedform transition, as well as to investigate the dependence of sediment strength to grain size, it was essential (i) to deploy the dynamic penetrometer, and (ii) to take sediment samples at the exact same position (particularly with respect to the sorted bedform depression where large wave-generated ripples are present and the associated troughs/crests can be characterized by different sediment properties). To achieve this aim, divers dropped the dynamic penetrometer from ~ 2.5 m above seafloor precisely in the required positions and collected sediment samples at the impact spots (Fig. 4.19). This method was repeated at ten positions along a 20 m long transect crossing the south transition of the sorted bedform (Fig. 4.20, see A) (from fine to coarse



Figure 4.19: Diver during survey 2009 at the transition from fine sand domains (left) to coarse sand domain (right).

sediment in 2 m steps), at ten positions along a 20 m long transect crossing the north transition (Fig. 4.20, see C) (from coarse to fine sediment in 2 m steps) and on 20 positions along a 10 m long transect in the middle of the coarse sediment characterized by ripples, sampling alternately on crests and troughs with a spacing of approximately 0.5 m (Fig. 4.20, see B). Along the latter transect, sediment samples were only taken at the first 10 positions.

Dynamic penetrometer The survey demanded easy handling and precise free-fall performance from the dynamic penetrometer. Furthermore, suitability for the use on sand (hard seafloors) was required. Because of the above, we used the device *Nimrod*, recently developed at MARUM, University of Bremen, (Fig. 4.21). One of its designing targets was an easy deployment technique (Stark et al., 2009a) and it has already proven its suitability for sandy seafloors in previous studies (Stark et al., 2009b, Stark et al., *subm.*). Furthermore, it has been recently shown that the device is capable of displaying layers of density differences in areas of sediment remobilization (Stark et al., *in prep.*).

The divers lifted the device (~ 9 kg in water) up (~ 2.5 m from the seafloor), held it in an approximately vertical direction with tip aiming to the seafloor and let it fall freely. *Nimrod's* fins and the tip-concentrated center of mass led to a sufficient free-fall performance and acceleration despite the short fall. The device impacted into the sediment and measured acceleration/deceleration during fall and impact (Stark et al., 2009a). To increase

the sensitivity to sediment strength, a hemispheric tip geometry (Fig. 4.21) was chosen, which imposes a higher resistance on the sediment, instead of the conical tip usually used on sandy seafloors (Stark et al., 2009b). The high recording frequency makes it possible to achieve a vertical profile with a resolution of less than 1 cm (Stark et al., 2009a/b) and to detect and quantify even thin layers (1-5 cm thickness) (Stark et al., *subm.*).

During the data processing, the deceleration of dynamic penetrometers is commonly used to deliver impact velocity and penetration depth by single, and respectively, double integration (e.g., Stoll and Akal, 1999; Stegmann et al., 2006; Stark et al., 2009a). The deceleration reflects the sediment strength (Stoll and Akal, 1999; Stoll et al., 2004; Stark and Wever, 2008). However, the size and the geometry of the device influence the deceleration - depth profiles significantly (Terzaghi, 1943; Meyerhof, 1953; Das, 1990) as well as the impact velocity (Stoll et al., 2007). To account for the artifacts of the device's geometry and the influences of impact velocity on the sediment strength - penetration depth profiles, an approach to derive a range of quasi-static bearing capacity was applied. We calculate dynamic sediment resistance force F_{sr} from the measured deceleration dec (Aubeny and Shi, 2006):

$$m_{Nim}dec = F_{sr}, \quad (4.14)$$

with m_{Nim} being the weight of *Nimrod* in water. Inertial forces are neglected here (Aubeny and Shi, 2006). The buoyancy of the probe in sand is neglected here because of the small penetration depths of a few centimeters. The bearing capacity is the maximum load the sediment can bear before failure (e.g., Terzaghi, 1943; Das, 1990) and corresponds to the maximum force the sediment can resist before breaking and letting the penetrometer penetrate further. This can be expressed as:

$$q_u = \frac{F_{sr}}{A}, \quad (4.15)$$

where A is the area of the plane subjected to load, which changes within the first 10 cm of penetration due to the hemispherical tip. Stoll et al. (2004, 2007) as well as Aubeny and Shi (2006) showed the influence of changing impact and penetration velocity on the sediment strength. Stoll et al. (2007) found that the empirical approach by Dayal and Allen (1975) works well to derive a quasi-static sediment strength for a chosen constant penetration velocity. It uses the strain rate factor f_{ac} , which depends on the actual penetration velocity v and a reference velocity v_0 :

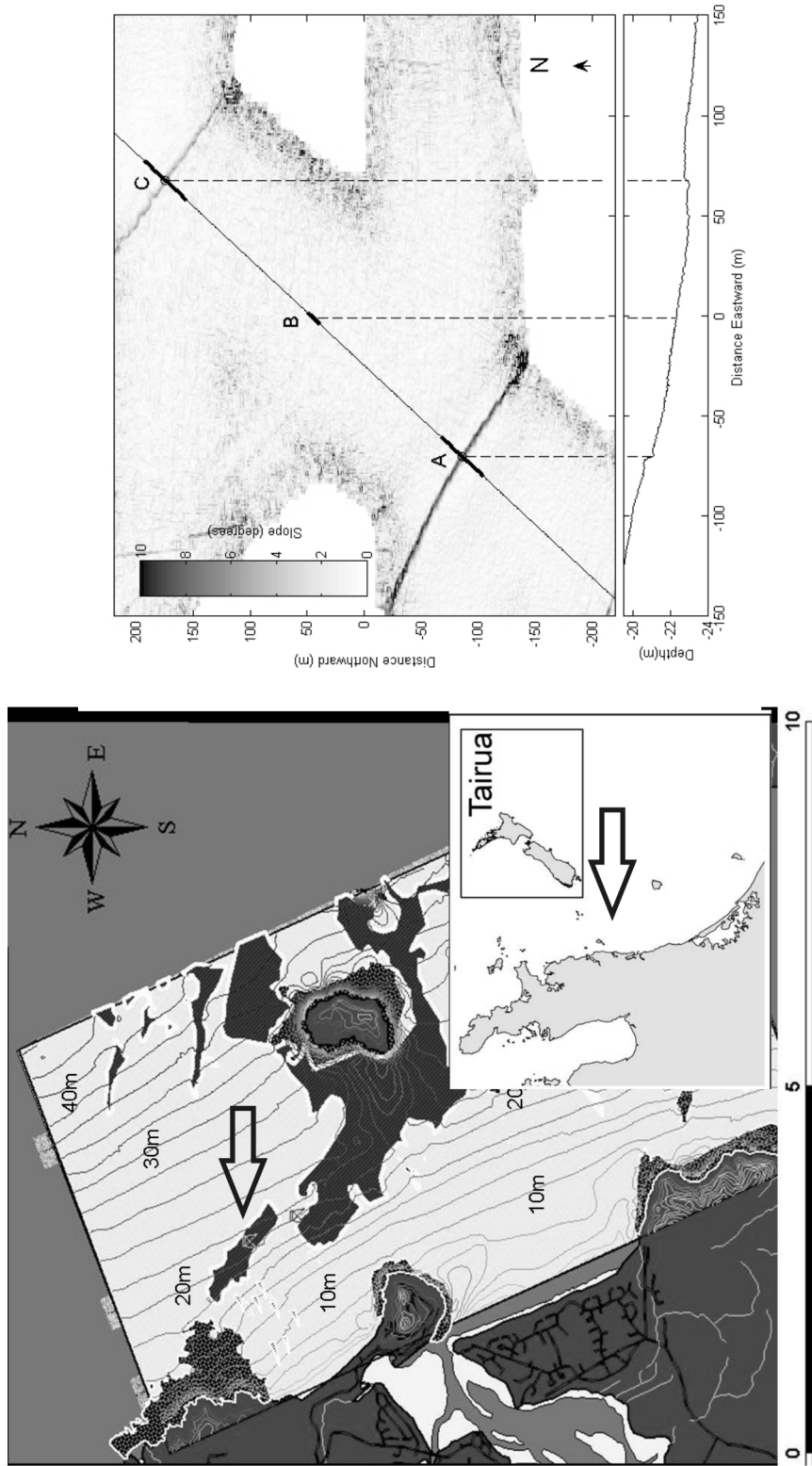


Figure 4.20: Left: Overview map of the study area (box) and grey scaled side scan sonar picture showing significant grain size differences. The arrow indicates the investigated sorted bedform. Right: Multibeam echosound image of the survey area showing the measurement transects: A) crossing the more southern transition which is bathymetrically sharper, B) middle transect within the coarse sand domain, C) crossing the northern transition.

$$f_{ac} = 1 + K \log \left(\frac{v}{v_0} \right), \quad (4.16)$$

with K being a dimensionless factor ranging from 1.0 to 1.5. We will display the whole range adding error bars to the results.

To convert the sediment resistance force from high-speed dynamic deployments to quasi-static (= constant rate) values, the dynamic sediment resistance force F_{sr} and accordingly the dynamic bearing capacity q_{udyn} should be divided by f_{ac} :

$$q_{uqs} = \frac{q_{udyn}}{f_{ac}}. \quad (4.17)$$

The reference velocity v_0 used here equals 0.02 m/s, which is the standard for quasi-static penetration tests (Lunne et al., 1997; Cai et al., 2009).

Sediment samples The sediment samples were taken from the seafloor surface by the divers (by hand). They were disturbed and do not provide information about subsurface layers. The grain size of all samples was determined by dry sieving (mesh sizes: 4 mm, 2 mm, 1 mm, 0.5 mm, 0.25 mm). We focused on the differentiation of coarse to fine sand and desisted from measuring finer grain size distributions than 0.25 mm. The amount of shell hash was determined for grain sizes > 1 mm and for grain sizes ranging from 0.25 mm to 1 mm by dissolving of the shell particles using hydrochloric acid.

Results

Dynamic penetrometer At 32 of the measured 40 positions *Nimrod* delivered interpretable results (Tab. 4.6). At two positions of the transition transects (transitions position No.1 and 14 in Tab. 4.6) the results were disturbed by a data acquisition error of the device, and at 6 other positions (transitions position No. 3, 6, 9, 10, 20; middle transect pos. No. 9 in Tab. 4.6) the impact velocity was very small (0.3–0.7 m/s), which can lead to a deviation of the sediment strength and has as consequence a small penetration depth (~ 1 cm). The impact velocity ranged between 3 and 9 m/s (± 1 m/s) and the penetration depth from 3 to 13 cm (± 1 cm) which implies that the penetration depth into the fine sand reached just up to 6 cm. Penetration depths ≥ 10 cm were only found in the coarse sand areas precisely on crests/troughs of the wave-generated ripples present in the inner part of the sorted bedform depression. The deepest penetration depth was found in the

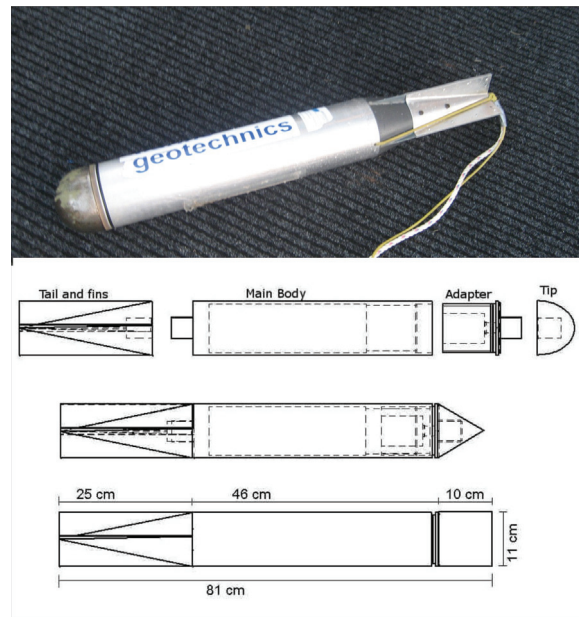


Figure 4.21: *Nimrod* in picture and sketches. In this study the hemispherical tip was used to get on the one hand a sufficient penetration depth, but on the other hand a high sensitivity regarding sediment strength changes with depth.

trough at middle transect position No. 10 (Tab. 4.6).

The decelerations on fine sand were ranging from 68 to 124 g (± 1 g) with generally higher values at the northern transition transect (93–214 g) (Tab. 4.6, Fig. 4.22). On coarse sand, we found deceleration values from 37–66 g (± 1 g) along the transition transects (Tab. 4.6, Fig. 4.22), and from 60 g to 106 g (± 1 g) along the first half of the middle transect tending toward harder to the end of the middle transect with up to 210 g (Tab. 4.6, Fig. 4.22).

The quasi-static bearing capacities show similar tendencies to the penetration surface and velocity. We found quasi-static bearing capacities ranging from 56–109 kPa (± 18 kPa) on fine sand with higher values of 72–109 kPa in the northern transition transect (Tab. 4.6, Fig. 4.22). On coarse sand, the quasi-static bearing capacity ranged from 25 to 46 kPa (± 10 kPa) (Fig. 4.22). In the first half of the middle transect on coarse sand the quasi-static bearing capacity was ranging between 38–55 kPa (± 10 kPa) (Fig. 4.22) and increased up to 141 kPa at the end of the transect (Tab. 4.6). Varying error ranges of the quasi-static bearing capacity follow the influence of the dimensionless factor K .

In the vertical profiles, a thin surface layer (2–3 cm) can be observed at some locations along the transition transects (transition position no. 2 and 4 on

No.	Site	Meters along transect	Sediment, sediment bag no.	Penetration depth (m)	Impact velocity (m/s)	Deceleration (g)	Qs. BC (kPa)	Thickness of overlying layer (m)
transitions								
1	south	0	fine (1)	disturbed				
2	south	2	fine (2)	0.06	5	85	56	0.03
3	south	4	fine (3)	0.01	0.4	2.8	37	0
4	south	6	fine (4)	0.04	4	68	60	0.02
5	south	8	fine (5)	0.02	5	120	195	0
6	south	12	coarse (6)	0.01	0.5	3	26	0
7	south	14	coarse (7)	0.04	5.5	57	37	0
8	south	16	coarse (8)	0.06	5	48	33	0.02
9	south	18	coarse (9)	0.01	0.5	3	20	0
10	south	20	coarse (10)	0.01	0.3	1.5	17	0
11	north	0	fine (5)	0.04	6	100	95	0
12	north	2	fine (1)	0.05	6	93	72	0
13	north	4	fine (2)	0.03	5	124	109	0
14	north	6	fine (3)	disturbed				
15	north	8	fine (4)	0.04	6	105	101	0
16	north	12	coarse (6)	0.07	7	37	25	0
17	north	14	coarse (7)	0.07	5	66	46	0.03
18	north	16	coarse (8)	0.08	6	55	35	0.02
19	north	18	coarse (9)	0.08	3	46	43	0.02
20	north	20	coarse (10)	0.01	0.72	4.2	20	0

fine sand along the southern transition transect, transition position no. 8 on coarse sand along the southern transition transect, transition position no. 17-19 on coarse sand along the northern transition transect) (Fig. 4.22) and at all of the crest/trough measurements on coarse sand (middle transect) with a thickness of up to $6\text{ cm} \pm 1\text{ cm}$ (Tab. 4.6, Fig. 4.22) and a decrease of thickness with increase in sediment strength.

Grain size The grain size analysis indicated that along the transect crossing the southern transition the dominant grain size of the fine sediment domain (transitions position no. 2-5) is $< 0.25\text{ mm}$, whereas it is $> 0.5\text{ mm}$ on the coarse sediment domain (transition position no. 6-10). Along the transect crossing the northern transition this difference is even more obvious, because the dominant grain size on the fine domain (transition pos. no. 11-15) is again $< 0.25\text{ mm}$, but on the coarse side (transition pos. no. 16-20) it is even coarser with a dominant grain size $> 1\text{ mm}$. In the middle transect, corresponding to the sorted bedform depression, characterized by coarse sediment, the dominant grain size is mainly $> 1\text{ mm}$. The difference between the two transition zones is also evident in the detailed grain size distributions (Fig. 4.23) where a large gap between fine and coarse sands characterizes the northern transition, whereas the southern transition does not show such an obvious gap. Along the middle transect all sediment samples show similar grain size distributions, and the only difference between crests and troughs is that the mean grain size observed at troughs is slightly coarser than at crests (Fig. 4.23).

Shell content The amount of shell in the sediment samples was generally high, especially in the coarse sand zones. In the middle transect within the coarse sand zone the shell content ranged from 36-70% with only 7-14% shell fractures $> 1\text{ mm}$ (Fig. 4.24). In the northern transect the amount of shell hash $< 1\text{ mm}$ generally ranged between 8-19%, whereas the whole shell content strongly increased along the transect from 12% in the fine sand zone and up to 100% in the coarse sand zone (Fig. 4.24). At the southern transition there was a more abrupt change in shell content. In the fine sand zone the shell fractions $> 1\text{ mm}$ and $< 1\text{ mm}$ are approximately similar with 25-30%, whereas in the coarse sand zone the shell fractions $< 1\text{ mm}$ decreases to 12-15% and the shell fractions $> 1\text{ mm}$ increases to 64-72%. However, the total shell content stayed approximately constant in this region, ranging from 52-100% in the fine sand zone and from 76-87% in the

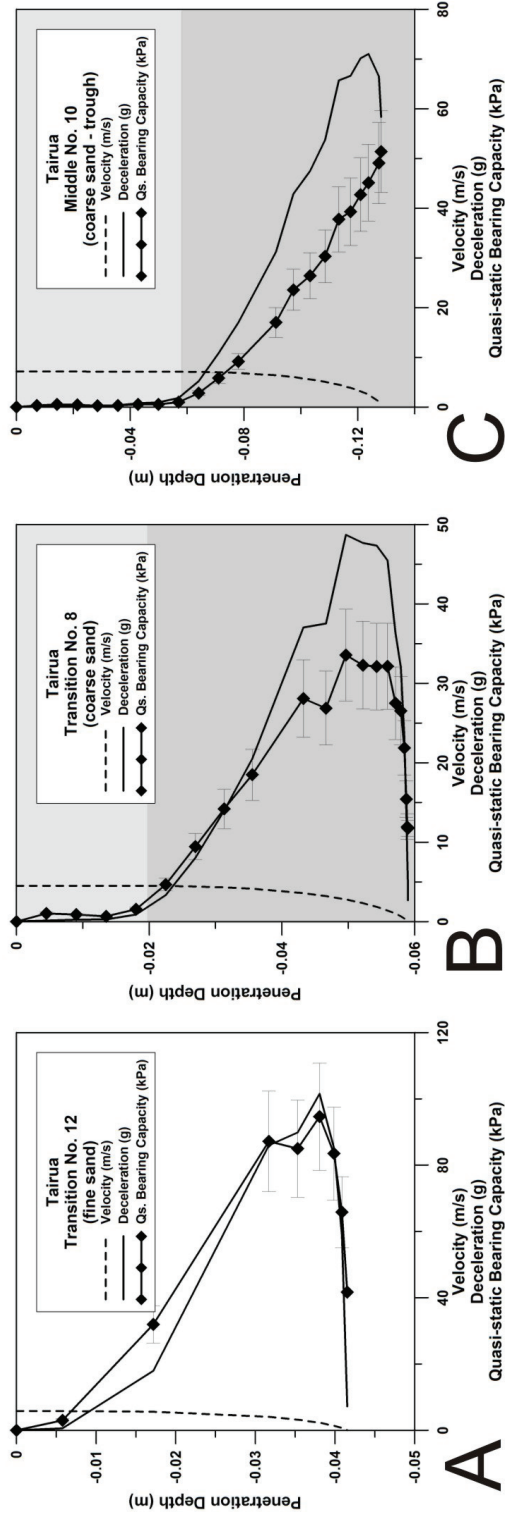


Figure 4.22: *Nimrod* results presenting the measured deceleration in g (solid line), the penetration velocity in m/s (dashed line) and the calculated quasi-static bearing capacity equivalent in kPa for a quasi-static penetration with $0.02 m/s$ (solid line with rhombs) versus penetration depth in m . A) displays a result from the fine sand domain without significant changes in gradient (layering). B) and C) show two examples from coarse sand domains (B) close to a transition, C) in the middle transect). A thin uppermost softer layer can be detected here.

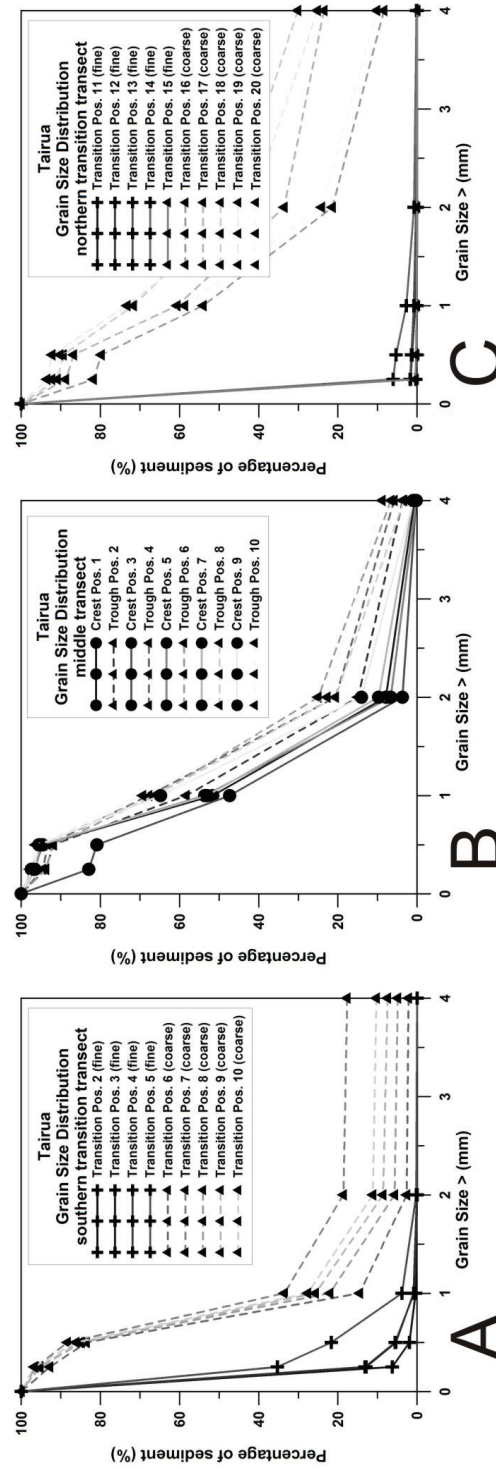


Figure 4.23: Grain size distributions from the transect crossing the southern transition (A), the middle transect (B) and the transect crossing the northern transition (C). The grain size in the middle transect (B) is approximately homogenous with a slight tendency to coarser particles in the troughs. Comparing the northern transect (C) to the southern transect (A), a significantly sharper grain size difference can be detected at the northern transect.

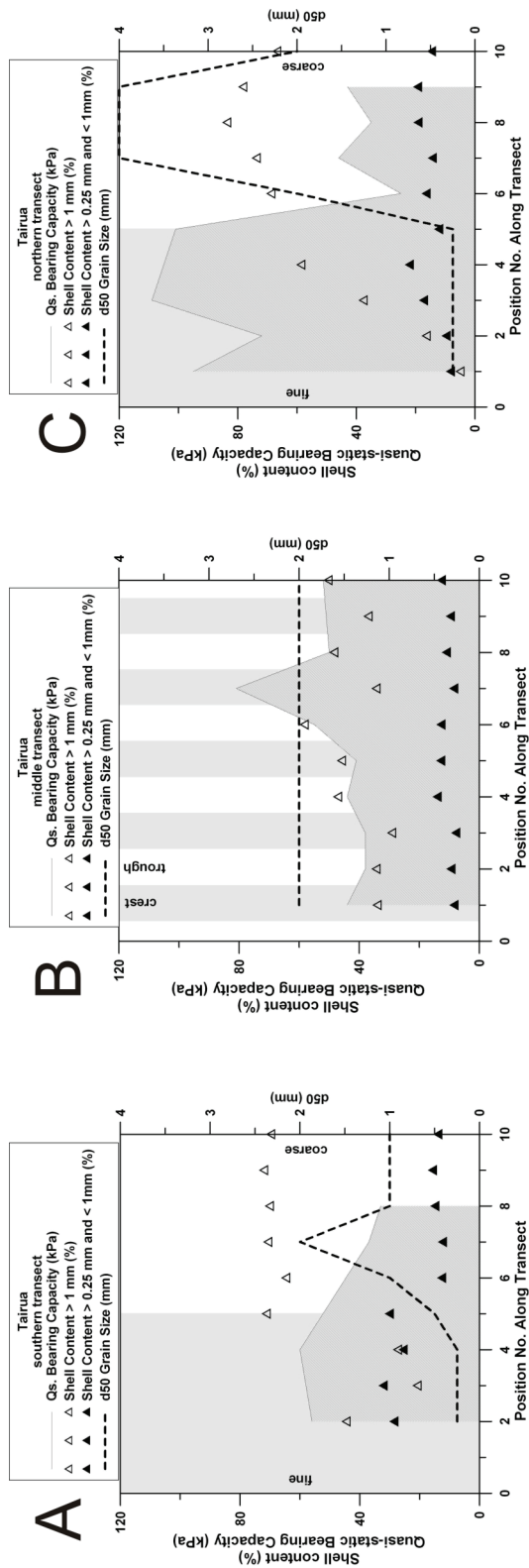


Figure 4.24: d_{50} grain size in mm , quasi-static bearing capacity equivalent in kPa and shell content in % plotted along the transects. At the transitions (A, C) fine sand corresponds to higher sediment strength. Shell content does not seem to have a significant influence. In the middle transect, d_{50} grain size, shell content and sediment strength do not show a dependence to the position along the large ripple features (crest/trough).

coarse sand zone (Fig. 4.24).

Discussion

Instrument performance Diver deployments were performed from a height of ~ 2.5 m above seafloor. From that height the instrument had not reached its terminal free-fall velocity and, as a result, the impact velocity changed considerably at some locations. In 8 out of 40 cases the impact velocity was too low for an interpretation of the results and these measurements had to be discarded. In most of the cases, the approach by Dayal and Allen (1975) to derive a quasi-static penetration velocity delivered comparable results so that the technique can be considered reliable and adopted.

Grain size vs. sediment strength The grain size of sediments influences the sediment strength and bearing capacity (e.g., Trask, 1959), and it has been shown that differences such as mud/sand are reflected in dynamic penetrometer results (e.g., Stoll and Akal, 1999; Stoll et al., 2007; Stark and Wever, 2008). Furthermore, a denser packing of finer particles leads to a higher density, in turn leading to a higher sediment resistance against a dynamic penetrometer (e.g., Al-Refeai and Al-Suhaibani, 1997; Mohammadi et al., 2008). Following that, grain size differences between fine and medium-coarse sands can be retrieved from the dynamic penetrometer results. However, it is difficult to obtain sediment samples from precisely the same spots of dynamic penetrometer impacts during offshore *in-situ* surveys, where the penetrometer is dropped from the sea surface. In this study diver support offered a precise positioning of the dynamic penetrometer and the sediment sampling so that an exact grain size vs. dynamic penetrometer comparison was possible. The spatial variability in sediment properties associated with the sorted bedform provided a variety of cases for comparison. Figure 4.25 shows the d50- and d90-grain size, the typical measures to assess bed roughness and/or sediment transport, plotted against the quasi-static bearing capacity derived by *Nimrod*. The quasi-static bearing capacity decreased significantly from fine sands (< 0.25 mm) to medium sands (0.5 mm). But the coarser the sand gets, the smaller the gradient of the decrease in sediment strength is (Fig. 4.25). This trend was evident along the two transects crossing the transitions (A and C in Fig. 4.20) as well as the middle transect (B in Fig. 4.20). The higher strength of fine sand found with *Nimrod* can be explained with the likelihood of denser packing of particles (e.g., Al-Refeai and Al-Suhaibani, 1997; Mohammadi et al., 2008) as well as its higher ef-

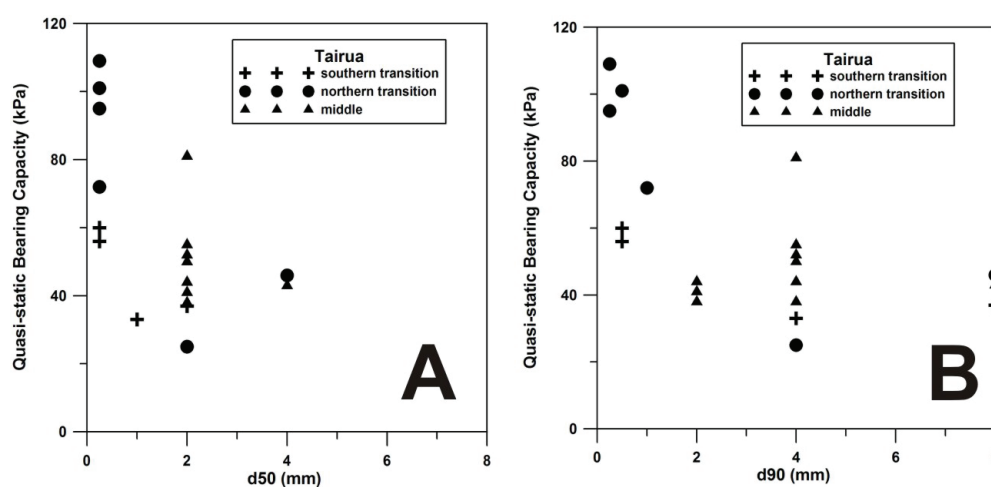


Figure 4.25: d_{50} (A) and d_{90} (B) grain size (in mm) vs. quasi-static bearing capacity in kPa . Finer particles lead to a higher sediment strength.

fective particle contact area. However, the settling history of the material has an effect, too, and leads to a difference in density. This affects especially areas of sediment accumulation and seems to cause the sediment strength differences of the fine sand zones of the southern transition compared to the fine sand zones in the northern transition. To understand the combined effects of grain size and sediment remobilization in detail, controlled laboratory tests and numerical modeling addressing geotechnical and sediment dynamical processes are required.

Another potential sediment weakening factor in the coarse sand zones appears to be the increased amount of coarser shell hash in the coarse sand zones. Stark and Wever (2008) showed that effects of shells can be displayed in dynamic penetrometer results, however, this is anticipated to be more profound if intact shell structure rather than shell hash is found. In case of shell hash, crushing of the particles seems to be likely and might weaken the sediment, but even in sediment failure zones containing shell hash mainly other reasons (e.g., oversteepening) caused sediment weakness and the slip surface cannot be found in the shell hash layers (e.g., Stanley et al., 1966). Comparing the amount of shell hash in our results to sediment strength (Fig. 4.24) does not lead to a clear correspondence such as the comparison between grain size and sediment strength (Fig. 4.24, Fig. 4.25). Even in the fine sand zone of the northern transition the increasing amount of coarse shell particles does not lead to a decrease in sediment strength (Fig. 4.24 C). Following this, the amount of shell hash in the sediment seems to have no significant influence on the sediment strength determined by the dynamic penetrometer.

Transition transects Hume et al. (2003) depicted the transitions of the sorted bedforms as sharp to diffuse and mapped a depth of 0.4–0.5 m. Furthermore, they presented mean grain sizes of 0.07–0.12 mm in the surrounding areas of fine sand and mean grain sizes of 0.6–2 mm in the depression. During the survey presented here, diver observations indicated that the bedform had not moved significantly. The stability of the bathymetry of sorted bedforms has already been described at different locations by other authors (e.g., Goff et al., 2005; Diesing et al., 2006).

The divers also described that the depth variation at the southern transition was sharper than at the northern transition (Fig. 4.20). Asymmetry of the sorted bedforms is well known from the literature (e.g., Goff et al., 2005, Gutierrez et al., 2005). However, the grain size distribution (Fig. 4.23) shows a more substantial difference between the coarse sand to the fine sand at the northern transition, which is the transition with the less steep slope. This is corroborated by the sediment strength results (Tab. 4.6), which illustrate a more significant difference in sediment strength at the northern transition. In particular, the fine sediment at the northern transition shows a high sediment strength (Tab. 4.6). Layering in the vertical strength profiles appears rarely in the transition transects, but it seems to be located primarily in the coarse sand areas of the northern transition and the fine sand areas of the southern transition (Tab. 4.6). In any case the observed surface layer was very thin with 2–3 cm thickness (Fig. 4.22). Overall, (i) the more steep transition appeared to be less strictly sorted than the more diffuse transition (Fig. 4.23 and Fig. 4.24), and (ii) sediment remobilization along the transition during the surveys (calm weather) appeared to be very low. The approximate stability of the feature (Hume et al., 2003) over 9 years agrees with the finding of a low sediment remobilization in the area. Green et al. (2004) investigated the sediment in suspension in this area. Under calm conditions, there was no coarse sand detected in suspension and fine sand was remobilized as “washload” (Green et al., 2004) in or close to the depression. They assumed that the fine sand deposition rate in the depression was small. Unfortunately, the measurements were carried out a few hundred meters away from the southern transition and at a different time, so that no direct comparison was possible. Other authors (e.g., Gutierrez et al., 2005) showed that significant sediment transport events on the sorted bedforms were limited to storm conditions and cannot be expected during calm weather.

A high sediment strength and no layering in the vertical sediment strength

profiles are an indication of a stable and well consolidated sediment surface and for the scenario that looser sediment is eroded easily in this area (Stark et al., 2009b). From our results, the fine sand area at the northern transition appeared not to be an area of sediment deposition, whereas the fine sand area at the southern transition showed some hints of sediment deposition (lower strength, layering, Tab. 4.19). On the coarse domains of the transitions, we found coarse sand and layering at the northern transition, but medium sands and no layering at the southern transition. Both might be hints that at the coarse site of the northern transition more sediment remobilization of finer to medium particles occurs than at the southern transition. These results are in line with detailed observations of sorted bedform profiles collected on the inner shelf off Wrightsville beach in North Carolina (USA) (Thieler et al., 2001; Murray and Thieler, 2004). Our observations also support the self-organization hypothesis put forward through numerical modeling (Murray and Thieler, 2004; Coco et al., 2007a). In this hypothesis Murray and Thieler (2004) suggest that the sorted bedforms develop as an instability driven by sediment composition. The theory is based on the idea that in locations showing a coarser sediment composition, wave-generated ripples tend to be larger than in areas of finer sediments. The large ripples enhance turbulence causing an entrainment and suspension of the finer sand. The suspended fine sand will then preferentially be advected by mean currents and more likely settle away from the coarse areas (Coco and Murray, 2007). With respect to the mechanism leading to sharp transitions in depth (southern boundary of the sorted bedform) and grain size (northern boundary) our results correspond with the detailed observations of suspension dynamics collected in the same area. Green et al. (2004) assumed in fact that exhumation of fine material during mobilization of coarse material is possible. This process might be concentrated at the northern transition, where no finer-grained material was found at the coarse side and some layering, although minimal, was detected. Following that, fine sand seemed to be more eroded at the northern transition, leaving behind a more homogenous pure coarse sand on the coarse side and a hard eroded surface at the fine sand side. This might also have caused the more smooth transition here due to the reworking. At the southern transition, less reworking in the coarse sand and a higher degree of sediment settling (layering at the fine side, Tab. 4.19; Green et al., 2004) might explain the preservation of this sharp transition. Further measurements such as those carried out by Green et al. (2004) aiming at the transitions, in particular, numerical modeling of the development and also of the maintenance of these sorted bedforms, and long-term observation with, for example, a stationary side-scan sonar system (e.g., Wever et al., 2008) would be helpful methods to confirm the above.

Central transect – coarse sand zone The features inside the depression were described by Hume et al. (2003) as poorly sorted and large symmetrical wave orbital ripples with a height of 15–30 cm and a length of 70–100 cm. This is confirmed by our results. The divers found the ripple length to be ~ 100 cm (Fig. 4.19). The samples showed marginal differences in the comparison of crests to troughs (Fig. 4.23 B). However, these are too small to affect the sediment strength results (Tab. 4.19, Fig. 4.24). Layering with a surface layer thickness ranging from 2–6 cm appears at 19 of the 20 positions. This suggests a more significant sediment mobilization in the middle of the feature than in the transition areas, where the transitions themselves might shield the sediment from the currents. Green et al. (2004) illustrated that no coarse sediment suspended during moderate conditions. Following that, the layering that we detected might be the consequence of exhumed fine material and remaining mobilized coarse material. Another possibility would be bedload transport of coarse material, however, after Gutierrez et al. (2005) this seems to be also unlikely under calm weather conditions. Also here, further measurements and long-term observations during different weather conditions would be helpful to confirm the conclusions.

It remains unclear why the sediment strength increases significantly after middle transect position 12. Unfortunately, no sediment samples were taken here. Hume et al. (2003), in line with other studies (Murray and Thieler, 2004) concluded that the coarse sand is not generally underlying the fine sands, but instead shows up in lenses underlain by fine sand with a thickness of approximately ripple height. The device reached a small penetration depth of 4–7 cm here. This makes it quite unlikely that the device penetrated the coarse surface layer completely, especially on the crests. An additional survey and collection of short sediment cores would be necessary to clarify this issue.

Conclusions

The following conclusions can be drawn regarding the results derived from sediment samples and dynamic penetrometer measurements using *Nimrod*:

1. Dynamic penetrometer results reflect differences in grain sizes of sands.
2. Shell hash in sands does not lead to significant sediment strength variations determined by dynamic penetrometers.

3. The northern transition of the investigated sorted bedforms is noticeably smoother than the southern transition slope.
4. The grain size distribution as well as the sediment strength display a more obvious difference between the coarse and the fine domains at the smoother northern transition.
5. In the transition areas of the sorted bedforms the sediment seems to be less mobilized than in the middle of the depression. However, the northern transition appears as an area of more sediment erosion, whereas more sediment seems to be settled in the area of the southern transition.
6. In the depression, neither grain size distribution nor sediment strength showed significant differences between crests and troughs and confirm the poor sorting of the sand described by Hume et al. (2003).

Further *in-situ* measurements with focus on the two different transitions and the inside of the depression as well as numerical modeling of the development and maintenance would be necessary to confirm the sediment mobilization ideas in this area coming out of this study. Controlled tests with dynamic penetrometers would be a helpful complement to get a more detailed correlation between dynamic penetrometer results and grain size distributions and the amount of shall hash in sand.

Nevertheless, this unique survey using a dynamic penetrometer with diver support made it possible to investigate geotechnical properties of a feature of sediment remobilization on sand with an outstanding position precision.

Acknowledgments

We acknowledge the German Research Association (via MARUM, Center of Excellence at the University of Bremen, and GLOMAR, Bremen International Graduate School for Marine Sciences), the German Academic Exchange Service and the National Institute of Water and Atmospheric Research in New Zealand (NIWA) (through a grant from the Foundation of Research, Science and Technology in New Zealand) for funding this study. We thank Rod Budd, Luca Chiaroni and Scott Edhouse for diving and Ron Ovedon for sediment analysis (all from NIWA). Furthermore, we thank Bryna K. Flaim, Alexandre Schimel, Dirk Immenga and Prof. Terry Healy (all Coastal Marine Group, University of Waikato) for general support during the research stay and for collecting the survey data presented in Figure 2.

We thank Matthias Lange, Hendrik Hanff (both MARUM, University of Bremen) and Matthias Colsmann (AVISARO, Hannover) for technical support with the dynamic penetrometer *Nimrod*.

References

- Al-Refeai, T., Al-Suhaibani, A., (1997). Prediction of CBR using dynamic cone penetrometer. *J King Saud Univ*, Vol. 9, Eng Sci (2), pp. 191 - 204.
- Aubeny, C.P., Shi, H., (2006). Interpretation of impact penetrometer measurements in soft clay. *J Geotech Geoenviron Eng* 132(6), pp. 770 - 777.
- Cacchione, D.A., Drake, D.E., Grant, W.D., Tate, G.B., (1984). Rippled scour depressions on the inner continental shelf off Central California. *J. Sedim. Petrol.*, 54(4), pp. 1280 - 1291.
- Cai G., Liu S., Tong L., Du G., (2009). Assessment of direct CPT and CPTU methods for predicting the ultimate bearing capacity of single piles. *Engineering Geology* 104, pp. 211 - 222.
- Coco, G., Murray, A.B., (2007). Patterns in the sand: from forcing templates to self-organization, *Geomorphology*, 91(3-4), pp. 271 - 290.
- Coco, G., Murray, A.B., Green, M.O., (2007). Sorted bedforms as self-organizing patterns. Part 1: model development, *Journal of Geophysical Research*, 112, F03015, doi:10.1029/2006JF000665.
- Coco, G., Murray, A.B., Green, M.O., Hume, T., Thieler, R., (2007). Sorted bedforms as self-organizing patterns. Part 2: complex forcing scenarios, *Journal of Geophysical Research*, 112, F03016, doi:10.1029/2006JF000666.
- Das, B.M., (1990). *Principles of Geotechnical Engineering*. PWS-Kent Publishing Company, Boston.
- Dayal, U., Allen, J.H., (1975). The effect of penetration rate on the strength of remolded clay and sand samples. *Can Geotech J* 12, pp. 336 - 348.
- Diesing, M., Kubicki, A., Winter, C., Schwarzer, K., (2006). Decadal scale stability of sorted bedforms, German Bight, southeastern North Sea. *Cont. Shelf Res.*, 26, pp. 902 - 916.

Ernstsen, V.B., (2005). Dune dynamics in a tidal inlet channel of the Danish Wadden Sea. Dissertation submitted to the Department of Geology at the University of Bremen.

Ferrini, V.L., Flood, R.D., (2005). A comparison of rippled scour depressions identified with multibeam sonar: Evidence of sediment transport in inner shelf environments. *Cont. Shelf Res.*, 25, pp. 1979 - 1995.

Goff, J.A., Mayer, L.A., Traykovski, P., Buynevich, I., Wilkens, R., Raymond, R., Glang, G., Evans, R.L., Olson, H., Jenkins, C., (2005). Detailed investigation of sorted bedforms, or "rippled scour depressions," within Martha's Vineyard Coastal Observatory, Massachusetts. *Cont. Shelf Res.*, 25, pp. 461 - 484.

Gorman, R.M., Bryan, K., Laing, A.K., (2003). A wave hindcast for the New Zealand region-nearshore validation, coastal wave climate. *New Zealand J. of Marine, Freshwater Res.*, 37(3), pp. 567 - 588.

Green, M.O., Vincent, C.E., Trembanis, A.C., (2004). Suspension of coarse and fine sand on a wave-dominated shoreface, with implications for the development of rippled scour depressions. *Cont. Shelf Res.*, 24, pp. 317 - 335.

Gutierrez, B.T., Voulgaris, G., Thieler, E.R., (2005). Exploring the persistence of sorted bedforms on the inner-shelf of Wrightsville Beach, North Carolina. *Cont. Shelf Res.*, 25, pp. 65 - 90.

Hume, T., Trembanis, A., Liefting, R., Stephens, S., (2003). Spatially variable, temporally stable, sedimentary fascies on an energetic inner shelf. *Coastal Sediment 2003*, ASCE, pp. 1 - 14.

Karl, H.A., (1980). Speculations on the processes responsible for mesoscale current lineations in the continental shelf, southern California. *Marine Geology*, 34, M9-M18.

Lunne, T., Powell, J.J.M., Robertson, P.K., (1997). *Cone Penetration Testing in Geotechnical Practice*. Spon Press, London, ISBN: 04192375X.

Meyerhof, G.G., (1953). The bearing capacity of foundations under eccentric and inclined loads. *Proc 3rd Int Conf on Soil Mechanics and Foundation Engineering* 1, pp. 16 - 26.

Mohammadi, S.D., Nikoudel, M.R., Rahimi, H., Khamehchiyan, M., (2008). Application of the dynamic cone penetrometer (DCP) for determination of the engineering parameters of sandy soils. *Eng Geol* 101, pp. 195 – 203.

Murray, A.B., Thiel, E.R., (2004). A new hypothesis and exploratory model for the formation of large-scale inner-shelf sediment sorting and "rippled scour depressions". *Cont. Shelf Res.*, 24, pp. 295 - 315.

Phillips, E.L., Storlazzi, C.D., Dartnell, P., Edwards, B.D., (2007). Exploring rippled scour depressions offshore Huntington Beach, CA. *Coastal Sediments 2007*, ASCE.

Reimnitz, E., Toimil, L.J., Shepard, F.P., Gutierrez-Estrada, M., (1976). Possible rip current origin for bottom ripple zones to 30-m depth. *Geology*, 4, pp. 395 - 400.

Soulsby, R., (1997). *Dynamics of marine sands: a manual for practical applications*. Thomas Telford Publications. London.

Stanley, D.J., Krinitzky, E.L., Compton, J.R., (1966). Mississippi River Bank Failure, Fort Jackson, Louisiana. *Bull. Geol. Soc. Am.*, 77(8), pp. 859 - 866.

Stark, N., Wever, T., (2008). Unraveling subtle details of expendable bottom penetrometer (XBP) deceleration profiles. *Geo-Mar Lett*, DOI: 10.1007/s00367-008-0119-1.

Stark, N., Hanff, H., Kopf, A., (2009). Nimrod: a tool for rapid geotechnical characterization of surface sediments. *Sea Technology*, April 2009, pp. 10 - 14.

Stark, N., Hanff, H., Stegmann, S., Wilkens, R., Kopf, A., (2009). Geotechnical investigations of sandy seafloors using dynamic penetrometers. *MTS/IEEE Oceans 2009*, Biloxi, USA.

Stark, N., Wilkens, R., Ernstsen, V.B., Lambers-Huesmann, M., Stegmann, S., Kopf, A., *subm.* Geotechnical properties of sandy seafloors and the consequences for dynamic penetrometer interpretations: quartz sand vs. carbonate sand. Submitted to *Geol Geotech Eng*.

Stegmann, S., Moerz, T., Kopf, A., (2006). Initial results of a new free fall-cone penetrometer (FF-CPT) for geotechnical in-situ characterisation of soft marine sediments. *Norwegian J Geol* 86, pp. 199 - 208.

Stoll, R.D., Akal, T., (1999). XBP-tool for rapid assessment of seabed sediment properties. *Sea Technology* 40(2), pp. 47 - 51.

Stoll, R.D., Sun, Y.F., Bitte, I., (2004). Measuring sea bed properties using static and dynamic penetrometers, Lamont-Doherty Earth Observatory of Columbia University, NY, USA.

Stoll, R.D., Sun, Y.F., Bitte I., (2007). Seafloor properties from penetrometer tests. *IEEE J Oceanic Eng* 32(1).

Svenson, C., Ernstsens, V.B., Winter, C., Bartholomae, A., Hebbeln, D., (2009). Tide-driven sediment variations on a large compound dune in the Jade tidal channel, southeastern North Sea. *J Coastal Res*, SI 56, pp. 381 - 365.

Terzaghi, K., (1943). *Theoretical soil mechanics*. John Wiley and Sons, New York.

Thieler, E.R., Pilkey, O.H., Cleary, W.J., Schwab, W.C., (2001). Modern sedimentation on the shoreface and inner continental shelf at Wrightsville Beach, North Carolina, USA. *J. Sed. Res.*, 71, pp. 958 - 970.

Trask, P.D., (1959). Effect of grain size on strength of mixtures of clay, sand and water. *Bull. Geol Soc Am*, 70, pp. 569 - 580.

Traykovski, P., Hay, A.E., Irish, J.D., Lynch, J.F., (1999). Geometry, migration, and evolution of wave orbital ripples at LEO-15. *J. Geophys. Res.*, 104, C1, pp. 1505 - 1524.

Trembanis, A.C., Wright, L.D., Friedrichs, C.T., Green, M.O., Hume, T.M., (2004). The effect of spatially complex inner shelf roughness on boundary layer turbulence and current and wave friction: Tairua Embayment, New Zealand. *Cont. Shelf Res.*, 24, pp. 1549 - 1571.

Wever, T.F., Voss, H., Luehder, R., (2008). High-resolution observation of small-scale variability in a bedform field. *Marine and River Dune Dynamics*, 1-3 April 2008, Leeds, UK.

Winter, C., Chiou, M.D., Riethmüller, R., Ernstsens, V.B., Hebbeln, D., Flemming, B.W., (2006). The concept of representative tides in morphodynamic numerical modelling. *Geo-Mar Lett* 26, pp. 125 - 132.

Chapter 5

Ongoing projects

Several surveys were carried out where data have not been published or submitted to a journal, yet. The preliminary results will be presented here in a section about sandy areas and one about muddy areas. Furthermore, the idea and a first attempt of simulating penetrometer - sediment interaction numerically is another ongoing project that will be described.

5.1 Cohesionless sediments

In sandy areas two more projects have to be introduced. The first addresses scouring at wind energy converter (WEC) foundations in the framework of the Research at *Alpha Ventus* (RAVE) project. Four expeditions to the wind farm test field were accomplished: two prior to the WEC erection and two after the WECs were in place. Additionally, measurements were done in a wave flume in Hannover including a physical model of a tripod foundation scaled 1:12 compared to the tripod foundations in RAVE.

The second survey was carried out along a highly mobile sandbar in front of Raglan's (NZ) harbor mouth estimating sediment remobilization. The data will be correlated to a commercial current model by ASR Ltd.

5.1.1 Scouring at WEC tripod foundations (RAVE)

The impact of objects in a flow is well-known and rather complex (chapter 3.1.1). The behavior becomes even more complicated if we shift the object into a 2-phases-space consisting of water and sediment. The typical patterns of sediment remobilization around, e.g., foundations or objects lying on the

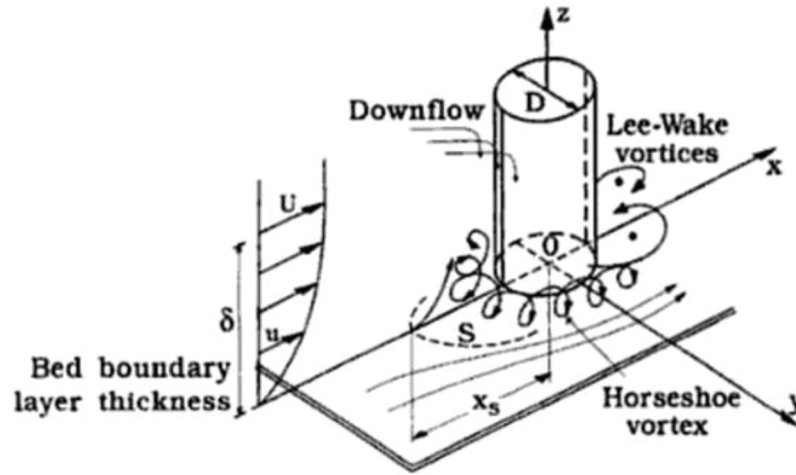


Figure 5.1: The changes of flow due to a single pile foundation (after Sumer and Fredsoe, 2002). In front of the pile it will come to a formation of a horseshoe vortex and to a downflow due to a flow deceleration in front of the pile. At the side edges of the pile streamlines will be contracted, and in the lee vortex flow patterns will form.

seafloor such as pipelines, are called scour and are of high interest for marine and coastal engineers. Is the scour around a structure underestimated, the structure is at risk to loose its stability and mooring.

Regarding a slender pile planted into an erodible bed and exposed to a flow, the following changes of flow will occur (Fig 5.1) (Sumer and Fredsoe, 2002): (i) a horseshoe vortex will be formed in front of the pile, and (ii) a downflow will be the consequence of flow deceleration, (iii) in the lee of the pile a vortex flow pattern will develop, (iv) at the sides of the pile the streamlines will contract. These changes in flow and the increasing turbulence will lead to an increase of sediment remobilization resulting in a typical pattern of scour (e.g., Soulsby, 1997) including areas of erosion (scour holes) and areas of sediment accumulation (e.g., Fig. 5.2).

Scouring is investigated mostly using numerical models (e.g., Fig. 5.3) and physical models (e.g., Fig. 5.4). There is a lack of *in-situ* surveys and geotechnical measurements after planting of the foundations. In the framework of RAVE the conditions are given to carry out such surveys in a frequency of about 6 months.

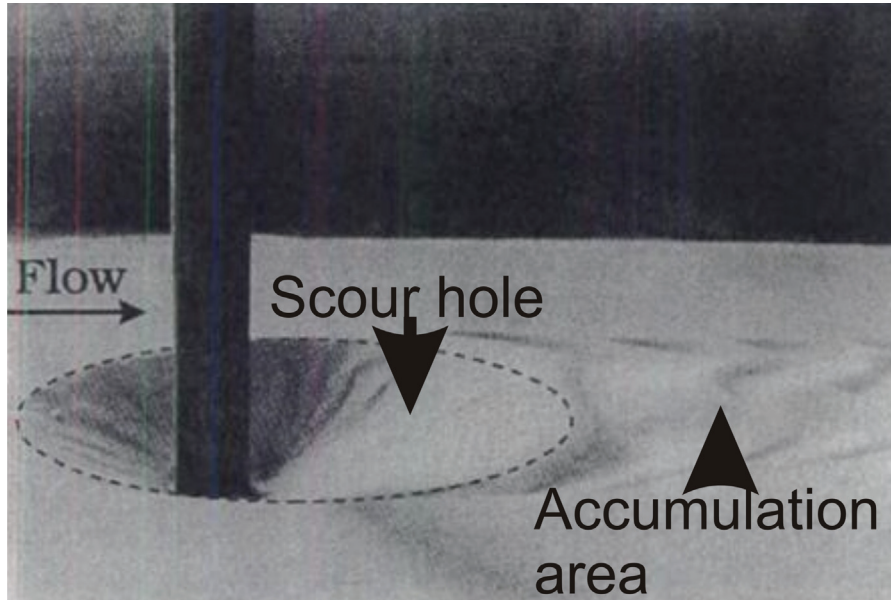


Figure 5.2: An example for patterns of clear water scouring (modified after Eadie and Herbich, 1986).

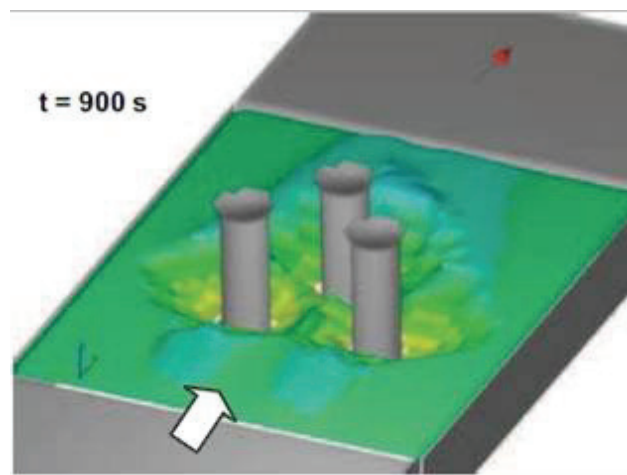


Figure 5.3: Example of numerical simulation of scouring around three piles (after Vasquez and Walsh, 2009).

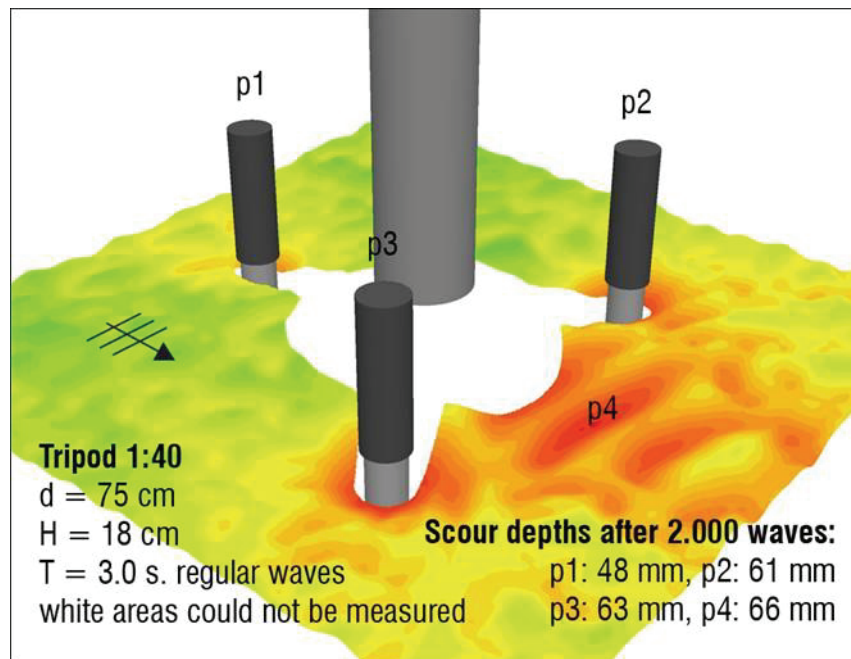


Figure 5.4: Example of results of physical modelling of tripod foundations by Stahlmann et al. (2009).

The test field

The first German offshore wind energy farm is called test field, because it is accompanied by a research project (RAVE). The outcome affects the authorization process of other proposed offshore windfarms in German waters.

The test field consists of twelve 5-MW-turbines, six in the north having jacket foundations and six in the south having tripod foundations, a transformer platform in the south-eastern corner and the research platform FINO 1 in the west (Fig. 5.5). The area is located about 45 km off the coast in water depths ranging from 27–31 m. The area is influenced by tides leading to dominant current directions along the east-west-axis with maximum current velocities up to ~ 0.6 m/s. For a detailed geotechnical sediment description see chapter 4.1.

The RAVE project brings together scientists from different disciplines addressing, e.g., offshore engineering, material sciences, oceanography, geology, geotechnics, biology and sediment dynamics. The working group for Marine Geotechnics at MARUM, University of Bremen, is involved in geology, geotechnics and sediment dynamics.

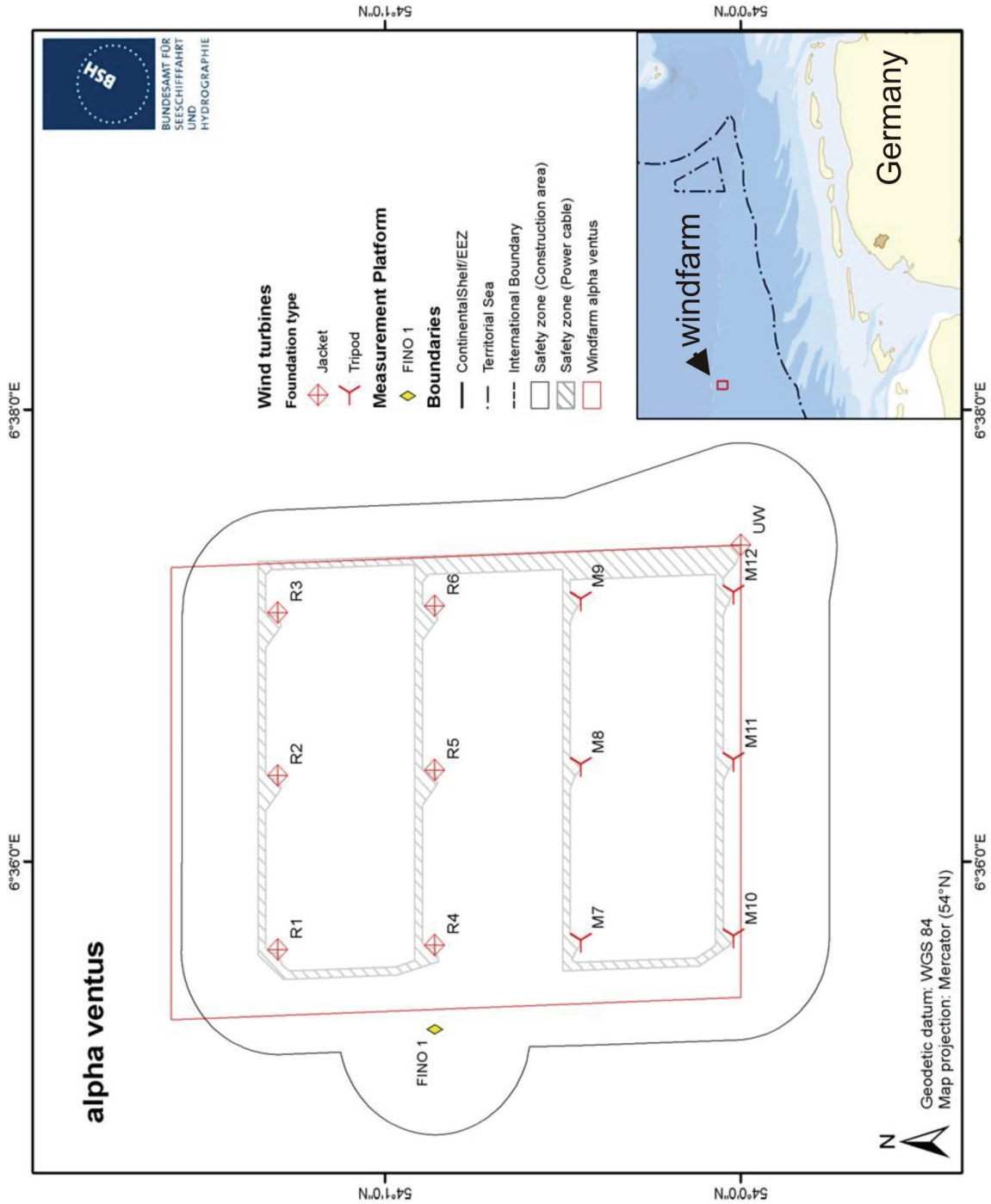


Figure 5.5: Sketch of the wind energy test field *Alpha Ventus*.

Methods applied

During two surveys prior to WEC erection, *in-situ* dynamic penetrometer measurements were done using the FFCPTU (Fig. 5.6) and the *Nimrod* (Fig. 5.7). Furthermore, grab samples for the determination of geotechnical properties in the laboratory (e.g., oedometer, shear box, etc.) were taken covering the whole test field. The Federal Maritime and Hydrographic Agency (BSH) provided multibeam echo sounder (MBES), side scan sonar (SSS), chirp sonar and current data for a comparison to the geotechnical results.

After WEC erection, this was repeated twice (erection in 2009, 1st survey Nov 2009, 2nd survey April 2010). However, the number of grab samples was reduced in the latter survey. The taken samples confirmed that the sediment supply remained the same. Furthermore, deployments requiring the bigger vessel (e.g., FFCPTU) could not be accomplished closer to the WECs than 50 m. *Nimrod* measurements were carried out from a small vessel along tracks approaching the center pile of the tripods M10, M11 and M12 from a distance of 50 m in eastern direction and southwestern direction, respectively (Fig. 5.8). Along each track the instrument was deployed every ~ 10 m, and the final position is already in between the tripod legs. Transects from the northwest were not possible due to the restricted area where the cable is located. In case of M10, also a southwest transect was impossible, because a stationary, circumferential sonar tower was installed here.

Results prior to WEC erection

The detailed geotechnical results can be found in the manuscript presented in chapter 4.1. The two independent research cruises delivered a reliable data base covering the whole test field. They are part of a larger data set where silica, and carbonate sands are compared (chapter 4.1).

Results after WEC erection

Acoustic visualization depicts significant topographic changes of the seafloor surface. At tripod as well as jacket foundations scour patterns can be detected (Fig. 5.9, Fig. 5.10), however, apparently more sediment is remobilized at the tripod foundations. There, the global scour hole had a depth of up to 2.5 m in November 2009 (Fig. 5.11) and up to 5 m in April 2010 (assumed from unprocessed MBES data during the survey). Furthermore, scars from the construction phase such as footprints from jack-up platforms are still



Figure 5.6: FFCPTU configuration used in RAVE: short rod (~ 0.5 m), all weights (mass in total ~ 100 kg), deployed by winch.



Figure 5.7: *Nimrod* deployment from VWFS Wega.



Figure 5.8: Small vessel for *Nimrod* deployments close to the WECs. Example of positions measured during the November 2009 survey at M11 (small window upper right corner).

preserved after ca. 3 months (Fig. 5.12).

The FFCPTU results expressed in tip resistance, pore pressure and deceleration before and after WEC erection are approximately similar (e.g., Fig. 5.13). Only in a few cases differences can be seen. For example, at the position 100 m north of M11 (middle tripod of the southern line) the results from November 2009 can be interpreted as similar to the results prior to erection, but in April 2010 a softer top layer can be observed (Fig. 5.14). This position is close to the cable track. Working or scouring processes at the cable tracks might have loosened up sediment here.

Regarding the *Nimrod* results in the vicinity of the WECs, the sediment strength results vary with respect to the single WECs and with respect to the different surveys in November 2009 and April 2010 (Fig. 5.15, Fig. 5.16). At M12, the tripod erected first, negligible changes can be observed between the surveys. In November 2009 along the southwestern transect, the sediment appears slightly harder (quasi-static bearing capacity with constant reference velocity 0.02 m/s [qsbc] ~ 80 kPa) in comparison to the base measurements prior to erection (qsbc ~ 60 kPa). In April 2010 the strength decreased (qsbc ~ 40 kPa). Along the eastern transect in November 2009, an increase in strength further away from the WEC is monitored (qsbc ~ 130 kPa) whereas the deployments close to the WEC are similar to the base measurements (qsbc ~ 60 kPa). However, half a year later the strength is lower (qsbc ~ 35 kPa), and a very soft spot can be detected between the eastern tripod legs (qsbc ~ 14 kPa) (Fig. 5.16).

The area of M11 was characterized by conspicuously hard sediment already prior to WEC erection (qsbc ~ 110 kPa). In November 2009, very hard spots (qsbc up to 400 kPa) can be found in the close vicinity of the tripod decreasing to values matching the previous survey with increasing distance to the center pile (qsbc ~ 100 kPa). This observation applies to the southwestern transect as well as to the eastern transect. The profiles look different in April 2010. Here, the sediment strength decreases to ranges similar to the average around M12 (qsbc ~ 40 kPa), but still a slight trend to a higher sediment strength close to the WEC can be noticed (qsbc ~ 60 kPa). The gradient of this trend decreased significantly from November 2009 to April 2010 (Fig. 5.16).

At M10 we also found the trend of sediment hardening towards the WEC (qsbc ~ 120 kPa) in November 2009, however, less pronounced compared to M11. This trend is inverted in April 2010. That means the sediment strength decreases coming closer to the center pile of the tripod. Similar to the 2010 eastern profile of M12 a soft spot can be detected between the eastern tripod legs (qsbc ~ 10 kPa) (Fig. 5.16).

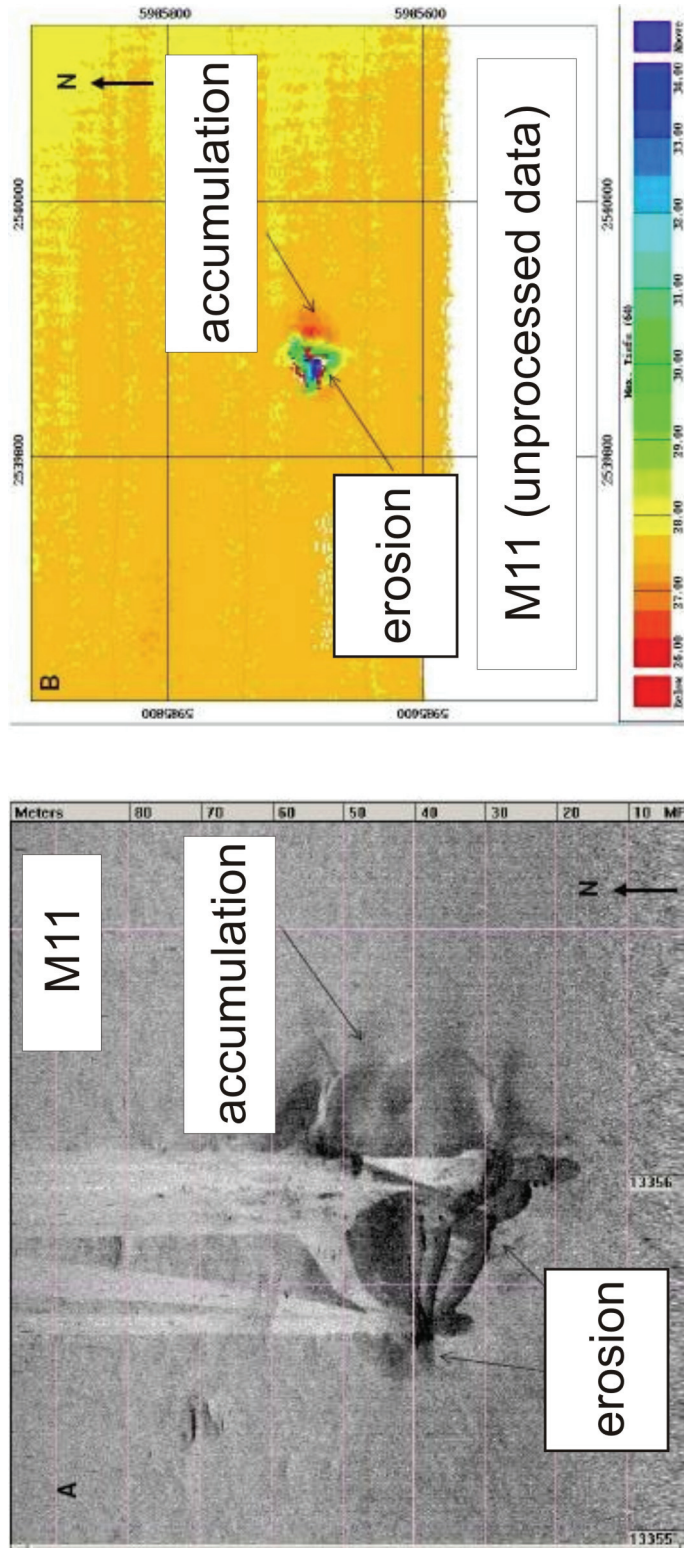


Figure 5.9: Side scan sonar picture of the M11 tripod in November 2009 (left). Erosion edges and accumulation areas can be indicated. This is confirmed by multibeam echosounder data (here still unprocessed, sufficient only for qualitative examination) (right).

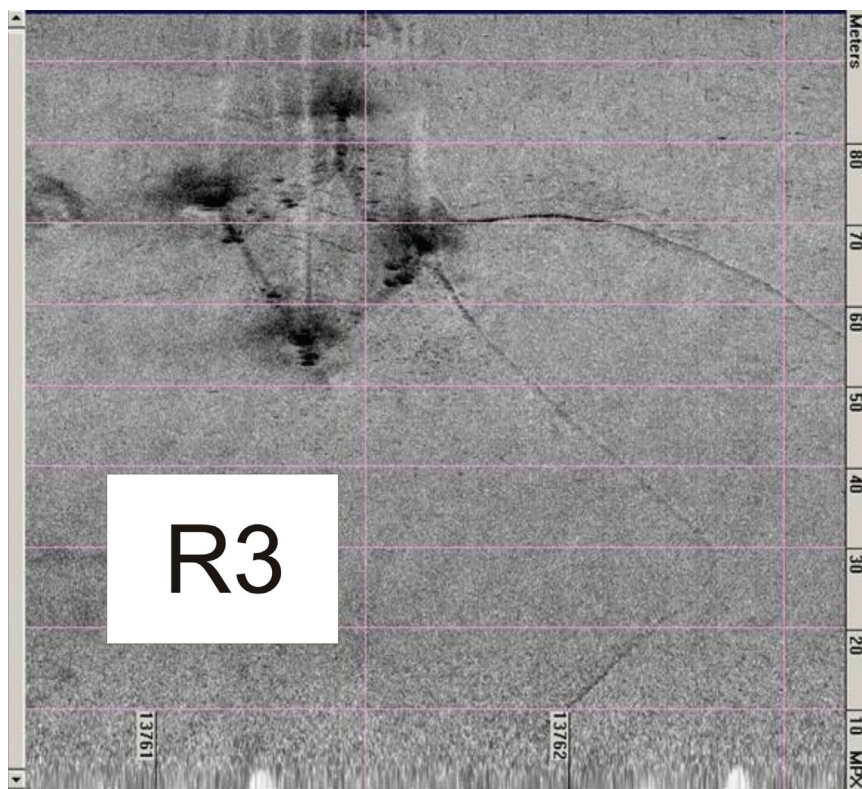


Figure 5.10: Side scan sonar picture of the R3 jacket foundation. Scouring is less significant compared to the tripod. The cable can be indicated, too (right side).

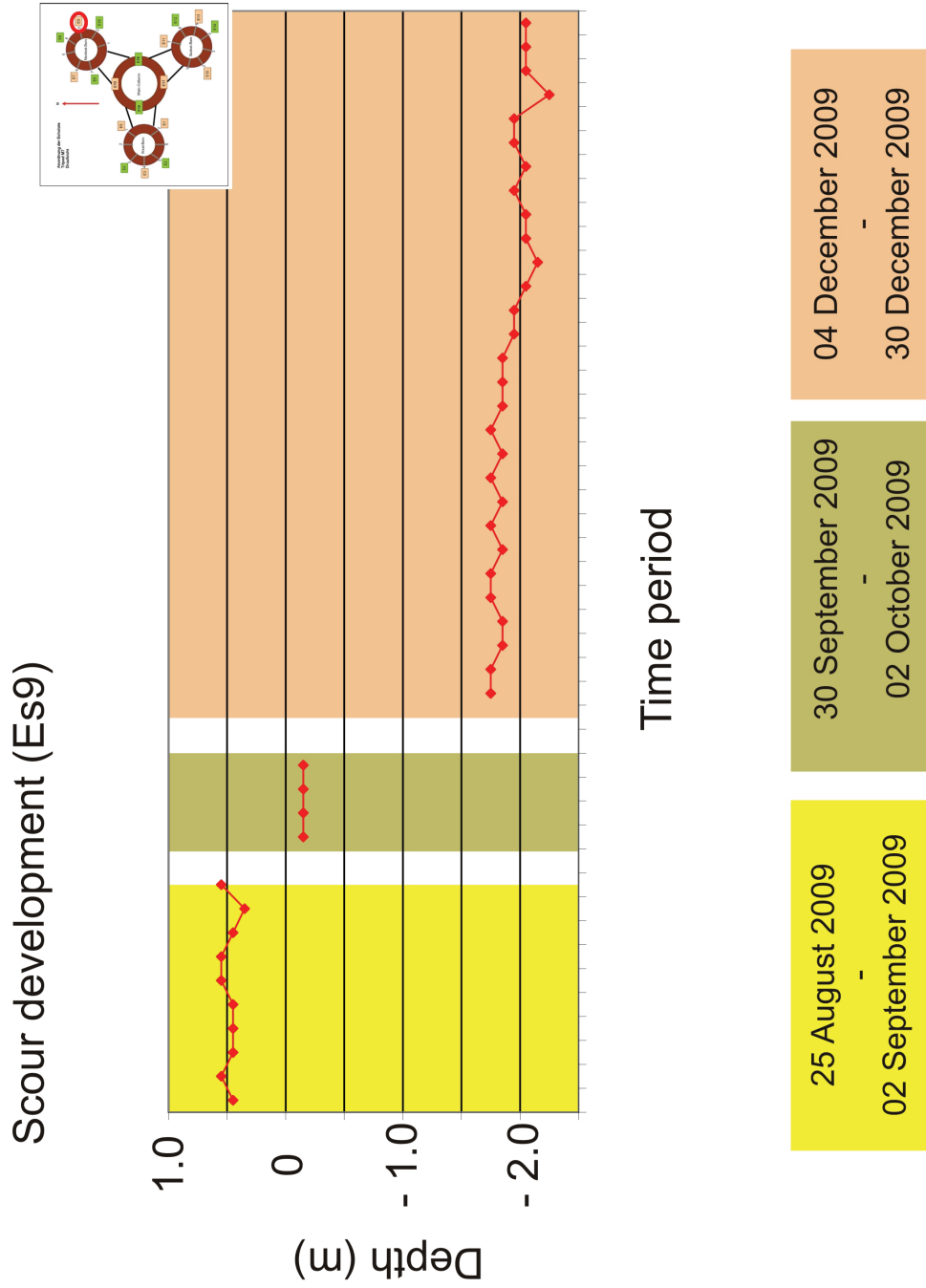


Figure 5.11: Scour development from 25 August 2009 to 02 September 2009 (yellow shade), from 30 September 2009 to 02 October 2009 (green shade), and from 04 December 2009 to 30 December 2009 (red shade) monitored at the eastern side of the northeastern tripod foot (see red circle in small sketch in the upper right corner) using single beam echosounder (figure provided by the BSH).

Preliminary discussion

The following observations can be made:

1. The sediment strength appears slightly decreased during the survey in April 2010. Different explanations are possible. First, the presence of the foundations changes the current profiles. This increases the hydrodynamically induced shear stress along the sediment-water-interface and might provoke particle rearrangement and general loosening up of the uppermost seafloor surface (within a radius of 60 m from the center pile). Another explanation would be that the seafloor surface is disturbed by storms which hit the area imminently before the survey. A third possibility would be a consequence of a change in impact velocity. In May 2008 impact velocities of about 6 m/s were reached. In November 2009 the impact velocities were about 10 m/s and in April 2010 only 4 m/s. In April 2010 the tether was directed via a lug potentially leading to a deceleration of free-fall due to friction. However, the reached impact velocity depends not only on the device and the tether, but also on water conditions such as currents. Especially, in April 2010 strong currents and a significant swell were observed. Actually, the calculation of a quasi-static bearing capacity should remove effects of changing impact velocities. However, even though the approach used (Dayal and Allen, 1975) is well established (e.g., Stoll, 2006), the possibility of deviations cannot be ruled out entirely. Further surveys in the windfarm area, and further investigations of the rate dependence problem of dynamic penetrometers will indicate the true explanation for the observed decrease in sediment strength in April 2010.
2. The geotechnical reaction of the seafloor to the foundations follows a timeline. First, a trend towards a high sediment strength can be monitored close to the foundations. This can be a consequence of erosion of loose material and exposition of harder underground. It is reasonable that especially the harder seafloor around M11 is hit by this effect. M12 is the oldest tripod. Following that, this effect might not have been seen at M12, because the stage of first strong erosion of loose material might be already finished before the first survey in November was carried out. Singlebeam echosounder measurements under a WEC confirm the strong development of scour during the survey in November 2009 (Fig. 5.11). Towards spring 2010 the sediment remobilization seems to decrease and to come closer to an equilibrium. This is confirmed by the penetrometer results showing values in the range of the base survey and slightly decreased. Further measurements in a

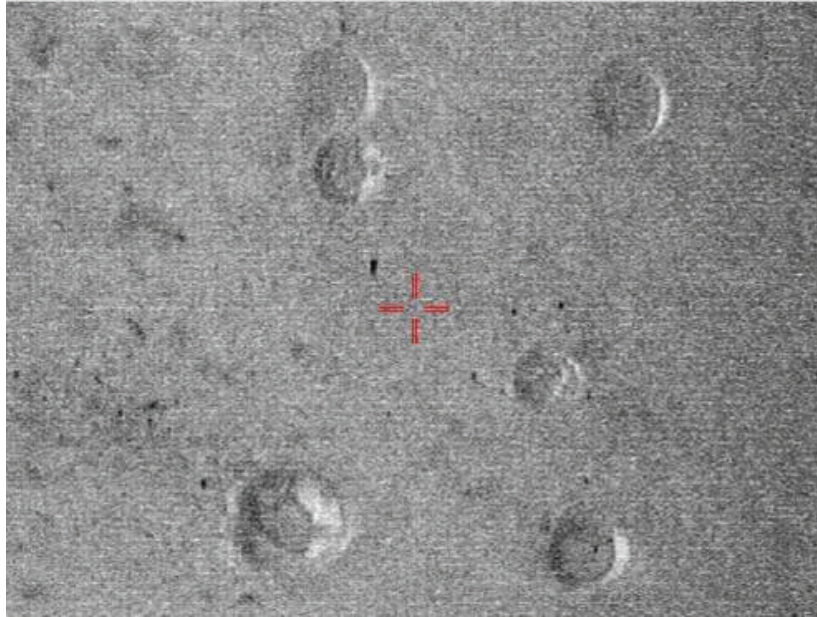


Figure 5.12: Side scan sonar image of construction traces. Here footprints of a jack-up platform.

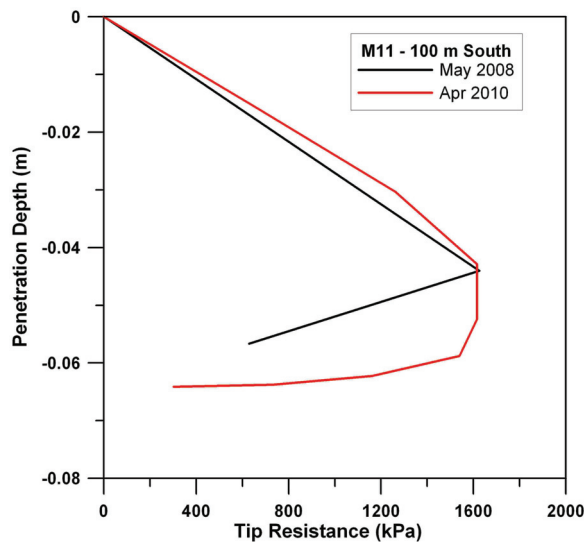


Figure 5.13: FFCPTU measurement at a position 100 m south of M11 in May 2008 (prior to WEC erection) and in April 2010 (after WEC erection). The profile can be described as similar. No changes due to WEC erection are visible. Changes in curvature can be related to an improvement of sampling frequency of the data logger.

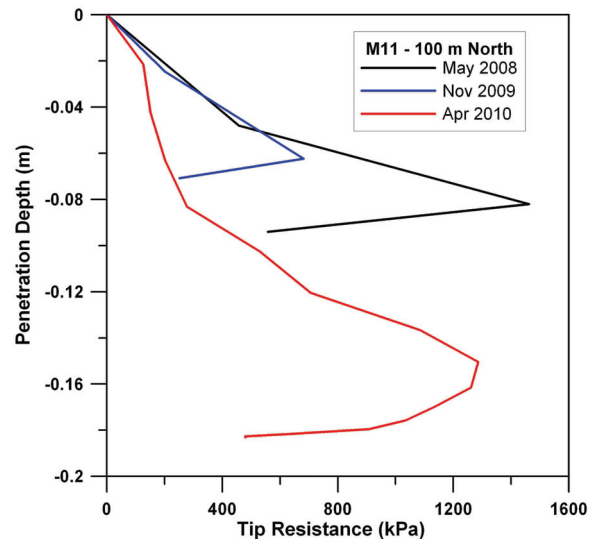


Figure 5.14: FFCPTU measurements at a position 100 m north of M11 (close to the cable tracks). The profile gradient is comparable, however, in case of the latest survey the upper sediment surface appears looser (down to ~ 8 cm). This might be a consequence of construction work at the cable tracks.

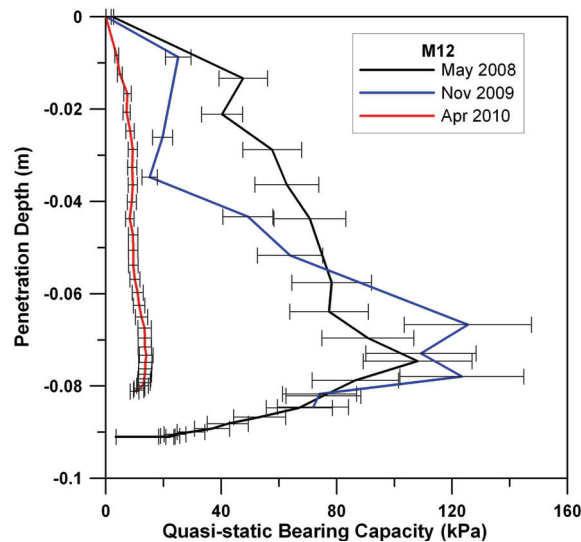


Figure 5.15: *Nimrod* results close to M12 prior to WEC erection (May 2008) and after (Nov 2009 and Apr 2010). In May 2008 no layering can be detected. In November 2009 a softer uppermost layer of ~ 3 cm can be indicated. In April 2010 the sediment shows loose material down to a penetration depth ~ 8 cm.

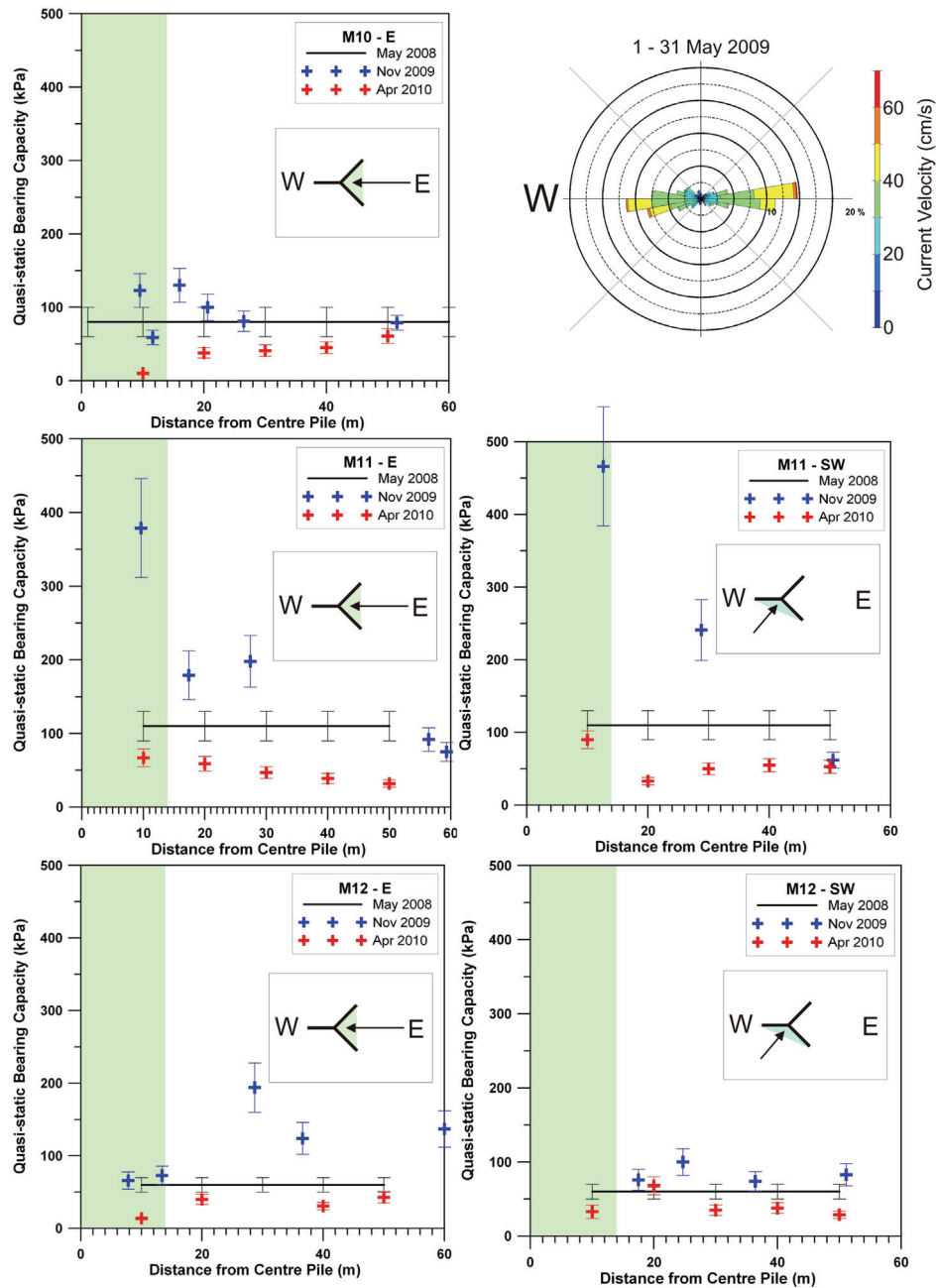


Figure 5.16: *Nimrod* measurements close to the WEC M10 (top), M11 (middle) and M12 (bottom) coming from the east (left) and the southwestern (right). Deployments in May 2008 form the baseline prior to WEC erection (black line). The post-erection surveys are from November 2009 (blue crosses) and April 2010 (red crosses). The green shade indicates the area in-between the tripod legs. Currents focus on the eastern direction (current rose, top right). In May 2008 deployments were carried out at the position of the proposed WEC, respectively. In November 2009 the positions were related to the center pile (x-axis). In April 2010 the measurements were carried out in approximately 10 m – steps. A correction of the precise position related to the center pile will be done as soon as the exact GPS positions are available.

frequency of about six months will clarify this hypothesis. However, this does not explain the very soft spots between the eastern tripod legs at M10 and M12. Divers observed the accumulation of fine material in these areas. It is still unclear what kind of material this is specifically and where it comes from. The infill of scour pits in sandy areas with mud in quiescent periods after energetic wave events was already shown by Traykovski et al. (2007) for scour experiments with mines. At *Alpha Ventus*, sampling will cast light on this question.

3. Above mentioned patterns only apply especially on the eastern transects. In the southwest the seafloor seems to be only poorly affected by the foundations. And if they are, this seems to focus on the developments in the early stage of the sediment remobilization (hardening close to the foundation).
4. The long preservation of construction scars (weeks to months) might be interpreted as an expression of low sediment dynamics in areas not affected by the WEC piles. In further surveys the presence of such traces should be monitored and compared with the schedule of maintenance actions.

These initial results were presented at the European Geological Union General Assembly in Vienna (see appendix) and another abstract was accepted for the OCEANS 2010 in Sydney. However, these results must be regarded as a first data set to investigate the geotechnical behavior of the seafloor in the vicinity of tripod foundations. A comparable study is not known to the author. After an upcoming third post-erection survey (fall 2010) to prove some of the above mentioned hypotheses a publication in collaboration with the BSH is planned. Furthermore, these geotechnical patterns around the tripods and their indication for ongoing sediment remobilization should be investigated at other foundation types, in later surveys, related to storm events, and also in physical and numerical models. The currently existing numerical as well as physical models above all aim for simulating the morphological changes during scouring (e.g., Stahlmann et al., 2009; Vasquez and Walsh, 2009). For example, Stahlmann et al. (2009) observe during their wave channel experiments morphological changes using multi beam echosounders, changes in pore pressure using embedded pore pressure gauges and the turbulences using acoustic Doppler current profilers, however, changes of sediment strength during the scouring are not measured. Regarding numerical models, the differences in geotechnical sediment properties of the bed and the bed-load are considered in some cases (e.g., Roulund et al., 2005), but changes in sediment strength before, during and after the sediment mobilization are not

targeted. Following our *in-situ* results, this might be an important aspect to include in physical as well as numerical simulations of scour.

5.1.2 Wave flume

In collaboration with the BSH and the Franzius-Institute in Hannover, *Nimrod* measurements were possible in a wave flume during testing the impact of waves on tripod foundations. Two issues were addressed using *Nimrod*: (i) the detection of sediment remobilization due to wave action under controlled conditions, and (ii) scouring due to wave action at tripod foundations.

The experiment was carried out in April – May 2010. The processing of the gathered data sets has not been finalized, yet. Following that, only the set up of the experiment and the *Nimrod* results can be presented at this stage. However, in this thesis it may serve as an example how flume experiments might be integrated in the investigation of sediment remobilization processes from the geotechnical perspective using dynamic penetrometers.

Set up

The big wave flume at the Franzius-Institute in Hannover has a total length of ~ 300 m and a width of ~ 5 m. A tripod model (scaling 1:12 compared to tripods at *Alpha Ventus*) was installed approximately in the middle of the wave flume. The foundation was embedded into sand spreading out ~ 17 m from the tripod model up and down the wave flume. The sand is characterized by a medium grain size $d_{50} = 0.146$ mm and was applied as an about 0.5-1 m thick layer. A non-uniform consolidation of the sand bed has to be considered after different working processes at the tripod models.

Nimrod deployments were carried out from a hanging cage (Fig. 5.17) or a bridge at six chosen positions (Fig. 5.18): (i) 10 m in front of the tripod, (ii) 5 m in front of the tripod, (iii) between the front leg and the right leg of the tripod, (iv) behind the two back tripod legs (in-between was impossible due to installed pressure gauges in this area), (v) 5 m behind the tripod, and (vi) 10 m behind the tripod. At all positions in 5 m or 10 m distance from the model measurements with and without wave action were done. Close to the model, only measurements without wave action were carried out. Though, the impacts of scouring due to the previous wave action should still be noticeable.

The water depth during the experiment was 2.5 m. The created wave height ranged from 0.71–0.78 m with a wave period of 3.55–5.48 s.

Besides *Nimrod* measurements, changes of the bed profile were detected using MBES, and the turbulences caused by the interaction between waves and tripod model were observed using ADCP. The results of the two latter methods are not available at this point, but they will be compared to the *Nimrod*



Figure 5.17: *Nimrod* deployments from a hanging cage over the wave flume.

results at a later stage.

Preliminary results

At the positions (i) and (ii), it can be assumed that sediment remobilization is only influenced by the waves. An impact of the tripod model can be neglected there. At position (i) (10 m in front of the tripod) an approximately homogenous increase of sediment strength in terms of a quasi-static bearing capacity up to $15 \text{ kPa} \pm 4 \text{ kPa}$ can be observed without wave action (Fig. 5.19). With waves this profile shifts 3 cm down due to an appearing top layer of lower sediment strength ($q_{sbc} \sim 1 \text{ kPa} \pm 0.3 \text{ kPa}$). This expresses a looser layer developing at the sediment surface under wave action, and can be observed at position (ii), too (Fig. 5.19). Furthermore, an increase in maximum sediment strength ($q_{sbc} \sim 26 \text{ kPa} \pm 5 \text{ kPa}$) can be monitored. This might be a consequence of different states of sediment consolidation due to working processes at the tripod model.

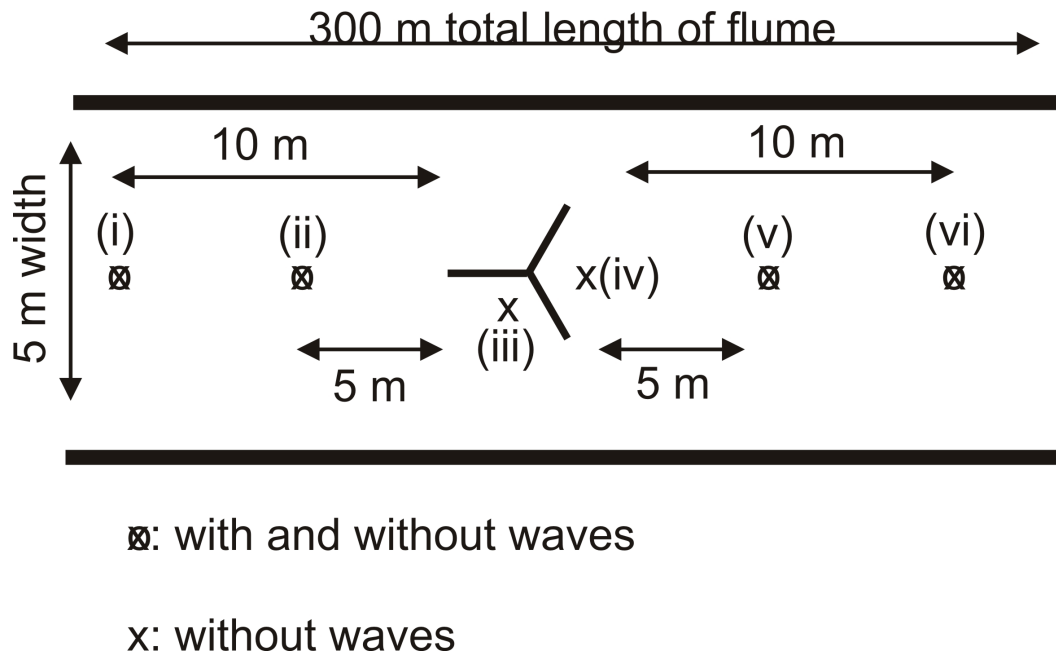


Figure 5.18: The six *Nimrod* positions in the wave flume related to the tripod model.

Comparing the different positions related to the tripod model, three types of profiles can be distinguished (Fig. 5.20). As mentioned above, a very homogenous, undisturbed sediment bed was profiled 10 m in front of the tripod model. The three positions under strongest influence of the tripod model (at the side, directly behind and 5 m behind) show a two-layer profile with a lower increase of sediment strength with depth in the upper 0.03 m of the sediment (Fig. 5.20). Similar profiles are reasonable at these positions due to the fact that they are influenced most by the tripod model, however, what the layering expresses in detail, e.g., accumulated sediment or a lower density due to looser packing, has to be clarified using, e.g., the MBES data. The measurements 5 m in front of the tripod and 10 m behind correspond well to each other. The gradient is smaller in the upper 0.08 m of the sediment than below (Fig. 5.20). This is surprising because the one is in the far wake of the tripod and the other in front of the tripod where the influence of the tripod should be negligible. Using MBES, ADCP and pressure gauges results, it has to be checked if this might be a consequence of differences in the original consolidation state or if other explanations have to be considered.

In summary, we monitored differences in the penetrometer signatures (i) with waves compared to without waves, and (ii) depending on the position with respect to the tripod model.

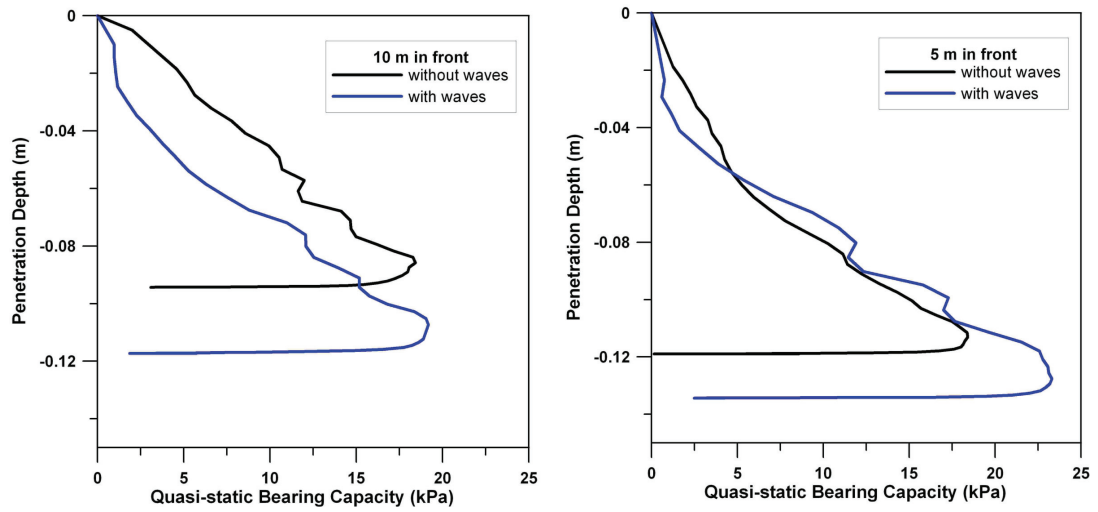


Figure 5.19: Results from the positions in front of the tripod model with and without waves. Under wave action there is a change of profile gradient at a penetration depth of ~ 3 cm indicating layering.

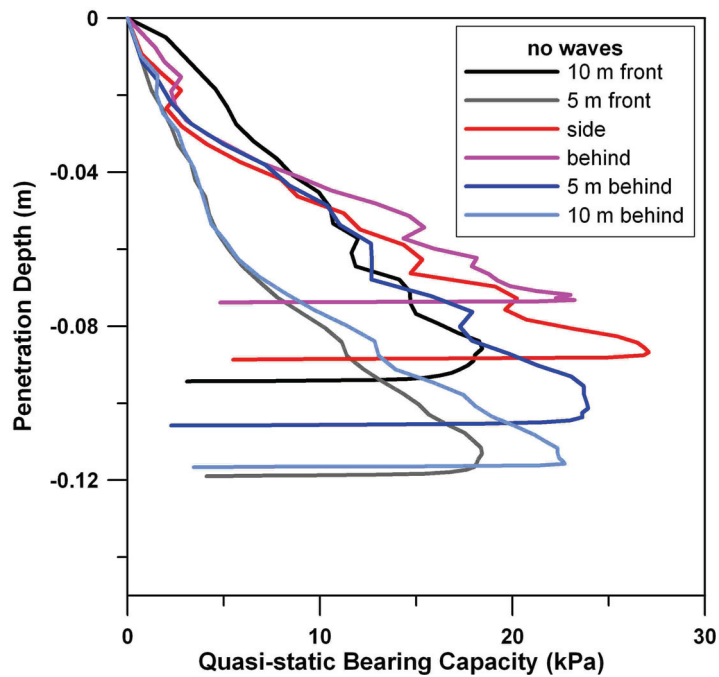


Figure 5.20: *Nimrod* results for all six positions relative to the tripod without waves. Three types of profiles can be distinguished: constant gradient (black line), change in gradient at a depth of ~ 3 cm (red, pink and blue line) and a change in gradient at a depth of ~ 8 cm (grey and light blue line).

The next step will be the comparison of the *Nimrod* results (i) to the MBES and ADCP data, and (ii) to the *in-situ* results from the wind farm *Alpha Ventus*. For the latter, the scaling, the limited space and the neglect of currents in the flume have to be considered.

5.1.3 Shifting sandbar

In a collaboration with ASR Ltd., Raglan, a highly mobile sandbar at the entrance to Whaingaroa Harbour, Raglan, was investigated. The area is characterized by strong currents, tides and waves. The seafloor is covered with a titanomagnetite black sand the west coast of the Northern Island of New Zealand is famous for. The *Nimrod* results are correlated to ASR's Whaingaroa Harbour model, which has been in development for a number of years and aims to better the understanding of the coastal dynamics and human impact on the coast.

Regional context

Raglan is located on the west coast of the North Island of New Zealand (Fig. 5.21). The area is characterized by a complex estuary system formed by a post-glacial drowning of the lower part of a branching river system lying in a structurally depressed fault-block (Sherwood and Nelson, 1979). Sediments range from sands on the beaches and in the channels and bars in the harbor mouth region to mainly muds in the tidal flats (Fig. 5.22). Phillips and Mead (2009) characterized the sand at the harbor mouth as titanomagnetite blacksand and highlighted that the sand appears fine-grained and dense compared to quartz sands at the east coast of New Zealand. Sherwood and Nelson (1979) found mean grain sizes ranging from medium to fine sand (about 0.2–0.35 mm). They also monitored dominating tidal currents with surface speeds of 0.75–1.5 m/s and suspended sediment concentrations between 10–100 mg/l.

In front of the Whaingaroa Harbour mouth and in the large ebb tide delta a big sandbar ('the bar'), described by Phillips and Mead (2009) as a "massive sand slug" (Fig. 5.23), changes shape and position overtime. ASR Ltd. studies these changes using georectified webcam images (www.surf.co.nz). The photographs are taken at an oblique angle to the sea surface, but they are further rectified to convert the view to an overhead perspective. The west coast of New Zealand has a energetic wave climate, and waves breaking outside the harbor indicate the seaward edge of the bar. This is seen on the rectified images as a band of white water. Gridded images of the bar are time averaged, and over periods (weeks or longer), the images of the broken waves indicate the temporal morphological changes to the bar. The northern arm of the sandbar moved about 20 m, the middle section about 120 m and the southern arm about 220 m shorewards during a time period from October 2004 to June 2005.

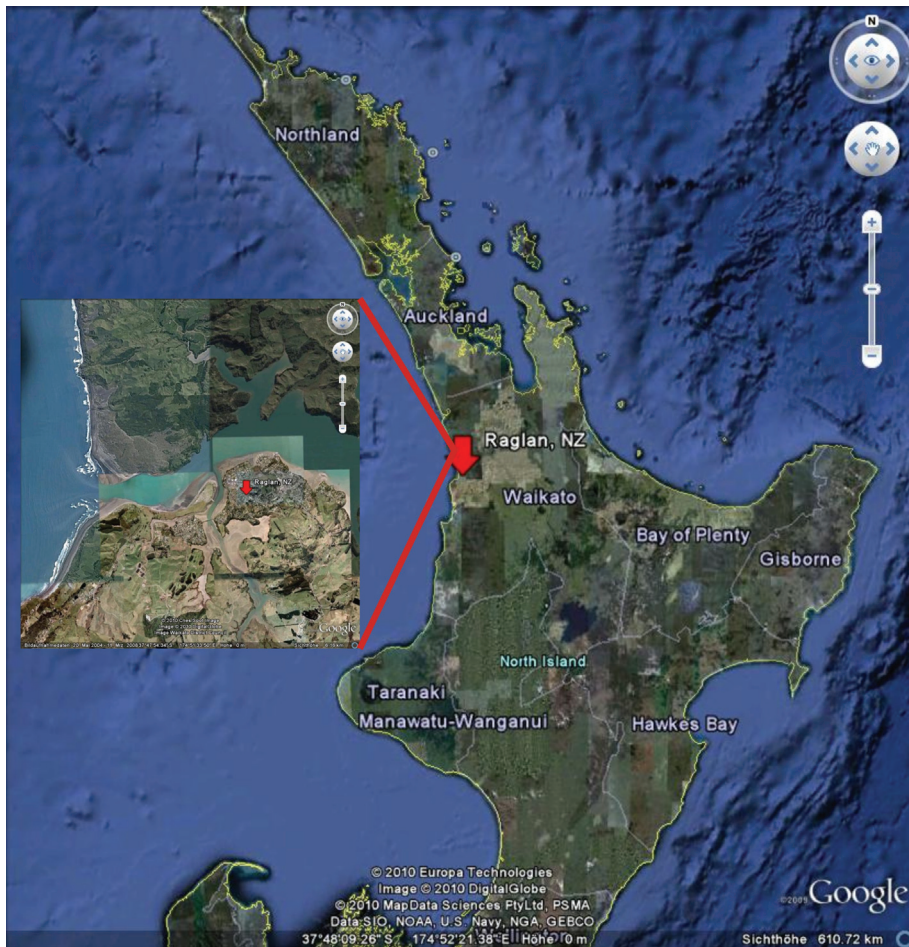


Figure 5.21: Google Earth image of the North Island of New Zealand showing Raglan (red arrow) and the harbor mouth (small picture left).

The mean wave and current direction over the bar comes from south-west (Fig. 5.24) (Scarfe et al., 2009) and is predominantly incident on the southern wing of the sandbar system (Fig. 5.25). During big swell events (up to 3.25 m), Phillips et al. (2003) observed a dramatic increase in current speed up to 0.8 m/s and maximum bed orbital velocities of up to 2 m/s.

Methods

A radial pattern of deployment positions was planned to cover the whole sandbar system (Fig. 5.25). However, water depths ranging from 1–12 m and breaking waves along the bar complicated the collection of *in-situ* mea-

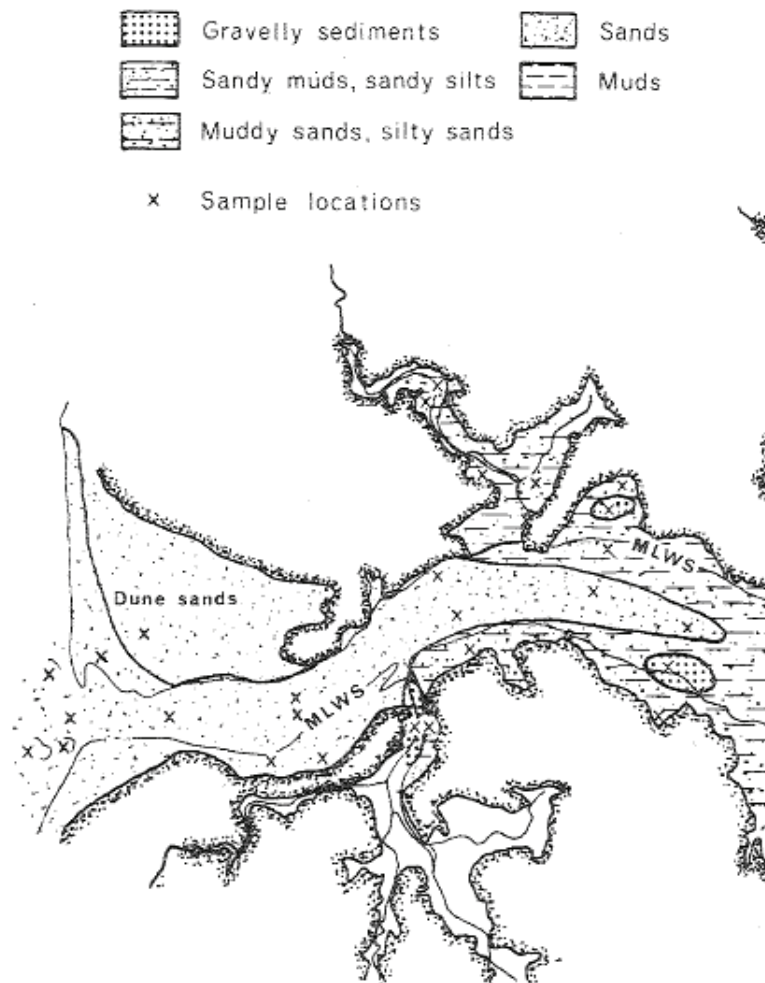


Figure 5.22: Distribution of sediment types at the Whaingaroa's Harbour mouth (modified after Sherwood and Nelson, 1979).



Figure 5.23: Aerial photo of Raglan's harbor mouth and breaking waves along the sandbar (ASR Ltd., Raglan).

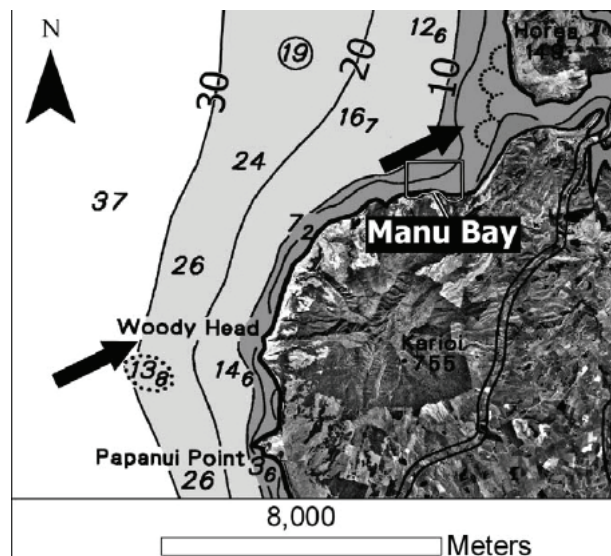


Figure 5.24: Main wave direction in Manu Bay (after Scarfe et al., 2004).

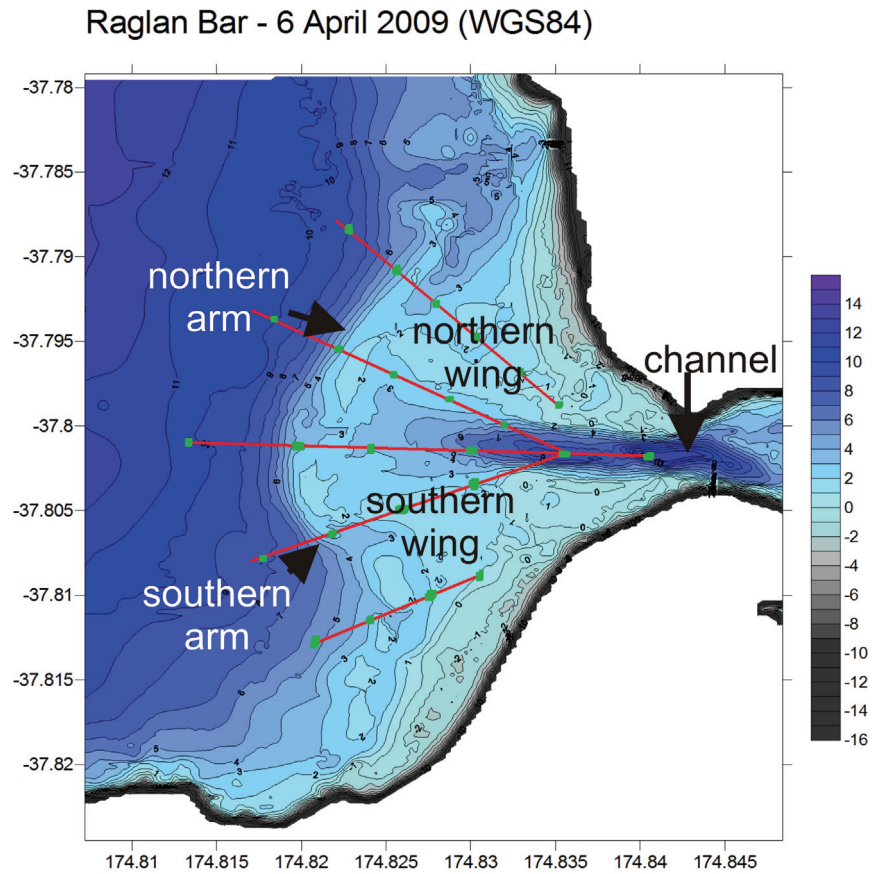


Figure 5.25: Bathymetry (in m) and survey planning of the sandbar area.



Figure 5.26: During the Raglan survey, *Nimrod* was deployed from the back of the jetski, and the tether was laid out on a towed safety sled.

surements. A large boat cannot be used in such shallow waters, and small boats do not provide the necessary stability in the Raglan wave climate. With this in mind, the survey was carried out using a jetski towing a safety sled (Fig. 5.26), and this configuration was manoeuvrable to navigate the breaking waves.

Later, three grab samples were taken by hand in calmer waters close to the sandbar. The grain size was determined by laser diffractometry and the friction angle using a uniaxial shear box under loads of 150 kPa, 300 kPa and 450 kPa.

The Whaingaroa Harbour hydrodynamic model simulating hydrodynamics was calibrated and ran for a period of one month shortly before the survey date to compare the current behavior with the estimated sediment remobilization derived by the *Nimrod*. The model and its purpose including the correlation with *Nimrod* data is briefly introduced in the following abstract:

**Greer, D., Phillips, D.J., Borrero, J.C.,
Mead, S., Stark., N., Harrison, S.,
The Whaingaroa Harbour modelling project
and its uses.
Submitted to the Coasts and Ports conference
in Perth, 2011.**

The Whaingaroa (Raglan) Harbour modelling project has been in progress for a number of years and aims to provide a comprehensive tool for the community towards a better understanding of the natural dynamics of the harbor and the human impact on the harbor.

This paper describes the development and uses of a detailed hydrodynamic model of Whaingaroa Harbour. The model includes the open ocean to the west and north and was developed using the 3DD modelling suite. The model is capable of integrating a variety of environmental factors such as wind, offshore waves, tides and freshwater inputs to drive the hydrodynamics. In the last year, the model has been fully calibrated to sea levels inside and outside of the harbor and to currents in the harbor mouth and over the ebb

tidal bar outside the harbor mouth.

The behavior and trajectory of treated effluent discharged from the Raglan sewage treatment plant was investigated using the model coupled with the Lagrangian model POL3DD and the wave refraction model WBEND. The results show that if the official discharge guidelines are adhered to (i.e. on the outgoing tide), very little of the effluent remains in the harbor. However, if discharge continues into the flood phase of the tide, sewage effluent can be widely dispersed throughout the harbour waters.

The model has also been used to investigate storm water runoff from Raglan town to investigate the propagation of toxins from these outlets throughout the harbor and their effects on local shell fish and juvenile fish populations.

In a collaboration between ASR Ltd, NZ, and MARUM, University of Bremen, GER, the model was used to validate the findings of a new free falling dynamic penetrometer known as *Nimrod*. The device can be used for the estimation of sediment remobilization and is suitable for measurements in sandy areas. Along the highly mobile sandbar at Whaingaroa Harbour mouth, the *Nimrod* results and the model provided currents are being used to map areas of high and low sediment mobility, and in doing so, enhance the understanding the sediment remobilization processes around the harbor mouth.

Future uses of the model will include investigations into harbor resonance and wave penetration into the harbor. In parallel to this project, ASR Ltd has been creating a data base of rectified aerial images of the Raglan bar which depict the movement of the bar over times scales from weeks to years. This database can be used in conjunction with the results from the *Nimrod* survey and the hydrodynamic model coupled with wave data to form the basis of a comprehensive study on the morphology of the Raglan bar.

Results

Nimrod was deployed at 23 positions (Fig. 5.27). On average the deceleration of the device when impacting the seafloor was about ~ 191 g, reaching maximum values > 250 g ± 5 g. The corresponding quasi-static bearing capacity was on average 105 kPa reaching up to 155 kPa ± 30 kPa.

The hardest sediment (Fig. 5.28) was found mainly in the shallowest areas of the southern wing of the bar (pos. 7, 16-18). Furthermore, the southern

arm and middle section of the bar (pos. 10-11, 19-20), showed hard sand. At the left wing, and in the trench of the channel, a lower sediment strength was measured (~ 60 kPa). Position no. 3 did not match this trend, however, contact between *Nimrod* and a boulder or stone might have caused this deviation. Another hard spot occurred at pos. 21, which is also an area of energetic wave action in Manu Bay.

Concerning layering (Fig. 5.29), most of the deployments indicated a two-layer profile with a top layer thickness ranging from 1–7 cm. The thickest top layer can be located in the deeper trench (pos. 2–8), on the southern arm and the middle section of the sandbar (pos. 10, 19-20). No layering was measured at the northern wing of the sandbar (pos. 12–14).

The three sediment samples can be described as black, magnetic sand. The medium grain size ranged from 0.16–0.19 mm. The friction angle was 34° – 37° .

The hydrodynamic model showed spatial variation in current velocity. The results from seven characteristic positions are presented here. In the channel, high mean current velocities (averaged over the water column) of up to 1.7 m/s were predicted predominantly along the east-west axis (Fig. 5.30). At position 8, on a shallow area of the bar, the direction was still orientated along the east-west axis (Fig. 5.30). The maximum current velocities were ~ 0.98 m/s. On the southern wing of the bar (pos. 17), the current velocity reached magnitudes up to ~ 0.61 m/s and the direction tended to be along the southwest-northeast axis (Fig. 5.30). In the southern corner of the bar (pos. 19) the currents changed direction frequently, but the maximum current speed was relatively small (~ 0.27 m/s). Mixed current directions with slightly higher current velocities of up to 0.35 m/s were observed in the middle of the bar (pos. 10 in Fig. 5.30), as well as in the northern corner of the bar (pos. 12 in Fig. 5.30) with a maximum current speed of ~ 0.33 m/s. In the northern wing of the bar system (pos. 14) the current direction ran predominantly along the northwest-southeast axis (vice versa to the southern wing: northeast-southwest) with maximum velocities of ~ 0.43 m/s (Fig. 5.30).

Preliminary discussion

The sediment resistance to the dynamic penetrometer was very large. The monitored decelerations were much higher than the ones measured in previous surveys (mean maximum deceleration: wind farm *Alpha Ventus*, North Sea: ~ 70 g; Kailua Bay, Hawaii: ~ 165 g; Raglan sandbar, NZ: ~ 191 g) (chapter 4.1). The dominant grain size (0.16–0.19 mm) can be assumed to be similar to the one in the wind farm *Alpha Ventus*, North Sea, (0.063–3 mm)

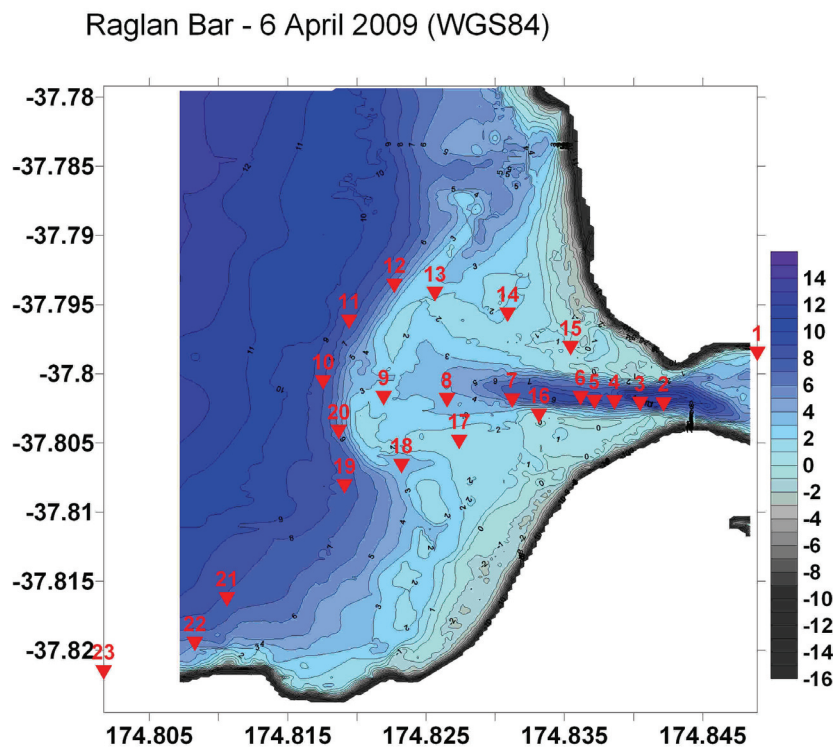


Figure 5.27: The 23 final deployment positions. The wave climate prohibited the deployment of *Nimrod* at the precise proposed positions.

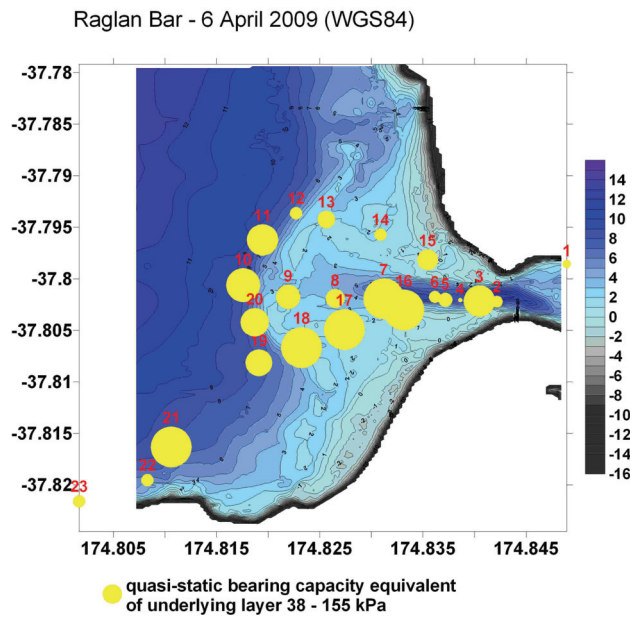


Figure 5.28: Qualitative comparison of sediment strength in terms of a maximum quasi-static bearing capacity in the underlying sediment layer in the *Nimrod* profiles.

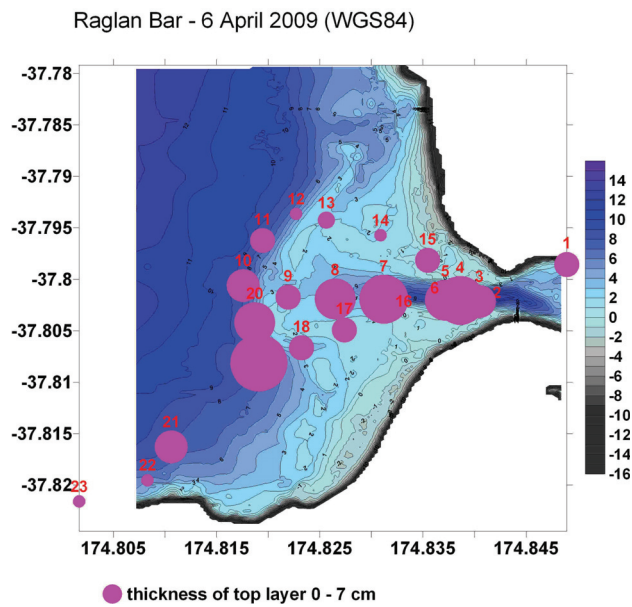


Figure 5.29: Qualitative comparison of the thickness of the top layer in the *Nimrod* profiles.

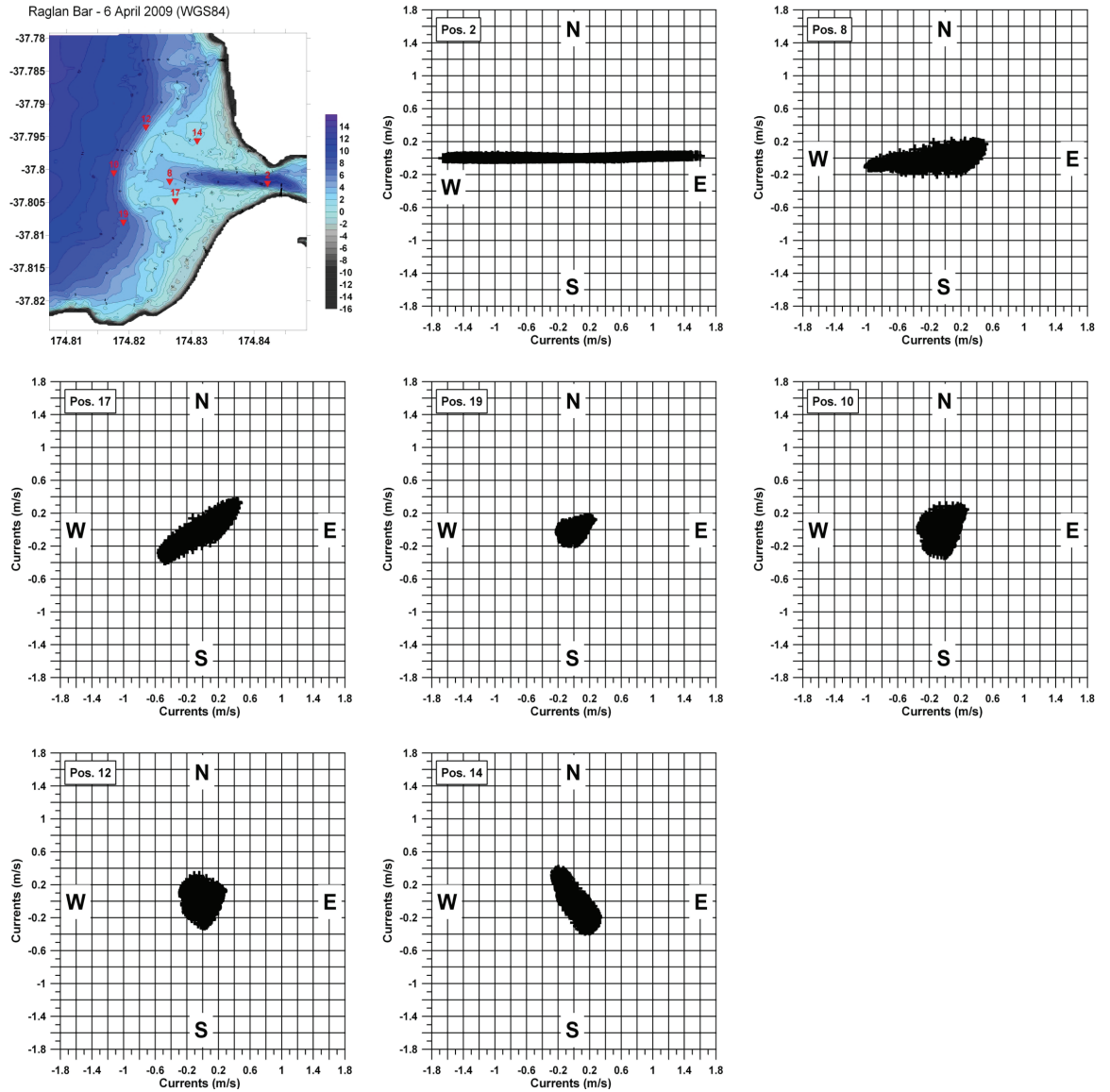


Figure 5.30: Current velocities in the respective direction of seven chosen positions in the sandbar system.

and in Kailua Bay, Hawaii, (0.063–3 mm) considering the different accuracy of the sieving analysis (applied on the samples from the North Sea and Hawaii) compared to the laser diffraction analysis (applied on the samples from Raglan). Our results match the description of Phillips and Mead (2009) characterizing the seabed as dense and fine-grained.

Compared to the medium grain size presented by Sherwood and Nelson (1979) our three sand samples showed slightly smaller mean values, but the differences in position and time have to be considered (Sherwood and Nelson, 1979: measurements in the estuary in 1978; Stark et al.: measurements on the bar in 2009).

The current directions predicted by the model follow the morphological contours of the bathymetry. The predicted current velocities show more variability than those presented by Sherwood and Nelson (1979) (0.75–1.5 m/s). This might be explained with the different measurement location. Sherwood and Nelsons (2004) hydrologic observation station was located about 2 km further into the estuary than the model domain presented here making a direct comparison impossible.

Concerning the different locations within the bar - harbor mouth system, different zones of sediment remobilization can be identified comparing the *Nimrod* results and the model. The channel (pos. 2 – 7) showed high velocities along the east-west axis. This hints at high sediment erosion and no deposition in keeping with results by Sherwood and Nelson (1979). Nevertheless, a low sediment strength and a thick looser top layer were derived from *Nimrod* results. Sherwood and Nelson (1979) did not consider current changes to bathymetry. In the deeper trench in the middle of the channel, sediment might settle and get trapped during periods of low current velocity around slack tide. This would explain the *Nimrod* results despite the strong currents. The fact that the *Nimrod* measurements were carried out during slack tide supports this hypothesis. In general, the channel can be described as an area of high and complex sediment mobility due to high current velocities and a bathymetry with steep gradients.

In the shadow of the bar or in the center of the sandbar system (pos. 8 - 9), we still found high current velocities decreasing towards the bar, and the current direction orientates in line with the channel. The sediment strength was low and the top layer thickness high to moderate, so that the area appeared as a runoff of the channel dynamics.

Comparing the northern wing (pos. 13- 15) and the southern wing (pos. 16 – 18) of the sandbar system, in both cases the current directions followed the morphology (i.e., they flow perpendicular to the bar) and are axis-symmetric to the east-west axis. However, the currents were stronger on the southern wing. Also, the sediment strength was high and the top layer moderately

thick here. This might indicate a high rate of sediment erosion in this area. The sediment appears very hard, because looser material already got eroded and left dense material at the surface. The thin top layer might be a result of freshly settled material during the slack tide, which was transported there from outside the system (note: that the survey was carried out during high water). In contrast, the northern wing showed no hints of sediment mobilization. The current velocities are lower, the sediment strength moderate and the top layer thin to non-existent. It follows therefore that sediment from inside or outside of the system moves over the southern wing of the system increasing erosion in this area by a process like sanding.

Focussing on the northern (pos. 12) and southern corner (pos. 19) of the sandbar, the northern corner corresponded closely with results from the northern wing, whereas the deployment position no. 19 was very different. However, it should be noted that the position 19 was slightly in front (i.e., west) of the sandbar (Fig. 5.30). The current direction was mixed and the current velocities generally low. The sediment strength was moderate whereas the thickness of the top layer was very high. Mobile sediment settles easily, and might even get trapped due to low current velocities and frequently changing current directions. This suggests this point to be a location for sediment accumulation and change of shape of the bar. This agrees well with the findings by ASR Ltd. that the southern arm changes much more in shape than the northern arm of the bar. If sediment accumulates at position 19 and sediment erodes at the southern wing (e.g., positions 17 and 18), the southern end of the bar would move more offshore, and the southern arm would open.

Regarding the middle section of the bar (pos. 10 – 11) varied current directions and low current velocities can be found. The sediment was hard, but not that hard as at the southern wing (Fig. 5.28) and the thickness of the top layer moderate (thinner than at the southern arm or in the channel, but thicker than at the northern areas, Fig. 5.29). In consequence, the results indicate ongoing sediment remobilization, however, this occurs less than in the southern areas and more than in the northern areas. This also agrees with the observations by ASR Ltd.

In summary, (i) the black sand displayed a very high sediment strength, and (ii) the *in-situ Nimrod* results compared with the Whaingaroa Harbour model deliver an unique insight into the sediment mobility of the sandbar system and the following changes of shape of the bar. Comparison with aerial images, documenting the change of shape with time will be another important point concerning the validation of the described findings. Furthermore, similar surveys undertaken on a regular basis, e.g., annually, would lead to a better understanding of the ongoing processes with time. For example,

shifting of the sediment accumulation at pos. 19 would be interesting to track along with changes in shape of the bar. *In-situ* current profiling and sampling of suspended matter would complement such a study, although the wave climate on the bar may hamper *in-situ* measurements.

These results of this chapter 5.1.3 will be presented in a manuscript for publication in the near future.

5.2 Cohesive sediments

So far the presented geological projects focussed on cohesionless sediments. However, sediment remobilization occurs in case of cohesive sediments as well. The three sites investigated within this chapter are induced by human impact and/or have an impact on the industrial usage of the region. The results are not published yet, but manuscripts are in preparation.

5.2.1 Fluid mud and mud accumulation in ports

Fluid mud (Kirby, 1988) is a complex sedimentary phenomenon in estuaries or rivers and can be regarded as an expression of ongoing sediment remobilization. As mentioned in section 2.2.1, the formation of fluid mud is influenced by flocculation mainly following the collision of particles (Mehta, 1993). The respective particles can have different origins. For example, they can be entrained from the bed by currents, waves or turbulences (e.g., Kusuda et al., 1993), or they can be transported as river discharge coming from the river catchment areas (e.g., Foster and Carter, 1997). In such areas not only the fluid mud layer, but also mud accumulation is an issue. It can occur temporarily (e.g., at slack water in tidal channels, e.g., Nichols, 1984) or permanently (e.g., current velocity decrease at river mouths compared to river current velocities, e.g., Kuehl et al., 1982). Both, fluid mud layers as well as mud accumulation areas, might become problematic due to the resulting decrease in navigable depth (Wolanski et al., 1992). Following that, it is essential to detect, quantify the thickness and characterize such fluid mud layers and areas of mud accumulation.

However, this can be difficult (e.g., McAnally et al., 2007). Most of the conventional echosounders installed on commercial vessels cannot detect mud in its unconsolidated and highly dynamic fluid state (Schrottke et al., 2006), and side scan sonars have inherent difficulties in detecting the bottom in areas of freshly deposited fluid mud (Schrottke et al., 2006). In this study, it was investigated if fluid mud, soft mud layers and mud accumulation areas in ports can be detected by a small dynamic penetrometer such as *Nimrod* using the deceleration and derived sediment strength profiles. The following abstract accepted for the Coastal Sediments conference 2011 sums up the results from surveys in the Port of Tauranga and Port Lyttelton of Christchurch.

The Port of Tauranga is a large coastal lagoon impounded by a Holocene sandy barrier island and tombolo system (Davies-Colley and Healy, 1978) at the east coast of the North Island of New Zealand. The port entrance is a tidal inlet with a tidal range of about 2 m. However, in the Port of Tauranga

no sediment from the harbor entrance is transported to the study area (Stella Passage) (Davies-Colley and Healy, 1978), but approximately 120,000 tonnes of sediment washes into the harbor coming from the farmland and forested areas via rivers and streams (Inglis et al., 2005).

Port Lyttelton of Christchurch is located at the east coast of the South Island of New Zealand in Lyttelton Harbour, a 15 km long narrow embayment on the northern side of Banks Peninsula (Inglis et al., 2006). The entrance is almost 2 km wide and approximately 16 m deep. The channel is maintained by dredging to a water depth of ~ 11.6 m (Inglis et al., 2006). Mud covers most of the harbor, however, in the middle of the harbor fine sediments are easily carried away by the currents leaving behind a coarse sand containing a large proportion of shell hash (Inglis et al., 2006). The mean tidal range is 1.67–1.94 m. Similar to the Port of Tauranga, Lyttelton Harbour has a big catchment area and its sedimentation was first documented by Brodie (1955).

**Stark, N., Tear, G., Healy, T., Kopf, A.,
High resolution fluid mud and soft mud layer
quantification in ports
using a dynamic penetrometer.
Accepted for the Coastal Sediments conference
in Miami, 2011.**

Introduction

Fluid mud and mud accumulation may be highly contentious issues in ports and waterways. Thus, there is need for a detection and high resolution quantification including information about sediment strength of such mud layers. Small dynamic penetrometers are easily deployable and can provide such information, although resolving very soft to fluid mud layers is hampered by their very low strength.

Here we present two case studies in New Zealand using the dynamic penetrometer *Nimrod*: The Stella Passage of the Port of Tauranga (June 2009), and the harbor mouth of Port Lyttelton (February 2010). Both ports are known for muddy sediments and thick suspensions at the uppermost seafloor surface, and remain subject to further development (e.g., dredging). The aim of this study is (i)

to ascertain if a dynamic penetrometer is suitable to detect, quantify and geotechnically describe fluid and soft mud layers, and, if yes, (ii) to map such areas and stratification to understand ongoing sediment deposition processes.

Methods

The dynamic penetrometer *Nimrod* (Stark et al., 2009a) mainly measures deceleration and pressure during its impact and penetration into the sediment. A high sampling rate of 1 kHz offers a high vertical resolution of ~ 1 cm and 5 accelerometers of different ranges ensure a high sensitivity. The instrument can detect layering, but to exclude artifacts of changes in penetration surface area and penetration velocity, we also calculate a quasi-static bearing capacity (qs. BC) for a constant penetration velocity of 0.02 m/s (Stark et al., 2009b).

Results

In the Port of Tauranga we found significant differences between the western, middle and eastern side of the Stella Passage. In the western transect we found a soft layer (qs. BC ~ 3 kPa) with ~ 5 cm thickness above a layer of a qs. BC ranging from 20 - 50 kPa, and in some spots even a third stiff layer with a qs. BC of up to 80 kPa. Along the middle transect, two top layers similar to the western transect were detected, but no third layer. Furthermore, deployments here presented frequently disturbed results which hint at gravel, wood or trash lying on the seafloor. Along the eastern transect we observed a soft layer corresponding to the top layer from the middle and western transect under a very soft layer (qs. BC < 1 kPa) of ~ 5 cm thickness (Fig. 5.31).

In the harbor mouth of Port Lyttelton, we monitored a very soft layer (qs. BC < 1 kPa) with a thickness of up to 19 cm above a mud layer with qs. BC ~ 4 kPa at a former disposal site. The mud, representing the natural sediment in the inactive caldera hosting Lyttelton Harbour, is getting stiffer (up to qs. BC ~ 30 kPa) towards the port. In the shipping channel, the very soft upper layer reaches ~ 7 cm in thickness and is underlain by mud of qs. BS ~ 7 kPa. At a proposed future disposal site ~ 5 km offshore from

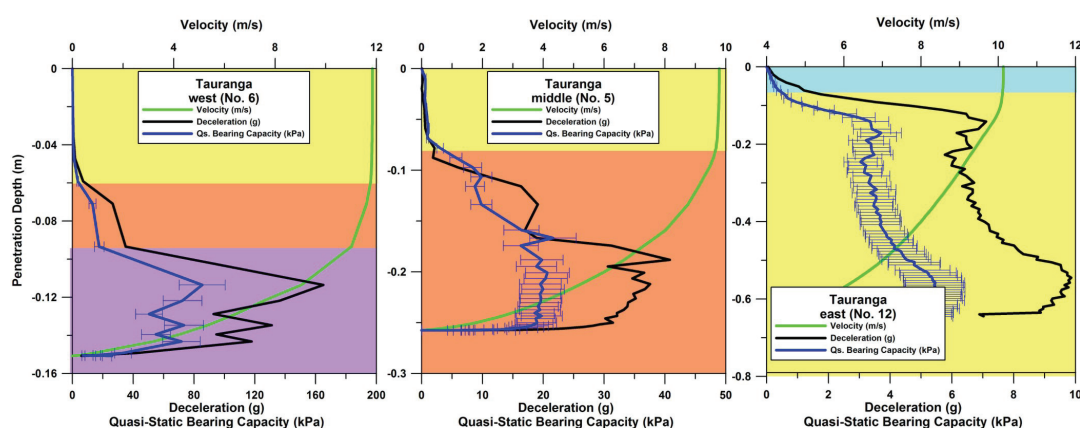


Figure 5.31: Examples of *Nimrod* results from each transect of the survey in Port Tauranga. Color shades indicate different strength layers. Be aware of different scaling.

the harbor mouth entrance, the very soft upper layer is ~ 6 cm thick and underlain by mud of qs. BC ~ 8 kPa.

Discussion and conclusions

In the Port of Tauranga soft sediments seem to be transported preferentially to the eastern side. A very soft layer, potentially fluid mud, on top of soft mud that reached down to the maximum penetration depth of 0.8 m was identified, whereas this very soft material only shows up as thin top layer (< 0.1 m) in the middle and the western side. Along the western transect even sandy substrate (Krüger and Healy, 2006) was displayed (Fig 5.31).

Port Lyttelton is characterized by mud as the natural substrate and a top layer of very soft, potentially fluid mud composed of altered tephra (Inglis et al. 2006). The results from the channel and its seaward prolongation, the designated future disposal site, are relatively similar. Only a slight increase of sediment strength can be observed offshore. However, the previous dumping site (used in 2009) still shows a poorly consolidated substrate with about 50 % less strength than the channel and the offshore sediment, and a very soft top layer of up to 19 cm thickness. The increase in strength towards the port is consistent with decreasing distance towards the pier, where qs. BC values correspond to sandy silt and the soft top layer vanishes. Geotechnical analysis of samples

from Port Lyttelton supports the results of the dynamic penetrometer interpretations.

In summary, the dynamic penetration tests proved to be a powerful tool to identify mobile soft layers at the two locations. Nevertheless, the results can only provide a snapshot of sediment stratigraphy. If to be related to currents, fluid dynamics and sediment mobility, a series of such surveys (e.g., over a tidal cycle), ideally complemented by other devices, would be necessary.

Acknowledgments

We acknowledge the German Research Association (via MARUM and GLOMAR, University of Bremen), the German Academic Exchange Service, Port of Tauranga and Lyttelton Port of Christchurch for funding this study. We thank Geoffrey Thompson (Port of Tauranga) and Neil McLennan (Lyttelton Port of Christchurch) for support. We are particularly indebted to Matthias Lange (MARUM), Christian Zoellner (MARUM), Matthias Colsmann (AVISARO, Hannover) and Mike Baker (N-Viro).

References

- Stark N., Hanff H., Kopf A., (2009). Nimrod: a tool for rapid geotechnical characterization of surface sediments. *Sea Technology*, April 2009, pp. 10-14.
- Stark N., Hanff H., Stegmann S., Wilkens R., Kopf A., (2009). Geotechnical investigations of sandy seafloors using dynamic penetrometers. *MTS/IEEE Oceans 2009*, Biloxi, USA.
- Krüger J.C., Healy T. R., (2006). Mapping the morphology of a dredged ebb tidal delta, Tauranga Harbor, New Zealand. *Journal of Coastal Research*, 22(3), pp. 720-727.
- Inglis G., Gust N., Fitridge I., Floerl O., Woods C., Hayden B., Fenwick G., (2006). Port of Lyttelton. *Biosecurity New Zealand Technical Paper No. 2005/01*, ISBN 0-478-07922-2.

5.2.2 Harbor mud disposal sites

There are different concepts to deal with dredged harbor mud. In some areas of strong tides or currents the material is mixed up into the water column and is washed away by the currents (e.g., Cameron et al., 1998). This is only possible if not too much material is dredged and the currents are sufficient to carry the material away. Often, these conditions do not apply, and the material has to be collected and disposed (e.g., Wakeman and Themelis, 2001). From the geotechnical perspective, such disposal sites are poorly investigated. In a collaboration with the Coastal Marine Group of the University of Waikato, NZ, the possibility was offered to accompany a pilot study at a disposal site on the continental shelf of New Zealand's northeast coast. The dredging site is Pine Harbor Marina located in the sheltered Turanga-Waikaopua embayment east of Auckland City, NZ. The marina approach channel crosses a broad intertidal zone, and has regularly required maintenance since construction. The dredged material is predominantly mud and fine sand (Healy et al., 1999). The disposal site at the outer continental shelf is characterized by muds, and is affected by the East Auckland Current and trade wind drifts (Carter, 1975).

The *Nimrod* was used to detect disposed material following the assumption that the sediment strength of the disposed material can be distinguished from the one of the seafloor. The results were presented in the following abstract accepted for the Coastal Sediments 2011 conference.

**Flaim, B., Stark, N., Healy, T., Kopf, A.,
Detecting dredged material
disposed on the continental shelf
using a dynamic penetrometer.**

**Accepted for the Coastal Sediments conference
in Miami, 2011.**

Introduction

In December 2009, consent was awarded for disposal of dredged harbor mud (silty clay) as a pilot study at a proposed disposal site (~140 m water depth) on the continental shelf of New Zealand's northeast coast. Conditions stipulated post-disposal monitoring surveys of the site, the results of which would be assessed to deter-

mine the long-term suitability of the site for ongoing disposal operations. Through *in-situ* measurements on sediment strength and layering in the uppermost layers of the seafloor (Stark and Wever, 2008), dynamic penetrometers could be used to determine the fate of disposed material, a critical factor in site suitability. However, accurate resolution of the deposited layers may be limited by vessel capabilities, and a combination of water depth and substrate properties. Dredging at the Auckland area marina began in March 2010, with the disposals 1 and 2 (40 and 1 hrs post-disposal and 765 m^3 each) occurring on March 14th and 20th. Here, we present the results of post-disposal surveys undertaken using the dynamic penetrometer *Nimrod* (Stark et al., 2009a) at the proposed site and compare them to results of a baseline survey from June 2009. The aim of this study is to determine whether a dynamic penetrometer can be used in monitoring disposal sites and if so, detect the fate of the deposited material.

Methodology

The dynamic penetrometer *Nimrod* was deployed twice at 24 locations after each disposal. With disposals at the site center, locations were chosen in the southeast quadrant of the site by reason of the southeasterly flowing boundary current (Stanton et al., 1997) thought to influence the fate of the disposed material. With a high vertical resolution ($\sim 1\text{ cm}$) and high sensitivity, *Nimrod* provides depth profiles of both deceleration and pressure. Quasi-static bearing capacity (hereafter qs. BC) is calculated to account for artifacts from changes in penetration surface area and velocity (Stark et al., 2009b).

Results

The predominant substrate observed during the baseline survey, a silty sand, displayed an average deceleration of 1.5 g , an average qs. BC of $\sim 1.4\text{ kPa}$, and no layering. The majority of sites visited during the post-disposal surveys displayed average values of deceleration and qs. BC of 2.3 g and $\sim 1.9\text{ kPa}$, respectively, with both showing a smooth increase with depth, as seen in baseline survey (Fig. 5.32 A). We found 3 locations after disposal 1, slightly

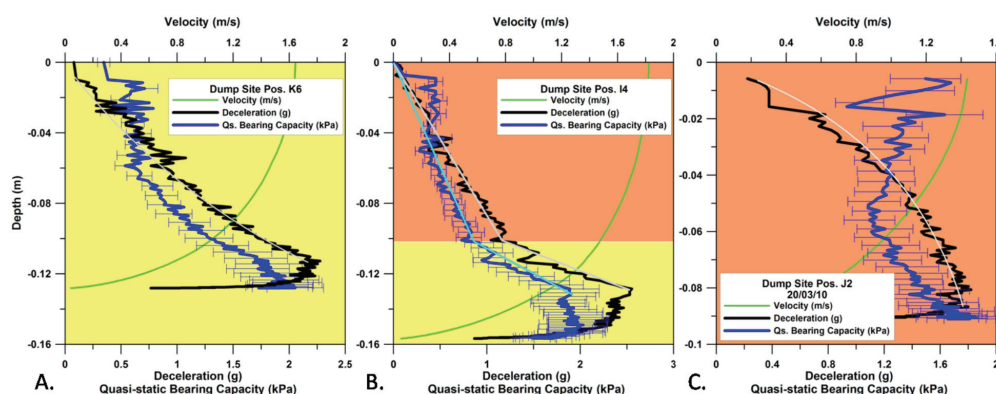


Figure 5.32: Examples of *Nimrod* results from 3 deployments with (A) no layer (disposal 1), (B) a top layer (disposal 1), and (C) uncharacteristic deceleration and qs. BC profiles (disposal 2). Shown is the measured deceleration (black), the calculated qs. BC with errors (blue), and the penetration velocity (green).

east and progressively south of the disposal location (~ 0.75 , 1, and 2 km away) that exhibited a top layer 7, 10, and 6 cm thick, with lower sediment strength compared to the underlying substrate (< 1.3 g and < 1 kPa) (Fig. 5.32 B). After disposal 2, layering was less pronounced, but 6 sites showed unusual sediment strength profiles (Fig. 5.32 C). Here, the range of values along the profiles for deceleration and qs. BC were somewhere in between those from the 2 layers observed at the 3 sites from disposal 1 with qs. BC remaining relatively constant.

Discussion and conclusion

Average qs. BC observed in the baseline survey and that of the predominant substrate sampled in the post-disposal surveys were geotechnically similar and within the error range of each other, indicating that in general, the substrate did not change between June 2009 and March 2010. The increase in average deceleration can be attributed to *Nimrod*'s increased weight (1.8 kg) after tail replacement with a heavier, solid aluminum tail. The sediment strength variations observed in the 3 specified locations after disposal 1 are apparent, if only on a fine scale, but may be somewhat masked by the combination of the low strength of both the native and disposed material and the significant water depth, which slows down the device due to tether drag. The observed top layer is

thickest approximately 1 km from the disposal location suggesting horizontal displacement of the main component of the material to this point, while the impact cloud may have contributed to the layers observed at the sites 0.75 and 2 km away from the disposal location. Settling of entrained sediments following initial impact may have added to the thickness of the top layer in all 3 locations. In the sites specified after disposal 2, uncharacteristic deceleration curves and approximately constant q_s . BC may reflect a less consolidated substrate which could be a result of the timing of the survey (only 1 hr post-disposal). The disposed material may have mixed significantly upon impact with native and previously disposed sediments, but had yet to undergo settling. Such tendencies can be significant in soft bottom substrates (Bokuniewicz and Gordon, 1980). Additional data collected at the site illustrate the influence of current velocities on descent, deposition, and the possibility of re-suspension. These findings indicate that *Nimrod* can be a useful tool for monitoring disposal sites as information provided can be linked to many aspects of disposal mechanics (Bokuniewicz and Gordon 1980). However, in this case, owing to logistical aspects of the site, *Nimrod* could be more effective with an added weight of ~ 10 kg.

Acknowledgements

This research was funded by the University of Waikato Doctoral Scholarship, Kaipara Limited, the German Research Association (via MARUM and GLOMAR, University of Bremen), and the German Academic Exchange Service (DAAD). We would also like to thank Alan Drinkrow, Mike Roycroft, and Gary Larsen for their field assistance. We are particularly indebted to Matthias Lange (MARUM), Christian Zoellner (MARUM), and Matthias Colsmann (AVISARO, Hannover).

References

Bokuniewicz, H. and Gordon, R., (1980). Deposition of dredged sediment at open water sites. *Estuarine and Coastal Marine Science*, 10(3), pp. 289-303.

Stanton, B., Sutton, P. and Chiswell, S., (1997). The East Auckland Current 1994-95. *New Zealand Journal of Marine and Freshwater Research*, 31, pp. 537-549.

Stark, N. and Wever, T., (2008). Unraveling the subtle details of expendable bottom penetrometer (XBP) deceleration profiles. *Geo-Marine Letters*, 29(1), pp. 39-45.

Stark, N., Hanff, H. and Kopf, A., (2009). Nimrod: a tool for rapid geotechnical characterization of surface sediments. *Sea Technology*, April 2009, pp. 10-14.

Stark, N., Hanff, H., Stegmann, S., Wilkens, R., and Kopf, A., (2009). Geotechnical investigations of sandy seafloors using dynamic penetrometers. *MTS/IEEE Oceans 2009*, Biologix, USA.

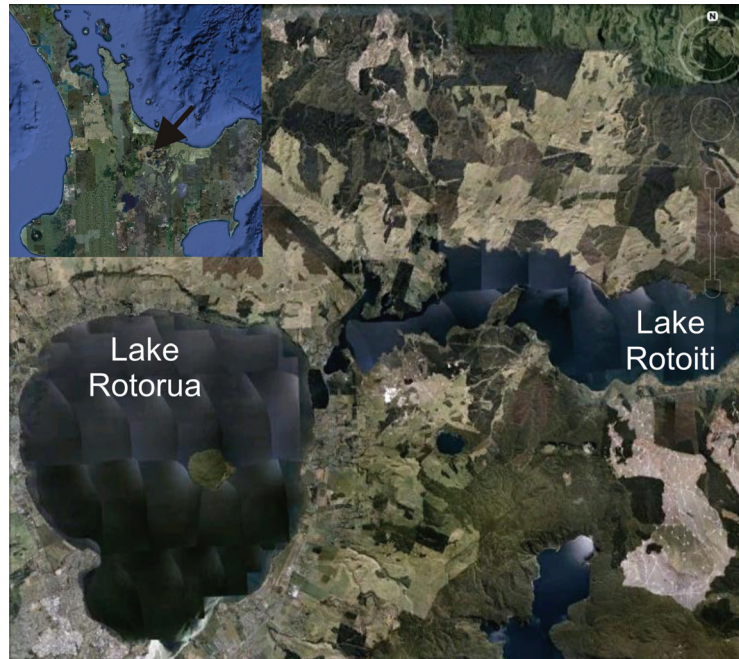


Figure 5.33: Google Earth image of Lake Rotoiti and Lake Rotorua and the location on the North Island of New Zealand (upper left corner).

5.2.3 The diversion wall in Lake Rotoiti as a sediment trap for fine sediment transported from Lake Rotorua via the Ohau Channel to Lake Rotoiti and the Kaituna River, New Zealand

Collaborating with the Department of Biology and the Department of Chemistry of the University of Waikato, geotechnical surveys were carried out in the geothermal lakes Rotorua, Rotoiti (Fig. 5.33) and Tarawera on the Northern Island of New Zealand in 2009 and 2010. In 2009 general surveys covering each lake in terms of big cross transects were done, whereas in 2010 the surveys concentrated on geothermal spots in Lake Rotorua and Lake Rotoiti, pockmark structures in Lake Rotorua and the area influenced by the diversion wall in Lake Rotoiti. This wall was set up to direct the inflow from the Ohau Channel and Lake Rotorua to Kaituna River. It can be assumed that the wall not only influences the water flows but also the sediment redeposition of material transported with the flow. In the following section, only results related to the channel are presented. More results from the lakes can be found in the appendix.

Regional context

Lake Rotorua, Lake Rotoiti (Fig. 5.33) and a number of other lakes have formed in the multiple caldera complex of the Okatania Volcanic Centre (OVC) which is one of five major volcanic centers in the Taupo Volcanic Zone (TVZ) (Cole, 1979).

Lake Rotoiti formed 11850–20000 years ago when lava flows dammed the drainage system through the Okatania caldera and has gone through a stage of infilling in the last 20000 years (Pickrill, 1993). Today Lake Rotoiti is ~ 13.5 km long, has a surface area of 33.9 km^2 and a small catchment of about 85.7 km^2 (Pickrill, 1993). Lake Rotorua drains into the western end of the lake via the Ohau Channel and contributes 73% of the $24.5 \text{ m}^3/\text{s}$ mean annual discharge down the Kaituna River. The remaining input comes from a multitude of small creeks (Pickrill, 1993). The bathymetry (Fig. 5.34) is complex reflecting the composite of origins (Pickrill, 1993). The lake floor is characterized by bedrock mostly covered with diatomaceous mud (Craig, 1985). In sediment cores two young tephtras (Tarawera Tephra and Kaharoa Tephra) can be detected as pumiceous sandy units 4–10 cm and 25–27 cm thick, respectively (Pickrill et al., 1993).

Lake Rotorua is one of the oldest continuously inundated lakes in New Zealand, occupying a caldera formed by or closely associated with the emplacement of the Mamaku ignimbrite some 140 ka ago (Wood, 1992) and the collapse of the Rotorua caldera (Healy, 1975; Lowe and Green, 1987). In the last 60 ka (since the Rotoehu eruption) the lake has fluctuated between 120 m above present (270 asl) and 10 m below present level (Hamilton et al., 2007). It has a surface area of $\sim 79 \text{ km}^2$ and a mean depth of 10 m. The bathymetry is complex including faulted blocks, craters, springs and pockmarks (Hamilton et al., 2007). The lake floor presents two different sediment types. In water depths shallower than ~ 10 m the sediment is coarse sand and pumiceous gravel reworked from the Kaharoa (AD 1314 + 12) and earlier tephtras. The accumulation of fine sediments is prevented by wind-driven turbulences here (Gibbs, 2004). However, in deeper waters the sediment consists predominantly of fine diatomaceous ooze interspersed with tephtra from, e.g., Okatania and Taupo (Hamilton et al., 2007).

The water entering Lake Rotoiti from Lake Rotorua via the Ohau Channel may have important implications for the water quality of Lake Rotoiti. Lake Rotorua water is enriched in nutrients and organic matter. This enrichment might lead to significant increase of nutrient load of Lake Rotoiti (Hamilton et al., 2005). Following that, in 2008 a 1275 m long diversion wall was installed in Lake Rotoiti to prevent water from Lake Rotorua flowing into the main body of Lake Rotoiti and direct it into Kaituna River. Before installation,

several surveys were carried out to provide data for numerical models estimating the impact of the diversion wall. Stephens (2004) presented current data for an Ohau Channel plume ranging between 0.05–0.2 m/s. In 2005 Stephens et al. published a study on bed samples and suspended sediment samples from three positions in the Ohau Channel (entrance Lake Rotorua [1], middle [2], close to the end of the channel and Lake Rotoiti [3]) and one in the Ohau Channel delta in Lake Rotoiti [4]. The suspended sediment concentrations were ranging between 2.3–5.7 g/m³ at positions 1-3. d₅₀ grain sizes of the bed samples were at position no. 1 about 3 mm, at position no. 2 about 1.4 mm and at position no.3 and 4 about 0.6 mm. The results express deposition of coarser material along the Ohau Channel getting finer towards the Ohau delta in Lake Rotoiti.

After installation of the wall, first surveys were carried out to estimate if the wall fulfils its purpose. Hamilton et al. (2009) concluded that the diversion wall is acting in a manner with its design and that there is no substantial leakage of water into Lake Rotoiti. However, the impact on the lake floor was not investigated here.

Results

In 2009, the *Nimrod* was deployed at 39 positions in Lake Rotoiti and at 54 positions in Lake Rotorua in crossing transects covering the whole lakes, respectively. In 2010, 6 deployments were carried out inside the wall area (Fig. 5.35) and 26 outside in Lake Rotoiti. 34 deployments were done in Lake Rotorua of which 8 were in the Hamanana Ohau area (Fig. 5.36).

The *Nimrod* data are supported by a big archive of sediment cores from Lake Rotorua available at University of Waikato (e.g., Pearson, 2006). Recently sampled sediment cores from Lake Rotoiti are currently investigated at University of Waikato. The data will be available soon. However, no sediment cores have been taken in the vicinity of the diversion wall.

Regarding measurements of general coverage in Lake Rotorua (no pockmarks, spring, vicinity of the shore, etc.), the *Nimrod* reaches in 2010 penetration depths ranging between 1 - 2 m, a maximum deceleration of on average ~ 2.2 g and a quasi-static bearing capacity of ~ 1.4 kPa on average. In most of the cases, no layering was detected (Fig. 5.37, upper left). The water depth varied from 12 m up to 18 m. In comparison to 2009, the sediment strength appears slightly lower (in 2009 q_{sb} ~ 2.2 kPa).

Along the Hamanana Ohau transect (close to the shore), the water depth was < 0.5 m. With a penetration depth of less than 5 cm, the deployment can be described more as an impact than as a penetration (Fig. 5.37, lower

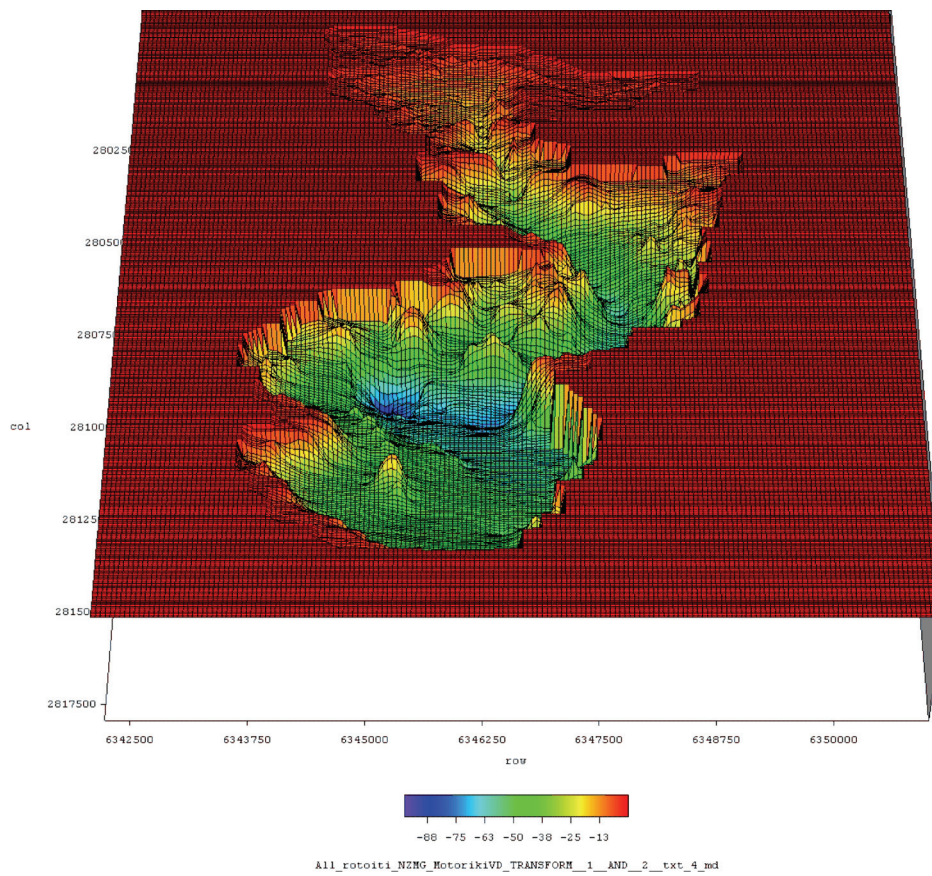


Figure 5.34: Multibeam Echo Sounder Image of the complex bathymetry of Lake Rotoiti (in m).

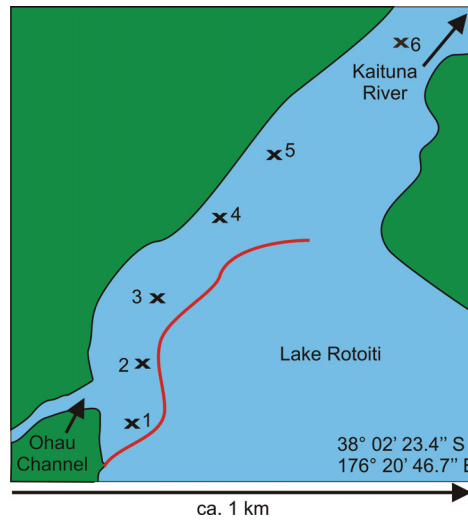


Figure 5.35: Deployment positions (crosses) in the vicinity of the diversion wall (red line) of Lake Rotoiti.

left). This is also reflected in the sediment strength. The deceleration in this area is on average 50 g and the quasi-static bearing capacity is on average 68 kPa. Layering was not detected.

Measurements of general coverage (not in the crater region) in Lake Rotoiti (Fig. 5.37, upper right) deliver similar results compared to the general deployments in Lake Rotorua. The quasi-static bearing capacity is on average 1.2 kPa. Deceleration (~ 1.5 g) and penetration depth (~ 1 m) are often decreased compared to Lake Rotorua due to a smaller impact velocity. This is the consequence of tether drag in the deeper water depths (16–75 m). In most of the cases, layering cannot be observed.

Behind the diversion wall, it is much shallower (1–6 m) leading to a higher impact velocity and higher deceleration values of ~ 4.6 g on average. However, also the velocity corrected values seem to be slightly increased (~ 2.7 kPa on average). Also, layering ranging from 0.23–1.8 m can be detected (Fig. 5.37, lower right).

Preliminary discussion

Despite the different water quality and nutrient content, the sediments of Lake Rotorua and Lake Rotoiti show similar geotechnical *in-situ* signatures in areas undisturbed by, e.g., pockmarks, springs, geothermal hotspots. Furthermore, these areas include no hint of layering. Sediment accumulation

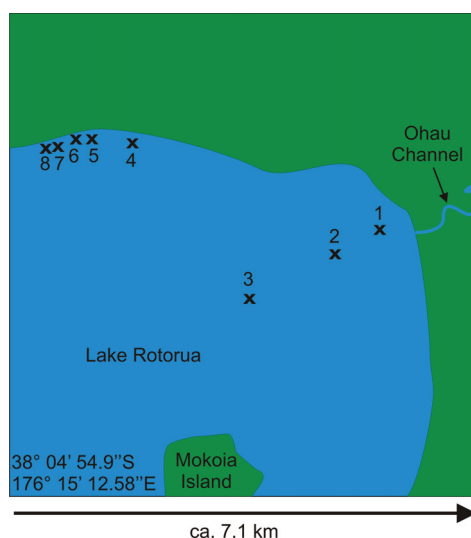


Figure 5.36: Deployment positions (crosses) in the vicinity of the Ohau Channel in Lake Rotorua.

areas seem to focus on depressions such as craters and pockmarks (see appendix C.7 - C.8).

In shallow waters in Lake Rotorua different profiles were monitored. The sediment appears hard, agreeing well with the observation of sandy sediments during the survey, and the coarse sand and gravel described by Hamilton et al. (2007).

The results by Stephens et al. (2005) prove that suspended sediment transport occurs in the Ohau Channel. Due to the morphology, it can be expected that the water flow slows down when reaching the Ohau Channel delta in Lake Rotoiti. This provides the conditions for sediment deposition. Regarding the dynamic penetrometer results, we can find layering that likely expresses sediment accumulation. Also, the area is getting conspicuously shallow that might be an indication for silting up.

Unclear is the slight increase of sediment strength of the underlying lake floor. One explanation might be that it is an artifact of the rate-dependency calculation and the higher penetration velocity in this area. As mentioned before, the used approach by Dayal and Allen (1975) includes some approximations (e.g., assuming K equals 1 - 1.5) that might lead to small deviations in the results. However, more likely seems to be an increase in consolidation due to the surcharge by the top layer or a change of geotechnical properties due to the enrichment of nutrients. Another possibility might be that not only in Lake Rotorua, but also in Lake Rotoiti the shallow water sediments are coarser, although not as coarse as in Lake Rotorua. This would clearly

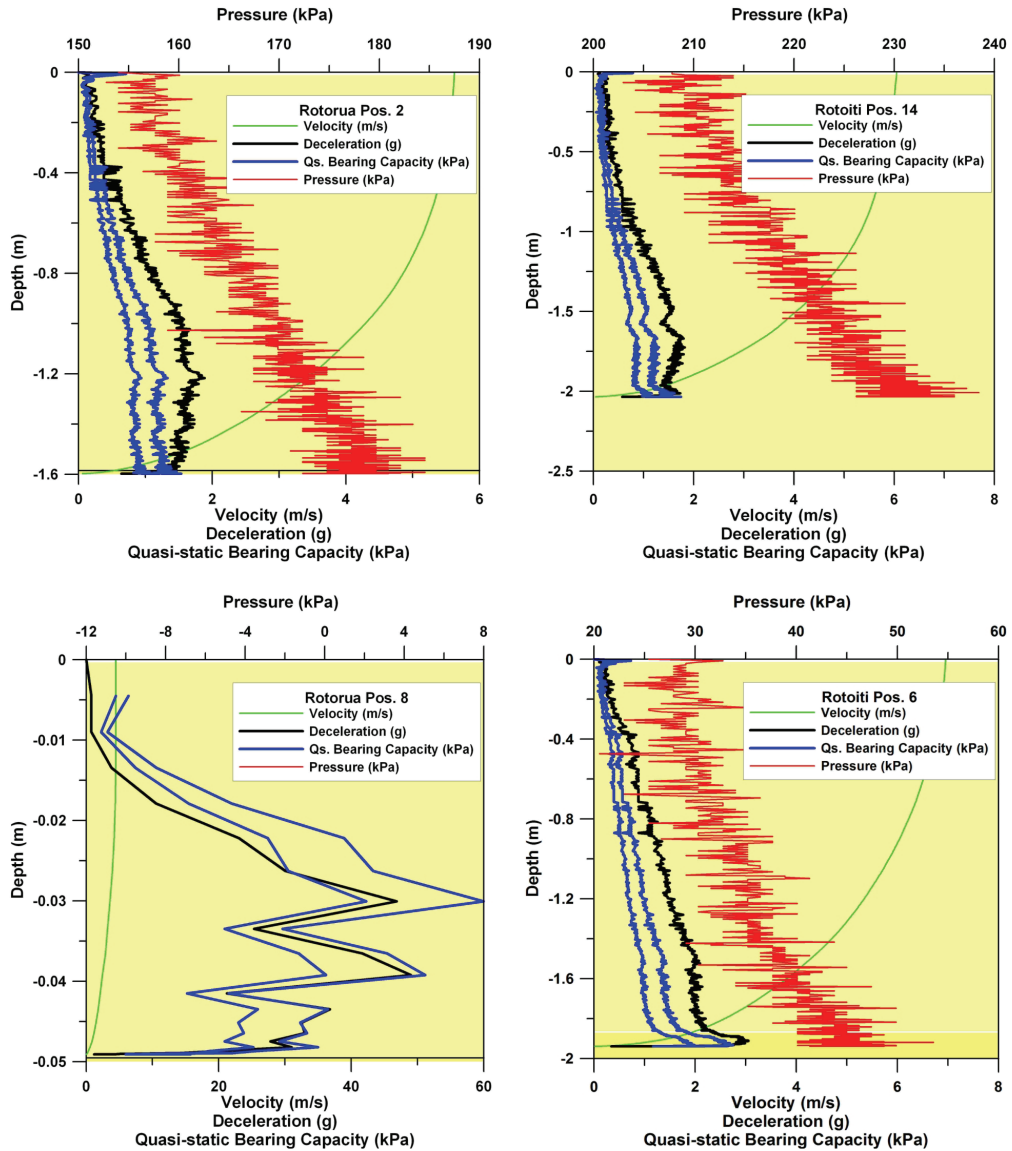


Figure 5.37: Dynamic penetrometer signatures from general coverage measurements in Lake Rotorua (upper left) and Lake Rotoiti (upper right), from a position close to the northern shore of Lake Rotorua (lower left) and within the diversion wall area in Lake Rotoiti (lower right). Layering can only be interpreted within the area of the diversion wall at a depth of ca. 1.9 m (light yellow-yellow shading).

identify the layering as border between original lake floor and deposited sediment. The geotechnical analysis of sediment cores reaching down to the lower layer would clarify this question.

For the development of the lake it would be essential to explore whether the assumed sediment accumulation reached an equilibrium or if a further silting up of the area must be expected. The former could be explained with an increase in flow velocity due to shallower water depths. This leads to a decrease in sediment deposition and more sediment is carried further away. If such an equilibrium cannot be reached, dredging of material might become necessary. Further measurements in a fixed frequency (e.g., every six months) would answer this question.

5.3 Attempt of a numerical simulation

In most of the studies in this thesis, the dynamic penetrometer results are in good accordance with other field measurements, laboratory methods, or the predictions of numerical simulations of hydrodynamics. However, further questions have been arisen from the results that could not be solved in the field, for example:

- May the approach by Dayal and Allen (1975) be improved by adapting it to the used dynamic penetrometer ? Dayal and Allen (1975) presented their approach for a lance-like dynamic penetrometer and applied it on clayey sediments only. Stoll et al. (2006) and Aubeny and Shi (2006) used it successfully for a projectile-shaped penetrometer, too, and Stoll et al. (2006) also proved the suitability for sandy seafloors. However, they admitted that the Dayal and Allen (1975) approach appears as the most suitable method, but that deviations are possible. Following that and the fact that we observed deviations in the results from Lake Rotoiti, Lake Rotorua and the wind energy field (see chapter 5.1.1 and 5.2.3), tests under more controlled conditions (regarding hydrodynamics, impact velocity, vessel stability, etc.) than in the field must be suggested.
- How does the sediment react in terms of compression and shearing during the penetration process with respect to different sediment properties? We found different penetration signatures for quartz and carbonate sands, respectively. The field and laboratory experiments suggested a different relationship between shearing and compression as a possible explanation, but, e.g., a visualization of the penetration process and sediment response to prove this hypothesis was lacking in the field.
- Can a correlation between sediment strength derived from the penetrometer and *in-situ* density be formulated? Density differences in the field are mirrored in the dynamic penetrometer signatures (e.g., chapter 4.2), however, the field experiments lacked *in-situ* density measurements to derive an empirical correlation.
- Can an empirical correlation between grain size and derived sediment strength be found? In particular, the results from the Tairua survey (chapter 4.3) proved the strong dependence of derived sediment strength and grain size, but to find an empirical correlation between these properties a higher variation of grain sizes would be helpful.

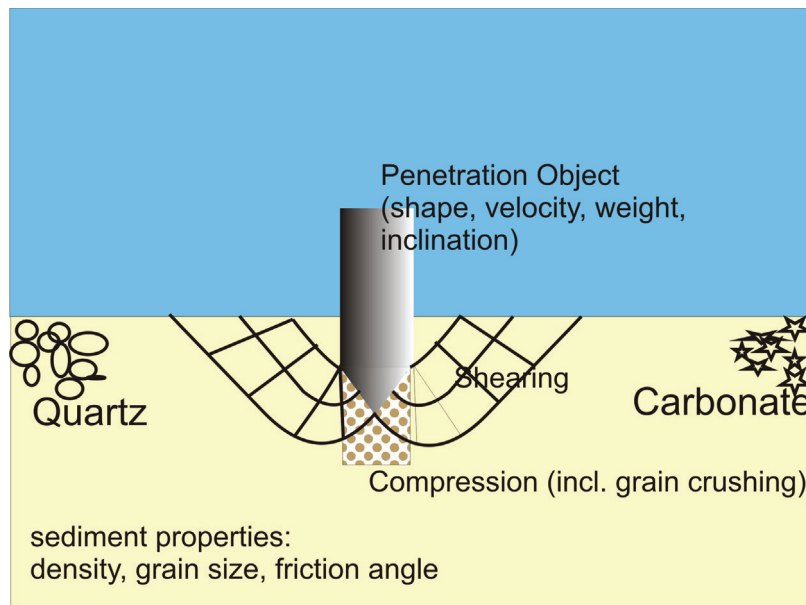


Figure 5.38: Sketch of the aspired model in the first stages of development.

Controlled tests in terms of physical modeling and numerical modeling would be powerful tools to address such questions. Despite the strong focus on field work in this thesis, the collaboration with the working group for Modeling of Sedimentation Processes at MARUM, University of Bremen, in the framework of a Master Thesis project made it possible to add numerical modeling to the field and laboratory experiments. In this thesis only the conceptual idea and a start-up will be presented. Results will be published in Jannis Kuhlmann's Master Thesis at the end of 2010.

In this numerical attempt, it is aimed for the investigation of the dynamic penetrometer – sediment – interaction with regard to varying penetrometer properties (e.g., weight, shape, velocity, inclination) as well as to varying sediment properties (e.g., density, grain size, friction angle) (Fig. 5.38). At a later stage, layering as seen in areas of sediment remobilization may be included (Fig. 5.39). To narrow down these wide ambitions, the simulation of *Nimrod* penetrating into a homogenous sand (corresponding to the geotechnical properties found during surveys in the North Sea and around Hawaii, chapter 4.1) was targeted.

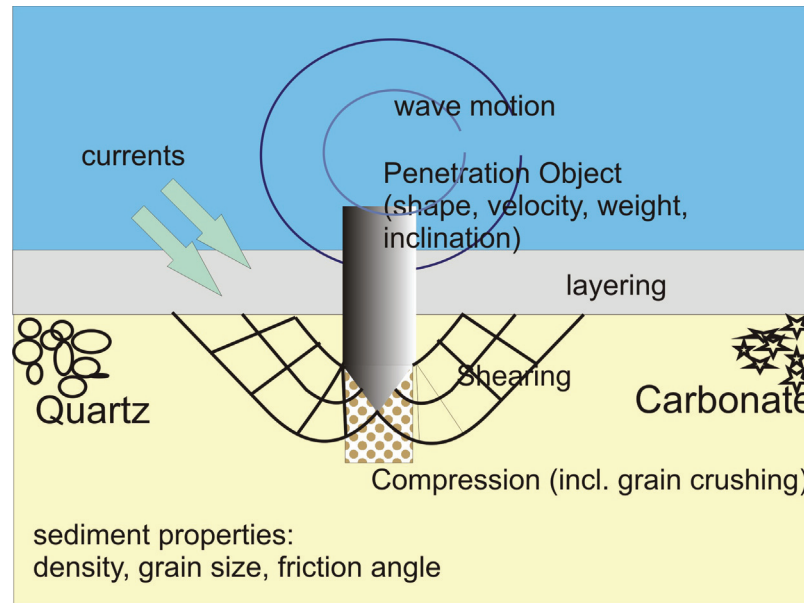


Figure 5.39: Sketch of the aspired model in the later stages of development.

5.3.1 Numerical modeling of dynamic penetrometer – sediment – interaction (a state-of-the-art)

The numerous attempts of numerical simulations of penetrometer deployments in the last years express the increasing interest in this topic and its high complexity (e.g., Ahmadi, 2000; Markaukas et al., 2002; Shi, 2005; Tekeste et al., 2006; Cetin and Isik, 2007; Abelev et al., 2009 a/b; Liyanaoathirana, 2009; Carter et al., 2010). Major differences can be found in (i) the discretization method, (ii) the coordinate specification, (iii) the type of soil (cohesionless/ cohesive), and (iv) the type of penetration (static/dynamic). In the following paragraphs, these important points will be briefly introduced, and examples for the use in the framework of penetrometer simulations presented.

Discretization method

The starting point of any numerical model is the mathematical model. This is a set of partial differential or integro-differential equations and boundary conditions (Ferziger and Peric, 2002). Thus, in case of geotechnical applications, mechanical and kinematic variables are related for particular geometries and properties (FLAC 3D manual, 2006). The mathematical model may include approximations depending on the target application (Ferziger

and Peric, 2002).

The discretization method approximates the differential equations by a system of algebraic equations for the variables at some set of discrete locations in space and time (Ferzinger and Peric, 2002). There are many approaches, but the most common ones in geotechnical applications are the finite difference method (FDM) and the finite element method (FEM) (e.g., Ahmadi, 2000; Markaukas et al., 2002; Shi, 2005; Tekeste et al., 2006; Cetin and Isik, 2007; Thevanayagam and Ecemis, 2007; Abelev et al., 2009a/b; Liyanapathirana, 2009).

In both cases, a numerical grid consisting of grid nodes and grid lines is defined, however, the methods mainly differ (i) in the location of the nodes (Fig. 5.40 and 5.41), where the partial differential equations are solved, and (ii) how they are solved. The FDM bases on the definition of derivatives, whereas the FEM uses the integral form of the conservation equation as a starting point. The FDM is simple and very effective in case of structured grids, however, complex geometries may be difficult to address (Ferzinger and Peric, 2002; Dahmen and Reusken, 2008). Analogous, the advantage of the FEM in case of geotechnical problems which include large deformations can be noted (e.g., Bathe et al., 1975; Braun and Sambridge, 1994). Consequently, FEMs are frequently used for simulations of penetrometer deployments (e.g., Lu et al., 2001; Abelev et al., 2009b; Carter et al., 2010). Nevertheless, also successful simulations of penetration processes using FDMs can be found in the literature (e.g., Bolton and Gui, 2005; Cetin and Isik, 2007; Abelev et al., 2007a; Ahmadi and Khabbazian, 2009). Following that and the fact that we target a small penetration of about 10-20 cm (typical penetration depth of *Nimrod* into sandy seafloors), both methods appear suitable.

Coordinate specification

Changes in a coordinate system can be observed in a different manner: using the Eulerian or the Lagrangian specification. In case of the former, the coordinates are fixed in space, whereas in case of the latter, the coordinates move with the particle (Tritton, 1988). In consequence, the point of view and the perspective on the outcome differ depending on the specification used. Furthermore, it has to be considered in the calculation scheme. For example, in case of the Lagrangian analysis the incremental displacements are added to the coordinates leading to a grid that moves and deforms with the material it represents (e.g., Ahmadi, 2000).

A combination of both approaches in one simulation can be realized by the

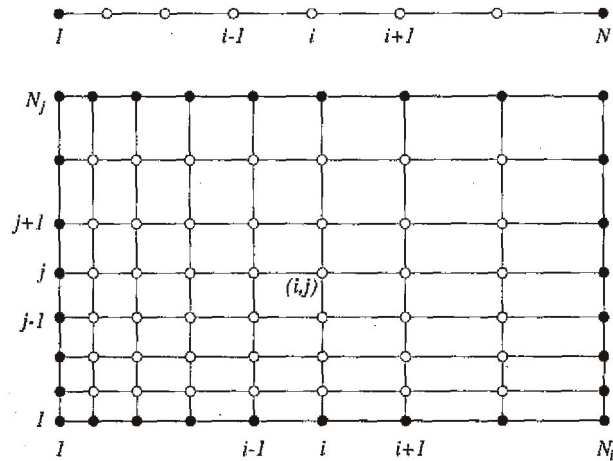


Figure 5.40: An example of a 1D (above) and 2D (below) Cartesian grid for finite difference methods (after Ferziger and Peric, 2002).

so-called Arbitrary Lagrangian-Eulerian computing method (ALE) using a mesh that may be moved with the material (Lagrangian), be held fixed (Eulerian), and be moved in any other prescribed manner (Hint et al., 1974). Regarding the simulation of deformation problems in geotechnics, a Lagrangian coordinate specification offers significant advantages compared to the Eulerian approach by reflecting the deformation of the soil or rock within the grid movements (e.g., Braun and Sambridge, 1994). Though, it might come to mesh distortions in case of “relatively large” deformations (e.g., Ahmadi et al., 1999; Carter et al., 2010). In the most recent publications dealing with dynamic penetrometer simulations, the ALE method was presented as a successful approach even when the Lagrangian approach failed (Carter et al., 2010).

In consequence, the ALE seems to be the most promising coordinate specification for the proposed simulation, however, for the targeted small deformations the Lagrangian approach might be sufficient.

Type of soil and the constitutive model

A constitutive model describes various aspects of soil behavior in detail, and represents the soil mechanical base in numerical models of geotechnical applications (e.g., Ti et al., 2009). For example, the cohesion of the simulated

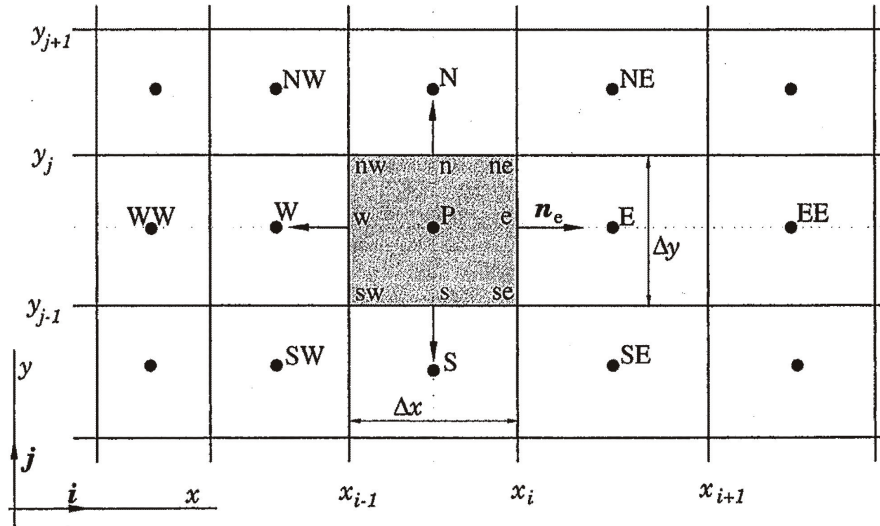


Figure 5.41: A typical Cartesian 2D grid for the finite element method (after Ferzinger and Peric, 2002).

sediment plays an important role within the choice of the constitutive model (FLAC 3D manual, 2006). Some constitutive models cover only either cohesionless or cohesive sediment (e.g., Cam-Clay; FLAC 3D manual, 2006). Following that, a numerical model dealing with a geotechnical problem can often be simplified by focussing on either cohesive or cohesionless sediment and choosing the respective constitutive model. In the literature only a few numerical simulations are presented dealing with sand as well as clay (e.g., Cetin and Isik, 2007).

In penetrometer simulations, predominantly constitutive models were used which assume that the sediment is elasto-plastic and follow a Mohr-Coulomb yield criterion (see chapter 2.2.1) (e.g., Ahmadi, 2000; Cetin and Isik, 2007; Abelev et al., 2009a/b). This applies to sandy sediments (Ahmadi, 2000) as well as to muddy sediments (Abelev et al., 2009a/b). However, input properties such as cohesion, density, bulk and shear modulus may vary significantly. Consequently, we will aim for an elasto-plastic Mohr-Coulomb model, and integrate the sediment properties presented in chapter 4.1 for the different sands, respectively.

Type of penetration: static or dynamic

Similar to the field, static and dynamic penetrations have to be regarded differently in numerical simulations. In case of a dynamic penetration, the non-linear strain rate dependency of the sediment has to be considered (Dayal and Allen, 1975). This has to be taken into account during setting up material properties and grid geometries (Abelev et al., 2009b; Liyanapathirana, 2009).

In the literature, different ways to deal with penetrometer simulations are presented:

- Dynamic penetration: Here the penetrometer (specified by geometry, weight, surface roughness, etc.) impacts the soil with a chosen initial velocity and under influence of gravity. The following prediction of the soil deformation as well as of the penetration process including penetration depth and penetration velocity profile result from the penetrometer properties, the initial velocity and the soil properties. For example, Abelev et al. (2009b) and Carter et al. (2010) presented such simulations matching *in-situ* results for clays using a FEM and an ALE coordinate specification.
- “Pseudo-static” penetration: A “pseudo-static” (Abelev et al., 2009a) approach computes a static collapse load for a pre-embedded penetrometer of specific geometry and surface properties at a series of depths. It neglects effects of prior strains and deformations occurring during the penetration process. The results are presented in terms of maximum sediment strength at various penetration depths. This method was successfully (numerical results match *in-situ* results) applied on clays by Aubeny and Shi (2006) using the FEM and the ALE coordinate specification, and by Abelev et al. (2009a) using the FDM and Lagrangian coordinates.
- Static penetration: In case of a static penetration, the concept of a pre-embedded penetrometer can be found, too. For example, Cetin and Isik (2007) perform a cone penetration simulation in three stages: The first stage involves the generation of an *in-situ* stress state. In the second stage a cavity in the soil mesh is created equivalently to the penetrometer dimensions by pushing the corresponding soil elements horizontally by an amount equal to the radius of the penetrometer. Finally, in the third stage, the penetrometer is pushed into the soil with a constant velocity. Ahmadi et al. (1999) treated the problem as a deformation process only, and pushes soil elements located along the path

of an imaginary penetrometer away. The grid points associated with these soil elements are given a vertical downward as well as a horizontal displacement. The outcome is a prediction of sediment resistance which can be compared to *in-situ* static results. Cohesionless as well as cohesive sediment were addressed this way, mostly using the FDM and Lagrangian coordinates (Cetin and Isik, 2007; Ahmadi, 2000).

In summary, to predict the penetration behavior of a dynamic penetrometer and the penetrometer – sediment – interaction in the dynamic case only from initial conditions, a more complex numerical model set up using the FEM and an ALE coordinate specification, as well as the consideration of strain rate effects within the material properties is required (Abelev et al., 2009b; Carter et al., 2010). To derive sediment strength results which are comparable to *in-situ* dynamic experiments, and to observe the sediment response during collapse load in a certain depth, a “pseudo-static” approach seems to be sufficient, and theoretically, the results from the static simulation should be comparable to *in-situ* quasi-static strength results.

5.3.2 Choice of commercial code

It was aimed for a numerical simulation of the small dynamic penetrometer *Nimrod* into homogenous sand. In the first attempts, the true *Nimrod* geometry with conical tip (see chapter 3.1.5) was targeted. The sand should correspond to sands from the North Sea and Bays of Hawaii, respectively (for detailed geotechnical description see chapter 4.1). The penetration should be straight vertically (no inclination of the probe at this stage), and should reach a depth of about 20 cm with an initial penetration velocity of 4–10 m/s (see chapter 4.1). As a successful result (i) a sediment strength profile comparable to the *in-situ* measurements, and (ii) detailed information about the sediment response are aspired.

To simplify the first tests, a static simulation with constant penetration velocity was targeted first. A successful run would be defined by sediment strength results comparable to quasi-static *in-situ* profiles as well as to analytically derived bearing capacity predictions (chapter 4.1), and by deformation patterns being in line with the theoretical approaches by, e.g., Terzaghi (1943). After accomplishment of this task, it is planned to replace the constant penetration velocity by an *in-situ* derived *Nimrod* penetration velocity profile (dynamic) and to observe the sediment reaction.

Following the literature review presented in chapter 5.3.1, the proposed simulation seems to be realizable using a FDM or FEM, because we expect

relatively small deformation patterns. Furthermore, a Lagrangian or ALE coordinate specification seems to be sufficient as no prediction of the penetration performance of the probe is targeted. The use of an elasto-plastic constitutive model satisfying the Mohr-Coulomb criterion appears as method of choice for the proposed problem.

In accordance with the successful simulations by, e.g., Ahmadi (2000), Cetin and Isik (2007), and Abelev et al. (2009a), we chose the commercial code FLAC 3D (Fast Lagrangian Analysis of Continua in 3 Dimensions) to approach this project. FLAC 3D developed by the Itasca Consulting Group, Minneapolis, USA, is an explicit (i.e., forward) finite difference program using the Lagrangian calculation scheme to study the mechanical behavior of a continuous three-dimensional medium as it reaches equilibrium or steady plastic flow numerically. The mechanics of the medium are derived from general principles (definition of strain, laws of motion), whereas the idealized material is defined by constitutive equations. Following the Lagrangian formulation, a point in the medium is characterized by the vector components of position, displacement, velocity and acceleration (FLAC 3D manual, 2006). FLAC 3D Version 3.1 provides twelve basic constitutive models distinguished into null, elastic and plastic model groups. For the proposed simulation, the Mohr-Coulomb model for shear failure in soils and rocks was chosen. FLAC 3D offers the use of interfaces as planes on which sliding or separation can occur. Such interfaces are important for the contact zones between penetrometer and soil.

5.3.3 Set up

In the following section, the set up of the first attempts to simulate a static penetration of *Nimrod* are described.

Grid

Considering the fact that the penetrometer inclination is planned to be tested at a latter stage, we have chosen a full cylindrical grid (3D) with two different meshing zones: (i) a fine meshed cylinder having double the penetrometer radius, and (ii) a wider meshed cylindrical shell around it. This concept provides a high resolution in highly affected areas without wasting calculation capacity and time on lowly affected areas, and was realized by using the primitive mesh shape provided “cshell”. It is defined by 10 reference points P, 4 size entries n (number of grid points related to a chosen area), 4 di-

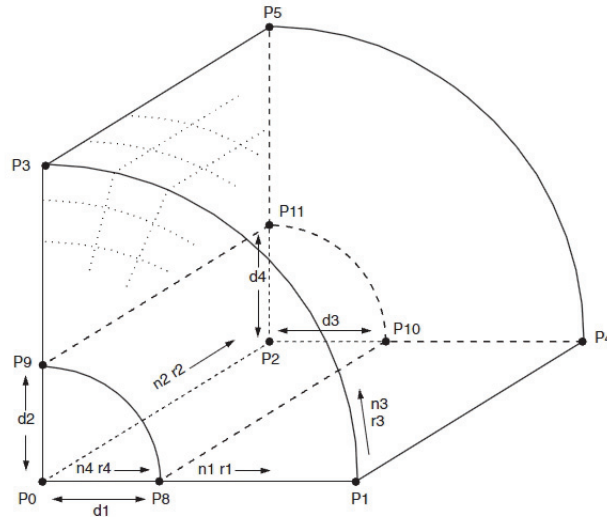


Figure 5.42: Concept of *cshell* grid in FLAC3D (FLAC manual, 2006).

mension entries d (size related to reality in meters), 4 ratio entries r (grid point spacing ratio), and the choice whether the center area should be filled or excavated (Fig. 5.42). The penetrometer is formed by a simpler cylindric grid (Fig. 5.43). In several runs different resolutions of grids were tested; these are presented in detail in Table 5.1.

Material properties

The Mohr-Coulomb elasto-plastic model is a reasonable approximation for the behavior of sand (Bolton and Gui, 1995; Ahmadi, 2000; Abelev et al., 2009a). The input parameters required are density, tension limit, friction angle, cohesion, dilation angle, bulk modulus and shear modulus. The bulk and shear modulus define the elastic behavior below the failure envelope, whereas friction angle, cohesion and dilation angle define the plastic response at failure (Ahmadi and Khabbazian, 2009).

Friction angles (ϕ) for targeted sands (quartz sands from the North Sea, and carbonate sands from the Pacific) were determined using an uniaxial shear box (chapter 4.1). Corresponding to these results, it is aimed for friction angles ranging from 30° to 37° . The cohesion equals zero in case of cohesionless sands. The dilation angle (ψ) expresses the behavior of loosening up ($\psi > 0$) or consolidating ($\psi < 0$) during deformation of soils. After Bolton (1985) the dilation angle for sands can be determined from the friction angle and the

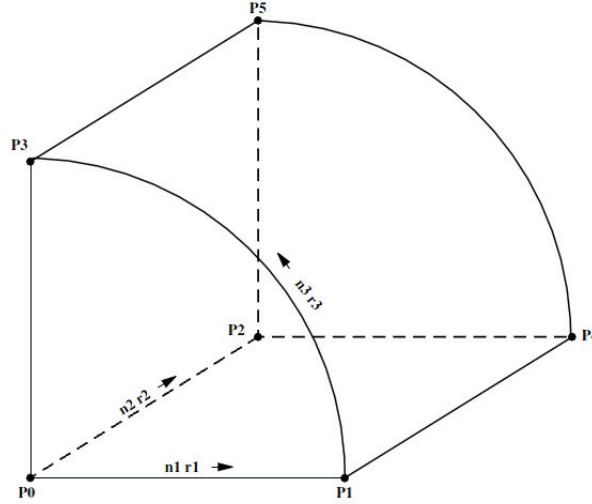


Figure 5.43: Concept of *cylinder* grid in FLAC3D (FLAC manual, 2006).

critical angle of friction (ϕ_{crit}) using:

$$\phi = \phi_{crit} + 0.8\psi. \quad (5.1)$$

The critical angle of shearing resistance of sand ranges generally between $31-35^\circ$. Bolton and Gui (1995) assumes it to be 32° , whereas Ahmadi and Khabbazian (2009) used 33° for their numerical simulation.

To estimate bulk modulus (K) and shear modulus (G), Ahmadi et al. (1999) and Ahmadi and Robertson (2005) suggested the following relations:

$$G = K_G P_A \left(\frac{\sigma'_m}{P_A} \right)^n \quad (5.2)$$

$$K = K_B P_A \left(\frac{\sigma'_m}{P_A} \right)^m, \quad (5.3)$$

with σ'_m being the mean effective stress and P_A the atmospheric pressure equal to 98.1 kPa. The exponents m and n range from 0.2 to 0.7, and the shear and bulk stiffness numbers K_G , K_B can be assumed to depend only on the relative density of sand. For the simulation, m and n were set equal to 0.4 (Ahmadi and Khabbazian, 2009), and the shear and bulk stiffness numbers were derived by comparison to the results from Ahmadi and Khabbazian (2009) leading to bulk stiffness numbers ranging between 280 and 358 and shear stiffness numbers between 167 and 215. In consequence, a bulk modulus of ~ 60 MPa and a shear modulus of about ~ 30 MPa follow the

File name	Dimensions			No. of cells/ ratio			Max. grid resolution x z (cm) (cm)		
	Outer radius (cm)	Inner radius (cm)	Height (cm)	Outer zone	Inner zone	Radial per quarter		Height	
Initial-cshell-60	100	11	60	40/1.05	20/1	10/1	20/1	0.55	3
Initial-cshell-60-II	100	11	60	20/1.05	10/1	5/1	10/1	1.1	6
Initial-cshell-60-III	100	11	60	40/1.05	20/1	10/1	10/1	0.55	6

Table 5.1: Tested grid variations.

geotechnical properties determined from quartz and carbonate sand samples (chapter 4.1). This agrees with the range of bulk and shear moduli (10–200 MPa) found in the literature as initial condition for sandy soils in numerical models using FLAC considering differences in density, void ration, etc. (e.g., Ahmadi, 2000; Benmebarek et al., 2005; Babu et al., 2008; Pisheh and Hosseini, 2010).

The density was assumed to be 2000 kg/m^3 following derived unit weights from chapter 4.1, and the tension limit was set equal zero after, e.g., Ahmadi (2000).

The penetrometer was simulated with a high density prohibiting deformation of the device during impact and penetration ($4000\text{--}10000 \text{ kg/m}^3$; for comparison: e.g., titanium $\sim 4500 \text{ kg/m}^3$; steel $\sim 7800 \text{ kg/m}^3$), and with a constant velocity (see below section about velocity scaling). Interfaces defined between penetrometer and sediment were characterized by a decreased friction angle ($< 50\%$ of the sediment friction angle) following the suggestions by Gerdes (2010).

Boundary conditions and scaling

The simulation deals with two objects: the penetrometer and the soil body. In accordance with the gridding (see above), the soil body is a cylinder having a radius of 100 cm and a height of 60 cm (Fig. 5.44). Regarding the simulated penetrometer size (conical tip and cylindrical body with a diameter of 11 cm), the aspired penetration depth (~ 20 cm), and examples from the literature (e.g., Ahmadi, 2000; Shi, 2005; Cetin and Isik, 2007; Abelev et al., 2009a/b), this scaling seems to be sufficient to cover all sediment movements induced by the penetrometer penetration. Three different types of boundary conditions are applied on the different boundary zones in the simulation. At this stage of simulations, the penetrometer should move only downwards. This can be realized by so-called Roller boundary conditions which allow movements only along one axis, in this case along the z-axis (Fig. 5.44). For the sediment body, different boundary conditions apply on different areas: The top of the soil body has free boundaries. Movements are allowed in all directions. Sediment can be elevated, sink and be pushed to the side. However, this does not apply on the side boundaries. Here, Roller boundary conditions are initialized again. The sediment is allowed to move along the z-axis, but not to the side. Following that, the cylindric shape is preserved (Fig. 5.44). Due to the scaling of the soil body compared to the penetrometer, no effects of the Roller boundary conditions of the soil body sides on the penetration performance or sediment deformation are expected.

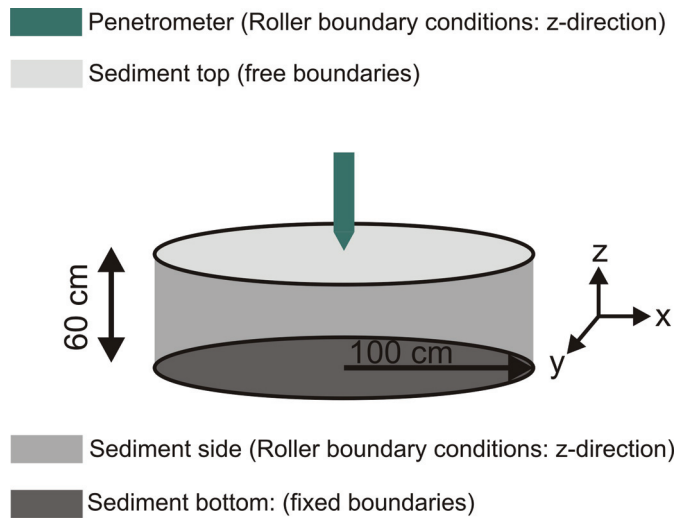


Figure 5.44: Sketch of simulation scaling with respect to the penetrometer size (here *Nimrod* with conical tip). The boundary conditions of the penetrometer mesh allows movements along the z-axis only (Roller conditions). The soil body (grey) is characterized by free boundaries at the top (light grey), Roller boundary conditions (allowing movements along the z-axis) at the side (medium grey), and fixed boundaries at the bottom (dark grey).

At the bottom of the soil body, the boundaries are fixed. No movements in any direction are allowed. This helps to conserve the original shape of the soil body. Without the stabilization at the bottom and at the sides, the sand cylinder would immediately collapse to a loose pile of sand. Following that, the soil body simulates a certain amount of sediment embedded in a greater framework of sediment like the seafloor. The scaling should make a simulation of infinite sediment depth and width possible, and should rule out effects on the penetration process or deformation patterns caused by the boundary conditions.

Velocity scaling

Nimrod's in-situ penetration velocities (4–10 m/s) were aspired, however, this would cause a scaling problem using FLAC 3D Version 3.1. Each iteration step represents a time step of one second. Consequently, the penetrometer would blast through the soil body within one iteration step, but a penetration process would not be calculated and simulated. Following that, it is not possible to simulate the *in-situ* penetration velocity with the aspired resolutions (Tab. 5.1) and geometries (Fig. 5.44). Thus, for the first tests, the

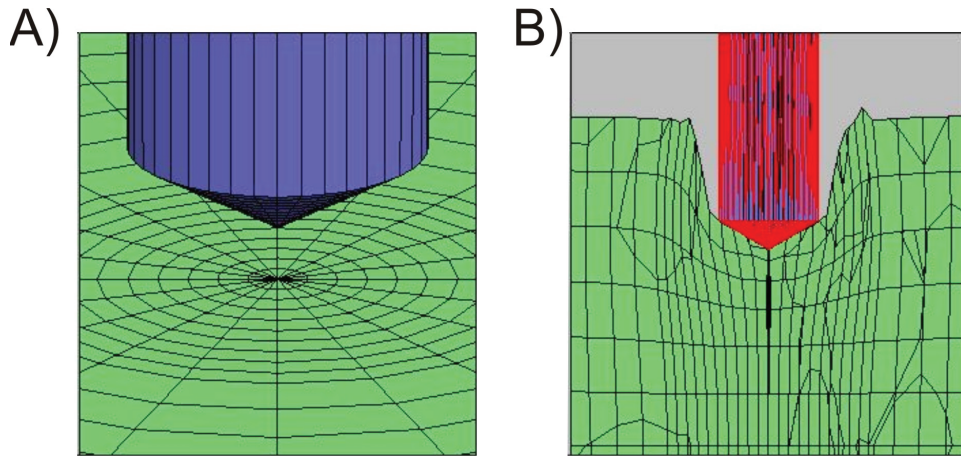


Figure 5.45: A) Initial position of the simulation: The penetrometer (blue) hovers over the middle of the soil body (green). B) Example of a simulation: The penetrometer (red-blue) penetrated the soil body (green) leading to deformation of the grid cells, and in doing so, the sediment.

penetration velocity was significantly scaled down to $5e-7$ m/s which proved to be a reliable range guaranteeing no calculation hiccups while keeping the original geometry scaling.

Course of action

In the initial position of the simulation, the penetrometer hovers above the soil body center (Fig. 5.45). The simulation starts with the constant downward movement of the penetrometer with the chosen velocity ($5e-7$ m/s). The penetrometer impacts the sediment and penetrates the soil body with the constant velocity. The sediment reacts with deformation (Fig. 5.45), and changes of stress and strain state. About 400000 iteration steps would be necessary to reach a penetration depth of about 20 cm.

5.3.4 Exemplary test run

Doing the first test runs (FLAC 3D input code example can be found in the appendix E), a major problem occurred. After a penetration of less than 20 cm, an “illegal geometry error” was announced by FLAC 3D, and the simulation was automatically aborted. The message means that due to a large distortion of some grid cells the execution cannot continue.

To better the understanding of this issue, tests with changing material prop-

erties and geometries were carried out. During these tests, above all seven data points at the sediment surface were observed to study the deformation patterns. The first is on a vertical axis (z-direction) with the penetrometer tip (Fig. 5.46). The other points follow along the x-axis with defined distances from the first point: 2.7 cm, 5.5 cm, 11 cm, 19 cm, 33 cm and 64 cm. The sediment surface represents the first collapse load during penetration and is not affected by surcharge.

Exemplary results in terms of displacement will be given for a run with the following initial sediment properties: Mohr-Coulomb constitutive model, Initial-cshell-60 grid (Tab. 5.1), a bulk modulus of 60 MPa, a shear modulus of 30 MPa, the cohesion equals zero, the dilation angle equals zero, a sediment density of 2000 kg/m^3 , and a friction angle of 34° .

During this test an “illegal geometry” occurred at a penetration depth of about 12 cm. Figure 5.47 shows the deformation patterns until abortion. Three main actions can be observed: i) grid points under the cone are pulled down with the cone, (ii) grid points under the cone bevel and in the close vicinity of the cone are additionally pushed to the side, and (iii) grid point in a distance from 14–59 cm from the cone are slightly elevated. *In-situ*, the sediment is compressed until the bearing capacity is exceeded, and then the sediment fails and is pushed to the side following, e.g., Terzaghi’s (1943) or Meyerhof’s (1953) deformation patterns (Fig. 2.3). The sediment pushed to the side might cause an elevation of the soil surface as seen in the simulation (e.g., Terzaghi, 1943). However, the dragging of the first grid points down with the penetrometer seems to be unrealistic, and is very likely the reason for a grid cell distortion and “illegal geometry”. This problem is caused by the fact that FLAC 3D does only allow failure at pre-defined failure planes, and a failure and separation of the sediment under the cone tip as it occurs *in-situ* is impossible using the above described set up. Following that, it has to be assumed that the whole deformation process and stress and strain development is disturbed by this affect, and that such results are not reliable. Finding a solution for this problem is the necessary next step and is currently approached. Ideas might be the definition of an interface at the failure zone. However, this might lead to problems with the 3D cylindric geometry. Another possibility might be to include an automatic remeshing routine as available for FLAC 2D. This would allow a splitting up of grid cells when a certain grid cell size or distortion is reached, but the central grid point would still be dragged down with the penetrometer. Following the current results, it might be necessary to accept approximations such as changing from a 3D full cylindric grid to a 3D quarter cylindric grid (solving the sediment separation problem), or a general coarsening of the grid (leading to a smaller distortion of grid cells) to approach *in-situ* results. In particular, regarding the velocity

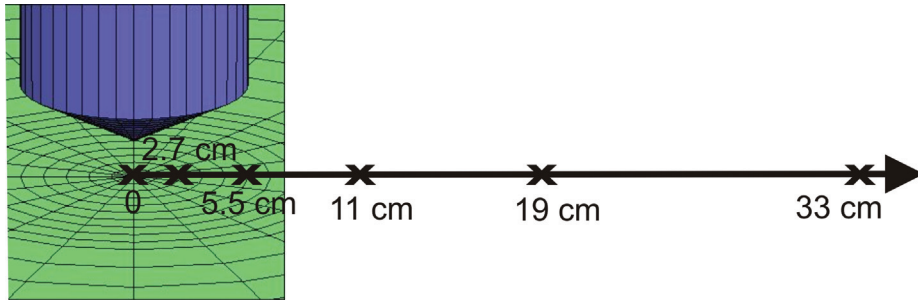


Figure 5.46: Location of monitored grid points during first test runs. All of them follow the x-axis. The last grid point in a distance of 64 cm is not depicted here.

issues, a change of commercial code or FLAC version might be considered, too. However, final conclusions cannot be drawn from these preliminary test runs. Further developments, results and conclusions will be presented in the framework of the corresponding Master Thesis.

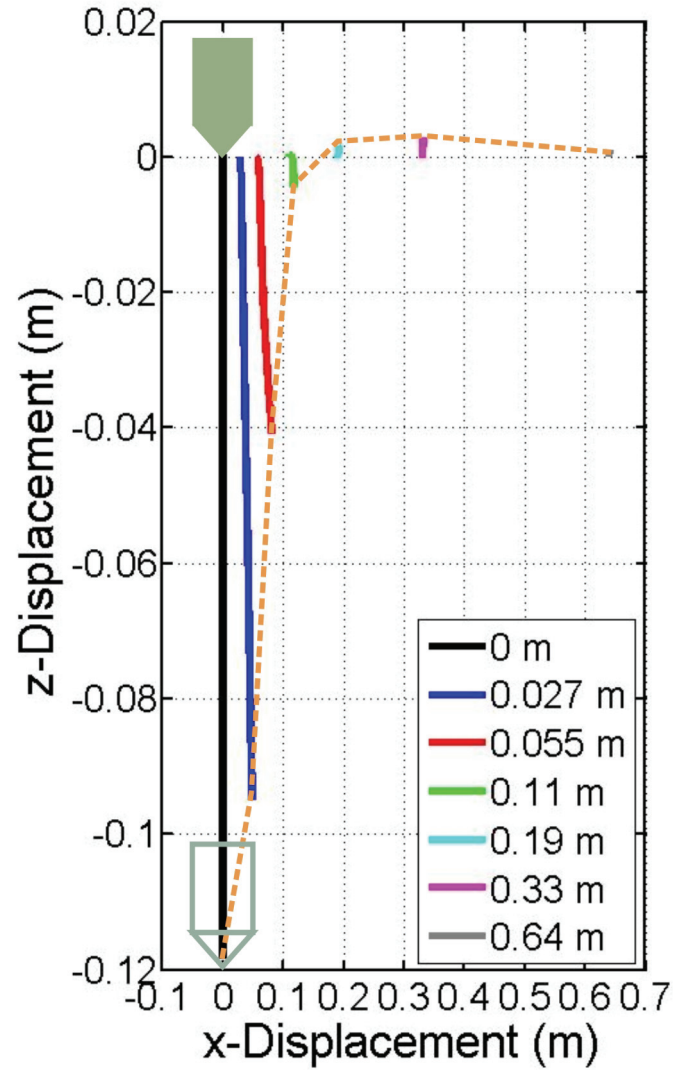


Figure 5.47: Results in terms of displacement of the presented test run example. The solid lines indicate the displacement of the respective grid point (see legend). The dashed orange line connects the final positions of the respective grid points, and for orientation, the penetrometer size at initial position (pale green filling) and at final position (pale green lines) is sketched.

Chapter 6

Conclusions

The aim of this thesis was the (i) development of a dynamic penetrometer suitable for the investigation of sediment remobilization in the uppermost sediment surface, (ii) the application of this device in the framework of geological and geotechnical studies of areas of sediment remobilization, and (iii) the interpretation of these *in-situ* geotechnical results of sediment remobilization processes. During the numerous studies the new device *Nimrod* was supported by a FFCPTU lance, acoustic methods such as MBES, ADCP and SSS, sediment sampling combined with standard geotechnical laboratory methods (e.g., determination of grain size distribution, uniaxial shear box, etc.) and/or by numerical modeling of hydrodynamics. The following conclusions can be drawn:

- The small dynamic penetrometer *Nimrod* developed in the beginning of this study delivers results comparable to other small dynamic penetrometers such as the eXpendable Bottom Penetrometer, and is suitable for deployments in challenging areas (e.g., strong hydrodynamics, small vessels, close to foundations). It is very robust and can be deployed on all kind of sediments from very soft clays to hard sand.
- The penetration is limited depending on the sediment strength (mean penetration depth for sand 0.08–0.16 m, for silt 0.3–0.8 m, for soft clay 0.6–2.5 m). The device is suitable only for the investigation of the uppermost sediment layers.
- Sediment strength in terms of a quasi-static bearing capacity equivalent can be estimated matching laboratory results in case of plain and homogeneous seafloors (chapter 4.1). However, the comparison with other methods may show deviations due to approximations made during the calculation process (e.g., neglect of penetrometer shape factors,

neglect of side friction and side adhesion, empirical factor $K = 1 - 1.5$).

- Different grain size classes such as sand, silt, clay can be distinguished, but differences in grain size on a smaller scale are reflected in the dynamic penetrometer results, too. A non-linear trend of increasing sediment strength with decreasing grain size of sands was observed (chapter 4.3).
- The sediment strength profile of quartz sand differs from the one of carbonate sands. Following that, mineralogical composition is reflected in the dynamic penetrometer results (chapter 4.1).
- Layers of different sediment density are displayed as different gradients in the sediment strength profiles. This is the base for investigations of sediment remobilization processes and makes the detection and vertical quantification of (recently) mobilized sediment layers possible (e.g., chapter 4.1-3, 5.1.1-3, 5.2.1-3).
- In doing so, the sediment remobilization of a subaqueous dune was observed depending on the tidal phase. Results could be correlated to acoustic methods and supported the existing theories about the sediment remobilization patterns in this region (chapter 4.2).
- The detection of sediment erosion and sediment accumulation areas on sorted bedforms and along a shifting sandbar provided a base to build up/ confirm a model of the ongoing sediment dynamics as well as development and maintenance of the features (chapter 4.3 and 5.1.3).
- In ports, harbor mud disposal sites and other areas of coastal or lacustrine engineering, mud accumulation areas could be localized and quantified. This might lead to a support in decision making of further interventions and the industrial utilization of the areas (chapter 5.2).
- A sediment strength pattern varying with time was derived from dynamic penetrometer surveys at tripod wind energy converter foundations. The patterns are related to scouring at the foundations. This unique *in-situ* geotechnical study might be useful for an improvement of scouring theories at offshore wind energy converter foundations (chapter 5.1.1).

In summary, it was achieved to design a dynamic penetrometer suitable for the investigation of seafloor stiffness and sediment remobilization. The results have the potential to contribute to the understanding of natural sediment remobilization processes as well as to the understanding and decision

making in case of sediment remobilization induced by human impact. The findings form a solid base for further studies of sediment remobilization using dynamic penetrometers, however, improvements should be targeted by addressing questions, e.g., for a correlation between *in-situ* density and measured sediments strength, and uncertainties such as the empirical factor K or shape factors in the calculation process of quasi-static bearing capacity. The numerical approach started here is one example and has to be continued.

Chapter 7

Outlook

The outcome of this thesis can be regarded as an introduction of dynamic penetrometers to the investigation of sediment remobilization processes. Thereby, it focussed on field work, and only first attempts of controlled measurements in a wave channel, and of numerical simulation of a *Nimrod* penetration into sand were introduced. The major aim was achieved, however, the improvement of the used approaches as well as arisen questions may be addressed in the future.

Concerning the used approach to derive quasi-static bearing capacity, for example, the so-called shape factors (Meyerhof, 1953), which consider the penetrometer geometry within the bearing capacity approach (Terzaghi, 1943), were neglected, because the penetrometer tip geometry was kept constant during the respective surveys. Nevertheless, the neglect of shape factors influences the derived values of bearing capacity, and in doing so, may lead to deviations in case of a comparison to other methods. Furthermore, deviations may be generated from the estimation of quasi-static bearing capacity from dynamic bearing capacity. The used empirical approach by Dayal and Allen (1975) is highly recommended (Stegmann et al., 2006; Stoll et al., 2006), but it has to be considered that it was developed for a more lance-like penetrometer, and that it was originally applied on clays (Dayal and Allen, 1975). Nevertheless, Stoll et al. (2006) showed that it is the most suitable approach to estimate quasi-static strength values for the eXpendable Bottom Penetrometer (projectile-shape) on sand, but they admitted that deviations may occur. Following that, at this stage it cannot be obviated that the slight deviations seen in Lake Rotoiti/ Lake Rotorua (chapter 5.2.3) and in the wind energy field (chapter 5.1.1) may follow the calculation procedure. A third approximation made, is the neglect of side friction and side adhesion. Theoretically, side adhesion and friction must be estimated and subtracted from the measured sediment resistance.

Furthermore, questions came up during the studies presented. For example, a non-linear dependence of grain size and sediment strength was observed, however, the variety of grain size distribution in the field were not sufficient to develop a mathematical correlation from the results. The same applies on the question for a correlation between *in-situ* density and sediment strength. The differentiation of density layers using the sediment strength profiles was possible, but to derive a mathematical correlation delivering *in-situ* density values was not possible during the surveys. Such aims should be targeted by physical and numerical modelling in the future.

Numerical modelling

First, the model must succeed to simulate an *in-situ* *Nimrod* deployment into the chosen sediment. This can be tested by comparing the simulated sediment strength predictions to *in-situ* results and analytical predictions. Also, it may be strived for predictions of the penetration performance from initial conditions (but then the use of another code than the one used in chapter 5.3 must be considered). Approximations may be accepted depending on the simulation target (see chapter 5.3). As soon as a suitable model is available, it may be aimed for the following issues:

1. Impact of fine-scaled changes in friction angle and density, respectively, on (i) the relationship of shearing and compression during penetration, and on (ii) sediment strength profiles.
2. Impact of changes of interface friction angle on the sediment deformation and derived sediment strength to test the impact of penetrometer surface smoothness.
3. Impact of different tip geometries and inclination of penetrometer on sediment deformation and sediment strength for various sediment properties.
4. Impact of changes on penetration velocity (static and dynamic) on sediment deformation and sediment strength for various sediment properties.
5. After testing of homogeneous sediments (not only sand, but also silt or mud), layering should be included. Sediment layers could vary in sediment properties such as friction angle, density, cohesion, etc.

A final goal would be the combination of this geotechnical model with a hydrodynamical one to induce layering by the hydrodynamics in correspon-

dence to the geotechnical sediment remobilization studies presented in this thesis.

Physical modelling

In accordance with the numerical model, the physical model should be carried out in two steps approaching the geotechnical and methodological questions first before including hydrodynamics.

For the former, a tank based on experiments presented by, e.g., Aubeny and Shi (2006), or Stoll (2006), being about ~ 2 m wide and providing a depth of at least 1 m (for sand about 1 m would be sufficient, but for mud deeper penetration depths might be desired) would be suitable to carry out the following controlled penetrometer measurements in water saturated sediments:

1. Variation of impact velocity using *Nimrod*.
2. Variation of impact velocity (static and dynamic) using, e.g., the FFCPTU (Static penetrations cannot be tested using *Nimrod*, because the deceleration sensors would only monitor a steady movement, and a tip resistance sensor is lacking.).
3. Variation of tip geometry and inclination of both instruments.
4. Variation of mineralogy using both instruments.
5. Large-/Fine-scaled variation of grain size using both instruments.
6. Fine-scaled variation of density using both instruments.
7. Layering in terms of grain size and density variations using both instruments.

For the set up, methods have to be developed to provide, e.g., a constant penetration (e.g., by using a hydraulic arm), or to fill in the sediment with the desired density and keep the density over a series of deployments (e.g., by stirring), etc.

To include sediment dynamics, the set up has to be shifted to a flume or wave channel depending on whether the impact of currents and/or waves should be investigated. The initial conditions should be simplified here in the first instance (e.g., only one type of sediment with a certain grain size and density), but density variations induced by the hydrodynamics should be monitored during the experiment.

Both approaches, the numerical as well as the physical model, represent highly complex experiments, however, the outcome would improve the methodology of dynamic penetrometers, especially with regard to sediment remobilization processes. This thesis provides a solid base of *in-situ* data for approval of the modeling.

Chapter 8

Acknowledgements

This work was only possible with the aid of several people. The ones who contributed most are mentioned in this chapter, but I also want to thank all the people who helped me with loads of small things over the last three years and who are not named in this chapter.

Funding

I acknowledge the German Research Association (via MARUM, Center of Excellence at the University of Bremen, GLOMAR, Bremen International Graduate School for Marine Sciences, and INTERCOAST), the German Federal Ministry for the Environment, Nature Conservation and Nuclear Safety (via the German Federal Maritime and Hydrographic Agency), and the German Academic Exchange Service for funding.

Supervisors, advisors and thesis committee

I am very grateful to my supervisor Achim Kopf for providing the possibility to realize my scientific ideas within numerous research projects all over the world. I deeply appreciate his supervision, advice, and review during the progress of this work. Especially, I am indebted to him for, on the one hand, the scientific and creative freedom I experienced, and on the other hand, the guidance when I got stuck or a problem occurred.

Furthermore, I would like to thank Roy Wilkens for giving me the chance to work in Hawaii, advice and great ideas when I got stuck, numerous reviews, constructive comments and discussions, and above all, for always giving me the feeling that there will be a solution for the problems I faced.

I am also deeply indebted to Thomas Wever, who introduced marine sciences to me, for numerous advices and discussions, and always finding a sympathetic ear.

I would like to acknowledge Heiner Villinger, Tobias Mörz and Kathrin Huhn for advice, review and constructive discussions.

Also, I am grateful to Sylvia Stegmann for creative discussions, introducing the FFCPTU to me and advice whenever I needed it, and to Verner B. Ernstsen for supporting me with all issues around sediment dynamics and for his work as advising postdoc within my GLOMAR research area.

Technicians

This work would not have been possible without the help of Hendrik Hanff, Matthias Lange, Christian Zoellner and Wolfgang Schunn. Hendrik, Matthias and Christian helped my realizing all my ideas concerning *Nimrod*. Hendrik backed me up on surveys, in the office, and even when I needed a ride home from the hospital in the late evening (even though I sent him to the wrong hospital first). I cannot count the numerous questions I asked Matthias, and I always got an answer, although I often totally interrupted his ongoing work. Christian kept *Nimrod* alive after I smashed it on so many rocks and hard sands and improved it every time he maintained it. Also, he saved me with his huge travel medicine cabinet when I got a cold on a cruise. Wolfgang helped me out with numerous small things like rechargers, screens, etc. when I did not have the time to organize it myself.

Matthias Colsmann and AVISARO, Hannover, made an important contribution to the development of *Nimrod* by developing the custom-made data logger.

Collaborations and research stays

The RAVE project

I would like to thank Maria Lambers-Huesmann and Manfred Zeiler for taking me on this project and the respective research cruises, supporting my publications and creative discussions. Furthermore, I would like to mention Arne Stahlmann who invited me to the wave channel in Hannover, and the crew of VWFS WEGA who helped me with a great performance, ideas and a perfect atmosphere.

Dunes

I acknowledge the collaboration with the working group for sediment dynamics at MARUM during the research project in the Jade estuary and in the Knudedyb. In particular, I would like to thank Verner B. Ernstsen, Christian Svenson, Christian Winter, Anne Graff and Alice Lefebvre for numerous reviews, advices all around sediment dynamics, discussions and great ideas. Also, I thank the crew of R/V Senckenberg for support during the cruises.

Hawaii

Besides Roy Wilkens, I have to thank Jennifer Dussault, Sergio Jaramillo and Nils Hoever for help during the surveys, and Horst Brandes for providing me a possibility to work in his geotechnical labs. Furthermore, I am deeply indebted to Nancy Niklis for endless discussions, distraction from my work by going surfing or at least to the beach when I needed a break, and giving me a home every time I hop on the island for a few days. Also, I would like to thank Ki Kippeur for discussions and keeping me alive in Hawaiian waters when I took it too serious with the distractions.

New Zealand

I am deeply indebted to Bryna Flaim for developing the whole plan to work with me in New Zealand, giving me a home in New Zealand, numerous discussions, and joining me watching teenage vampire romance movies. Also, I would like to thank Alex Schimel for loads of discussions, bringing me to Raglan and saving me with my kiteline-confusion. Furthermore, I am very grateful to Terry Healy who supported Bryna's and my plans without any doubts. I acknowledge Dirk Immenga who supported me with any technical and logistical questions during the surveys in New Zealand.

Then I would like to thank Karin Bryan and Giovanni Coco for the great reviews and comments, and Rod Budd, Luca Chiaroni and Scott Edhouse for diving with *Nimrod* within the survey close to Tairua.

I acknowledge Geoffrey Thompson for making the survey in the Port of Tauranga possible, Gary Teear and Neil McLennan for getting us over to Lyttelton Port of Christchurch, and Peter Attkinson and Peter McCombe for the collaboration in the Port of Taranaki.

I would like to thank Shawn Harrison and Jose C. Borrero for realizing the survey along the sandbar in Raglan and getting me safe back to the shore, and Dougal Greer and David Phillips for providing the numerical current model data, review and discussions.

Furthermore, I would like to thank David Hamilton, Chris Hendy and Lisa Pearson for the possibility to work on the lakes around Rotorua twice, supporting me with additional data, and creative discussions. Also, Rob French has to be mentioned who piloted the boat and helped me pulling up *Nimrod* when my arms got lame.

Eckernförde Bay

Besides Thomas Wever, I would like to thank Hannelore Fiedler and Ralph Lühder for helping us testing *Nimrod* in Baltic Sea and numerous discussions.

Laboratory

I am very grateful to the “lab specialists” in our group Annika Förster and Andre Hüpers for helping me with the laboratory devices and answering all my “beginner questions”, and to our “neighbour” working group for geological engineering and Geo-Engineering for advice and discussions all around their laboratory facilities and letting me use their devices without waiting in the queue. Especially, I would like to mention Stefan Kreiter, Daniel Hepp, Daniel Otto and Katharina Behrens, and their head Tobias Mörz.

Numerical model

I would like to thank Kathrin Huhn for providing a FLAC3D license to start the numerical modelling, supervision and review regarding the modeling. I am very grateful to Jannis Kuhlmann who made it possible to include numerical modeling into my thesis without neglecting my other projects, for numerous discussions and ideas.

In the office

I am deeply indebted to my former and current office mates from our working group: Annedore Seifert, Annika Förster, Roberto Andreula, Hendrik Hanff, Andre Hüpers, Christian Zoellner, Alois Steiner, Ai Fei, Vigneshwaran Rajasekaran, Timo Fleischmann, Anna Reusch and Gauvain Wiemer. They provided the perfect atmosphere, backed me up and had always a sympathetic ear. Furthermore, I enjoyed our lunch breaks and the recently introduced coffee breaks a lot. Thank you for listening to my sometimes endless talking without complaining.

Also, I would like to thank Petra Renken for help with all administrative issues.

GLOMAR

I would like to thank Uta Brathauer and Carmen Murken for support with all kind of administrative GLOMAR questions. Furthermore, I acknowledge the GLOMAR students for discussions and relaxing social events. To name a few: James Collins for reviewing some of my manuscripts from the out-of-my-field point of view, correcting my d-english and his help at one of the worst evenings of my life, Bevis Fedder for GLOMAR lunch and salsa demonstrations in front of the Mensa, Uwe Stoeber for inviting me to Oregon, Cyril Giry for always asking how it is going, etc.

Plan M

I am very grateful to Jane Rickson for welcoming me with open arms at Cranfield University, giving me a great insight into the British university system, numerous discussions, answering all my questions and always providing time for me, even for a great London sightseeing tour with her family.

I would like to acknowledge all the girls from the first Plan M at MARUM/GLOMAR round: Anna Fricke, Annika Förster, Diana Magens, Ute Merkel, Franciska Steinhoff, Simone Ziegenbalg, Solveig Bühring and Stephanie Kusch. The meetings, seminars and discussions helped me a lot.

Family and friends (not related to the work)

Besides the people who supported me related to my work, I am deeply indebted to some other people who made this work possible by backing me up in every possible way.

First of all, I would like to express my deep gratitude to my parents, Elisabeth and Ewald Stark, who always believe in me and support all of my ideas and dreams. Also, they make all my journeys possible by watching over my animals and providing me with the freshest news from home.

Additionally, there have to be mentioned a few more people who calmed down my conscience by entertaining my horses when I was not around: Annika Dumpe for scratching the grass from Ruben's back, Silvi and Andreas Kringler giving "Monty everything their horses got, too", Heike Dirkes for keeping the "chain-smoker pony" Aramis out of his depressions, Sandrine Blümel for grooming Obi-Wan Kenobi even though he bit her (several times), Micha Blümel for watching over night and dragging the dogs out of their beds in the morning, Jenny Van Hoben for brushing Alien even though he never stood still, Aggi Grohnfeld for jumping in for the whole pack, and Dorothee Rieken for caring for Ladin. I would like to thank them for their time, the numerous chats and their back-up.

Furthermore, I would like to thank a few more friends for discussions, listening to my complaints, and so many cool evenings and weekends during the last three years: Jutta Trautmann who is the first with me on the dance floor, Michi Grofmeier who comes to my birthdays even if he has to walk the whole way until his feet are bleeding, Sebastian Schneider who never complains even though he gets crabby birthday presents from us every year, Peter Köchling who cheered me up by saying that even if you are the worst of the best, you are still pretty good, and Henning Huenteler my birthday surprise guest from China.

Finally, I would like to thank my flatmate Timo Migeod for bearing to live in one flat with me and all the small chats in between the door frames.

Chapter 9

References

(not cited in the manuscripts)

Abelev, A., Tubbs, K., Valent, P., (2009). Numerical investigation of dynamic free-fall penetrometers in soft cohesive marine sediments using a finite difference approach. Proc IEEE/MTS OCEANS, 2009.

Abelev, A., Simeonov, S., Valent, P., (2009). Numerical investigation of dynamic free-fall penetrometers in soft cohesive marine sediments using a finite element approach. Proc IEEE/MTS OCEANS, 2009.

Abril, G., Riou, S.A., Etcheber, H., Frankignoulle, M., de Wit, R., Middelburg, J.J., (2000). Transient, tidal time-scale, nitrogen transformations in an estuarine turbidity maximum – fluid mud system (The Gironde, South-west France). Estuarine, Coastal and Shelf Science 50, pp. 703-715.

Ahmadi, M.M., Byrne, P.M., Campanella, R.G., (1999). Simulation of cone penetration with FLAC. Proceedings of the XI Pan American Conference on Soil Mechanics and Geotechnical Engineering 3, pp. 1365-1369.

Ahmadi, M.M., (2000). Analysis of cone tip resistance in sand. Dissertation thesis submitted to University of British Columbia

Ahmadi, M.M., Robertson, P.K., (2005) Thin layer effects on the CPT qc measurement. Can Geotech J 42, pp. 1-16.

Ahmadi, M.M., Khabbazian, M., (2009). End bearing capacity of drilled shafts in sand: a numerical approach. Geotech Geol Eng 27, pp. 195-206.

Babu, G.L.S., Vasudevan, A.K., Holder, S., (2008). Numerical simulation of fiber-reinforced sand behavior. Geotextiles and Geomembranes 26, pp. 181 – 188.

Bagnold, R.A., (1946). Motion of waves in shallow water. Interaction of waves and sand bottoms. Proc Roy Soc Ser A 187, pp. 1-15.

- Balla, A., (1962). Bearing capacity of foundations. *J Soil Mechanics and Foundations Div, ASCE*, 89(SM5), pp. 12-34.
- Balson, P.S., Collins, M.B., (2007). Coastal and shelf sediment transport. The Geological Society, London.
- Bathe, K.J., Ramm, E., Wilson, E.L., (1975). Finite element formulations for large deformation dynamic analysis. *International Journal for Numerical Methods in Engineering* 9, pp. 353-386.
- Black, K.S., Athey, S., Wilson, P., Evans, D., (2007). The use of particle tracking in sediment transport studies: a review. *Coastal and Shelf Sediment Transport. Geol Soc London, Spec. Publ.* 274, pp. 73-91.
- Benmebarek, N., Benmebarek, S., Kastner, R., (2005). Numerical studies of seepage failure of sand within a cofferdam. *Computers and Geotechnics* 32, pp. 264 – 273.
- Beard, R.M., (1985). Expendable Doppler penetrometer for deep ocean sediment measurements. Strength testing of marine sediments: laboratory and in-situ measurements. ASTM STP 883, American Society for Testing and Materials, Philadelphia, pp. 101-124.
- Blom, A., Ribberink, J.S., de Vriend, H.J., (2003). Vertical sorting in bedforms: Flume experiments with a natural and bimodal sediment mixture. *Water Resources Research* 39(2), 1025.
- Boguslavskii, Y., Drabkin, S., Salman, A., (1996). Analysis of vertical projectile penetration in granular soils. *J Phys D: Appl Phys* 26, pp. 905 – 916.
- Bolton, M.D., (1986). The strength and dilatancy of sands. *Geotechnique* 36(1), pp.65-78.
- Bolton, M.D., Gui, M.W., (1995). Modelling of sand over a wide stress range using FLAC. Proc 10th Asian Regional Conf on Soil Mechanics and Foundation Eng 1, Beijing, China.
- Braun, J., Sambridge, M., (1994). Dynamical Lagrangian remeshing (DLR): a new algorithm for solving large strain deformation problems and its application to fault-propagation folding. *Earth and Planetary Science Letters* 124, pp. 211-220.
- Brebner, A., Askew, J.A., Law, S.W., (1966). Effect of roughness on mass-transport of progressive gravity wave. Proc 10th Conf Coastal Eng Tokyo, pp. 175-184.
- Brevik, I., (1980). Flume experiments on waves and currents. 2. Smooth Beds. *Coastal Eng* 4, pp. 89-110.
- Brodie, J.W., (1955). Sedimentation in Lyttelton Harbour, South Island, New Zealand. *New Zealand J of science and technology* 36, pp. 603-621.
- Brooks, J.D., Lang, T.G., (1967). Simplified methods for estimating torpedo drag. Underwater missile propulsion, Compass Publications, Arlington, US.
- Cameron, P., Weichsel, T., Fick, A., Watermann, B., (1998). Tpb-t-Belastung

der Küsten-Sedimente und ihre hormonelle Auswirkung auf Meeresschnecken. Meeresumweltschutz. Umweltstiftung WWF-Deutschland, Frankfurt am Main.

Carter, L., (1975). Sedimentation on the continental terrace around New Zealand: a review. *Marine Geology* 19, pp. 209 – 237.

Carter, J.P., Nazem, M., Airey, D.W., Chow, S.H., (2010). Dynamic analysis of free-falling penetrometers in soil deposits. *GeoFlorida: Advances in Analysis, Modelling and Design*, ASCE Conference, pp. 53 – 68.

Cetin, K.O., Isik, N.S., (2007). Probabilistic assessment of stress normalization for CPT data. *J Geotech Geoenviron Eng*, pp. 887-897.

Chereskin, T.K., (1995). Direct evidence for an Ekman balance in the Californian current. *J Geophys Res* 100(9), pp. 261-269.

Cho, G.C., Dodds, J., Santamarina, J.C., (2006). Particle shape effects on packing density, stiffness and strength: natural and crushed sands. *J Geotech Geoenviron Eng* 132(5), pp. 591-602.

Chou, H.T., Foda, M.A., Hunt, J.R., (1993). Rheological response of cohesive sediment to oscillatory forcing. Nearshore and estuarine cohesive sediment transport. American Geophysical Union, Washington, D.C.

Cole, J.W., (1979). Structure, petrology, and genesis of Cenozoic volcanism, Taupo Volcanic Zone, New Zealand – review. *N.Z. J Geol Geophys* 22, pp. 631-657.

Cooper, J.A.G., Pilkey, O.H., (2007). Quantification and measurement of longshore sediment transport: an unattainable goal. *Coastal and Shelf Sediment Transport*. Geol Soc London, Spec. Publ. 274, pp. 37-43.

Copeland G.J.M., (1987). The quality of numerical models. Proceedings of the Modelling the offshore environment conference, April 1-2, 1987, London, UK.

Coulomb, C.A., (1776). Essai sur une application des regles de maximums et minimums a quelques problemes de statique, relatifs a l'architecture. *Memoires de Mathematique et de Physique*, Presentes a l'Academie Royale des Sciences, Paris, 3, p. 38.

Craig, G.C.P., (1985). Bottom sediments of Lake Rotoiti, central North Island, New Zealand. MSc thesis, University of Waikato, Hamilton, New Zealand.

Crowe, C. T., Elger, D. F., Roberson, J. A., (2005). Engineering fluid mechanics. John Wiley and Sons Inc.

Dahmen, W., Reusken, A., (2008). Numerik für Ingenieure und Naturwissenschaftler. Springer Verlag, Berlin.

Davies-Colley, R.J., Healy, T., (1978). Sediment transport near the Tauranga entrance to Tauranga Harbour. *NZ J of Marine and Freshwater Res* 12 (3), pp. 237-243.

Dayal, U., Allen J.H., Jones, J.M., (1973). Marine impact cone penetrometer. *Marine Geology* 117, pp. 912-923.

- Dayal, U., (1980). Free fall penetrometer: a performance evaluation. *Applied Ocean Research* 2(1), pp. 39-43.
- DeBeer, E.E., Vesic, A.S., (1958). Etude experimentale de la capacité portante du sable sous des foundations directes établies en surface. *Ann Trav Publics Belg* 59(3).
- DeBeer, E.E., (1970). Experimental determination of shape factor and bearing capacity factor of sand. *Géotechnique* 20 (4), pp. 387-411.
- Disperens, A.P., Ockenden, M.C., Delo, E.A., (1993). Application of a mathematical model to investigate sedimentation at Eastham Dock, Mersey Estuary. Nearshore and estuarine cohesive sediment transport. American Geophysical Union, Washington, D.C.
- Eadie, R.W., Herbich, S.B., (1986). Scour around a single cylindrical pile due to combined random waves and currents. *Proc 20th Coast. Eng. Conf. ASCE*.
- Eastgaard, A., Poeckert, R.H., Preston, J.M., (1997). STING manual. A.G.O. environmental electronics ltd.
- Esrig, M.I., Kirby, R.C., Bea, R.G., (1977) Initial development of a general effective stress method for the prediction of axial capacity for driven piles in clay. *Proc. 9th Offshore Technology Conf*, pp. 495-501.
- Exner, F.M., (1925). Über die wechselwirkung zwischen wasser und geschiebe in flussen. *Sitzenberichte Akad Wiss Wien* 3-4, p. 165.
- Ferziger, J.H., Peric, M., (2002). Computational methods for fluid dynamics. Springer, Berlin, ISBN 3-540-42074-6.
- Flemming, B.W., (2000). The role of grain size, water depth and flow velocity as scaling factors controlling the size of subaqueous dunes. *Proceedings of the Marine Sandwave Dynamics conference*. 23-24 March 2000, Lille, France.
- Foster, G., Carter, L., (1997). Mud sedimentation on the continental shelf at an accretionary margin – Poverty Bay, New Zealand. *NZ J of Geol Geophys* 40, pp. 157 – 173.
- Gerdes, U., (2010). Vergleich bodenmechanischer Schlüsselparameter aus Drucksondierung und Laborversuch an Sanden aus einem geplanten Offshore-Windparkgebiet in der deutschen Nordsee. Master thesis submitted to University of Bremen, Germany.
- Gibbs, M., (2004). Lake Taupo long-term monitoring programme 2002-2003: Including two additional sites. Environment Waikato Technical Report 2004/05. Environment Waikato, Hamilton, New Zealand.
- Greiner, L., (1967). Underwater missile propulsion. Compass Publications Inc., Arlington, Virginia, USA.
- Hamilton, D., McBride, C., Uraokka, T., (2005). Lake Rotoiti field work and modelling to support considerations of Ohau channel diversion from Lake Rotoiti. Centre for Biodiversity and Ecology Research, University of Waikato.

- Hamilton, D., Pearson, L., Hendy, C., Burger, D., McCarthy, M., Healey, T., (2007). Historical and contemporary perspectives on the sediments of Lake Rotorua. GSNZ Newsletter 143, pp. 7-13.
- Hamilton, D., Paul, W., McBride, C., Immenga, D., (2009). Water flow between Ohau channel and Lake Rotoiti following implementation of a diversion wall. CBER Contract Report 96. Centre for Biodiversity and Ecology Research, University of Waikato.
- Hansdorf, S., Janssen, M., Reuter, R., Toenneboen, S., Wachowicz, B., Willkomm, R., (1999). Submarine lidar for seafloor inspection. Meas Sci Tech 10, pp. 1178-1188.
- Hansen, J.B., (1970). A revised and extended formula for bearing capacity. Danish Geotech inst, Bulletin No. 28, Copenhagen.
- Healy, T., (1975). Volcanic lakes. New Zealand lakes, Auckland University Press, Auckland, pp. 71-83.
- Healy, T., Mehta, A., Rodrigues, H., Tian, F., (1999). Bypassing of dredged littoral muddy sediments using a thin layer dispersal technique. J of Coast Res 15(4), pp. 1119 – 1131.
- Hearn, C.J., (2008). The dynamics of coastal models. Cambridge University Press, NY.
- Hint, C.W., Amsden, A.A., Cook, J.L., (1974). An arbitrary lagrangian-eulerian computing method for all flow speeds. J of computational physics 14, pp. 227 – 253.
- Holdaway, G.P., Thorne, P.D., Flatt, D., Jones, S.E., Prandle, D., (1999). Comparison between ADCP and transmissometer measurements of suspended sediment concentration. Cont Shelf Res 19, pp. 421-441.
- Holtorff, G, (1982). Resistance to flow in alluvial channels. Proc ASCE J ydraul Div 108(HY9),pp. 1010-1028.
- Hughes, S.A., (1993). Physical models and laboratory techniques in coastal engineering. World Scientific Publishing, Singapore.
- Hurst, R., Murdoch, S., (1991). Measurement of sediment shear strength for mine burial predictions. Auckland, NZ: DSTO, p. 8.
- Ingle, J.C., (1966). The movement of beach sand: and analysis using fluorescent grains. Developments in Sedimentology 5.
- Inglis, G., Gust, N., Fitridge, I., Floerl, O., Woods, C., Hayden, B., Fenwick, G., (2005). Port of Tauranga. Biosecurity NZ Technical paper No. 2005/05. ISBN: 0-478-07934-6.
- Ingram, C., (1982). Expendable penetrometer fro seafloor classification. Geo-Mar Let 2(3-4), pp. 239-241.
- Itasca Consulting Group Inc. (2006). FLAC3D manual. Itasca Consulting Group, Inc., Minneapolis, Minnesota, USA.

- Kineke, G.C., Sternberg, R.W., Trowbridge, J.H., Geyer, W.R., (1996). Fluid-mud processes on the amazon continental shelf. *Cont Shelf Res* 16(5/6), pp. 667-696.
- Kirby, R., (1988). High concentration suspension (fluid mud) layers in estuaries. Springer Publishing.
- Knoth, J.S., Nummeda, D., (1977). Longshore sediment transport using fluorescent tracer. *Proc Coast Sed, ASCE*, pp. 383-398.
- Kock, I., Huhn, K., (2007). Influence of particle shape on the frictional strength of sediments – A numerical case study. *Sedimentary Geology* 196, pp. 217-233.
- Konert, M., Vandenberghe, J., (1997). Comparison of laser grain size analysis with pipette and sieve analysis: a solution for the underestimation of the clay fraction. *Sedimentology* 44, pp. 523-535.
- Kuehl, S.A., Nittrouer, C.A., DeMaster, D.J., (1982). Modern sediment accumulation and strata formation on the Amazon continental shelf. *Marine geology* 49(3-4), pp. 279 – 300.
- Kurihara, M., Shinohara, K., Tsubaki, T., Yoshioka, M., (1956). Sand movement on a sandy beach by wave action. *Proc 3rd Conf Coastal Eng Jpn*.
- Kusuda, T., Watanabe, R., Futawatari, T., Yamanishi, H., (1993). Fluid mud movement on an inclined bed. Nearshore and estuarine cohesive sediment transport. American Geophysical Union, Washington, D.C.
- Larras, J., (1956). Effects de la houle et du clapotis sur les fonds de sable, IV Journ Hydraul Rep 9, Paris.
- Lenhoff, L., (1982). Incipient motion of sediment particles. *Proc 18th Conf Coastal Eng Cape Town*.
- Li, F., Cheng, L., (1999). Numerical model for local scour under offshore pipelines. *J Hydr Eng* 125(4), pp. 400-406.
- Liu, P.L.F., (1973). Damping of water waves over porous bed. *Proc ASCE J Hydraul Div* 99(HY12), pp. 2263-2271.
- Liyanapathirana, D.S., (2009). Arbitrary Lagrangian Eulerian based finite element analysis of cone penetration in soft clay. *Computers and Geotechnics* 36, pp. 851-860.
- Loizeau, J.L., Arbouille, D., Santiago, S., Vernet, J.P., (1994). Evaluation of a wide range laser diffraction grain size analyser for use with sediments. *Sedimentology* 41, pp. 353-361.
- Lorke, A., Umlauf, A., Jonas, T., Wuest, A., (2004). Dynamics of turbulence in low-speed oscillating bottom-boundary layers of stratified basins. *Env Fluid Mech* 2(4), pp. 291-313.
- Lorke, A., Wuest, A., (2005). Application of coherent ADCP for turbulence measurements in the bottom boundary layer. *Journal of Atmospheric and*

Oceanic Technology 22 (11), pp. 1821-1828.

Lowe, D., Green, J.D., (1987). Origins and development of the lakes. Inland waters of New Zealand, DSIR, Wellington, pp. 1-64.

Lu, Y., Lueck, R.G., (1999). Using a broadband ADCP in a tidal channel. *J Atmos Ocean Tech* 16, pp. 1568-1579.

Lu, Q., Hu, Y., Randolph, M.F., (2001). Deep penetration in soft clay with strength increasing with depth. Proceedings of the 11th International Offshore and Polar Engineering Conference in Stavanger, Norway.

Lundgren, H., (1972). Turbulent currents in the presence of waves. Proc. 13th Conf Coastal Eng Vancouver, pp. 623-634.

Lundgren, H., Mortensen, K., (1953). Determination by theory of elasticity of the bearing capacity of continuous footings on sand. Proc 3rd Int Conf on Soil Mechanics and Foundation Eng 1, pp. 401-412.

McAnally, W.H., Teeter, A., Schoellhamer, D., Friedrichs, C., Hamilton, D., Hayter, E., Shrestha, P., Rodrigues, H., Sherement, A., Kirby, R., (2007). Management of fluid mud in estuaries, bays, lakes II: Measurement, modelling and management. *J Hydr Eng* 133(1), pp. 22-38.

Macon, C., Wozencraft, J., Park, J.Y., Tuell, G., (2008), Seafloor and land cover classification through airborne lidar and hyperspectral data fusion. IGARSS 2008, II, pp. 77-80.

Markauskas, D., Kacianauskas, R., Suksta, M., (2002). Modelling the cone penetration test by the finite element method. *Foundations of civil and environmental engineering* 2, pp.125-140.

Martin, C.S., (1970). Effect of a porous sand bed on incipient sediment motion. *J Water resour* 6(4), pp. 1162-1174.

Mehta, A.J., (1991). Understanding fluid mud in a dynamic environment. *Geo-Mar Lett* 11, pp. 113-118.

Mehta, A.J., (1993). Nearshore and estuarine cohesive sediment transport. American Geophysical Union, Washington, D.C.

Migniot, C., (1977). Action des courants, de la houle et du vent sur les sediments. *La Houille Blanche* 32(1), pp. 9-47.

Mimura N., Nunn P.D., (1998). Trends of beach erosion and shoreline protection in rural Fiji. *J Coast Res* 14(1), pp. 37-46.

Mohr, O., (1900). Welche umstände bedingen die elastizitätsgrenze und den bruch des materials. *Zeitschrift des Vereins Deutscher Ingenieure*, Vol. 44, pp. 1524-1530.

Muste, M., Yu, K., Pratt, T., Abraham, D., (2004). Practical aspects of ADCP data use for quantification of mean river flow characteristics. *Flow measurements and instrumentation* 15(1), pp. 17-28.

- Nichols, M.M., (1984). Fluid mud accumulation processes in an estuary. *Geo-Mar Lett* 4, pp. 171-176.
- Norris, G., (1977). The drained shear strength of uniform sands as related to particle size and natural variation in particle shape and surface roughness. PhD thesis, University of California, Berkeley.
- O'Reilly, W.C., Herbes, T.H.C., Seymour, R.J., Guza, R.T., (1996). A comparison of directional buoy and fixed platform measurements of Pacific swell. *Journal of Atmospheric and Oceanic Technology* 13(1), pp. 231-238.
- Osler, J., Furlong, A., Christian, H., Lamplugh, M., (2006). The integration of the free fall cone penetrometer (FFCPT) with the moving vessel profiler (MVP) for the rapid assessment of seabed characteristics. *Int Hydrographic Review* 7(3).
- Parker, W.G., Kirby, R., (1982). Time dependent properties of cohesive sediment relevant to sedimentation management – A European experience. *Estuarine Comparison*, Academic Press, NY, pp. 573-590.
- Pearson, L., (2006). Distribution of phosphorus in sediments of Lake Rotorua. MSc thesis, Department of Chemistry, University of Waikato.
- Phillips, D.J., Mead, S.T., Black, K., Healy, T., (2003). Surf zone currents and influence on surfability. *Proc 3rd Surfing Reef Symp*, Raglan, NZ, 22-25 June 2003. pp. 60-82.
- Phillips, M.R., Jones, A.L., (2006). Erosion and tourism infrastructures in the coastal zones: Problems, consequences and management. *Tourism Management* 27(3), pp. 517-524.
- Phillips, D.J., Mead S.T., (2009). Investigation of a large sandbar at Raglan, New Zealand: Project overview and preliminary results. *Reef Journal* 1(1), pp. 267-278.
- Pickrill, R.A., (1993). Shallow seismic stratigraphy and pockmarks of a hydrothermally influenced lake, Lake Rotoiti, New Zealand. *Sedimentology* 40, pp. 813-828.
- Pisheh, Y.P., Hosseini, S.M.M.M., (2010). Numerical simulation of cyclic behavior of double sand lenses and corresponding liquefaction-induced soil settlement. *J Cent South Univ Technol* 17, pp. 593 – 602.
- Poekert, B.H., Preston, J.M., Miller, T.L., Meakin, M., Hurst, R.B., Lott, D.F., (1996). A comparison of seabed penetrometers. *TTCP Subgroup G Symp Shallow Undersea Warfare*, Halifax, Nova Scotia, Canada, pp. 459-470.
- Preston, J.M., Collins, W.T., Mosher, D.C., Poekert, R.H., Kuwahara, R.H., (1999). The strength of correlations between geotechnical variables and acoustic classifications. *Proceedings of the OCEANS conference 1999*.
- Raudkivi, A.J., (1963). Study of sediment ripple formation. *Proc. ASCE J Hydraul Div* 89 (HY6), pp. 15-33.
- Reed, A.H., Faas, R.W., Allison, M.A., Calliari, L.J., Holland, K.T., O'Reilly, S.E., Vaughan, W.C., Alves, A., (2009). Characterization of mud deposit

- offshore of the Patos Lagoon, southern Brazil. *Cont Shelf Res* 29, pp. 597-608.
- Rennie, C.D., Villard, P.V. (2003). Bedload measurement in both sand and gravel using an aDcp. In 16th Canadian Hydrotechnical Conference. Canadian Society for Civil Engineers, October 22-24, 2003, Burlington, ON, p. 10.
- Reynolds, A.J., (1965). Waves on the erodible bed of an open channel. *J Fluid Mech* 22, pp. 113-133.
- Richards, K.J., (1980). The formation of ripples and dunes on an erodible bed. *J Fluid Mech* 99, pp. 597-618.
- Richardson, M., Valent, P., Briggs, K., Bradley, J., Griffin, J., (2001). NRL mine burial experiments. NRL report, project no. BE-782-001.
- Ross, M.A., Mehta, A.J., (1989). On the mechanics of lutoclines and fluid mud. *J Coastal Res* SI5(5), pp. 51-61.
- Roulund, A., Mutlu Sumer, B., Fredsoe, J., Michelsen, J., (2005). Numerical and experimental investigation of flow and scour around a circular pile. *J Fluid Mech* (354), pp. 351 – 401.
- Rudnick, D.L., Davis, R.E., Eriksen, C.C., Fratantoni, D.M., Perry, M.J., (2004). Underwater gliders for ocean research. *Marine Technology Society Journal* 38(1), pp. 48-59.
- Ruiter, J.D., Fox, D.A., (1975). Site investigations for North Sea Forties Field. *Proc. 7th Offshore Technol. Conf, OTC 2246*, pp. 471-480.
- Sato, S., Ijima, T., Tanaka, T., (1962). A study of critical depth and mode of sand movement using radioactive glass and. *Proc 8th Conf Coastal Eng Mexico*, pp. 304- 323.
- Scarfe, B.E., Healy, T.R., Rennie, H.G., Mead, S.T., (2009). Sustainable management of surfing breaks: Case studies and recommendations. *J of Coastal Res* 25(3), pp. 684-703.
- Schrottke, K., Becker, M., Bartholomä, A., Flemming, B.W., Hebbeln, D., (2006). Fluid mud dynamics in the Weser estuary turbidity zone tracked by high-resolution side-scan sonar and parametric sub-bottom profiler. *Geo-Mar Lett* 26, pp. 185 -198.
- Seifert, A., Kopf, A., (subm.). Dynamic CPTU deployments for rapid assessment of fluid mud – initial results. Submitted to *J Geotech Geoenviron Eng*.
- Sherwood, A.M., Nelson, C.S., (1979). Surficial sediments of Raglan Harbour. *New Zealand J of Marine and Freshwater Res* 13(4), pp. 475-496.
- Shi, H., (2005). Numerical simulations and predictive models of undrained penetration in soft soils. Dissertation thesis submitted to Texas A and M University.
- Shields, A. (1936). Anwendung der Ähnlichkeitsmechanik und der Turbulenzforschung auf die Geschiebebewegung. *Mitt Preuss Versuchsanst Wasserbau Schiffbau Berlin* 26, pp. 1-26.

- Sleath, J.F.A., (1984). *Sea bed mechanics*. John Wiley and Sons, NY.
- Smith, T.J., Kirby, R., (1989). Generation, stabilization and dissipation of layered fine sediment suspensions. *J Coast Res*, SI(5), pp. 63-73.
- Soulsby R.L., Hamm, L., Klopman, G., Myrhaug, G., Simons, R.R., Thomas, G.P. (1993). Wave-current interaction within and outside the bottom boundary layers. *Coastal Eng* 21(1-3), pp. 41-69.
- Soulsby, R.L., Whitehouse, R.J.S., (1997). Threshold of sediment motion in coastal environments. In: *Pacific Coasts and Ports 1997, 13th Australasian Coastal and Engineering Conference and 6th Australasian Port and Harbour Conference*, Christchurch, New Zealand, HR Wallingford, Oxon, pp. 149-154.
- Spiers, K.C., Healy, T.R., (2007). Investigation of sorted bedforms, Taurangi Harbour, New Zealand. *J of Coastal Res* SI50, pp. 353 - 357.
- Stahlmann, A., Hildebrandt, A., Schlurmann, T., (2009). Untersuchung von Seegangbelastungen und Kolk an Offshore-Windenergieanlagen im Testfeld Alpha Ventus. HTG-Kongress 2009, Lübeck.
- Stegmann, S., Strasser, M., Anselmetti, F., Kopf, A., (2007). Geotechnical in situ characterization of subaquatic slopes: The role of pore pressure transients versus frictional strength in landslide initiation. *Geophys Res Lett* 34, L07607.
- Stephens, S., (2004). Modelling the diversion of the Ohau channel outflow in Lake Rotoiti to Kaituna River. NIWA client report: HAM2004-165. NIWA project: BOP04222.
- Stephens, S., Ovenden, R., Murray, B., (2005). Ohau channel sediment grain size and density. NIWA client report: HAM2005-015, NIWA project: HSJ05201.
- Strasser, M., Stegmann, S., Bussmann, F., Anselmetti, F.S., Rick, B., Kopf, A., (2007). Quantifying subaqueous slope stability during seismic shaking: Lake Lucerne as a model for ocean margins. *Marine Geology* 240, pp.77-79.
- Stoll, R.D., (2006). Measuring sea bed properties using static and dynamic penetrometers. *Proc. ASCE Int Conf Civil Eng Oceans VI*, pp. 386-395.
- Sumer, B.M., Fredsoe, J., (2002). *The mechanics of scour in the marine environment*. World Scientific Publishing, Singapore.
- Swamee, P.K., Ojha, C.S., (1991). Bed-load and suspended-load transport of nonuniform sediments. *J Hydraul. Eng* 117, 774.
- Tekeste, M.Z., Tollner, E.W., Raper, R.L., Way, T.R., Johnson, C.E., (2006). Non-linear finite element analysis of cone penetration in layered sandy loam soil: considering the precompression stress state. *Proc Computers in Agriculture and Natural Resources*, 24-26 July 2006, Orlando, USA.
- Thevanayagam, S., Ecemis, N., (2007). Effects of permeability and compressibility on liquefaction screening using cone penetration resistance. *Proc 8th Pacific Conf on Earthquake Eng*, 5-7 December 2007, Singapore.

- Ti, K.S., Huat, B.B.K., Noorzali, J., Jaafar, M.S., Sew, G.S., (2009). A review of basic soil constitutive models for geotechnical applications. *The Electronic Journal of Geotechnical Engineering*.
- Traykovski, P., Richardson, M.D., Mayer, L.A., Irish, J.D., (2007). Mine burial experiments at the Martha's Vineyard coastal observatory. *IEEE J of Oceanic Eng* 32(1), pp. 150 - 166.
- Tritton, D.J., (1988). *Physical fluid dynamics*. Oxford Sciences Publications, Oxford.
- Trupin, A., Wahr, J., (2007). Spectroscopic analysis of global tide gauge sea level data. *Geophys. J Int.* 100(3), pp. 441-453.
- Tulldahl, M.H., Vahlberg, C., Axelsson, A., Karlsson, H., Jansson, H., (2007). Seafloor characterization from airborne lidar data. *Lidar technologies, techniques, and measurements for atmospheric remote sensing No. 3*, Florence, Italy, Vol. 6750.
- Vasquez, J.A., Walsh, B.W., (2009). CFD simulation of local scour in complex piles under tidal flow. 33rd IAHR congress: Water Engineering for a sustainable environment, ISBN: 978-94-90365-01-1.
- Ventura, E., Nearing, M., Norton, L.D., (2001). Developing a magnetic tracer to study erosion. *Catena* 43, pp. 277-291.
- Vincent, C.E., (2007). Measuring suspended sand concentration using acoustic backscatter: a critical look at the errors and uncertainties. *Coastal and shelf sediment transport*. The Geological Society, London., pp. 7-15.
- Waeles B., Le Hir, P., Lesueur P., Delsinne, N., (2007). Modelling sand/mud transport and morphodynamics in the Seine river mouth (France): an attempt using a process-based approach. *Hydrobiologia* 588(1), pp. 69-82.
- Wakeman, T.H., Themelis, N.J., (2001). A basin-wide approach to dredged material management in New York/ New Jersey Harbor. *J of Hazardous Materials* 85(1-3), pp. 1 - 13.
- Waters, C.B., (1986). Thermoluminescent tracer: further evaluations. *Dredge spoil and heavy metals in tidal waters*. Hydraul Res Wallingford, SR91, Appendix B.
- Watters, G.Z., Rao, M.V.P., (1971). Hydrodynamic effects of seepage on bed particles. *Proc ASCE J Hydraul Div* 97(HY3), pp. 421-439.
- Weill, P., Mouazé, D., Tessier, B., (2008). Hydrodynamic behavior of coarse bioclastic sand under current: A flume experiment. *Proceedings of the mraine and River Dune Dynamics Conference*, April 1-3, 2008, Leeds, UK.
- Wever, T., Lühder, R., Stender, I. (2004). Burial Registration Mines – 30 years of seafloor-mine interaction research. *Sea Technology* 45(11), pp. 15-19.
- Whitehouse, R., (1998). *Scour at marine structures*. HR Wallingford. Thomas Telford Publications.

- Whitmeyer, S.J., Fitzgerald, D., (2006). Sand waves that impede navigation of coastal inlet navigation channels. US Army Corps of Engineers. Report ERDC/CHL CHETN-IV-68.
- Wilcock, P.R., McArdell, B.W., (1993). Surface-based fractional transport rates: Mobilization thresholds and partial transport of a sand-gravel sediment." *Water Resour. Res.* 29(4), pp. 1297-1312.
- Winterwerp, J.C., (2002). On the flocculation and settling velocity of estuarine mud. *Cont Shelf Res* 22, pp. 1339-1360.
- Wolanski, E., Gibbs, R.J., Mazda, Y., Mehta, A., King, B., (1992). The role of turbulence in the settling of mud flocs. *J of Coastal Res* 8(1), pp. 35 - 46.
- Wood, C.P., (1992). Geology of the Rotorua geothermal system. *Geothermics* 21(1/2), pp. 25-41.
- Zeman, A.J., Patterson, T.S., (2003). Characterization and mapping of contaminated sediments, windermere arm, Hamilton harbour, Ontario, Canada. *Soil and Sediment Contamination* 12, pp. 619-629.
- Zhang, X.C., Friedrich, J.M., Nearing, M.A., Norton, L.D., (2001). Potential use of rare earth oxides as tracers for soil erosion. *Soil Science Soc of Am J* 65, pp. 1508-1515.
- Ziervogel, K., Bohling, B., (2003). Sedimentological parameters and erosion behavior of submarine coastal sediments in the south-western Baltic sea. *Geo-Mar Lett* 23, pp. 43-52.

Appendix A

Abstracts

The following abstracts have been submitted to the respective conferences within the dissertation time and have not been presented in this thesis yet.

Stark, N., Stegmann, S., Ernstsens, V.B.,
Seifert, A., Kopf, A.,

Mobile bed material layers characterized
and quantified by free-falling penetrometers.

Submitted to the 10th International Coastal Symposium
in Lisbon, 2009.

Erosion, transport and deposition of bed material induced by currents, waves and tides are important processes in estuaries and coastal environments. The migration of dunes, effects on navigability caused by the appearance of fluid mud layers or silting-up of shipping routes are examples of its consequences. To assess sediment mobility and its potential impact, the mobile layers have to be detected and quantified. Sediment cores and samples may recover the mobile layer if it is not too soft, but may compromise its *in-situ* thickness, texture and physical properties. Acoustic methods like high resolution seismic profiling (chirp sonar, resolution 40 cm) and parametric sub-bottom profiling (resolution about 6 cm) succeed displaying the thickness of the mobile layer if it is at least as thick as their maximum resolution. In some cases the mobile layer could

be thinner and cannot be shown by above mentioned methods. This study has tested the ability of two free-falling penetrometers, recently developed at Bremen University, to detect and quantify such thin mobile layers. The free-falling penetrometers measure profiles of, e.g., deceleration, pressure and tip resistance during penetration into the seabed to derive geotechnical properties such as strength and pore pressure *in-situ*. This has been done successfully in different scenarios and through layers of variable thickness and consistency in coastal environments of Germany and Denmark. This paper presents first results of quantifying and characterizing such mobile layers using the two free-falling penetrometers.

Stark, N., Lambers-Huesmann, M.,
Zeiler, M., Zoellner, C., Kopf, A.,

Impact of offshore wind energy plants
on the soil mechanical behavior of sandy seafloors.

Accepted for oral presentation at
the European Geological Union General Assembly
in Vienna, 2010.

Over the last decade, wind energy has become an important renewable energy source. Especially, the installation of offshore windfarms offers additional space and higher average wind speeds than the well-established windfarms onshore.

Certainly, the construction of offshore wind turbines has an impact on the environment. In the framework of the *Research at Alpha VEntus* (RAVE) project in the German offshore wind energy farm *Alpha Ventus* (north of the island Borkum in water depths of about 30 m) a research plan to investigate the environmental impact had been put into place. An ongoing study focuses on the changes in soil mechanics of the seafloor close to the foundations and the development of scour. Here, we present results of the first geotechnical investigations after construction of the plants (ca. 1–6 months) compared to geotechnical measurements prior to construction.

To study the soil mechanical behavior of the sand, sediment samples from about thirty different positions were measured in the laboratory to deliver, e.g., grain size (0.063–0.3 mm), friction angles ($\sim 32^\circ$), unit weight ($\sim 19.9 \text{ kN/m}^3$) and void ratios (~ 0.81). For acoustic visualisation, side-scan-sonar (towed and stationary) and multibeam-echosounders (hull mounted) were used. Data show a flat, homogenous seafloor prior to windmill erection, and scouring effects at and in the vicinity of the foundations afterwards. Geotechnical *in-situ* measurements were carried out using a standard dynamic Cone Penetration Testing lance covering the whole windfarm area excluding areas in a radius < 50 m from the installed windmills (due the accessibility with the required research vessel). In addition, the small free-fall penetrometer *Nimrod* was deployed at the same spots, and furthermore, in the areas close to the tripod foundations (down to a distance of ~ 5 m from the central pile). Before construction, CPT as well as *Nimrod* deployments confirm a flat, homogenous sandy area with tip resistance values ranging from 1200–1600 kPa (CPT with a mass of ~ 100 kg and an impact velocity of ~ 1 m/s) and quasi-static bearing capacities (q_{sb}c.) mainly ranging from 39–69 kPa (*Nimrod*: mass of ~ 13 kg, impact velocity of ~ 8 m/s). There was no evidence for layering in results of both *in-situ* instruments. After construction, most of the positions show changes in sediment strength ranging from 10 % up to 100 % compared to the results prior to windmill construction. Extreme changes (> 50 %) occur above all close to the foundations. Furthermore, patterns of relatively soft zones (q_{sb}c.: 50–80 kPa) and hard zones (q_{sb}c. > 100 kPa) were mapped during the high-resolution surveys close to the foundation. Beside that, a very soft sediment layer (0.03–0.05 m) drapes most of the soft zones. This may be recently eroded and re-deposited sediment, whereas the hard zones may indicate areas of sediment erosion where looser material has been carried away. Reasons for sediment remobilization and changes in geotechnical properties may be scouring as a consequence of the changed hydrodynamics in the vicinity of the windmills. Besides first developments of scour, the side scan sonar results show relicts of the wind turbine erection (e.g., footprints of jack-up-platforms). First multibeam-echosounder measurements confirm sediment re-deposition due to scour in the lee of the main current direction and show traces of wind turbine erection equipment in the same areas where also the penetrometer measurements took place. In summary, a local impact of the wind turbines on

the soil mechanical properties of the seafloor is attested from this initial post-erection survey. Future cruises (every 6 months) will complement those data, which will eventually allow us a comparison to, or even refinement of long-term scouring models.

Stark, N., Lambers-Huesmann, M.,
Zeiler, M., Zoellner, C., Kopf, A.,

In-situ Geotechnical Investigations of
Scouring at Offshore Wind Energy Turbines.

Accepted for oral presentation at
the OES/IEEE OCEANS
in Sydney, 2010.

Wind energy has become one of the most important renewable energy sources. After successful implementation onshore, offshore wind energy bringing up additional space and higher average wind speeds was introduced in the last years. The first projects started in very shallow areas (water depth ~ 10 m) close to the coast (e.g., Middelgrund, DK, 2001). Although, recently the offshore wind-farms have been installed farther away from the coast in water depths ranging from 28 to 45 m (e.g., Beatrice, UK, 2007). Because of the high cost of installation, the longevity of the turbines is essential and calls attention, amongst others, on the foundations. Following this, there is a need to model and predict scour, which is a typical pattern of sediment redistribution due to the installation of an object of defined shape in an area strongly influenced by currents, tides and waves. However, wind farms in open waters are a relatively new development and until now, it is not clear if the present scour models accurately simulate the processes occurring *in-situ*.

To investigate this, a research plan for sedimentological and geotechnical *in-situ* measurements within the framework of the *Research at Alpha VEntus* (RAVE) has been put into place, and special devices were developed. For visualization of the seafloor surface, side scan

sonar (towed and stationary) and multibeam-echosounder (hull-mounted) were used for surveying a full coverage grid of the whole area pre- and post-erection. Chirp sonar (towed) was also applied for very high resolution sub-bottom profiling. In the pre-erection phase, these methods showed a flat, homogenous sandy seafloor. This was confirmed by sediment samples taken at the position of each planned windmill and respectively at a distance of 100 m and 500 m. The samples contained pale brown, siliciclastic sand with well-rounded particles and a grain size of 0.063–0.3 mm. In the laboratory friction angles of $\sim 32^\circ$, a unit weight of $\sim 19.9 \text{ kN/m}^3$ and void ratios ~ 0.81 were determined. For *in-situ* geotechnical investigations of the seafloor a standard dynamic Cone Penetration Test lance (CPT) was deployed in the same positions at which sediment samples were taken. The pre-construction CPT tests delivered tip resistance values ranging from 1200–1600 kPa and decelerations ranging from 1–2.2 g penetrating the uppermost sediment surface with an impact velocity of $\sim 1 \text{ m/s}$ (maximum winch speed) and a mass of $\sim 100 \text{ kg}$. During the pre-erection measurements, the lightweight (13 kg mass) dynamic penetrometer *Nimrod* derived values of maximum deceleration ranging from 55–85 g and of quasi-static bearing capacity ranging from 39–69 kPa at impact velocities of 6–12 m/s. These results form the base for a comparison between pre- and post-erection geotechnical data.

A few months after the installation of the tripod foundations, a second measurement campaign was started. Now, the closest position accessible for the CPT lance, the stationary circumferential sonar tower and the box corer was 50 m from the installed foundations. However, since *Nimrod* can be deployed from a dinghy, measurements very close to the tripod foundation (down to $\sim 3 \text{ m}$ from the central pile) were possible. These measurements were carried out in straight tracks of 5–12 deployments radial from the central pile of tripod and in-between of the tripod legs.

Hydroacoustic and sedimentological as well as geotechnical data show a local impact of the wind turbine foundations on the seafloor. Multibeam-echosounder images attest sediment re-deposition due to scouring in the lee of the main current direction as well as traces of construction equipment (e.g., footprints of jack-up-platforms). The geotechnical results in the same areas present changes in sediment strength ranging from about 10–100 % compared to the results prior to erection. Close to the wind turbines, patterns of hard zones (quasi-static bearing capacity $> 100 \text{ kPa}$) and the de-

velopment of a looser sediment layer (0.03 - 0.05 m thick) in the remaining soft zones can be detected. Zones of higher strength may be the consequence of erosion of the uppermost material. Conversely, a looser surface layer and soft zones may express sediment that has been freshly re-deposited. A variation of the patterns around the different windmills might be a consequence of exact time of construction (i.e. less time for the seafloor to adjust to changes in hydrodynamics owing to the obstacle) and different positions in the grid of wind turbines.

The initial results illustrate our strategy for *in-situ* geotechnical investigation of scour at offshore wind energy plants, results of the first post-erection survey in comparison to pre-erection and an assessment of the techniques used. Regular surveys (every 6 months) in the future will gather complementary data, which will eventually allow us a comparison to, or even refinement of long-term scouring models.

Stark, N., Greer, D., Phillips, D.J.,
Borrero, J.C., Harrison, S., Kopf, A.,

In-situ Geotechnical Investigation of
Sediment Characteristics over
"The Bar", Raglan, New Zealand.

Submitted to the
American Geophysical Union Fall Meeting
in San Francisco, 2010.

The geotechnical characteristics of surficial sediments on a highly mobile, N-S-oriented ebb tidal shoal ('*The Bar*') near the entrance to Whaingaroa Harbor, in Raglan, NZ, were investigated using the dynamic penetrometer *Nimrod* developed at MARUM, University of Bremen. The penetrometer is suitable for deployments in areas characterized by strong currents and active wave climate common to this site. Vertical sediment strength, based upon penetrometer deceleration and a quasi-static bearing capacity equivalent, was

profiled at 23 positions along as well as in the vicinity of *The Bar* during slack water. Recently deposited or loosened up sediment was detected as a top layer of lower sediment strength (quasi-static bearing capacity equivalent [qs. bc.] < 10 kPa) over a stiff substratum (mean maximum qs. bs. ~ 105 kPa), and quantified (thickness: 0 - 7 cm) indicating areas of sediment accumulation and areas of sediment erosion. These results were correlated to mean current velocities and directions predicted by ASR Ltd.'s Whaingaroa Harbor Model.

Concerning sediment dynamics, *The Bar* area can be divided into different zones: (i) the channel connecting *The Bar* to the harbor, (ii) the southern arm, (iii) the mid-section, (iv) the northern arm, and (v, vi) the northern and southern wings covering the area between *The Bar* and the shore. The channel is characterized by high current velocities (up to 1.7 m/s) along the W-E-axis, suggesting a strong sediment erosion and no (re-)deposition. However, the penetrometer results hint at sediment deposition that can be explained by the deep trench in the channel that might trap sediment despite the high mean current velocities. Comparing the northern and the southern wing, the currents follow the bathymetry and coastline and are mirrored at the W-E-axis, but the mean current velocities are higher at the southern wing (northern wing: up to 0.4 m/s; southern wing: up to 0.6 m/s). The penetrometer results suggest strong sediment erosion on the southern wing (qs. bc. up to 155 kPa, top layer thickness ~ 2 cm), and show no evidence of sediment remobilization on the northern wing (no layering). On the northern and southern arms, low currents (~ 0.3 m/s) with very mixed directions were predicted, and in front (west) of the most southern corner an area of strong sediment accumulation was localized following the penetrometer results (top layer thickness: 7 cm). This leads to the hypothesis that in the ebb-shoal system at Whaingaroa Harbor, mobile sediment is mainly transported via the southern wing of the *The Bar* potentially leading to an increase of sediment erosion in this area due to effects like sanding. Sediment deposition might occur in the trench of the channel as well as in the vicinity of the southernmost portion of the sandbar. This matches observations according to which the southern arm shifted about 220 m whereas the northern arm only moved 20 m within one year.

The *in-situ* penetrometer as well as the numerical results agree neatly with observations of *The Bar*'s morphology. Both methods

provide valuable insights which enhance our understanding of the sediment dynamics in this area.

Appendix B

List of field work

I was involved in the following surveys within the dissertation time (tests of devices in small rivers or ponds are not listed):

Date	Location	Vessel	Chief scientist	Methods
Apr 2008	Emden harbor	R/V Delfin	A. Seifert (MARUM)	CPT, grab samples, gravity cores, water samples
Apr 2008	Kiel harbor	R/V Bussard	T. Wever (FWG)	CPT, grab samples
Apr 2008	Jade estuary, North Sea	R/V Senckenberg	V.B. Ernstsen (MARUM)	CPT, grab samples, <i>Nimrod</i> , MBES
May 2008	<i>Alpha Ventus</i> , North Sea	VWFS Wega	M. Lambers-Huesmann (BSH)	MBES, SSS, chirp sonar, CPT, <i>Nimrod</i> , grab samples
Jul 2008	Eckernförde Bay, Baltic Sea	MzB Breitgrund	H. Fiedler (FWG)	gravity cores, CPT, <i>Nimrod</i> , FWG penetrometer, re-search mines, parasound
Jan 2009	Waikiki, Hawaii	University boat	R. Wilkens (SOEST)	<i>Nimrod</i> , grab samples, <i>Re-mus</i> (SSS-AUV)
Jan 2009	Waimanalo Bay, Hawaii	kayak	R. Wilkens (SOEST)	<i>Nimrod</i> , grab samples
Jan 2009	Kailua Bay, Hawaii	kayak	R. Wilkens (SOEST)	<i>Nimrod</i> , grab samples
Jan 2009	Kaneohe Bay, Hawaii	kayak	R. Wilkens (SOEST)	<i>Nimrod</i> , grab samples
May 2009	<i>Alpha Ventus</i> , North Sea	VWFS Wega	M. Lambers-Huesmann (BSH)	MBES, SSS, chirp sonar, CPT, <i>Nimrod</i> , grab samples
Jun 2009	Tauranga harbor, NZ	pilot boat	T. Healy (Univ of Waikato)	<i>Nimrod</i>
Jun 2009	Lake Rotorua, NZ	pilot boat	D. Hamilton (Univ of Waikato)	<i>Nimrod</i>

Jun 2009	Lake Rotoiti, NZ	pilot boat	D. Hamilton (Univ of Waikato)	<i>Nimrod</i>
Jun 2009	Lake Tarawera, NZ	pilot boat	D. Hamilton (Univ of Waikato)	<i>Nimrod</i>
Jul 2009	Tairua, NZ	NIWA boat	G. Coco (NIWA)	<i>Nimrod</i> , grab samples
Jul 2009	Raglan, NZ	jetski	S. Harrison (ASR Ltd)	<i>Nimrod</i> , grab samples
Jul 2009	Proposed disposal site, east coast, NZ	Ten60	B. Flaim (Univ of Waikato)	<i>Nimrod</i> , video
Jul 2009	Port of Taranaki	pilot boat	P. Attkinson (Port of Taranaki)	<i>Nimrod</i>
Nov 2009	<i>Alpha Ventus</i> , North Sea	VWFS Wega	M. Lambers-Huesmann (BSH)	MBES, SSS, chirp sonar, CPT, <i>Nimrod</i> , grab samples
Mar 2010	Lyttelton harbor, NZ	Soundz Image	G. Teear (OCEL Ltd)	<i>Nimrod</i> , CPT, samples
Mar 2010	Tauranga harbor, NZ	pilot boat	T. Healy (Univ of Waikato)	<i>Nimrod</i>
Mar 2010	Proposed disposal site, east coast, NZ	Ten60	B. Flaim (Univ of Waikato)	<i>Nimrod</i> , plume observation
Mar 2010	Lake Rotorua, NZ	pilot boat	D. Hamilton (Univ of Waikato)	<i>Nimrod</i>
Mar 2010	Lake Rotoiti, NZ	pilot boat	D. Hamilton (Univ of Waikato)	<i>Nimrod</i>
Apr 2010	<i>Alpha Ventus</i> , North Sea	VWFS Wega	M. Lambers-Huesmann (BSH)	MBES, SSS, chirp sonar, CPT, <i>Nimrod</i> , grab samples

Appendix C

More data

In the following chapter, penetrometer results from the surveys which are not represented within a manuscript or as ongoing project will be shown here. The data has to be regarded as raw data. No detailed processing or interpretation has been carried out.

C.1 Emden harbor, GER

Besides the experiments carried out by Annedore Seifert, tests using the FFCPTU lance with different tip geometries were carried out in Emden Harbor in April 2008. The chosen position was $53^{\circ} 20.8721' \text{ N}$ and $7^{\circ} 11.9332' \text{ E}$, inside of the locks with a water depth of about 10 m. The FFCPTU lance was used with two additional rods each being 1 m long, having a total weight of approximately 70 kg, and was truly free-falling. The tip geometries varied from the commonly used cone (diameter: 4 cm), over a cylinder (diameter: 10 cm) to a disc (diameter: 25 cm) (Fig. C.1). The results in terms of maxima of the deceleration, impact velocity, penetration depth, tip resistance and excess pore pressure are shown in Tab. C.1.

Tip	Deceleration (m/s^2)	Impact velocity (m/s)	Penetration depth (m)	Tip resistance (kPa)	Excess pore pressure (kPa)
Cone	8.0	1.3	1.50	101	10
Cone	7.5	1.8	1.45	150	1
Cone	8.2	1.8	1.40	105	-
Cone	16.5	1.5	0.85	310	1
Cone	10.5	4.0	0.80	340	1
Cylinder	15.0	3.2	2.70	125	77
Cylinder	15.0	3.0	2.60	160	12
Cylinder	12.5	1.6	1.00	110	4
Cylinder	15.5	2.2	1.40	130	4
Cylinder	15	2.2	1.40	125	4
Disc	7.5	1.2	1.15	15	65
Disc	13.0	2.2	2.20	23	63
Disc	9.5	1.9	1.40	14	33
Disc	10.0	1.5	1.30	9	32
Disc	9.5	1.4	1.60	13	36

Table C.1: FFCPTU lance results using different tip geometries from Emden harbor. Five deployments per tip were carried out at the approximately same position. Slight variations in position and deployment performance might have led to deviations of the results.

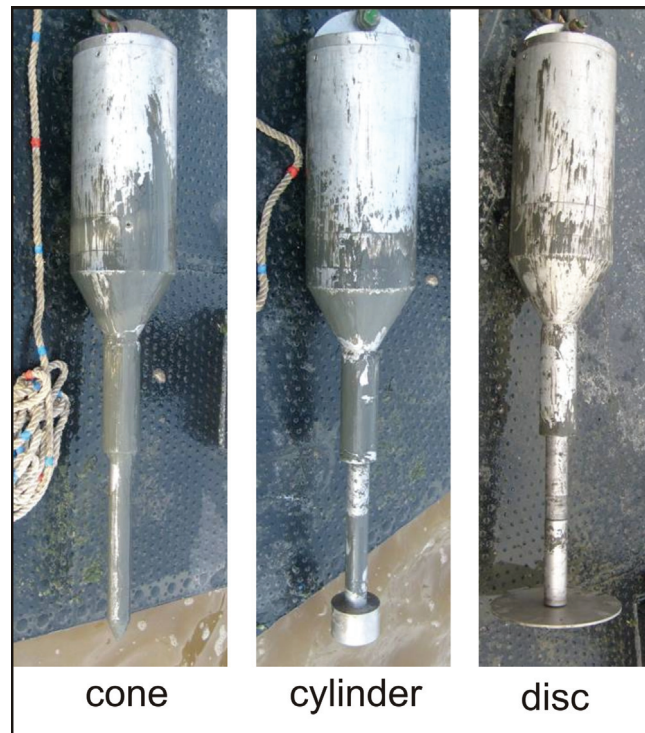


Figure C.1: FFCPTU lance with the three tip options: cone, cylinder, disc at a test in Bremerhaven.

C.2 Kiel harbor, GER: *Tirpitzhafen*

In the *Tirpitzhafen*, part of the western Kiel Navy harbor, it was planned to extend the tests with different tip geometry using the FFCPTU. However, the thread connecting tip and sensor section was damaged at the sixth position. For the twenty remaining positions only the cylindrical tip could be used. Additionally, at position 15 a failure of the electronic data logging system occurred, and the gathered data were deleted. In consequence, only data from twelve of the twenty-six positions (pos. 15-26) using the cylindrical tip remained (Fig. C.2). Each position was measured five times at approximately the same position, however, drifting had been noticed and has probably caused deviations in the results. This led to 58 deployments of which eleven were disturbed by inclined impacts and were not processed. The pore pressure sensor failed due to a filter problem at position 23 and could not be interpreted at the following positions. Due to the number of disturbances and problems and the fact that no complementing measurements with the standard conical tip were recorded, it was resigned to carry

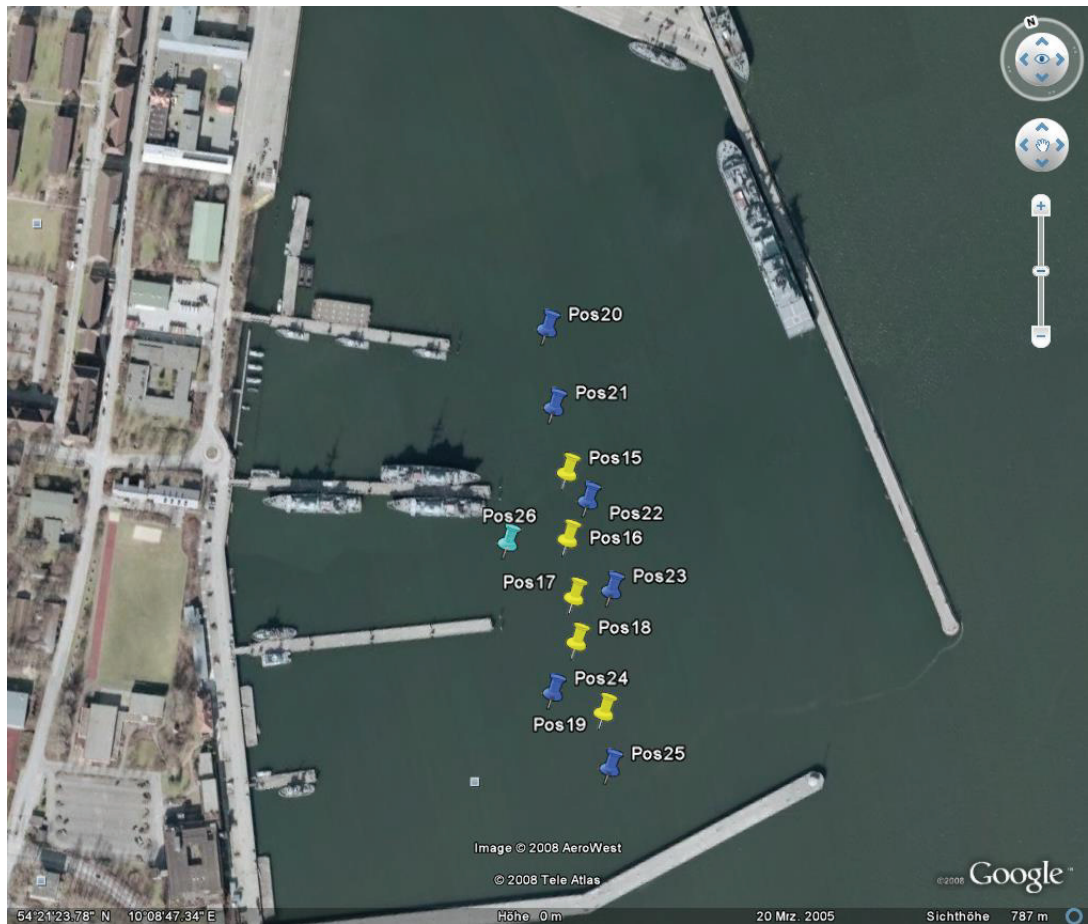


Figure C.2: Google Earth image showing the positions 15 - 26 in the *Tirpitzhafen* in Kiel. The lower left corner corresponds to the coordinates $54^{\circ} 21' 23.78''$ N and $10^{\circ} 09' 47.34''$ E.

out a detailed data processing.

C.3 Kaneohe Bay, HI

During the research stay in Hawaii, *Nimrod* measurements have been carried out in the framework of a collaboration with Charles Bachmann (ONR). At five positions (Fig. C.3), two deployments were made in a water depth of about 1 m, respectively. Kaneohe Bay is characterized by muddy sediments close to the shore. The unprocessed results are shown in Tab. C.2.

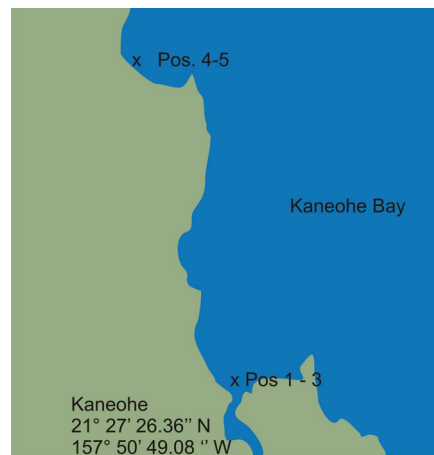


Figure C.3: Sketch of Kaneohe Bay indicating the deployment areas. The positions 1 - 3 and the positions 4 - 5, respectively, are located in a distance of only a few meters from each other.

Pos.	Deceleration (g)	Impact velocity (m/s)	Penetration depth (m)
1	2	2	0.26
2	28	10	0.69
3	39	9	0.28
4	56	9	0.34
5	60	10	0.28

Table C.2: *Nimrod* results from Kaneohe Bay averaged over two deployments at the same position.

C.4 Lake Tarawera, NZ

In the framework of the collaboration with David Hamilton (University of Waikato), *Nimrod* was deployed at 26 positions in Lake Tarawera (Fig. C.4). At each position two deployments were made. The results averaged per position are presented in Tab. C.3.

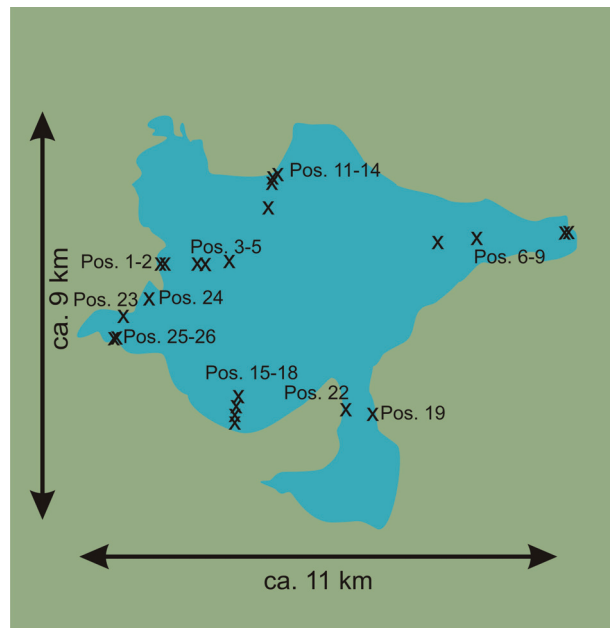


Figure C.4: Sketch of Lake Tarawera indicating the deployment areas.

Pos.	Water depth (m)	Deceleration (g)	Impact velocity (m/s)	Penetration depth (m)
1	10.2	26	9	1.0
2	20.1	4	8	1.8
3	40.8	3	6	1.1
4	60.1	4	5	1.5
5	80.0	3	3	0.6
6	60.8	3	4	0.6
7	40.6	4	5	0.6
8	19.7	24	4	0.1
9	7.8	16	5	0.3
10	12.5			
11	22.6	36	5	0.1
12	40.7	25	4	0.1
13	59.5	3	5	0.7
14	80.5	3	4	0.7
15	56.7	70	5	0.1
16	41.3	4	6	0.9
17	21.0	19	8	0.7
18	10.2	9	9	1.3
19	10.5	55	8	1.5
20	24.4	28	5	0.2
21	24.4	11	6	0.5
22	10.1	11	1	0
23	10.2			
24	20.4	2	1	0
25	20.1	40	8	1.0
26	9.9	32	8	0.6

Table C.3: *Nimrod* results from Lake Tarawera averaged over two deployments at the same position. Some results were disturbed by an unknown cause (no data or low impact velocities).

C.5 Port of Taranaki, New Plymouth, NZ

Nimrod measurements were carried out in the Port of Taranaki, New Plymouth, NZ. 68 deployments were done at 34 positions along 5 transects (Fig. C.5). The unprocessed results are listed in Tab. C.4. The results have not been correlated to the coordinates, however an assignment to the transects was made. Due to time issues, the surveying of transect 2 and 4 was kept short. Layering occurred at some places, but has not been interpreted.

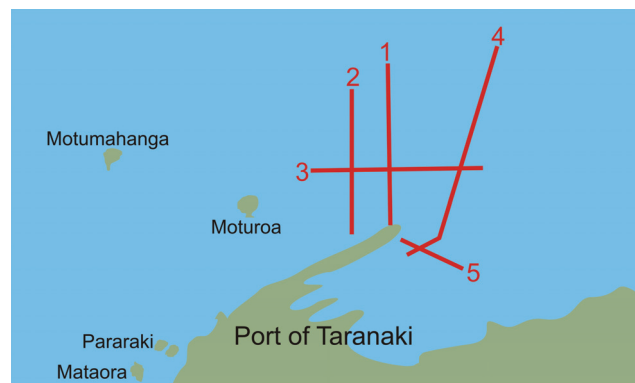


Figure C.5: Sketch of survey transects in the Port of Taranaki. For orientation, the island Moturoa is located at $39^{\circ} 02' 57.47''$ S and $174^{\circ} 01' 39.17''$ E.

Transect No.	Water depth (m)	Deceleration (g)	Impact velocity (m/s)	Penetration depth (m)
1		14	9	1.7
1	15.2	8	0.0	
1	15.8	97	10	0.1
1	17.1	83	10	0.1
1	17.3	59	9	0.1
1	17.8	87	9	0.1
1	18.4	80	9	0.3
1	17.9	124	7	0.1
1	17.3	105	6	0.0
1	18.8	230	10	0.0
1	18.9	144	9	0.1
1	20.0	6	1	0.0
1	5.6	180	9	0.1
2	19.0	2	1	0.0
2	20.3	4	1	0.0
2	5.4	9	1	0.0
3	11.0	153	8	0.1
3	17.5	126	7	0.1
3	19.3	163	7	0.1
3	21.6	137	7	0.1
3	23.6	132	8	0.1
3	16.2	1	2	0.3
3	15.7	143	7	0.1
3	15.3	125	7	0.1
3	15.6	133	8	0.1
3	16.5	15	4	0.1
3	17.0	1	4	1.7
3	17.0	32	1	0.3
4	16.8	66	9	0.1
4	9.3	62	7	0.3
5	2.3	5	4	0.1
5	14.5	18	8	0.6
5	14.5	71	3	0.1
5	10.6	7	2	0.2

Table C.4: *Nimrod* results from the Port of Taranaki averaged over two deployments at the same position. The data express the maximum of the respective property at the respective position. Some results were disturbed by an unknown cause (low impact velocities).

C.6 Port of Tauranga, NZ, 2010

The survey in the Stella Passage in Port of Tauranga (see chapter 5.2.1) was repeated in March 2010. Again a western, a middle and an eastern transect were measured using *Nimrod*. Two deployments were done at each position: one with a slow impact velocity and one truly free-falling. The data was provided to the INTERCOAST IC10 project and has not been processed. The deployment coordinates are listed in Tab. C.5.

No.	Lat	Long	Time	Water depth (m)
1	37° 39' 52"	176° 10' 56"	11:29	11.9
2	37° 39' 57"	176° 10' 56"	11:32	11.1
3	37° 39' 67"	176° 10' 54"	11:35	14.4
4	37° 39' 81"	176° 10' 50"	11:38	14.9
5	37° 39' 88"	176° 10' 50"	11:40	14.9
6	37° 39' 52"	176° 10' 71"	11:44	12.5
7	37° 39' 60"	176° 10' 69"	11:46	12.5
8	37° 39' 70"	176° 10' 67"	11:48	12.7
9	37° 39' 83"	176° 10' 63"	11:51	12.5
10	37° 39' 90"	176° 10' 61"	11:53	12.7
11	37° 39' 50"	176° 10' 85"	11:57	13.0
12	37° 39' 61"	176° 10' 82"	12:00	10.6
13	37° 39' 71"	176° 10' 81"	12:02	10.6
14	37° 39' 84"	176° 10' 76"	12:05	12.3
15	37° 39' 92"	176° 10' 74"	12:08	12.0

Table C.5: *Nimrod* deployment list from Port of Tauranga March 12, 2010.

C.7 Lake Rotoiti, NZ: crater and geothermal area

In March 2010, *Nimrod* measurements were carried in the Lake Rotoiti crater (Pos. 8-10) and potentially geothermal area (Pos. 11-33). The results (Tab. C.6) and a preliminary interpretation (Fig. C.6 and Fig. C.7) were provided to Lisa Pearson who investigates the development of the geothermal zones of Lake Rotoiti.

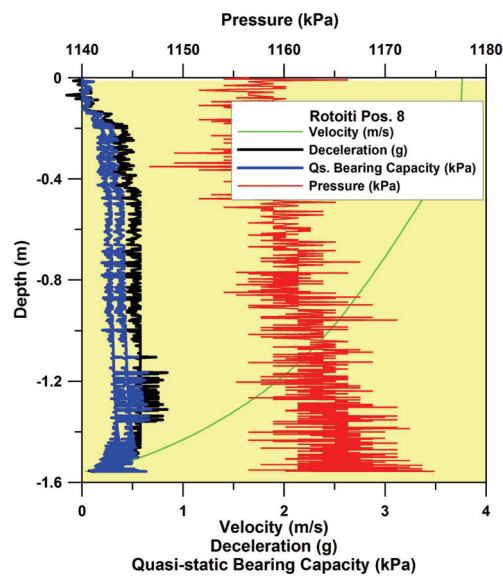


Figure C.6: *Nimrod* result from the crater area in Lake Rotoiti (Pos. 8): Mostly very soft mud. The crater might work as a sediment trap, and the penetration depth of the device is not big enough to penetrate the whole top layer. Another possibility is that the sediment is loosened up by geothermal activity.

No.	Lat	Long	Water depth (m)	Deceleration (g)	Impact Velocity (m/s)	Penetration Depth (m)
8	38° 02' 43" S	176° 25' 28" E	120.0	1	4	1.6
9	38° 02' 42" S	176° 25' 29" E	95.8	2	3	0.7
10	38° 02' 44" S	176° 25' 26" E	96.9	2	3	0.8
11	38° 02' 38" S	176° 25' 32" E	75.3	6	4	0.4
12	38° 02' 30" S	176° 25' 40" E	66.9	1	3	0.9
13	38° 02' 23" S	176° 25' 42" E	69.4	2	4	0.7
14	38° 02' 16" S	176° 25' 46" E	63.2	2	4	0.7
15	38° 02' 09" S	176° 25' 45" E	69.4	2	3	0.6
16	38° 02' 03" S	176° 25' 50" E	70.4	1	3	0.7
17	38° 01' 57" S	176° 25' 51" E	68.1	1	4	1.0
18	38° 01' 52" S	176° 25' 52" E	57.2	5	4	0.4
19	38° 01' 49" S	176° 25' 54" E	16.0	43	4	0.1
20	38° 02' 07" S	176° 25' 18" E	48.4	27	3	0.1
21	38° 02' 06" S	176° 25' 23" E	56.7	2	5	1.1
22	38° 02' 06" S	176° 25' 30" E	60.0	3	4	0.9
23	38° 02' 06" S	176° 25' 37" E	64.1	3	4	0.7
24	38° 02' 06" S	176° 25' 43" E	64.8	5	4	0.5
25	38° 02' 07" S	176° 25' 53" E	69.9	2	4	0.8
26	38° 02' 07" S	176° 26' 0" E	65.9	2	4	0.7
27	38° 02' 07" S	176° 26' 08" E	61.1	4	4	0.9
28	38° 02' 07" S	176° 26' 20" E	59.0	2	5	1.0
29	38° 02.018' S	176° 25.694' E	69.1	2	4	0.7
30	38° 02.029' S	176° 25.923' E	69.6	1	4	0.7
31	38° 02.015' S	176° 25.924' E	69.5	1	4	0.9
32	38° 02.075' S	176° 25.733' E	69.9	1	4	1.0
33	38° 01.999' S	176° 25.825' E	70.5	1	4	1.0

Table C.6: *Nimrod* data and deployment positions in the crater and geothermal areas in Lake Rotoiti, 2010.

C.8. LAKE ROTORUA, NZ: POCKMARKS AND GEOTHERMAL AREA 293

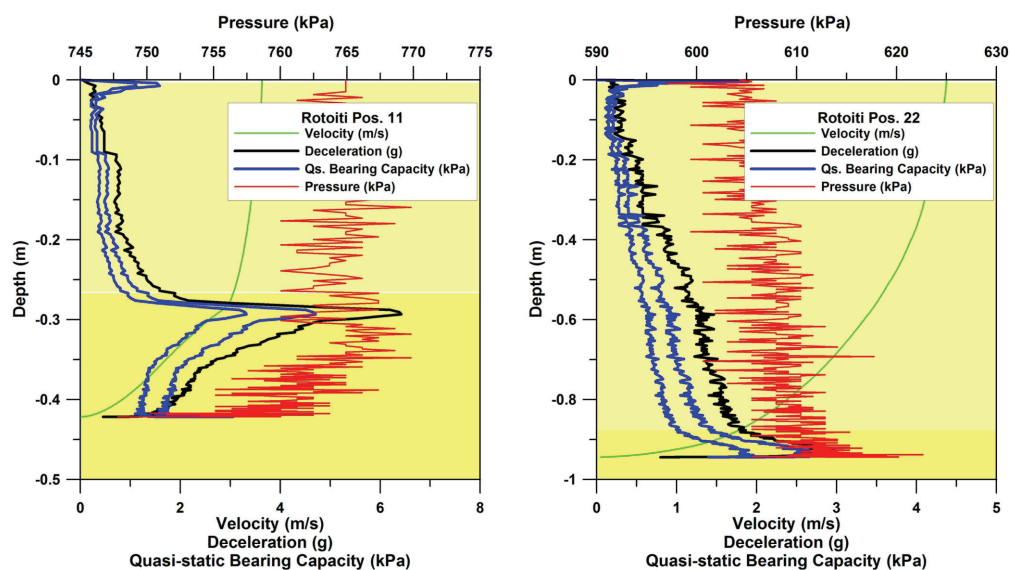


Figure C.7: *Nimrod* results from the potentially geothermal area in Lake Rotoiti (Pos. 11 and 22): Above all, very soft surface sediment. If the very soft top layer can be completely penetrated a soft muddy underground can be found. Very hard spots can be found at position 19 and 20 (Tab. C.6). Subhydrostatic pressure (gas in the sediment?) was detected at spot 11.

C.8 Lake Rotorua, NZ: pockmarks and geothermal area

In March 2010, *Nimrod* measurements were carried in Lake Rotorua's geothermal zone (Pos. 1-5) and in some of Lake Rotorua's pockmarks (Pos. 6-18). The results (Tab. C.7) and a preliminary interpretation (Fig. C.8 and Fig. C.9) were provided to Chris Hendy and Lisa Pearson for student projects.

No.	Lat	Long	Water depth (m)	Deceleration (g)	Impact Velocity (m/s)	Penetration Depth (m)
1	38° 07.679' S	176° 15.963' E	35.7	3	4	0.7
2	38° 07.631' S	176° 15.981' E	46.1	1	5	1.3
3	38° 07.541' S	176° 16.008' E	28.0	7	4	0.7
4	38° 07.385' S	176° 16.025' E	32.4	1	5	1.7
5	38° 07.300' S	176° 15.997' E	47.7	1	3	0.8
6	38° 05' 37" S	176° 16' 13" E	26.3	3	5	0.6
7	38° 05' 36" S	176° 16' 13" E	24.0	3	5	0.7
8	38° 05' 36" S	176° 16' 14" E	21.1	2	6	2.1
9	38° 05' 35" S	176° 16' 14" E	20.8	1	5	1.7
10	38° 04' 53" S	176° 15' 30" E	16.3	2	6	1.7
11	38° 04' 51" S	176° 15' 32" E	16.2	2	6	1.8
12	38° 04' 54" S	176° 16' 10" E	21.4	2	5	1.6
13	38° 04' 53" S	176° 16' 11" E	25.4	5	5	0.5
14	38° 04' 52" S	176° 16' 12" E	21.1	2	6	2.0
15	38° 04' 33" S	176° 16' 44" E	11.0	59	7	0.1
16	38° 04' 32" S	176° 16' 45" E	10.5	53	5	0.1
17	38° 04' 16" S	176° 16' 01" E	18.0	2	6	1.8
18	38° 04' 14" S	176° 16' 01" E	17.8	2	6	1.8

Table C.7: *Nimrod* data and deployment positions in the geothermal area (Pos. 1 - 5) and 5 pockmarks of Lake Rotorua, 2010.

C.8. LAKE ROTORUA, NZ: POCKMARKS AND GEOTHERMAL AREA 295

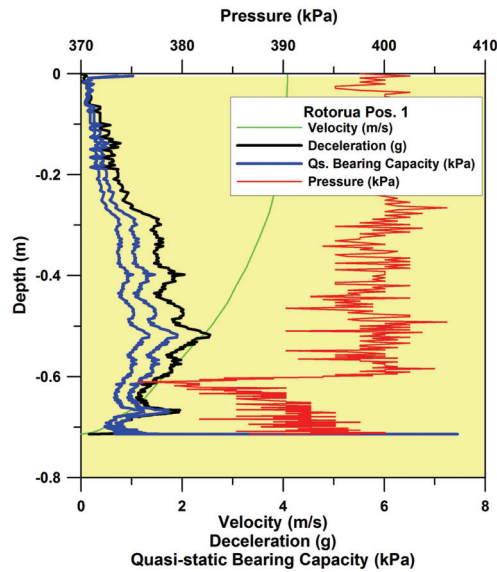


Figure C.8: *Nimrod* result from the geothermal area in Lake Rotorua (Pos. 1): Mainly very soft mud (qs BC 0.7–1.5 kPa). At the cold springs subhydrostatic pressures can be detected.

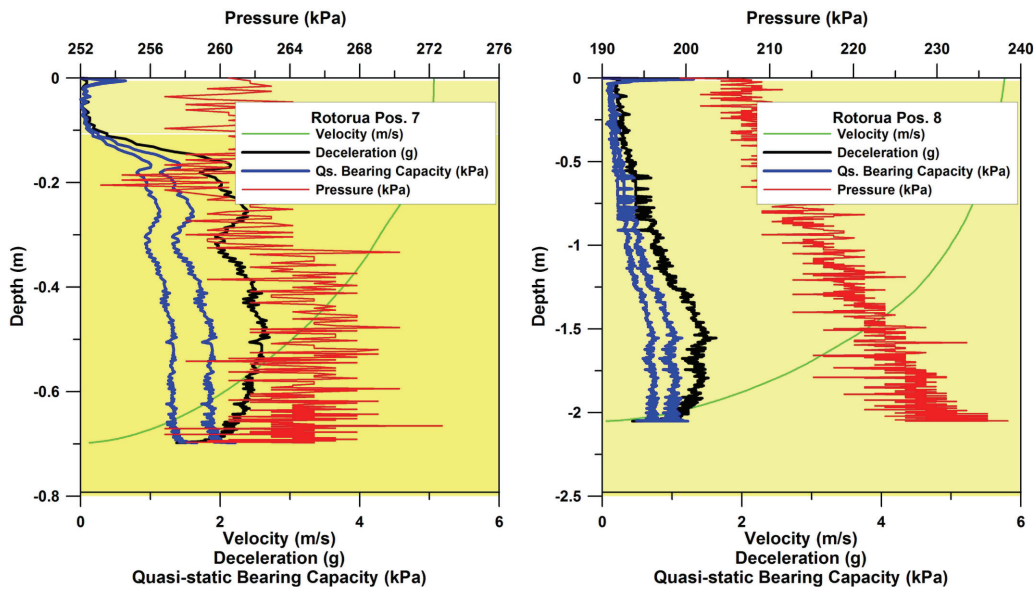


Figure C.9: *Nimrod* result from inside (left) and outside (right) of a pockmark in Lake Rotorua (Pos. 7 and 8): The pockmarks show different results. Inside pockmark 1 stiffer (qs BC 1.7 kPa) sediment with layering (0.1 m thickness) can be found and outside soft sediment with qs. BC ranging from 0.7-0.8 kPa.

Appendix D

Penetrometer raw data

The penetrometer raw data used in this thesis is in preparation for upload to *Pangaea - Publishing network for geoscientific and environmental data* (www.pangaea.de).

Appendix E

FLAC3D input code example

In this chapter an example of the used FLAC3D code for (i) generation of the grid, constitutive model and initialization of the soil and the penetrometer with their interfaces (initial-cshell-60.dat), and for (ii) execution of a model run (bench-01-cshell-60.dat) are given.

initial-cshell-60.dat

```
new
;-----
;define FISH functions
;-----

;define variables
def def-var
;set cone radius [m]
cone-rad=0.055
;set velocity of penetrometer (constant)
vel-pen=-5e-5
;set point of origin for the model (sediment surface, axis of rotation)
x-o=0
y-o=0
z-o=0
;set overall model dimensions (length, width and depth [m])
dim-x=1
dim-y=1
dim-z=0.6
;set model type (1=full model,2=quarter of model)
mod-type=1
;set mesh shape (1=radial cylinder,2=cylindrical shell,3=cylindrical shell inside
cylindrical shell)
mesh-shape=2
;set sediment density
sed-dens=2000
;set nimrod density
nim-dens=4000
;set constitutive model (1=mohr, ...??)
const-mod=1
```

```

;set properties for mechanical model
if const-mod = 1
command
macro prop-mohr bulk 6e6 shear 3e6 coh 40 fric 24 dilation 0 tens 0
macro prop-nim bulk 1e8 shear 1e8 coh 0 fric 10 dilation 0 tens 0
endcommand
endif
; INITIALISATION for grid generation
;set number of zones for inner mesh (has to be an even number!!!)
;-> note: inner mesh is double the size of penetrometer radius
inner-zone=10
inner-zone-2=1
;set number of zones for outer mesh
outer-zone=20
outer-zone-2=10
;set number of zones for y dimension
y-zone=5
;set number of zones for z dimension
z-zone=10
;set spacing ratio for zones
rat-inner=1
rat-outer=1.05
rat-outer-2=1
rat-z=1
rat-y=1
;set radius for inner element
hole=0.005
;set temporary variables for grid generation
p1-x=x-o+dim-x
p2-z=z-o-dim-z
p3-y=y-o+dim-y
p8-x=x-o+2*cone-rad
p9-y=y-o+2*cone-rad
p8-x-2=x-o+hole
p9-y-2=y-o+hole
dims=hole

; INITIALISATION for nimrod generation
nim-length=1
dist-nim-sed=0.5
nim-x-zone=10
nim-y-zone=10
nim-z-zone=5
rad-increment=cone-rad/nim-x-zone
math=3.1754264805e-3
end

;generate model grid
;-----
def gen-grid
;create grid
if mesh-shape = 1
command
gen zone radcylinder p0 (x-o,y-o,z-o) &
p1 (p1-x,y-o,z-o) &
p2 (x-o,y-o,p2-z) &
p3 (x-o,p3-y,z-o) &

```

```

p4 (p1-x,y-o,p2-z) &
p5 (x-o,p3-y,p2-z) &
p6 (p1-x,p3-y,z-o) &
p7 (p1-x,p3-y,p2-z) &
p8 (p8-x,y-o,z-o) &
p9 (x-o,p9-y,z-o) &
p10 (p8-x,y-o,p2-z) &
p11 (x-o,p9-y,p2-z) &
size inner-zone z-zone y-zone outer-zone &
ratio rat-inner rat-z rat-y rat-outer &
dim dims dims dims dims fill
endcommand
else
if mesh-shape = 2
command
gen zone cshell p0 (x-o,y-o,z-o) &
p1 (p1-x,y-o,z-o) &
p2 (x-o,y-o,p2-z) &
p3 (x-o,p3-y,z-o) &
p4 (p1-x,y-o,p2-z) &
p5 (x-o,p3-y,p2-z) &
p8 (p8-x,y-o,z-o) &
p9 (x-o,p9-y,z-o) &
p10 (p8-x,y-o,p2-z) &
p11 (x-o,p9-y,p2-z) &
size outer-zone z-zone y-zone inner-zone &
ratio rat-outer rat-z rat-y rat-inner &
dim dims dims dims dims fill
endcommand
else
if mesh-shape = 3
command
gen zone cshell p0 (x-o,y-o,z-o) &
p1 (p1-x,y-o,z-o) &
p2 (x-o,y-o,p2-z) &
p3 (x-o,p3-y,z-o) &
p4 (p1-x,y-o,p2-z) &
p5 (x-o,p3-y,p2-z) &
p8 (p8-x,y-o,z-o) &
p9 (x-o,p9-y,z-o) &
p10 (p8-x,y-o,p2-z) &
p11 (x-o,p9-y,p2-z) &
size outer-zone z-zone y-zone inner-zone &
ratio rat-outer rat-z rat-y rat-inner &
dim dims dims dims dims
gen zone cshell p0 (x-o,y-o,z-o) &
p1 (p8-x,y-o,z-o) &
p2 (x-o,y-o,p2-z) &
p3 (x-o,p9-y,z-o) &
p4 (p8-x,y-o,p2-z) &
p5 (x-o,p9-y,p2-z) &
p8 (p8-x-2,y-o,z-o) &

```

```

p9 (x-o,p9-y-2,z-o) &
p10 (p8-x-2,y-o,p2-z) &
p11 (x-o,p9-y-2,p2-z) &
size outer-zone-2 z-zone y-zone inner-zone-2 &
ratio rat-outer-2 rat-z rat-y rat-inner &
dim dims dims dims dims
endcommand
endif
endif
endif
;create full model if desired
if mod-type = 1
command
gen zone reflect dip 90 dd 90
gen zone reflect dip 90 dd 0
endcommand
endif
;specify the group created (marine sediment)
command
group sediment
endcommand

;generate nimrod grid
pn-z=z-o+nim-length+dist-nim-sed
pn2-z=z-o+dist-nim-sed
pn-x=x-o+cone-rad
pn-y=y-o+cone-rad
command
gen zone cylinder p0 (x-o,y-o,pn-z) &
p1 (pn-x,y-o,pn-z) &
p2 (x-o,y-o,pn2-z) &
p3 (x-o,pn-y,pn-z) &
p4 (pn-x,y-o,pn2-z) &
p5 (x-o,pn-y,pn2-z) &
size nim-x-zone nim-z-zone nim-y-zone &
ratio rat-inner rat-z rat-y
endcommand
;specify the group created (marine sediment)
command
group nimrod range group sediment not
endcommand
;create full model if desired
if mod-type = 1
command
gen zone reflect dip 90 dd 90 range group nimrod
group nimrod range group sediment not
gen zone reflect dip 90 dd 0 range group nimrod
group nimrod range group sediment not
endcommand
endif
end

;assign constitutive model and properties
;


---


def ass-props
;assign constitutive model

```

```

command
model mohr
prop prop-mohr range group sediment
ini dens sed-dens range group sediment
prop prop-nim range group nimrod
ini dens nim-dens range group nimrod
endcommand
end

;create interfaces
;-----
def interfaces
int-nim-lower=z-o+dist-nim-sed-0.01
int-nim-upper=z-o+dist-nim-sed+nim-length+0.01
command
interface 1 face range z int-nim-lower int-nim-upper
int 1 prop ks 1e8 kn 1e8 fric 0
endcommand
end

;assign velocity ranges for cone penetration
;-----
def vel-ranges
;generate ranges for velocity assignment
ad1=gp-near(x-o,y-o,pn2-z)
id1=gp-id(ad1)
counter-end=nim-x-zone+1
counter=0
rad-temp=rad-increment/10
z-l=pn2-z-0.005
z-u=pn2-z+0.005
loop while counter counter-end
r-name='r'+string(counter)
command
range name @ r-name cylinder end1 x-o y-o z-l end2 x-o y-o z-u radius rad-temp
fix x y range @ r-name
endcommand
counter=counter+1
rad-temp=rad-temp+rad-increment
endloop
end

;calculate profile
def bla
whilestepping
z-disp=pn2-z-gp-zpos(ad1)
counter-end=nim-x-zone+1
counter=1
loop while counter counter-end
r-name='r'+string(counter)
if z-disp >= (counter)*math
command
ini zvel vel-pen range @ r-name
fix zvel vel-pen range @ r-name
endcommand
endif
counter=counter+1

```

```

endloop
end

;-----
;call FISH functions
;-----
def-var
gen-grid
ass-props
vel-ranges

ini zvel vel-pen range r0
fix zvel vel-pen range r0

set large

bla

cycle 2000

ini z add -0.38 range group nimrod

plot create view-int
plot add surface lgreen range group sediment
plot add surface lblue range group nimrod
plot add interface red
plot show

set fishcall 0 remove bla

ini zvel vel-pen range group nimrod
fix zvel vel-pen range group nimrod

;fix x range x -0.001 0.001
;fix y range y -0.001 0.001
fix x y z range z -0.599 -0.601

hist n=1
hist gp zdisp id=1

save initial-cshell-60.sav

bench-01-cshell-60.dat

new

;restore initially created file (source: initial-hole.dat)
restore initial-cshell-60.sav

set fishcall 0 remove bla

;DEFINE VARIABLES
def ini-var
;gravity option (1=gravity,other=no gravity)
grav-opt = 0
if grav-opt = 1
command

```

```

endcommand
endif
;interface option (1=nimrod+sediment,other=nimrod only)
int-opt = 0
;nimrod variables
bulk-nim = 1e12
shear-nim = 1e12
coh-nim = 0
fric-nim = 10
dil-nim = 0
tens-nim = 0
dens-nim = 6000
;velocity nimrod
command
set vel-pen = -5e-7
ini zvel vel-pen range group nimrod
fix zvel vel-pen range group nimrod
endcommand
;nimrod interface
command
interface 1 face range z 0.001 2
int 1 prop ks 1e10 kn 1e10 fric 5
endcommand
;sediment variables
bulk-sed = 6e7
shear-sed = 3e7
coh-sed = 0
fric-sed = 34
dil-sed = 0
tens-sed = 0
dens-sed = 2000
;sediment interface
if int-opt = 1
command
interface 2 face range z -0.601 0.001
int 2 prop ks 6e6 kn 3e6 fric 24
endcommand
endif
end

```

```

;ASSIGN PROPERTIES

```

```

def assign-properties
command
model mohr
prop bulk bulk-sed shear shear-sed coh coh-sed fric fric-sed dilation dil-sed tens
tens-sed range group sediment
ini dens dens-sed range group sediment
prop bulk bulk-nim shear shear-nim coh coh-nim fric fric-nim dilation dil-nim tens
tens-nim range group nimrod
ini dens dens-nim range group nimrod
endcommand

```

end

;BOUNDARY CONDITIONS

def bound-con

command

range name outer cylinder end1 0 0 -0.7 end2 0 0 2 radius 0.99 not

fix x y range outer

fix x y z range z -0.599 -0.601

fix x y range group nimrod

ini xvel 0 range group nimrod

fix xvel range group nimrod

ini yvel 0 range group nimrod

fix yvel range group nimrod

endcommand

end

;PROGRAM RUN

def run

command

hist gp disp 0 0 0

hist gp force 0 0 0

hist gp xdisp 0 0 0

hist gp xf 0 0 0

hist gp xvel 0 0 0

hist gp ydisp 0 0 0

hist gp yf 0 0 0

hist gp yvel 0 0 0

hist gp zdisp 0 0 0

hist gp zf 0 0 0

hist gp zvel 0 0 0

hist zo smax 0 0 0

hist zo smid 0 0 0

hist zo smin 0 0 0

hist zo ssi 0 0 0

hist zo SSR 0 0 0

hist zo sxx 0 0 0

hist zo sxy 0 0 0

hist zo sxz 0 0 0

hist zo syx 0 0 0

hist zo syz 0 0 0

hist zo szz 0 0 0

```
hist zo vsi 0 0 0
hist zo vsr 0 0 0

hist rat
hist unb

hist n 1000
endcommand

loop n(1,1000)
str="bench-01-cshell-60" + string(n) + ".sav"
command
cycle 5000
save str
endcommand
endloop

end

;-----
;call fish functions
ini-var
assign-properties
bound-con

ini z add -0.015 range group nimrod

set fishcall 0 remove bla

run
```


Appendix F

Erklärung

Hiermit versichere ich, dass ich

1. die Arbeit ohne unerlaubte fremde Hilfe angefertigt habe.
2. keine anderen als die von mir angegebenen Quellen und Hilfsmittel verwendet habe.
3. die den benutzten Werken wörtlich oder inhaltlich entnommenen Stellen als solche kenntlich gemacht habe.

Bremen, den 01.09.2010

(Nina Stark)